1994

Computer simulation of particle matrix interactions in silicon carbide reinforced aluminium metal matrix composites.

Xiao Qun. Xu
University of Windsor

NOTICE

The quality of this microform is heavily dependent upon the quality of the original thesis submitted for microfilming. Every effort has been made to ensure the highest quality of reproduction possible.

If pages are missing, contact the university which granted the degree.

Some pages may have indistinct print especially if the original pages were typed with a poor typewriter ribbon or if the university sent us an inferior photocopy.

Reproduction in full or in part of this microform is governed by the Canadian Copyright Act, R.S.C. 1970, c. C-30, and subsequent amendments.

AVIS

La qualité de cette microforme dépend grandement de la qualité de la thèse soumise au microfilmage. Nous avons tout fait pour assurer une qualité supérieure de reproduction.

S'il manque des pages, veuillez communiquer avec l'université qui a conféré le grade.

La qualité d'impression de certaines pages peut laisser à désirer, surtout si les pages originales ont été dactylographiées à l'aide d'un ruban usé ou si l'université nous a fait parvenir une photocopie de qualité inférieure.

La reproduction, même partielle, de cette microforme est soumise à la Loi canadienne sur le droit d'auteur, SRC 1970, c. C-30, et ses amendements subséquents.

Canada

COMPUTER SIMULATION OF PARTICLE MATRIX INTERACTIONS IN SiC REINFORCED ALUMINIUM METAL MATRIX COMPOSITES

By
Xiao Qun Xu

A Dissertation
Submitted to the Faculty of Graduate Studies and Research
Through the Engineering Materials Program in the
Department of Mechanical Engineering in
Partial Fulfilment of the Requirements for
The Degree of Doctor of Philosophy at the
University of Windsor

Windsor, Ontario, Canada
January, 1994

ISBN 0-315-93322-4

Name _____

Dissertation Abstracts International is arranged by broad, general subject categories. Please select the one subject which most nearly describes the content of your dissertation. Enter the corresponding four-digit code in the spaces provided.

Materials Science

SUBJECT TERM

0	7	4	4

SUBJECT CODE

U·M·I

Subject Categories

THE HUMANITIES AND SOCIAL SCIENCES

COMMUNICATIONS AND THE ARTS

Architecture	0729
Art History	0377
Cinema	0900
Dance	0378
Fine Arts	0357
Information Science	0723
Journalism	0391
Library Science	0399
Mass Communications	0708
Music	0413
Speech Communication	0459
Theater	0465

EDUCATION

General	0515
Administration	0514
Adult and Continuing	0516
Agricultural	0517
Art	0273
Bilingual and Multicultural	0282
Business	0688
Community College	0275
Curriculum and Instruction	0727
Early Childhood	0518
Elementary	0524
Finance	0277
Guidance and Counseling	0519
Health	0680
Higher	0745
History of	0520
Home Economics	0278
Industrial	0521
Language and Literature	0279
Mathematics	0280
Music	0522
Philosophy of	0998
Physical	0523
Psychology	0525
Reading	0535
Religious	0527
Sciences	0714
Secondary	0533
Social Sciences	0534
Sociology of	0340
Special	0529
Teacher Training	0530
Technology	0710
Tests and Measurements	0288
Vocational	0747

LANGUAGE, LITERATURE AND LINGUISTICS

Language	
General	0679
Ancient	0289
Linguistics	0290
Modern	0291
Literature	
General	0401
Classical	0294
Comparative	0295
Medieval	0297
Modern	0298
African	0316
American	0591
Asian	0305
Canadian (English)	0352
Canadian (French)	0355
English	0593
Germanic	0311
Latin American	0312
Middle Eastern	0315
Romance	0313
Slavic and East European	0314

PHILOSOPHY, RELIGION AND THEOLOGY

Philosophy	0422
Religion	
General	0318
Biblical Studies	0321
Clergy	0319
History of	0320
Philosophy of	0322
Theology	0469

SOCIAL SCIENCES

American Studies	0323
Anthropology	
Archaeology	0324
Cultural	0326
Physical	0327
Business Administration	
General	0310
Accounting	0272
Banking	0770
Management	0454
Marketing	0338
Canadian Studies	0385
Economics	
General	0501
Agricultural	0503
Commerce-Business	0505
Finance	0508
History	0509
Labor	0510
Theory	0511
Folklore	0358
Geography	0366
Gerontology	0351
History	
General	0578
Ancient	0579
Medieval	0581
Modern	0582
Black	0328
African	0331
Asia, Australia and Oceania	0332
Canadian	0334
European	0335
Latin American	0336
Middle Eastern	0333
United States	0337
History of Science	0585
Law	0398
Political Science	
General	0615
International Law and Relations	0616
Public Administration	0617
Recreation	0814
Social Work	0452
Sociology	
General	0626
Criminology and Penology	0627
Demography	0938
Ethnic and Racial Studies	0631
Individual and Family Studies	0628
Industrial and Labor Relations	0629
Public and Social Welfare	0630
Social Structure and Development	0700
Theory and Methods	0344
Transportation	0709
Urban and Regional Planning	0999
Women's Studies	0453

THE SCIENCES AND ENGINEERING

BIOLOGICAL SCIENCES

Agriculture	
General	0473
Agronomy	0285
Animal Culture and Nutrition	0475
Animal Pathology	0476
Food Science and Technology	0359
Forestry and Wildlife	0478
Plant Culture	0479
Plant Pathology	0480
Plant Physiology	0817
Range Management	0777
Wood Technology	0746
Biology	
General	0306
Anatomy	0287
Biostatistics	0308
Botany	0309
Cell	0379
Ecology	0329
Entomology	0353
Genetics	0369
Limnology	0793
Microbiology	0410
Molecular	0307
Neuroscience	0317
Oceanography	0416
Physiology	0433
Radiation	0821
Veterinary Science	0778
Zoology	0472
Biophysics	
General	0786
Medical	0760

EARTH SCIENCES

Biogeochemistry	0425
Geochemistry	0996
Geodesy	0370
Geology	0372
Geophysics	0373
Hydrology	0388
Mineralogy	0411
Paleobotany	0345
Paleoecology	0426
Paleontology	0418
Paleozoology	0985
Palynology	0427
Physical Geography	0368
Physical Oceanography	0415

HEALTH AND ENVIRONMENTAL SCIENCES

Environmental Sciences	0768
Health Sciences	
General	0566
Audiology	0300
Chemotherapy	0992
Dentistry	0567
Education	0350
Hospital Management	0769
Human Development	0758
Immunology	0982
Medicine and Surgery	0564
Mental Health	0347
Nursing	0569
Nutrition	0570
Obstetrics and Gynecology	0380
Occupational Health and Therapy	0354
Ophthalmology	0381
Pathology	0571
Pharmacology	0419
Pharmacy	0572
Physical Therapy	0382
Public Health	0573
Radiology	0574
Recreation	0575
Speech Pathology	0460
Toxicology	0383
Home Economics	0386

PHYSICAL SCIENCES

Pure Sciences

Chemistry	
General	0485
Agricultural	0749
Analytical	0486
Biochemistry	0487
Inorganic	0488
Nuclear	0738
Organic	0490
Pharmaceutical	0491
Physical	0494
Polymer	0495
Radiation	0754
Mathematics	0405
Physics	
General	0605
Acoustics	0986
Astronomy and Astrophysics	0606
Atmospheric Science	0608
Atomic	0748
Electronics and Electricity	0607
Elementary Particles and High Energy	0798
Fluid and Plasma	0759
Molecular	0609
Nuclear	0610
Optics	0752
Radiation	0756
Solid State	0611
Statistics	0463

Applied Sciences

Applied Mechanics	0346
Computer Science	0984
Engineering	
General	0537
Aerospace	0538
Agricultural	0539
Automotive	0540
Biomedical	0541
Chemical	0542
Civil	0543
Electronics and Electrical	0544
Heat and Thermodynamics	0348
Hydraulic	0545
Industrial	0546
Marine	0547
Materials Science	0794
Mechanical	0548
Metallurgy	0743
Mining	0551
Nuclear	0552
Packaging	0549
Petroleum	0765
Sanitary and Municipal	0554
System Science	0790
Geotechnology	0428
Operations Research	0796
Plastics Technology	0795
Textile Technology	0994

PSYCHOLOGY

General	0621
Behavioral	0384
Clinical	0622
Developmental	0620
Experimental	0623
Industrial	0624
Personality	0625
Physiological	0989
Psychobiology	0349
Psychometrics	0632
Social	0451

To my dear husband

Without his understanding, encouragement and love, the fulfilment of this dissertation would not have been possible.

ABSTRACT

The present work aims at understanding particle matrix interactions in SiC reinforced aluminium metal matrix composites (MMCs) by means of computer simulation. Firstly, to explore the basic role of hard particles, the stress field around a spherical SiC particle, the stress and the energy gathering capabilities of particle, interfacial characteristics, and the particle size effect have been examined by applying and extending Eshelby's classic approach. Secondly, a new method has been developed to calculate the inhomogeneity problem with an arbitrary shaped particle. This method combines boundary integral equations with a sequence of cutting, straining, and welding procedures to numerically acquire stress and strain distribution at an inhomogeneity. Thirdly, an elastic-plastic FEA has been used to investigate the plastic behaviour of the matrix (i.e. plastic relaxation and plastic accumulation) and its effect on the stress transfer and the stress concentration. Fourth, the influence of the volume fraction, the particle shape, the particle clustering, the particle size, and thermally induced residual stresses on deformation characteristics of Al/$(SiC)_p$ MMCs has been studied by using FEA and applying the concept of the Flower-Watt unit cell. Fifth, the ductility of MMCs has been discussed. It has been found that the major distinctions between MMCs and unreinforced alloys are the mechanisms of the stress transfer to the particles, the enhanced work hardening in the matrix, and the significant contribution of the triaxial stress to the stored strain energy. These characteristics of the MMCs give them their high strength, high stiffness and low ductility.

ACKNOWLEDGEMENTS

The author wishes to express her sincere gratitude to Dr. D.F. Watt for his academically inspiring guidance, supervision, suggestions, as well as his encouragement during her graduate study at University of Windsor.

She would like to express her thanks to Dr. N. Zamani for his invaluable help and instruction on finite element analysis.

Special thanks are due to Dr. D.J. Lloyd for his constructive suggestions and discussion as well as for kindly supplying experimental results.

Thanks are also due to Dr. W. W. Sun and Mr. M. Esteghamatian for their assistance on modelling techniques and mathematical approaches, and their helpful discussions.

She is also grateful to Dr. D.O. Northwood, Dr. A. Alpas, Dr. G. Morforton and Dr. J. Goldak for reviewing this dissertation.

She would also like to thank Mrs. Barbara Denomey for arranging her graduate study.

Particular appreciation is expressed to the Metal Matrix Composite Consortium (OCMR-NSERC) for providing financial support for the research.

She is also extremely indebted to her grandmother and her parents for their encouragement and confidence throughout her education.

VOLUME I

TABLE OF CONTENTS

VOLUME II

TABLE OF CONTENTS

NOMENCLATURE

MISES = Von Mises stress

PRESS = effective hydrostatic pressure

S22 = normal stress

E22 = normal strain

SENER = strain energy density

PENER = dissipated energy density (or effective plastic energy density)

S_{ij} = stress components

E_{ij} = strain components

MMCs = metal matrix composites.

$(SiC)_p$ = silicon carbide particles.

FEA = finite element analysis.

FEM = finite element method.

BIE = boundary integral equation.

BEM = boundary element method.

U_i = displacement components.

a = particle radius.

F = field variable.

F_0 = uniform field variable (or far field variable).

E = Young's modulus of particles.

E_0 = Young's modulus of matrix.

p_{ij}, e_{ij} = elastic stress and strain components, respectively.

p'_{ij}, e'_{ij} = deviatoric components of elastic stress and strain, respectively.

^{A} = uniform far field component.

^{T} = phase transformation component.

^{c} = constraint component.

k^*, k = the bulk moduli of the particle and the matrix, respectively.

μ^*, μ = the shear moduli of the particle and the matrix, respectively.

ν = the Poisson ratio of the matrix.

ϕ = the harmonic or Newtonian potential.

ψ = the biharmonic potential.

$_{,i}$ or $_{,j}$ = the derivative with respect to the ith or jth coordinate.

σ_{ij} = stress components.

$R^{(k)}$, $R^{(0)}$ = the particle region and the matrix region, respectively.

$S^{(k)}$, $S^{(0)}$ = the particle surface and the inner matrix region, respectively.

t_j = the surface traction force.

u_j = the displacement components.

U_{ij} = the fundamental displacements.

T_{ij} = the fundamental tractions.

n_j = the surface normals.

$\lambda^{(k)}$, $\lambda^{(0)}$ = elastic constants of the particle and the matrix, respectively.

A_{ij}, a_{ij}, B_{ij}, b_{ij} = the coefficients of the matrices.

$\check{u}_i$, $\check{e}_{ij}$, $\check{p}_{ij}$ = the field components.

$\mathring{u}_i$, $\mathring{e}_{ij}$, $\mathring{p}_{ij}$ = the uniform field components.

$\tilde{u}_i$, $\tilde{e}_{ij}$, $\tilde{p}_{ij}$ = the perturbation field components.

CTE = coefficient of thermal expansion.

ABAQUS = a software package for FEA.

I-DEAS = a software package for mesh generation.

CHAPTER 1

INTRODUCTION

1.1 Al/$(SiC)_p$ Particulate Reinforced Metal Matrix Composites

As a family of potentially new materials, Metal Matrix Composites (MMCs) are defined by Feest[1] as "materials whose microstructures comprise a continuous metallic phase (the matrix) into which a second phase, or phases, have been artificially introduced".

These materials have attracted worldwide attention and industrial interest in the past three decades. The enthusiasm for research on MMCs was stimulated mainly because of:

(1) the potential for achieving materials with much higher stiffness and strength, compared to conventional alloys, in spite of cost[1,2,3,4];

(2) the potential for achieving materials with dimensional, thermal, environmental, and radiative stability and good dynamic performance (e.g. high transverse properties, low coefficient of thermal expansion, good properties at high temperature, great fatigue resistance, etc.), compared to fibre reinforced plastics[1,3,4];

(3) the potential for achieving a comprehensive understanding of the physics and the physical metallurgy of structure-property relationships after a fair amount of experiments and exploratory studies have been completed;

(4) the potential for spurring the development of new processing techniques; (e.g. recently, there have been some outstanding achievements, such as spray technique in processing particulate-reinforced metal matrix composites[2,5,6,7], the technique of

plasma-activated sintering which densifies powder metals and ceramics in seconds[8]).

Specific important applications of MMCs occur in industries such as aerospace, automobiles or robotics, where the use of stiff and lightweight materials can help to meet service criteria. Among those potential MMCs, silicon-carbide particulate reinforced aluminium metal matrix composites Al/$(SiC)_p$ are becoming competitive. For example, in Japan the research on Duralcan particle-reinforced aluminum brake rotors and callipers, aluminum brake disks, and pads coated with a plasma-sprayed aluminum-matrix composite for use in Toyota's AXV-IV experimental ultralight weight commuter vehicle has demonstrated the potential of MMCs[9].

The Al/$(SiC)_p$ MMCs are made from two basic ingredients: aluminum alloys as metal matrices and silicon carbide particles as ceramic reinforcement.

Aluminium production essentially involves two sequential processes[10,11,12]: The Bayer process and the Heroult-Hall process. The Bayer process prepares pure alumina from bauxite ores by digesting the crushed and powdered bauxite with a strong caustic soda solution (Na(OH)) at temperatures up to 240° C. After filtration, dilution and cooling, crystals of the trihydrate $Al(OH)_3$ are precipitated and deposited. Then, the trihydrate is calcined at 1200° C to remove the water and to leave the alumina. Aluminium is produced by electrolysis of alumina in a bath of fused cryolite. The process was devised in 1886 by Heroult and Hall. The cryolite consists of aluminium fluoride and sodium fluoride with alumina solubility of 4-20 wt% at a temperature just below 1000° C. The process uses carbon as a cathode and also carbon as an anode electrode to avoid the strong corrosion of the fluoride solution. At the anode, pure

oxygen gas is liberated, which immediately reacts with the carbon anode material. Aluminium is deposited as a liquid at the cathode. The detailed description can be found in standard text books (e.g. [10,11]). Since the invention of the Heroult-Hall process, the aluminum industry has rapidly grown from a world production of about 100 tons per year in 1890[13] to a present production of over 4 million per year in the U.S. alone and to the usage of an average of 87 kilograms per car in North American-produced automobiles currently[14]. This historical increase in consumption is partially because aluminum exhibits a superior low density of 2.8 g/cm^3, (which is only about one third of that of carbon steel[15] at 7.9 g/cm^3), and the abundance of the aluminum element in the earth's crust[13], which is important in industries such as aerospace and construction, where its corrosion resistance is also a factor. To improve its properties, such as strength, durability, good strength/weight ratio, or castability, etc, conventionally aluminum is alloyed with a small amount of other elements, (e.g. copper, silicon, magnesium, zinc, etc.). For example, 6061 aluminum alloy, the metal matrix this thesis is concerned with, belongs to the aluminum-magnesium-silicon-zinc alloy system (1.0 Mg, 0.6 Si, 0.2 Zn)[16]. Generally, magnesium reduces the alloy density and increases corrosion resistance. Zinc hardens the alloy by a result of the precipitation of an intermediate semicoherent phase based on $MgZn_2$, and silicon with magnesium forms a coherent pre-precipitate based on Mg_2Si. The actual mechanisms of hardening are internal strain hardening due to the coherent strains, chemical hardening due to solute-solvent bonds, or hardening due to a dispersion of non-deforming precipitates, after appropriate heat treatment.

The silicon carbide particle, the reinforcement which usually has α-SiC structure,

also offers a low density of 3.2 g/cm^3, in addition to its relatively high modulus, 450 GPa, compared with 70 GPa for aluminum alloy. These factors favour the use of SiC to improve alloyed composites as a dispersion hardener.

To make discontinuously reinforced Al/(SiC)$_p$ MMCs from aluminum alloy and silicon carbide particles, four fabrication routes may be used; powder metallurgy, squeezing casting, molten metal mixing, and the spray deposition method, all of which have been clearly described in Lloyd's review paper on MMCs[2]. The greatest advantages of these type of materials are their cost-competitive character and near isotropic properties[1,2] when compared to the continuously reinforced MMCs. They can be further easily manufactured by conventional forming processes, (e.g. forging, rolling, extrusion, drawing, machining)

Since heat treatment also benefits the mechanical performance of MMCs, the Al/(SiC)$_p$ may be treated through different thermal paths. The material on which the present modelling is based is 6061-T4 Al/(SiC)$_p$ MMCs, which typically is subjected to the solution and quench procedures. (They are typically solutionized at 540 °C for 4 hours and quenched to and aged at room temperature for at least 16 hours, i.e. T4 temper aging.)[17]

1.2 Research Focus in Present Work

Al/(SiC)$_p$ MMCs, like other MMC systems, exhibit low density, high strength and high stiffness. However, their primary disadvantage is that they suffer from low ductility[18,19], especially when a high volume fraction of reinforcement is involved. Similar

effects have been observed in copper-based alloys and MMCs[20,21], and is closely related to the fact that the discontinuously reinforced composites are not homogeneous and the material properties are sensitive to the properties of each constituent, the interfacial properties, the geometric shape and distribution of the reinforcement, the thermal treatment, etc. The static-tensile mechanical responses of MMCs are a consequence of the details of their microstructures. Experimental work shows that the factors that influence the mechanical properties are:

(1) the volume fraction of reinforcement;

(2) the interparticle spacing (or particle distribution);

(3) the shape of the reinforcing particle;

(4) the size of the reinforcing particle.

Also, the effect of thermal treatment on overall properties needs to be considered. All these and the properties of the particle can affect the effectiveness of the reinforcement.

In other words, inhomogeneity affects almost every aspect of the physical and mechanical responses of MMCs, including stiffness, strength, thermal stability, stress states and plastic flow during loading, extension and fracture, so that to optimize the properties of the promising materials, a full understanding their role is essential.

In Chapter 2, the previous work done in this area is reviewed.

Chapter 3 is devoted to the study of general matrix-particle interactions and stress concentration around an isolated spherical particle (or inclusion) by means of Eshelby's theory. It visualizes the stress fields numerically from the formulation of displacement constraints, in which an aluminum matrix and SiC particle are involved. The interface

characteristics are examined focusing on polar, circumferential and radial perturbations of individual components (i.e. Von Mises stress, mean stress, normal stress, normal strain and strain energy). The constraints by SiC, rigid inclusions and void inclusions on the aluminum metal matrix are considered respectively to emphasis the nature of the functions of particle stiffness nature on stress concentration. The particle size effect is stressed in terms of derivation of the stress and strain fields. Also, the stress gathering capability of an inclusion with a large range of mechanical properties is investigated. General discussion on interactions and stress concentration is emphasized.

Chapter 4 presents a new approach to determine the stress distribution around an arbitrary-shaped inhomogeneity by applying Betti's reciprocal principle. The computational formulation and numerical procedures are derived. Primary physical concepts and major steps are elucidated. As a demonstration, the interaction traction forces around a cubic SiC particle are calculated. Further, a comparison with FEM (finite element method) results is carried out.

Chapter 5 deals with the study of interactions and stress concentrations in Al/$(SiC)_p$ MMCs by FEM with appropriate meshes in order to:

(1) explore the general usage of FEM in micromechanics;

(2) describe the unit cell model of Flower and Watt;

(4) verify the results of FEM with classical field theory at a low volume fractions of $(SiC)_p$ reinforcement.

Chapter 5 is also concerned with the elastic-plastic behaviour of the matrix. The plastic relaxation due to the non-linear behaviour of material at the 0.2% strain yield

point of the composite is studied and it is found that a lower stress carrying capability is calculated in MMCs than that predicted by classical elasticity at the same total strain level. The analysis takes up the further accumulation of plastic deformation in MMCs, and consequent changes in stress concentration at increasing strain levels. The rest of the chapter discusses the general effect of stress concentration on ductility in MMCs.

Chapter 6 deals individually with the key parameters (particle shape, distribution, size, volume fraction) mentioned above, and how these affect the overall mechanical properties in 6061-T4 Al/$(SiC)_p$ MMCs, including the stress-strain curve, material yield, and fracture.

The effect of volume fraction on stress concentration is considered by changing reinforcement densities from 5.0 vol.% to 25.0 vol.% in 5.0 vol.% steps. The stress contour plots are illustrated in Von Mises stress, effective hydrostatic stress, normal stress, normal strain, strain energy and effective plastic energy densities. The overall stress-strain curves are predicted. The results for the low ductility found at high volume fractions of reinforcement are discussed.

The effect of particle shape on stress concentration and static mechanical response is also treated. The comparisons at 1.94 vol.%, 6.18 vol.% and 25.0 vol.% with spherical and cubic reinforcement are illustrated. The change of overall mechanical properties and ductility due to particle shape is stressed.

This is followed by the study of the particle distribution, where the particle clustering is concerned with two aspects: tensile clustering (i.e. clustering along the loading direction) and transverse clustering (i.e. clustering normal to the direction of the

tensile loading). The stress concentrations are illustrated. The significance of avoiding particle clustering during metal manufacture is emphasised due to its consequences of high triaxial stress leading to interfacial bonding failure. Also the determination of the relationship between mechanical behaviour and particle clustering is made.

Chapter 7 takes into account the thermally induced stresses due to the severe difference in coefficients of thermal expansion (CTE). The comparison of overall mechanical properties between model materials with thermal stress and without thermal stress is carried out in order to characterize the microstructural interactions on a more realistic basis.

Chapter 8 gives the conclusions from the present work.

Chapter 9 provides comments on possible further work.

CHAPTER 2

LITERATURE REVIEW ——— The Role of the Second Phase Particle

The unity of opposites philosophically embodies the role of the second phase particles in metal alloys and MMCs. On one hand, the existence of second phase particle provides harder and stronger materials. As a result, the more reinforcement added into the metal matrix, the stiffer the composite gets. On the other hand, second phase particles initiate material damage. The ductility degrades. Each of them works against the other, but in fact the two are coupled in an unsplinterable unity. The compromised integration of the two determines the rules for their use.

To trace the development of practice and theory, the research on the role of the second phase particles is roughly trifurcated into different but closely related branches. They are:

(a) the role of the second phase particles in ductile fracture, in which first-hand experimental observations play the most important role in understanding the mechanisms. The means include the simple tensile test, transmission electronic microscopy, scanning electronic microscopy, X-Ray diffraction, non-destructive testing, neutron diffraction, acoustic emission and chemical analysis;

(b) the role of the second phase particle in material hardening, in which one tries to explain the hardening mechanisms physically. The application of dislocation theory characterizes this branch;

(c) the role of the second phase particle on local stress concentration, in which one relates inclusion and inhomogeneity problems to conventional continuum mechanics.

Progress here correlates to advanced achievements in applying mathematics.

The following is an outline.

2.1 The Role of the Second Phase Particle in Ductile Fracture

It appears that Joseph Henry, of electro-magnetism fame, recognized as early as 1822 that metals fracture prematurely by a process of internal necking when extended by stretching. Tipper[22] (1949), when she investigated the ductile fracture on mild steel, identified fracture as the most interesting of the properties of solids. She found that the internal holes almost certainly originate by the drawing away of the metal from a non-metallic inclusion. The major role played by particles in cavity initiation was later demonstrated by Puttick[23] (1959) who tested polycrystalline copper containing small non-metallic inclusions at the room temperature. By cycling the load level above and below yielding, controlled cavity growth was obtained. His observations on sections, which are cut parallel to the tensile axis, revealed that the extensive internal cavitation always initiated at inclusions either by separation of the particle-matrix interface or by fracture of the inclusions themselves. Once nucleated, the cavities elongate along the tensile axis as shown in Fig. 2.1. The holes expand under the triaxial stresses in the neck and coalescence in a macroscopic fissure.

In the 1960's, the literature concerned with ductile rupture proliferated and established that cavities nucleate at inhomogeneities in metals. There were mainly non-metallic inclusions, precipitates or artificially induced strengthening dispersions. For example, Fig.2.2 shows the typical dimple structure on the fracture surface of a steel

containing very large carbides. It is clear that fracture occurred by the growth of internal cavities and that cavity nucleation occurred around the carbide particles. In other words, tensile fracture of metals involves three stages: (i) void formation; (ii) void growth; and (iii) void coalescence in the neck of a tensile specimen starting from inclusions.

The influence of second phase particles on fracture has been emphasised in all this literature. Among excellent works on the topic, Edelson & Baldwin[20] (1962) reported correctly the effect of volume fraction on ductile rupture by examining copper-based composites. They concluded that all second-phase particles as well as voids were found to embrittle the alloys in a manner which depended upon the volume fraction of second phase only, and further was independent of particle size, shape, and composition. However, much evidence has proven that the particle size[19,21,27,29,32,33], shape[30,31,33], composition[21,26,27], interfacial strength[21,26,27,28] and distribution of the second phase[21,27,34] also strongly affect the material ductility. Despite underestimating the importance of these secondary factors, Edelson and Baldwin were correct in that the particle volume fraction is indeed the most significant factor causing ductile rupture, as shown in Fig. 2.3. Gurland & Plateau[21] (1963) and Gurland & Parikh[27](1969) confirmed that the elongation to rupture depends primarily on the volume fraction of particles. They also stated that only those second phase particles which developed a strong particle-matrix bond strengthened the alloys.

Chin, Hosford & Backofen[28] (1964) took up the influence of "temperature" on the ductile fracture of aluminum. They found that inclusion-free aluminum was ruptured by essentially 100% reduction of area down to temperatures as low as 77 °K, whereas, as

shown in Fig. 2.4(a), in high purity aluminum not treated to be inclusion-free, the reduction of area decreased as the temperature was lowered. These results illustrate the degradation of ductility caused by the second phase, the brittle-ductility transition phenomenon and the correlation of ductility with temperature. They also pointed out that fracture of inclusion-populated materials is nucleated by the formation of voids as the local tensile stress exceeds the strength of the inclusion-matrix interface or of the inclusion itself.

With respect to the thermally induced stress around particles, Liu & Gurland[39] (1965) tested Al-Si alloys at room temperature by x-ray diffraction. They observed that as silicon content increases, the condition in the silicon phase changes from a predominantly compressive to a predominantly tensile state of stress, shown in Fig. 2.5. They also found that the experimental results qualitatively agreed with some simple elastic and elastic-plastic models. From this, two indications can at least be given: one is that the existence of the second phase does cause residual stresses due to the difference of the coefficients of thermal expansion; the other is that the conventional continuum mechanics with thermal coupling can be used to give a reasonable explanation. Although the thermally induced stresses do not directly cause the ductile fracture, local stress concentration caused by differences in CTE was evident.

Palmer, Smith & Warda[29] (1966) carefully investigated the void nucleation process in copper sample containing dispersed silica particles by means of thin-film electron microscopy. By changing the temperatures of oxidation, the particle size of (SiO_2) can be controlled (50 Å - 5000 Å). They found that voids can be nucleated on second-phase

particles as small as 50 Å, particularly at a low testing temperature.These voids formed as small patches which spread over the surface of the particles before increasing in length. Usually two voids appeared on each particle in line with the maximum tensile stress applied to the specimen. Their observation also showed that near the fracture edge many voids had extended considerably in length and grew wider than the particle so that sideways coalescence was taking place. It was postulated that fracture was a consequence of the stresses built up at the interface during plastic deformation, i.e. particles act as barriers against which dislocations can pile up until the strength of the interface between inclusion and matrix is exceeded, so that a crack forms and then grows by plastic deformation. It is reasonable to emphasis the role of localized stress concentrations at the particles.

With respect to the effect of a superimposed hydrostatic pressure on fracture behaviour in general materials, the extensive classical experimental work by Bridgman[40] (1964) has dominated the literature (e.g. Fig. 3.6). By increasing hydrostatic pressure, an increasing fracture stress can be obtained and the reduction in area can improved. The function of hydrostatic tension would be expected to have the opposite influence on ductility. McClintock[37] (1968) pointed out that in plastically deforming materials there is a very strong inverse dependence of fracture strain on hydrostatic tension.

Other key work by Rogers[35] (1960), Beachem[36] (1963) and Ashby[97,98] (1966,1969) also provided an insight into ductile rupture in two phase alloys or composites. The "double-cup" and "cup-cone" failure mechanisms were related to "alternating slip" and further void formation by Rogers, whereas the modes of void coalescence on ductile

rupture surfaces were illustrated and classified as "normal rupture" (where equiaxed dimple are formed), "shear rupture" (where elongated dimples are recognized) and "tearing" by Beachem. Ashby's experiments and models were helpful in understanding the function of the second phase in work-hardening and fracture, which will be reviewed in the next section.

Much experimental evidence from the literature of this period has been accumulated and is summarized as follows:

(A) General variables affecting ductile fracture are

(a) the volume fraction of second phase particles[20,21,27];

(b) particle size[21,27,29,97];

(c) composition of the two phase alloys or composites[21,26,27];

(d) thermally induced stress[39], (though it might be a second order factor);

(e) interfacial strength[21,26,27,28].

(B) Environmental variables affecting ductile fracture are

(a) hydrostatic pressure[37,40,41];

(b) temperature[28,39];

(c) atmosphere (e.g. vacuum, nitrogen, or hydrogen atmosphere)[35].

(C) The role of the localized stress concentration at the second phase has to be emphasised. The release of local stress occurs in two ways[26,29]:

(a) formation and motion of dislocations;

(b) formation and growth of the microcrack.

Voids nucleate on each particle at the point in line with the maximum tensile stress

applied to the specimen.

(D) The void coalescence is the most critical and least understood aspect of the fracture process[26].

To this point we have summarized the factors that affect ductility.

But, one fundamentally contradictory fact should be noted. As Chen et al.[28] and Palmer et al.[29] reported, at low temperature the elongation was greater than that at higher temperature, shown in Fig.4b, while the reduction in area had the opposite dependence, i.e. it was lower at low temperatures. Since commonly the reduction in area and the elongation in a tension test are both used as the measure of the material ductility, i.e. the capability of a material to undergo deformation, then the question arises: " What is a proper measure of ductility?"

Starting from the later 1960's, various kinds of models began to emerge and then converge to a physical picture of ductile rupture in two-phase materials as corresponding to three stages; void nucleation, void growth and void linkage.

With respect to the void formation, there were three kinds of criteria established, i.e. energy criterion[21,42,50,101], stress criteria[44,50,97] and strain criteria[37,49].

Typically, the energy criterion stated that cavitation by interface separation will not occur unless the elastic energy released by removing the stress (or some fraction of it) from the particle is at least equal to the surface energy created. Browns and Stobbs[101] (1971) proposed a nucleation model based on this criterion in a combined continuum micromechanical approach considering the incompatibility between the matrix and particle deformation. Based on the energy calculation in and around the spherical

inclusion following Eshelby's theory, Tanaka[42] (1970) predicted that in a purely elastic situation, the energy criterion is always satisfied for particles above a diameter of about 250 Å.

This argument favours a stress criterion for large particles. Stress criteria state that in order to nucleate cavities the interfacial strength must be reached. Ashby[97] (1966) has discussed this and interesting variations in which primary deformation incompatibilities do not produce cavities directly, but initiate highly organized secondary slip by punching out dislocation loops from the interface of the inclusion to reduce the local shear stresses. These loops then form reverse pile-ups and can build up increasing interfacial tensile stresses until they reach the interfacial strength when a cavity is formed. The interfacial stress criterion was also used in Argon's model[44].

Based on the argument that a high strain concentration can be developed around non-deforming particles in a non-strain hardening matrix, McClintock[37] (1968) suggested that cavity formation at interfaces may obey a critical local strain criterion, or alteratively a criterion that may be a mixture of a critical interfacial shearing strain and an interfacial normal stress.

Once a microvoid has been nucleated in a plastically deforming matrix, the surface of the void is created. With continuing plastic flow of the matrix, the microvoid will therefore undergo a volumetric growth and shape change which amplifies the distortion imposed by the remote uniform strain-rate field. The most successful and versatile model of this type was developed by Rice and Tracey[45] (1969). In their approach, a variational principle is employed to characterize the flow field in an

elastically rigid and incompressible plastic material containing an internal void shown in Fig. 2.7. The void radii in the principal directions R1 and R3 can be related to their rates of increase by

$$\dot{R}_1 = R_1[-\frac{\gamma_a}{2}\dot{\bar{\epsilon}}_3 + 0.56\dot{\bar{\epsilon}}_3 \sinh(\frac{3\sigma_m}{2Y})] \tag{2.1}$$

$$\dot{R}_3 = R_3[\gamma_a\dot{\bar{\epsilon}}_3 + 0.56\dot{\bar{\epsilon}}_3 \sinh(\frac{3\sigma_m}{2Y})] \tag{2.2}$$

where Y is the tensile flow stress of the material; σ_m is the mean stress; ϵ_3 is the tensile strain at a point remote from the void; γ_a is a factor which describes the amplification of the growth rate of the void relative to the strain rate of the matrix. The second term relates to volume change of the void which is controlled by the mean stress. The fact that the negative pressure controls the void growth is of physical importance, and helps to explain why void growth is most visible in necked regions. A weakness of the one void model is that it has ignored the influence of the continuing existence of the second phase particle from which the void is nucleated, and the subsequent interactions between that particle and the void.

To consider the essential features of the mechanics of microvoid coalescence, Thomason[46] (1968) established a simple two-dimensional plane-strain model for a state of incipient microvoid coalescence in a work-hardening plastic/rigid solid. The model stated that the large transverse growth which brings about complete microvoid coalescence begins only at incipient ductile fracture which is caused by localised internal necking of the intervoid matrix. Although the two dimensional model did not consider

the existence of the second phase, it was innovative in that it related the microfracture process to a macrostress state.

Correlating the three stages and emphasising the central role of the plastic strain, Brown & Embury[47] (1973) proposed that there exist local critical strains for the various stages of the fracture process. The failure condition requires that the length of void, $2r_0(1+\epsilon_g)$, be equal to the spacing of neighbouring voids centred in the same plane,

$$\varepsilon_f=\ln\frac{A_0}{A_f}=\ln(1+\varepsilon_g+\varepsilon_n)=\ln(\sqrt{\frac{\pi}{6V_f}}-\sqrt{\frac{2}{3}}+\varepsilon_n) \qquad (2.3)$$

where ϵ_f, ϵ_g, ϵ_n are the fracture, growth and nucleation strains respectively, V_f the volume fraction of the second phase, r_0 the void radius, A_0, A_f the original and fracture section areas.

But none of these models accounted for either the particle size and shape sensitivity of the local strain or stress states. Therefore these models cannot predict fracture correctly under certain circumstances.

In the 1970's, extensive experimental observations were continued. It was then well recognized that once internal cavities are nucleated from second phase particles, they can be plastically expanded under various combinations of shear stress and negative pressure.

Experimenting on spheroidized 1045 steel, Cu-0.6 pct Cr alloy, and maraging steel containing respectively Fe_3C, Cu-Cr, and TiC particles of nearly equiaxed shape, Argon et al.[48] (1975) determined the interfacial strength for these particles (1.67 GPa, 0.99 GPa, 1.82 GPa) by cutting sections parallel to the tensile axis and examining the

local condition along the axis where the density of inclusions with interfacial separation drops to zero. The interfacial stress was evaluated by a critical stress criterion, i.e. $\sigma_{rr}=\sigma_T+Y(\epsilon^p)$, where σ_T is the local negative pressure caused by the triaxial stress at the neck of the tensile specimen or other sources, and Y the plastic resistance in tension (i.e. the flow stress) corresponding to the local average plastic strain, had the inclusion been absent. Although the criterion was only suitable for spherical particles and was a semi-quantitative analysis, it was reasonable to recognize that a critical local elastic energy condition is necessary but not sufficient for cavity formation. A stress criterion must also be satisfied. Actually, Bridgman's work had already proved this point because under high hydrostatic pressure, the strain energy is much greater than that without pressure when fracture happens. The observations by Argon et al.[44] (1975) also revealed that:

(1) When the volume fraction is small, the particles act in isolation and the interfacial stress is independent of the particle size but depends only on the local flow stress and local long range triaxial stress.

(2) If the particles are of uniform size and quasi-uniform spacing, the interfacial stress becomes, in addition to the plastic strain, dependent also on the volume fraction of the second phase, but still remains independent of particle size.

(3) The interfacial stress becomes particle size dependent only if there are significant local variations of volume fraction of second phase from point to point for a given average second phase volume fraction.

These conclusions are important not only because the experiments gave the correspondence of particle size, particle volume fraction and particle distribution with

local stress concentration, but also because the results can be partially confirmed by other works (e.g.[19,57,71]), including the finite element analysis presented in this dissertation, though some conclusions, which are true for the conditions used by Argon, are not in agreement with some different experiments performed since that time. Besides, their argument on using continuum mechanics was that when the inclusion size is the order of a micron, the spacing of the surrounding dislocations in the high strain gradient zones are very much smaller than the particle diameter, which can be seen in Stobbs and Brown's work in Fig. 2.8. Therefore, at least for large particles a continuum analysis of deformation is proper.

In a study of the fracture morphology with the high aspect ratio second phase particles, Lindley et al.[30] (1970) found that the fracture occurred as internal cracking in ferrite/carbide system. They showed that the greatest incidence of cracking occurred in carbides oriented along the tensile axis. The probability of fracture increases as the centre of the carbide is approached and the carbide crack density increased with decreasing test temperature. By examining the fracture surface and microstructures of aluminium alloys, Broek[31] conformed a general conclusion, i.e. slender particles have a tendency to fracture in the centre of the particles as shown in Fig. 2.9. Comparing with the results of the scanning electron micrograph of an iron sample by Tanaka[21] (1970) shown in Fig.2.10, spherical particles lose coherence with the matrix, and tear at their interface with the matrix. The shape effect on ductile fracture was clearly demonstrated.

Kasteele and Broek[51] (1977) investigated the fracture of large second phase particles (1-20 μm in size) in advance of a crack tip of engineering aluminium alloys.

While their focus was to study the relationships of fracture toughness with the particle separation distance, the results of most interest to the present work are:

(1) In the case of plane strain, some void growth occurs at the cracked particles in the immediate vicinity of the crack tip. Crack extension by ligament failure occurs before these voids have grown very large.

(2) In the case of plane stress, the particles fail throughout the plastic zone. Some of them develop very large voids and secondary cracks. Crack extension is a result of merging of these microcracks with the main cracks.

A new interpretation by the present author makes use of a simple analysis in terms of linear fracture mechanics. For plane problems, by means of Airy stress function and Westergaard's complex variable stress formula[31], the equilibrium equations can be solved. At a crack tip, the tensile hydrostatic stresses are different. They are:

$$\sigma_m=\frac{1}{3}(\sigma_x+\sigma_y+\sigma_z)=\frac{1}{3}(\sigma_x+\sigma_y)=\frac{2}{3}\sigma\sqrt{\frac{a}{2r}}$$

for plane stress; and

$$\sigma_m=\frac{1}{3}(\sigma_x+\sigma_y+\sigma_z)=\frac{1}{3}(\sigma_x+\sigma_y+\nu(\sigma_x+\sigma_y))=(1+\nu)\frac{2}{3}\sigma\sqrt{\frac{a}{2r}}$$

for plane strain, where 'a' is the crack length, r is distance from crack tip, σ the remote tensile load. In plane strain, the tensile hydrostatic stress is $(1+\nu)$ times as great as that in plane stress. This suggests that ductile fracture of two phase materials is more or less controlled by high negative pressure for plane strain, while for plane stress it is

controlled by plastic strain resulting from the higher Mises effective stress. The $1+\nu$ times factor in mean stress is high enough to change the fracture morphology from small void fracture in plane strain to large void fracture in plane stress. Experimentally one observes that in a mode I fracture K_{IC} test, the notched sample fractures in shear in the plane stress condition, and in a brittle manner (normal orientation) in plane strain[53]. The change of fracture type implies that the ductility of material is a state variable, which is associated with not only local material expansion, but also local material shearing. Suppose we take the plane stress shear failure as the baseline fracture condition. Then in plane strain sample the effect of inhibiting this shear should be that a higher remote applied stress level should be required to cause failure in the plane strain case compared with plane stress. But in fact, a lower remote applied stress is required for plane strain. The dominant factor is therefore not the occurrence of plastic strain in the plane stress condition, but rather the absence of a large enough hydrostatic tension in plane stress. The large hydrostatic stress in plane strain causes early failure, which is not seen in plane stress.

Summarizing the literature during the 1970's, the experimental evidence indicated that:

(A) The stress concentration at interface of the two phases depends on the size, volume fraction, and distribution[44,48] of the second phase;

(B) Void growth to fracture is strongly controlled by long-range stress states[51];

(C) Long range negative pressure accelerates the void nucleation[44,48];

(D) A continuum analysis of deformation may be proper for large particles[44];

(E) Particles with high aspect ratios generally undergo internal fracture, while spherical particles undergo interface failure[29,30,31,33].

During the 1980's, literature[58-62] focusing on the role of superimposed pressure in the ductile fracture of two phase materials, contributed significantly to the further understanding of fracture. It was recognized at that time that the nucleation and growth of voids at particles is retarded by the superposition of pressure and the final fracture strain increases linearly with compressive pressure[59] (1983). Two phase materials may fail in different modes: i.e. fully plastic failure, shear failure, ductile failure and brittle failure, which compete with each other according to the stress states[61,62] (1984,1988) to which materials are imposed.

Since the later 1980's, the rapid development of advanced metal matrix composites has required investigating not only the general mechanical character of multiphase materials, but also the individual variations in the role of the different types of second phase on ductile fracture (e.g. for some specific MMC systems, such as whisker or particulate reinforced aluminium metal matrix composites). These changes, to some extent, reflect the fact that the mechanical properties and fracture behaviour of the MMCs closely relates to many aspects of practical production of MMCs. These include fabrication processing[64,68,72,74], secondary processing[19,72,93], heat treatment[34,63,66], material composition[57,68], reinforcement selection and even their geometries[19,55].

To probe the essence of the process of the damage accumulation in SiC whisker reinforced MMCs, Nutt & Dura[55] (1986) produced some excellent experimental results. By means of transmission electron microscopy (TEM). they looked into microstructural

aspects of the deformation at the whisker ends in SiC reinforced aluminum composites with a whisker size 0.5 μm in diameter and 5-10 μm in length and with sharp corners. The singularity causes intense plastic strain in the nearby matrix and leads to void initiation at the corners, as shown in Fig. 2.12. Once voids nucleate at corner sites, they tend to grow inward to the centre of the whisker. The whisker-matrix interface separates as this growth proceeds. With increasing plastic strain, the voids eventually coalesce to form a single equiaxed cavity approximately equal in size to the whisker diameter. Ultimately, there are a sufficient number of neighbouring cavities to form a fracture path[55,56]. These results showed strikingly the physical picture of damage accumulation. A similar TEM result was obtained by Lewandowski et al[63] (1989) on studying Al/(SiC)p MMCs, as shown in Fig. 2.13. The typical fracture paths of this type MMCs are shown in Fig. 2.11 (i.e. failure through particles, particle-matrix interface or matrix, which depends on particle size, volume fraction, particle shape, particle distribution, thermal stress, composition, etc.).

With respect to the fracture behaviour of particulate reinforced aluminium metal matrix and its correspondence with effects such as particle size, distribution, and volume fraction, it has been experimentally showed that:

(1) Reinforcement particle cracking generally occurs first in particles which are considerably larger than the mean particle size[19,71,172] (1990,1991,1991);

(2) The Young's modulus of plastically strained MMC was reduced with increase in plastic strain, which allows a damage parameter to be identified[34,71] (1991,1991);

(3) Fracture is usually initiated in particle clusters[19,34,64,74] (1990,1989,1991,1991),

because the matrix within the cluster is subjected to high levels of triaxial stress due to elastic misfit and constraints exerted on the matrix by the surrounding particles;

(4) The composite is less sensitive to hydrostatic tension compared with the unreinforced matrix[18] (1991), i.e. the hydrostatic tension causes only a small decrease in fracture strain, whereas it significantly reduces the fracture strain in unreinforced materials;

(5) Microstructures of the composites affect the deformation and fracture behaviour[63,66,34] (1989,1989,1991);

(6) Reaction between particles and the matrix during the processing may result in the degradation of the mechanical and physical properties of MMCs[68,69,72,87,91] (1988,1988, 1992,1992,1992).

The extensive and detailed investigation of discontinuously reinforced aluminium metal matrix composites and its development of understanding of the mechanical properties and fracture behaviour continues in the recent literature on the following subjects:

(a) *strengthening mechanisms*[54,73,80,174,178]

(b) *failure mechanisms*[55,56,65,70,19,71]

(c) *damage initiation and accumulation*[52,64,19,82,34,74,71,92,146]

(d) *toughness*[75,76]

(e) *fatigue*[77,83,90,154,38,67,105,109]

(f) *thermally induced stress*[79,89,143,152,175,177,178,171,176]

(g) *plastic flow and creep*[88,94,105]

(h) *aging response*[63,66,34,84,141,142]

(i) *recovery and recrystallization*[93]

(j) *composition*[16]

(k) *chemical reactions, spinel formation and their examination*[68,69,57,72,87,91,85]

(l) *the effect of hydrostatic tension or pressure*[18,95,24,25,172]

(m) *deformation*[70,78,86,172,173]

(n) *tensile properties*[38,144]

(x) *other aspects*[52,127,147,148,149,151]

However, to optimize the mechanical properties of MMCs a full understanding of the following questions is still required.

(A) What is the manner of stress transfer in two phase materials or multiphase materials?

(B) What causes the embrittlement and the low ductility in MMCs?

(C) Does the high local stress concentration change the flow behaviour of matrix?

(D) What affects the effectiveness of the reinforcement?

2.2 The Role of the Second Phase in Material Strengthening

Strength is defined as the resistance of a substance to distortion or fracture[113] (1946). Considering the straining process prior to the fracture, to strengthen materials implies an increase in the resistance to deformation or in the view of dislocation theory, this resistance to dislocation movement. Conventionally, the metallurgical methods to increase the resistance and to improve the service performance of the metals include solid solution hardening, precipitate strengthening, dispersion strengthening, and work-hardening. The strengthening mechanisms have been well documented by the dislocation

theory. Among them, precipitates and dispersion strengthening are those with which we will be concerned. Both of these hardening mechanisms involve the movement of dislocation against the resistance provided by second phase particles. In the case of the alloy used in this thesis, these are either precipitates of Mg_2Si and MgZn or SiC particles in an aluminum matrix.

Fundamentally, the role of the second phase in material strengthening can be best demonstrated by the following experiment.

While studying the stress strain behaviour in dispersion-hardened copper crystals, which are soft crystals containing hard non-deforming particles of a second phase (SiO_2), Ashby[97](1966) identified a new type of work hardening not found in pure single crystals; see Fig. 2.14. Ashby observed that the two phase matter hardens much faster than do those consisting of a single phase, starting with the initial flow stress. The rate of this work hardening increases with increasing volume fraction and decreasing size of particles, shown in Fig. 2.15.

Ashby[112] (1971) proposed that this strengthening is because the two phases are not equally easy to deform. One component plastically deforms more than the other, so that gradients of deformation form. The gradients of deformation require that dislocations be stored. These dislocations act as individual obstacles to slip and create a long-range back stress to contribute to the work-hardening of the two phase materials.

Ashby developed the following new formalism to describe strain in two-phase materials.

(A) The 'geometrically necessary' dislocations during straining give extra work-

hardening in two phase materials[112].

These 'geometrically-necessary' dislocations must be generated to allow the two phases to deform in a compatible way and to accommodate the gradients of deformation. These are characteristic of the microstructure. Concurrently, another set of dislocations called 'statistically stored', supply the gross strain and are accumulated by random mutual trapping during straining. These are characteristic of the material. The former ('geometrically-necessary' dislocations) accompany strengthening in non-homogeneous materials, in addition to the intrinsic hardening supplied by the latter ('statistically stored' dislocations) which occur in all deforming metallic materials.

(B) The density of geometrically-necessary dislocation during deformation increases with the increase of the shear strain and particle volume fraction, and with a decrease in particle size[97,112];

The stress strain curve of two phase materials shows a parabolic behaviour because the rate of work-hardening is proportional to the square root of the density of dislocations.

(C) Plastic relaxation must occur locally around particles during deformation, if the particles do not deform plastically, and if the interfaces between particle and matrix do not fracture[97].

The plastic relaxation supplying the geometrically necessary dislocations can occur by secondary slip, which includes many mechanisms[104,107], such as cross-slip, lattice rotation, dislocation punching, dislocation climb, even atomic diffusion at high temperatures. The consequence is that these dislocations impede the movement of the

primary glide dislocations. Eventually, if the local stress is highly concentrated, the sequence leads to shear or fracture of the particle, or decohesion at the particle-matrix interface.

Generally speaking, the process of material strengthening in two phase materials is that of dislocation multiplication and their interaction with glide dislocations around hard particles, which is followed by material failure. However, there are exceptions. For instance, examining the fatigue behaviour in the copper-silica, Stobbs, Watt & Brown[99] (1971) found that there was little or no fatigue-hardening in spite of the increase of dislocation density during the process. It was revealed that a high density of dislocations is a necessary condition for material strengthening, but not a sufficient condition. The multiplication of a high density of immobile dislocations is of importance.

In Ashby's model, the strengthening of two phase alloys or composites is controlled by the generation of the 'geometrically-necessary' dislocations during deformation. The 'geometrically-necessary' dislocations[97,101,102,104,110] consist of the three sources: primary, secondary, and multiple slip, which relate to the three processes: the initiation of the internal stress, the relaxation of the back stress and the continuation of the hardening, and the accumulation of the stress concentration leading to fracture. Each corresponds to a different strain level. Consider each of these stages in more detail.

When the strain is low, the strengthening mechanism favours a shear mode or Orowan by-passing model. The primary dislocations move by bowing between and by-passing particles only on the primary slip plane. Each dislocation that passes a particle by this process leaves one shear loop at the particle and a long range back stress.

The function of the back stress can be further explained in Fisher's model[97] (1953). When a shear stress is applied, up to a certain shear stress, both the matrix and particles deform elastically. At some critical value the matrix becomes plastic. Above it, an increment in applied stress must be balanced by an opposing increment in the average internal stress. The internal back stress increases with strain, giving work hardening.

When the strain increases, Fisher's model breaks down at high back stresses. Secondary slip dislocations are generated. For example, cross-slip favours the nucleation of prismatic arrays. The process involves transfer of a segment of primary dislocation onto the cross-slip plane. A dislocation approaching a particle on the primary slip plane is stopped by the long and short range repulsive forces exerted on it by the particle. Long range repulsion results from misfit or differing elastic constants between particle and matrix; a short range repulsion is related to the different interatomic force-displacement curves of the particle and matrix. The dislocation stops in a way that the net force in the primary slip plane is zero, whereas the net force on this section in the cross-slip plane is not zero, and the local stress does work. The prismatic loops exist as obstacles to further dislocation glide.

Alternatively, in Ashby's secondary slip model, the plastic stress may also be relaxed by lattice rotation, as has been proved by experiment[110] (1969) and/or by punching out of dislocations from the particle-matrix interface. The secondary slip dislocations stop or cut the glide primary ones to allow the continuation of work-hardening, until the nucleation stress for slip activates new slip systems. Ultimately, when the strength of interface, particle or matrix is exceeded, interfacial decohesion,

particle fracture, or matrix failure occurs.

Using copper dispersion-hardened with silica particles as a prototype of two phase alloys or composites, a sequence of significant literature emerged during the later 60's and the 70's on the investigation of the plastic relaxation, Bauschinger effect and fatigue behaviour (e.g.[99,100,101,102,104,107]). With respect to the effect of particle size and particle distribution on dislocation microstructure, the salient observations and proposals were:

(a) Examining the effect of hydrostatic pressure on deformation behaviour of the two-phase materials, Ashby et al.[98] (1969) found that plastic zones develop around the larger particles and that angular shape particles induce higher local stresses than spherical ones. Hence, the application of theoretical models is limited because of the ignorance of particle shape. Also, Stobbs, Watt & Brown[99] (1971) observed that platelets of primary edge dislocations are associated with the larger particles after fatigue.

(b) Brown & Stobbs[101] (1971) revealed that clusters of particles can strongly interact in their associated dislocation structures; see Fig. 2.16. This can be related to modes of failure in MMCs observed in recent experimental results (e.g. [19,34,63,64,74]).

(c) The slip lines around a particle are perturbed for a distance of up to three or four particle radii away from the centre of the particle (Ebeling 1970). The slip line spacing was about 400 Å (40 nm) at a strain of 0.015. It was also pointed out by Brown & Stobbs[101] (1971) that a plastic zone extends about three or four particle radii into the matrix. The slip-line spacing was about 300 Å (30 nm) at a strain of 0.08.

This result is not unexpected, if we apply Eshelby's theory[63,105] (1959, 1957). The stress field will rapidly die away as $1/r^3$ at far field, which is independent of particle

size.

In accord with the argument on the validity of using continuum mechanics in micromechanics, the observation provided the positive evidence.

As we know, continuum mechanics can describe the deformation behaviour of a continuous medium if the matrix deforms uniformly. Physically, we say, the continuous medium consists of a boundlessly large number of mass points. Each point possesses a certain characteristic. This characteristic is that the point is infinitesimal in size in the macroscopic view, and infinite in the microscopic view, i.e. the mass point should contain a substantial number of atoms. But how many atoms are necessary to be described as a mass point? Is there a clear line in microstructural scale for distinguishing the individual character using dislocation theory and the whole character using continuum mechanics?

When the particle size is large, e.g. 10 microns is common in MMCs, the slip-line spacing of 300 Å (30 nm) may be regarded as a very small distance, being approximately 3/1000 of the particle size. In particulate reinforced aluminium metal matrix composites, it may be reasonable to believe that the slip-line spacing in aluminium alloys has the same order of magnitude as in copper. This spacing ought to be the lower bound of the smallest 'unit' as an allowable measure of the macromechanical deformation. If the particle size is of the order of the slip line spacing, then continuum mechanics is not representative, and so dislocation theory is the only plausible approach. But, if the particle size is comparable to hundreds of 'units' in size, the case is different. The locally discontinuous jump of deformation at a slip line will be, to some extent,

smoothed as a result of the effect of 'zooming out'. Therefore, the application of continuum mechanics in micromechanics may be proper in these situations.

Of course, the practical MMC system is very complicated, especially if other aspects such as the chemical reaction, the deposition of spinel, and diffusion at the interface[57] (1989) are considered. However, extracting key physical parameters is still a proper approach to approximate the average mechanical properties. Generally, for this purpose, dislocation theory, continuum mechanics, and statistics may all serve as the tools.

(d) Brown & Clarke[106] (1975) proposed an attractive explanation for materials strengthening. They pointed out that two main contributions to the strength should be taken note of, in addition to the many other strengthening effects. The first is a mean stress in the matrix, which impedes flow by a back stress which is simply proportional to the volume fraction of inclusions and to the applied plastic strain. The mean stress in the matrix can be derived by differentiating the total elastic energy stored in the alloy with respect to the plastic strain. The second contribution from the internal stresses comes from the local fluctuating stresses about the mean value, and these act essentially to make it more difficult for successive glide dislocations to bypass the inclusions. This term is called "source-shortening".

If these are important, then it is necessary to incorporate these in the constitutive equations and flow potential used in continuum mechanics. Where the deformation behaviour of two phase materials is concerned, the local stress concentration may strongly affect the flow behaviour, while it is not considered in conventional continuum

plasticity theory in metals. For example, when a far field stress is imposed on a two phase system with an isolated inclusion, the local stress concentration is high at the poles along the loading direction. According to metal plasticity, the plastic flow would not be affected by the local mean stress. This cannot be true when dislocations are highly tangled near the interface with a high level of the mean stress concentration. The internal stress resulting from the fluctuation may slow down or stop further plastic flow in this region. So if possible, the fundamental study on flow potential and constitutive equations of the metal matrix is necessary, especially when the gradient of deformation is involved. Because as yet this new theory has not been developed, this dissertation uses conventional metal plasticity continuum theory.

Practically, with respect to the strength of particulate reinforced MMCs, the material hardening implies two major aspects: alloy hardening and particle hardening.

Alloy hardening involves the movement of dislocations against the resistance provided by solid solution or precipitates in alloy matrix, where the precipitate size is similar to the slip line spacing. In 6061 Al/$(SiC)_p$ MMC, the matrix contains additions of magnesium, silicon and a very small amount of zinc. Zinc hardens the alloy as a result of the precipitation of an intermediate semicoherent phase based on $MgZn_2$, and silicon with magnesium forms a coherent pre-precipitate based on Mg_2Si.

Particle hardening involves the movement of dislocations against the resistance provided by the existence of the large particulates and the increased dislocation density created during the MMC cooling process[54,73,80]. For example, due to the difference in the coefficient of thermal expansion (CTE) between the SiC and the Al matrix, the cooling

process results in an enhanced dislocation density in the matrix, which is unlikely to be recovered by subsequent aging. These dislocations act as the obstacles impeding the dislocation slip so that the materials are strengthened.

2.3 The Role of the Second Phase Particles on Stress Concentration

A review on stress concentrations by Sternberg[117] (1958) pointed out that one type of stress concentration is created by the material discontinuities, such as those due to inclusions of, or reinforced by, materials with elastic properties which differ from the elastic properties of the surrounding matter. When those materials are imposed into the stress field, stress concentrations arise which determine the strain hardening and the process of material failure. Particulate reinforced aluminum metal matrix composites belong to this group. For instance the MMC 6061-T4 Al/$(SiC)_p$ contains the hard silicon carbide phase and the soft aluminum alloy. These two ingredients possess different elastic properties and demonstrate different mechanical behaviours. The reinforcement can only deform elastically, while the matrix deforms elastically or plastically depending on microstructure and load. As a whole, the MMC is characterized by large differences of strain and/or stress between the phases.

As an alternative to dislocation theory to model the role of the second phase particles, continuum mechanics can be applied in a very straightforward way. This is mainly because:

(A) Continuum mechanics is a well developed subject, which is based on a series of physical laws defined in terms of strictly mathematical theories.

(B) Continuum mechanics, to some extent, compensates for some of the deficiencies of the other two methods: experimental observations and dislocation microstructure analysis. Experimental observations connect the study of fracture morphology and/or overall mechanical response. Although it is best known as the touchstone for testing the existing theories, the lack of an effective experimental means makes it difficult to directly inspect the interactions between the two phases during straining. Dislocation microstructural analysis provides a clear physical understanding of the material strengthening. However, it is difficult to obtain a satisfactory description of the overall mechanical behaviour and local stress concentration by accounting for different modes of dislocation movement, especially when irregular particle shapes and non-uniform particle distributions are of concern[98,101] (1969,1971).

But, as mentioned in the previous section, the application of continuum mechanics is also limited. It is valid only if particle is large enough to consider the surrounding matrix to be deforming continuously.

One hopes that one day there would exist a theory allowing the manipulation of information between continuum mechanics and dislocation theory to predict the macromechanical properties of MMCs. The theory should be able to provide some kind of macro- patterns or order from the micro- chaos of dislocation movement, when the feasibility of either theory is questioned.

Continuum Mechanics Applied to Inclusion/Inhomogeneity Problem

The study of the mechanical response of composites using continuum mechanics

has developed from the physical interests on "inclusion" and "inhomogeneity" problems.

Eshelby[116] (1957) described these two problems as those in which the uniformity of an elastic medium is disturbed by a region within it which has changed its form (called the inclusion problem) or which has elastic constants differing from those of the remainder (called the inhomogeneity problem).

To determine the elastic state after a region (the inclusion) in an infinite homogeneous isotropic elastic medium has undergone a change of shape and size, Eshelby[96,116,118] presented an elegant theoretical treatment to solve for the constraints by a series of cutting, straining and welding operations, based on the classical elastic theory of Love[164] (1927), using the point-force method (section 130 of Ref.[164]). Although before Eshelby solutions of the equations of elasticity pertaining to the effect of change of specific volume of inclusions have been considered by many authors, his work represented a significant step forward in understanding these type of problem. Earlier, for example, Goodier[165] (1937) had realized that when the temperature T(x,y,z) in an elastic solid is not uniform, the natural thermal expansion of every volume element is partially restrained by the surrounding material, and a state of stress exists. Robinson[115] (1951) determined the residual stress produced by a uniform heating (or cooling) of inclusion and matrix due to the difference of coefficient of thermal expansion. Eshelby's theory for transformation problems offered the most succinct form with a sound physical basis and without using the complicated curvilinear coordinates. The theory is applicable to inclusion problems with arbitrary shape but with the same elastic properties as the surrounding material. Its greatest application has been for martensitic reactions.

However, for the present study, the most profound breakthrough Eshelby[96,116,118] made was that of inhomogeneity problems, in which an ellipsoidal region has elastic constants differing from those of the surroundings. The mathematical approach was made operable by means of the assumption of an equivalent inclusion, which possesses the same elastic constants as the matrix. When a remote uniform stress is applied, the inclusion works as if it undergoes an imaginary transformation strain (or stress-free strain) while the inclusion region is mathematically cut out of the matrix. This strain is, broadly speaking, proportional to the remote field if the uniform constraint strain in the region is assumed. To accommodate the inclusion and the matrix, a series of squeezing and welding operations have to be performed to reunite the matrix and inclusion. The disturbance caused by the inclusion to the remote uniform field is then determined in terms of the classical potential theory by releasing the reaction forces at the interface. The theory is only applicable to inhomogeneity problems with ellipsoidal shape. The detailed delineation of the method, calculations and results are given in Chapter 3.

Different from Eshelby's point-force method, Mura & Cheng[120] (1977) made use of the Fourier integral to calculate the elastic field outside an ellipsoidal inclusion from known stress-free strains[96,116,118] (or eigenstrains [120,121,125]). The advantage of this method is that the solution may be applicable to arbitrarily distributed initial strains. Besides, the integrands of the these integrals, unlike Eshelby's, have no singularities so that numerical calculations on a computer can be easily performed. Chiu[119] (1977) derived expressions to obtain the stress field in an infinite isotropic elastic medium having a cuboidal domain (of the same material) within which a set of prescribed uniform strains is given.

Unfortunately, in inhomogeneity problems, the major concern is to find the "polarized eigenstrains" from the remote uniform field, if these exist. None of these works has given a clear relationship between them, except Eshelby's[86,116,118] and its applications in two dimensional problems (e.g.[166] (1961)). Actually in principle, when the medium is inhomogeneous, it is not possible to determine the Green functions[118] in a closed form required for the solution of an arbitrary shape region. The success of Eshelby's calculation is due to the special geometric shape of the inhomogeneity, in which the "polarized" field in the inhomogeneity is coincidentally able to be written as an uniform one. This situation is analogous to a static electric field. A dielectric with ellipsoidal shape would be polarized uniformly in a external electric field. But when the dielectric has arbitrary shape, the polarization distributes non-uniformly. The internal electric field intensity only can be solved by a numerical method and/or conformal mapping methods (e.g.(69)). Another common point of the two is that as long as a second medium is involved, the "polarization " cannot be avoided; the amount of "polarization" determines additionally stored energy and change of field depending on the nature of the individual second medium, which corresponds to the change of strain energy and the stress transfer in elasticity.

As a secondary topic in inclusion and inhomogeneity problems, the average elastic moduli of composites materials have been investigated by many authors, and has been reviewed by Mura[125,121] (1982,1988) and Walpole[167] (1985). The methods commonly used to predict the average elastic moduli of particulate reinforced materials are (1) the Voight approximation (1889) (the upper bounds); (2) the Reuss approximation (1929) (the lower

bounds); (3) Eshelby's method; (4) self-consistent method[104] (1965); (5) Hashin and Shtrikman's upper and lower bounds. These have been explicitly described by Mura[125] (1982), and the differences in the predicted results is shown in Fig. 2.17. These theories may be useful when the rigorous bounds are either not known or are too far apart for empirical interpolation.

Another topic to be considered in inclusion and inhomogeneity problems is that of interfacial sliding and debonding. Recent works on the subject assume that the inhomogeneity and the matrix are not perfectly bonded. Some models have been presented. For instance, Mura, Jasiuk and Tsuchida[126] (1985) discussed the stress fields of a ellipsoidal inhomogeneity under uniaxial tension at infinity by assuming no shear traction at interface. Hashin[123] (1991) proposed an imperfect elastic spring-type interface. The interface spring constants are expressed in terms of interphase elastic properties and thickness outside a spherical inhomogeneity. Levy[131] (1991) suggested that the inclusion or inhomogeneity interacts with the matrix through a prescribed interface law which depends on the displacement jump at the interface. However, although the interface sliding does provide a mechanism of stress relaxation, the prescribed interface laws should be verified by carefully prepared experiments before they can be used.

As mentioned, Eshelby's theory for inhomogeneity problems is only applicable for an isolated elliptical inhomogeneity. To extend the analysis to an arbitrary shape of inhomogeneity, Fan, Keer and Mura[122] (1992) proposed a modulus perturbation approach, which converts the inhomogeneity problem into a series of inclusion problems by using the eigenstrain concept. Such an approach requires that the difference between the moduli

of the matrix and inhomogeneity be small compared to the matrix modulus itself. In the case with which we are concerned, particles are much stiffer than the matrix (the ratio of Young's modulus is about 450:70). To examine the effect of particle shape on stress distribution within, and around, a single particle subjected to an uniform remote stress field, the above approach is therefore excluded.

In Chapter 4, a new method developed by the author will be presented for an arbitrary shape of inhomogeneity. The method allows the arbitrary difference of modulus between particle and matrix, and is performed by a sequence of cutting, straining and welding procedures, based on Betti's reciprocal theorem.

Some of the mathematical approaches used in classical elasticity as discussed previously will be employed by the present author for the purpose of:

(1) checking the corresponding finite element method (FEM) results to confirm the calculation accuracy and increasing the reliability of the prediction of deformation characteristics of MMCs;

(2) understanding the function of stress transfer by an isolated particle and its relationship to the type of reinforcement, i.e. the elastic constants of reinforcement;

(3) examining the stress concentration and discussing its influence on ductility in materials with an inhomogeneity;

(4) calculating the stress distribution within and around a particle with arbitrary shape in order to reveal the effect of particle shape on stress concentration and its effect on failure considerations.

However, the understanding of the stress distribution and the deformation

characteristics within particulate reinforced MMCs requires one to obtain not only the fundamental insights on the interactions between particle and matrix, but also on the interactions between particles. Dealing with a complex multiparticle system, classical elasticity becomes inadequate. Also, the application of the conventional mathematical analysis cannot easily be applied to the following cases:

(a) irregular geometries of reinforcement;

(b) an inhomogeneous medium;

(c) nonlinear behaviour of matrix;

(d) arbitrary loading;

(e) multiple particle arrays.

The advent of the computers and the availability of several approximate methods, such as FEM and boundary element method (BEM), have accelerated the further development of MMC micromechanics. Among such numerical methods, the finite element method has been the most commonly used approach to overcome the difficulties (a) to (e) above.

Finite Element Method (FEM) Applying to the Study of Metal Matrix Composites

Using FEM, the early investigations of the two-phase materials were largely done using two-dimensional calculations. For example, Karlsson & Sundstrom[133] (1974) and Ankem & Margolin[135,136] (1982) analyzed plastic deformation in ferrite-martensitic and ferritic-pearlitic steels, and in α-β titanium alloys, respectively. They both found that the strain field is very inhomogeneous due to the misfit of the two phases, which agrees with

dislocation observations (e.g.[98,99,101]). Argon, Im & Sofogu[44] (1975) and Thomson & Hancock[137] (1984) calculated the elastic-plastic stress field outside a rigid or elastic inclusion. They found that the plastic zone started above the pole of the inclusion but at a small distance from it, and that significant gradients of field components only developed near the inclusion-matrix interface. They also noted that the development of plastic strain displaces the position of the maximum radial stress around the interface, away from the pole[137]. These two dimensional calculations therefore provided some insight into deformation behaviour when a second phase exists, but they are limited to plane stress (a thin disc) or plane strain (an long rod) cases.

In practice, due to computation time-consumption, cost, and the computer calculation capacity required for FEM, modelling of the actual microstructure in three dimensions is extremely difficult. To extract key factors when studying the interactions between particles, an unit cell model was proposed by Flower & Watt[139,140] (1988) to simulate the tensile properties of two phase materials. The unit cell model allows the strong interaction between particles to be considered using a reasonable number of finite elements in a CRAY computer. This unit cell model has been adopted in the present work.

The model was constructed to behave as it would if it were one unit in a repeated pattern stretching out in all directions to represent an infinite medium, as shown in Fig. 2.18. A set of constrains are imposed on the surfaces of the unit. They are:

(1) the bottom surface nodes are fixed on imaginary rollers constrained in the vertical direction but are free to move horizontally;

(2) the top surface nodes are similarly constrained, but during deformation, they will be displaced in the vertical direction as a single plane;

(3) the front, back and side faces of the mesh are allowed to move toward each other due to Poisson contraction. However, each of them is constrained to remain a vertical plane at the end of each deformation step, and the sum of all the horizontal forces applied to each vertical plane is zero.

(4) All the shear traction vanishes at the boundary surfaces. This makes all the planes mirror symmetry planes.

Hence, the model applies to a pattern reflected to infinity. Apart from the model, Flower and Watt[139,140,145] showed that the stronger particles carry a higher stress than the matrix, and constraints between two phases extend the high stress regions from the particles into the matrix, along the direction of the maximum principal tensile stress. This produces a fibre-like stress distribution.

For Al/SiC ceramic whisker and particulate reinforced MMCs, non-linear FEM analyses may be divided into two groups, namely elastic-plastic analysis[143,144,147,148,149,152] and elastic-viscoplastic analysis[141,142,146,89,154]. Most of the literature focuses on an investigation of the dependence of tensile properties on the matrix microstructure and on the size, shape, and distribution of the reinforcement phase (so called "parametric" studies). In addition, the effects of the thermally induced stresses[147,89,152] and ductile failure[146,154] have also been simulated by FEM.

Using variations of the unit cell model, many FEM studies have been published. Among them, Christman et al.[141,142] (1989) studied experimentally and numerically the

deformation characteristics of SiC whisker-reinforced 2124 aluminium alloys and SiC particulate reinforced 1100-o aluminium alloys. The FE models which they adopted are axisymmetric or 2D plane strain unit cells, as shown in Fig. 2.19-20. The composite material was idealized in terms of a periodic array of identical cells. For example, Fig.2.19 assumed perfectly aligned end-to-end fibres. The boundary conditions for the axisymmetric region, for y_1 and y_2 greater than zero in Fig. 2.19, are:

(1) shear traction rate is zero at boundaries;

(2) displacement rate along tensile direction bottom surface ($y_2=0$) is zero;

(3) displacement rate along tensile direction at top surface ($y_2=b$) is determined by deformation rate;

(4) displacement rate along radial direction at the circular surface ($y_1=R_0$) is determined from the condition that the average lateral traction rate vanishes.

Compared with the elastic-plastic FEA model of Flower-Watt, the two dimensional model has a similar unit cell concept and boundary conditions except that the latter are described using variable rates. When considering the initial condition from the static state, the two actually are equivalent. For axisymmetric models, less geometric variation compared with the Flower-Watt model in particles and their arrangements is possible because the particles must lie on rotation axis.

In Fig. 2.20, a plane strain unit cell is used to examine the clustering effect from the particles or whiskers. Variations of these models have also been employed by some others (e.g. [146,89,154]) (1991,1992,1992), but these models assume particles which are infinitely long in the direction normal to the plane of the page (plane strain in 2D).

Considering the fact that as the fibres become more aligned during extrusion and injection moulding, and so neighbouring fibres are expected to be somewhat shifted relative to one another, Tvergaard[144] (1990) presented an alternative unit cell model, which is shown in Fig. 2.21. It is an axisymmetric model which uses elastic-plastic analysis. The changes in boundary conditions were to make the edge displacements to be compatible, i.e. $u(\xi)=-u(\eta)$ at the outer circular cell surface, where u is the displacement along tensile direction, ξ and η are equivalent distances from the bottom and the top of the cell, respectively. This FE study of SiC whisker reinforced 2124 aluminium alloys with the same aspect ratio (5-6), volume fraction (13%), and identical heat treatment conditions as in Christman's papers predicted a lower stress-strain response than these predicted by Christman. Christman's model predicted values about 40% higher than those values found experimentally. In addition, the results[144] showed only a slightly higher stress level predicted for rigid fibres than elastic SiC fibres. This is not easy to test by experiment. Shi et al.[152] (1992) have used the model to deal with the effect of thermally induced stresses on the tensile properties of MMCs.

Fig. 2.22 shows three dimensional models applied by Levy et al.[143,147] (1990, 1991), for aligned and staggered particle arrays. A problem with this work is that the boundary conditions used are not clearly spelled out. Also the mesh is coarse at the fibre ends. They claimed that FEA can be used for accurate prediction of the tensile stress-strain behaviour of composite using the experimentally observed mechanical properties of the matrix and the reinforcing phase as the starting point, if the two models are used at the same time to serve as the upper and lower bounds, provided that the thermally

induced stress is also considered.

Another three dimensional model was proposed by Hom[148] (1992) for a further FE study of SiC whisker reinforced 2124 aluminium alloys, shown in Fig. 2.23. In the unit cell, only one-eighth of a circular whisker is modeled, which actually is a modification of Christman's[141,142] and Tvergaard's[144] simulations. Hom's one-eighth of a circular whisker has been applied in the case of the staggered and aligned configuration of fibres.

Other papers have used two dimensional modelling of actual microstructures by Wang et al.[149] (1993) and Brockenbrough et al.[153] (1992) following the earlier method of Karlsson & Sundstrom[133] (1974). However, one foresees that with continuing development FEA will allow actual microstructure modelling in three dimensions so that more accurate field information on deformation characteristics and material failure can be acquired.

In general, the above FEA works on MMCs have quantitatively predicted the correct trend of the deformation characteristics and failure behaviour in MMCs. In accord with the application of continuum mechanics in FEM, their common characteristics may be summarized as follows: (a) A continuum theory of definite deformation, i.e. the Langrangian description of distortion is adopted; (b) The material yield is measured by Von Mises yield potential;(c) The plastic deformation is governed by the Prandtl-Reuss flow law, i.e. the direction of flow is the same as the direction of the outward normal to the yield surface; (d) a combination of iteration scheme and incremental method of numerical techniques is employed to monitor force balance or

equilibrium is monitored at any stress state. (e) The MMCs are assumed to have perfect bonding between the SiC particles and aluminium alloys.

With respect to the material concerns, (f) the whisker or particulate reinforcement is usually presumed to have a cylindrical shape in either two- or three- dimension models; (g) only the influence of the stress and strain concentration in the matrix on material failure is considered; stresses in the particle have been considered.

The objective of the present FE work has been described in Chapter 1. The differences from the above literature will be that:

(1) *the stress concentration within particles* will also be considered in addition to the deformation characteristics in matrix, based on the experimental fact of frequent particle cracking;

(2) a modified Flower-Watt 3D model will be adopted to predict the dependence of tensile properties on particle shape, volume fraction, distribution and residual stresses in MMC of *6061-T4 aluminium alloys reinforced with cubic or spherical SiC particles.*

(3) further work will be focused on:

.the function of stress transfer between particle and matrix;

.the ductility and damage relationships to the hydrostatic tension and the plastic distortion at local states;

.the plastic relaxation and the accumulation;

.changes in stress-strain behaviour due to the thermally induced residual stresses and their affect on strengthening mechanisms.

CHAPTER 3

STRESS CONCENTRATION AND INTERACTIONS

I. Basic Role of Hard Particle in Metal Matrix Subjected to a Tensile Loading

3.1 Introduction

One type of stress concentration may be generated due to the material discontinuities[117], when materials, such as SiC reinforced aluminium metal matrix composites, are subjected to a stress field. This stress concentration reflects the interactions among the different phases in alloys or composites.

To reveal the basic functions of each phase, the simplest prototype that can begin to represent a complicated alloy or composite system may be the one in which an isolated ellipsoidal inhomogeneity is embedded in an infinite domain. Within the ellipsoidal region, the elastic constants differ from those of the remainder (called the inhomogeneity problem).

Dealing with this inhomogeneity problem, it is well known that the most successful theory is due to Eshelby and is now called the classic approach (also see Chapter 2 (2.3)).

This approach[96,116,118] relies on the validation of uniform constraint strains within an ellipsoidal inhomogeneity when a uniform remote stress field is applied. In turn, the calculation of the constraint displacement field was achieved by Eshelby in an elegant closed form.

Motivated by a need to clarify the basic functions of hard-particle reinforcement in composite materials and, in addition, to provide an absolute calibration on concurrent

finite element analysis, the described work in this chapter attempts to get some revelation and insight for matrix-particle interactions by examining in detail the results calculated using the classical approach.

The study is mainly devoted to answering the following questions:

(1) How can the stress and strain distribution around an isolated spherical particle be visualized instead of leaving the classic fundamental approach as an analytical form?

The stress and strain concentrations will be visualized by means of the numerical integration and the ABAQUS and ABAQUS post- processing software. The individual field variables (such as Von Mises stress, mean stress, normal stress, normal strain and strain energy) are examined in order to reveal the general interactions between the two-phases as predicted by Eshelby's equations.

(2) What are the features of the matrix-particle interface characteristics ?

The study reveals the interfacial character of polar, circumferential and angular stress concentrations near the inhomogeneity in the aluminum metal matrix.

(3) How does the misfit of the elastic constants affect stress transfer ?

The stress carrying capability of the inhomogeneity will be measured using the ratio of the tensile stress carried by the inhomogeneity and the remote uniform tensile stress.

(4) Does the size of the inhomogeneity change the stress concentration?

In terms of the derivation of the elastic field, the size effect on the stress concentration is to be determined.

3.2 Visualization of the Stress Concentrations

3.2.1 Materials and Load

The present model consists of a SiC spherical inhomogeneity and an infinite aluminium matrix medium, whose elastic constants are shown in Table 3.1. The uniform far field has been assumed to be a tensiie stress 70.0 MPa (or 0.1% tensile strain).

3.2.2 Basic Relations

When a uniform far field stress is imposed onto a material in which an ellipsoidal inhomogeneity is embedded, stress concentrations arises near the inhomogeneity due to the misfit of elastic constants. In accord with Eshelby's analysis, the perturbation (or constraint) field may be calculated by introducing the concept of an equivalent inclusion.

This concept of the equivalent inclusion denoted that the inhomogeneity problem may be converted into a phase transformation problem as long as the inhomogeneous region is ellipsoidal. In Eshelby's method, the stress concentration generated by the existence of the inhomogeneity can be expressed in an equivalent way to that generated by an imaginary inclusion which has undergone a phase transformation but with the same elastic constants as the matrix. These equivalent 'phase transformation' strains, or eigenstrains, are directly related to and decided by the uniform far field.

In turn, it is well known that Eshelby has developed a sophisticated approach for solving the phase transformation problem. This approach involves a series of the cutting, squeezing and force releasing procedures. The cutting process allows the inclusion to

undergo the stress-free transformation without considering the constraint from the surrounding matrix. The squeezing process recovers the perfect bonding between the inclusion and the matrix. The force releasing indicates that a body layer force is exerted (or is released) on the interface and it generates the perturbation field, which can be calculated by Love's point force theory[164].

In the simulation, the following basic relations will be used.

(1) The relationship between 'phase transformation' strains and the far field;

These 'phase transformation' strains relate to the far field in the form of:

$$e^{T}=Ae^{\wedge};\qquad A=\frac{k^{*}-k}{(k-k^{*})\alpha-k};\qquad \alpha=\frac{1}{3}\frac{(1+\nu)}{(1-\nu)} \tag{3.1}$$

and

$$e'_{ij}{}^{T}=Be'_{ij}{}^{\wedge};\qquad B=\frac{\mu^{*}-\mu}{(\mu-\mu^{*})\beta-\mu};\qquad \beta=\frac{2}{15}\frac{4-5\nu}{1-\nu} \tag{3.2}$$

where $e^{\wedge}$ is the volume change per volume ($=e_{11}+e_{22}+e_{33}$) in the uniform far field; $e'^{\wedge}_{ij}$ the deviatoric strains in the uniform far field; k^{*} and k the bulk moduli of the inhomogeneity and the matrix, respectively; μ^{*} and μ the shear moduli of the inhomogeneity and the matrix; ν the Poisson ratio of the matrix.

(2) The constraint displacement field, i.e.:

$$u_i^{c}=\frac{1}{16\pi\mu(1-\nu)}p_{jk}{}^{T}\psi_{,ijk}-\frac{1}{4\pi\mu}p_{ik}{}^{T}\phi_{,k}$$
$$\psi=\int_{v}|r-r'|dv\quad;\quad \phi=\int_{v}\frac{1}{|r-r'|}dv \tag{3.3}$$

where ϕ is the harmonic, or Newtonian, potential; ψ the biharmonic potential; $p_{ij}{}^{T}$ the

surface tractions ($p_{ij}^T=\lambda e_{mm}^T\delta_{ij}+2\mu e_{ij}^T$, λ is Lamé constant of the matrix); r the vector of the field point, and r´ the vector of the force point.

(3) The relationship for the entire elastic field in the matrix:

The entire elastic field in the matrix consists of the constraint field and the uniform far field. To write the displacement, strain and stress fields individually, they are:

(a) Displacement field;

$$u_{i(out)}=e_{ij}^{A}x_j+u_i^c(r) \tag{3.4}$$

(b) Strain field;

$$e_{ij(out)}=e_{ij}^{A}+e_{ij(out)}^{c}(r) \tag{3.5}$$

(c) Stress field.

$$p_{ij(out)}=k\ (e_{(out)}^{c}+e^{A})\delta_{ij}+2\mu(e'^{c}_{ij(out)}+e'^{A}_{ij}) \tag{3.6}$$

(4) The relationship for the stress field inside the inhomogeneity.

Similarly, in the inhomogeneity, the elastic field may be written as:

(a) Displacement field;

$$u_{i(in)}=e_{ij}^{A}x_j+e_{ij(in)}^{c}x_j$$
$$e_{(in)}^{c}=\alpha e^{T}\ ;\quad e'^{c}_{ij(in)}=\beta e'^{T}_{ij} \tag{3.7}$$

(b) Strain field;

$$e_{ij(in)}=e_{ij}^{A}+e_{ij(in)}^{c} \tag{3.8}$$

(c) Stress field.

$$p_{ij(in)} = k^*(e^c_{(in)} + e^A)\delta_{ij} + 2\mu^*(e'^c_{ij(in)} + e'^A_{ij}) \tag{3.9}$$

or

$$p_{ij(in)} = k(e^c_{(in)} - e^T + e^A)\delta_{ij} + 2\mu(e'^c_{ij(in)} - e^T + e'^A_{ij}) \tag{3.10}$$

It should be noted that the stress and the strain field inside the ellipsoidal inhomogeneity is uniform.

3.2.3 Programming

The overall programming has been classified into three parts shown in Figure 3.14, namely preprocessing, field calculation and postprocessing.

Block 1 is the preprocessing part. A proper three dimensional mesh has been formed by IDEAS software shown in Figure 3.1a, in which the particle is geometrically defined as a unit radius sphere, with the origin at its centre. The number of the nodes is 2952 in the mesh. Each node in the model is a field point by which the displacement field is calculated (though it is not the only means to get a field point). Because the inclusion is symmetric, only the first quadrant of the field has been considered.

In the second part, the subroutines of MATTRANS, READIN, INTEGRAL, DIS AND PRINT determine the numerical procedures. MATTRANS operates the input information such as material properties, particle geometry and far field components. It also calculates the equivalent transformation strains and stresses, and the constraint uniform strains in the inhomogeneity. READIN locates the field points by transferring the coordinates in a one-to-one manner, connecting with the original mesh. The kernel

parts of the field calculation are INTEGRAL and 12 FUNCTIONS which collaborate with each other to obtain the derivatives of Newtonian potentials and the biharmonic potentials. The displacement field is calculated from the subroutines DIS1, DIS2, and DIS3. The results from PRINT are sent to calculate the elastic fields of strain, stress, effective stress (Von Mises stress), and strain energy. In order to use the facility of ABAQUS software, i.e. calculating the elastic field variables, the present simulation inputs the displacements as the three potentials attaching with the original mesh. An ABAQUS input file has been generated to obtain the complete information of the elastic field.

The third part, i.e. the postprocessing (Box 2), is to visualize the elastic field due to the misfit of the inhomogeneity and the matrix. The visualization has made use of the ABAQUS postprocessing software.

3.2.4 Field Disturbance

Significant perturbation has only been developed near the matrix-inhomogeneity interface due to the misfit of the two phases. This disturbance may be demonstrated by the contours of the field variables of Von Mises stress (or the effective stress), the hydrostatic pressure, the normal stress, the normal strain, and the transverse stress.

(a) Von Mises stress (or the effective stress)

In metal elasticity and plasticity, the effective stress is a measure of distortion in material, in which the effective stress is defined as: $\sigma_{eff}=[(\sigma_1-\sigma_2)^2+(\sigma_2-\sigma_3)^2+(\sigma_3-\sigma_1)^2]^{1/2}/\sqrt{2}$, where σ_1, σ_2, σ_3 are the principal stresses. Its contour plot is illustrated in Fig. 3.1(a)&(b)

(in the units of Pa, i.e. N/M^2). The results mainly show the following:

(1) The SiC particle carries higher effective stresses than the aluminium matrix;

(2) The highest value in the matrix is located along the pole a small distance away from the interface a small distance;

(3) A butterfly type of low stress region has been developed at an angle of about 50-60° degrees from the pole.

These results reflect the stress carrying capability of the inhomogeneity and imply that the aluminium matrix will yield first along the pole and a small distance away from the interface. In addition, SiC hard particle reinforcements will be distinguished from soft particle constituent composites in their stress concentration patterns, which ultimately determines the different failure mechanisms in the materials.

(b) The hydrostatic pressure

In continuum mechanics, the hydrostatic pressure is a measure of a mean stress state, which is defined as: $-\frac{1}{3}(\sigma_1+\sigma_2+\sigma_3)$. It directly relates to the specific volume change whereas the effective stress responds to the distortion at the local state. The hydrostatic pressure is usually not considered to play a significant role in metal yielding. Its contour plot is illustrated in Fig. 3.2 (in the units of Pa), which shows:

(1) In the spherical SiC particle, the tensile hydrostatic pressure (or mean stress) is higher than the value of the far field;

(2) The greatest tensile hydrostatic stress occurs in the matrix along the pole at the interface.

The stress transfer to the inhomogeneity is again demonstrated. However, what

is distinguishable from the other contour components is that the largest mean stress concentration occurs at the interface, which may play a very important role on the interface detachment in two-phase materials.

(c) The normal stress (S22)

The normal stress here means the stress along the tensile direction (S22), whose contour is shown in Fig. 3.3. In fracture mechanics, S22 is a key factor that determines whether materials fail or not, depending on the stress intensity at a small interfacial crack. The contour plot of this field variable indicates that:

(1) The SiC particle carries a higher tensile stress than the aluminium matrix;

(2) The highest value in the matrix is located along the pole a small distance away from the interface;

(3) Lobe regions of low normal stress exist at the side of particle.

The stress transfer to the SiC particle is evident. However, on the other hand, the inhomogeneity does function as a stress raiser within the matrix, which makes it more susceptible to fracture.

(d) The normal strain (E22)

The contour of the normal strain (E22) acting in the tensile loading direction is illustrated in Fig. 3.4 (in the units of m/m). This shows that:

(1) The SiC particle deforms less than the aluminium matrix;

(2) The highest magnitude of normal strain is located in the matrix along the pole at a small distance from the interface;

(3) A butterfly type of low strain region is formed at an angle of about 50-60°

degrees from the pole.

These results have shown a natural consequence that the constituent with higher elastic constants has the higher resistance against deformation, while in matrix the local disturbance would be the source of the considerable change of the dislocation microstructure along the pole.

(e) The transverse stress (S11)

The contour of the transverse stress, which is the stress normal to the tensile direction, is illustrated in Fig. 3.5 (in the units of Pa). This shows that:

(1) The SiC particle bears a compressive stress in the direction normal to the tensile loading;

(2) The contour in the aluminium matrix exhibits the highest transverse tensile stress along the pole at the interface and the greatest compressive stress at the mid-line circumference (the equator) normal to the loading direction;

(3) The magnitude of this perturbation is minor compared with that of the normal stress.

Having the compressive stress in the SiC particle reflects the constraint reaction from the surrounding matrix. This is because, when subjected to the tensile loading, the aluminium matrix (with high Poisson ratio) deforms more laterally, so that to accommodate the common interface the particle resists the deformation and so exhibits the compressive behaviour. In addition, the high triaxiality at the polar interface is escalated by the tensile stresses in all three principal directions.

In general, within the spherical SiC particle, the constraint and entire stress and

strain fields are uniform whereas the field disturbance is generated in the matrix and dies away rapidly from the interface, according to Eshelby's analysis, which has been demonstrated by the contours of the individual field variable.

To quantitatively elucidate the interface characteristics and the stress transfer to an inhomogeneity, the next two sections will highlight the variations with orientation and position of the interfacial stresses, and make an estimate of the stress carrying capability of the spherical inhomogeneity as a function of its elastic constants.

3.3 Interface Characteristics

3.3.1 Geometry Definition

Low stress gradients far away from, and large gradients near, an inhomogeneity have been demonstrated in the previous section by applying Eshelby's analysis. In order to measure such stress concentrations around a spherical inhomogeneity, we define the following three variations in analogy with a globe representing the earth:

(1) Polar characteristics, which represent the distribution of the relative elastic field along the axis parallel to the far field loading direction;

(2) Circumferential (latitudinal) characteristics, which represent the distribution of the relative elastic field in the plane of the equator;

(3) Angular characteristics, which represent the distribution of the specific elastic field at the interface along a longitudinal line changing in angle from 0 to 90° degrees from the pole.

Here, the relative elastic field means the ratio of $(F-F_0)/F_0$ where $(F-F_0)$ is the difference between the local and the far field values (called the "perturbation"), and F_0 the far field value. The specific elastic field means simply the ratio of the local and the far values, i.e. F/F_0. The elastic field variables include the effective stress, the mean stress (or the tensile hydrostatic pressure), the normal stress, the normal strain, and the elastic energy.

3.3.2 Calculation Procedures

As mentioned in Section 3.2.3, obtaining the elastic field is mainly a process of finding the displacements using Eshelby's analysis, and then making use of the ABAQUS software to acquire from the displacement field the local elastic values, such as the effective stress, the hydrostatic stress, the normal stress, and the normal strain.

These values, which are given from the ABAQUS output, are attached with the corresponding coordinates. The calculation for the relative elastic field follows the definition in Section 3.3.1. However, the calculation of the angular characteristics will apply Eshelby's analysis again right at the interface to avoid the inaccuracy of the ABAQUS calculation at the interface. The formula from reference[118] for calculating the constraint strains at the interface in terms of the dilatational and deviatoric parts of e_{ij}^c are:

$$e^{c}_{(out)} = e^{c}_{(in)} - \frac{1}{3}\frac{1+\nu}{1-\nu}e^{T} - \frac{1-2\nu}{1-\nu}e'^{T}_{ij}n_i n_j$$

$$e'^{c}_{ik(out)} = e'^{c}_{ik(in)} + \frac{1}{1-\nu}e'^{T}_{jk}n_j n_k n_i n_l - e'^{T}_{ik}n_k n_l - e'^{T}_{lk}n_k n_i \qquad (3.11)$$

$$+\frac{1-2\nu}{3(1-\nu)}e'^{T}_{jk}n_j n_k \delta_{il} - \frac{1}{3}\frac{1+\nu}{1-\nu}e^{T}(n_i n_l - \frac{1}{3}\delta_{il})$$

where n_i is the outward normal of the inhomogeneity, ν the Poisson ratio of the matrix, ^{T} represents the phase transformation terms, $'$ the deviatoric terms, and ^{c} the constraint terms. Afterwards, the elastic field may be acquired by means of Equation (3.5), Equation (3.6) and the corresponding definitions of the field variables.

Several drafting programs have been developed to illustrate the stress concentration in different orientations.

3.3.3 Interface Characteristics

Fig. 3.6 shows the polar perturbation of the elastic field, where **r** represents the field point distance from the origin and **a** is the radius of the spherical particle. The field disturbance demonstrates the strong fluctuation of the elastic field near the interface.

One striking result from Fig. 3.6 is that all the relative elastic field variables, except the elastic energy, die away from the interface in the almost same relative stress or strain concentration when the field point is located at a distance greater than one radius of the particle away from the interface. This is in spite of the severe difference in the stress or strain concentration pattern near the interface.

Specifically, Fig. 3.6 shows that:

(1) A dramatic perturbation of the tensile hydrostatic stress occurs at the interface, which is about 2.11 times larger than the far field level. This perturbation dies away from the interface very rapidly compared with any other components.

(2) The other perturbations at the interface in sequence are strain energy (0.89 times), normal stress(0.67 times), normal strain(0.2 times), respectively, which are not the maximum perturbations of these individual components.

(3) Except for the tensile hydrostatic pressure, the relative maximum perturbations of the elastic field have the ranked sequence of strain energy(1.52 times at 0.2a), normal stress(0.8 times at 0.11a), normal strain (0.57 times at 0.2a) and Von Mises stress (0.49 times at 0.3a) from particle interface, respectively.

(4) Eventually, the stress and the strain perturbation field vanishes at the rate of $1/r^3$ to zero.

What does the illustration present us in a practical sense ?

Of course, a straightforward inference is that yielding would first occur at about 0.3a from particle. However, consideration of the stress concentration makes it confusing to decide which component can be used as the most suitable measure for the damage initiation. Should it be the normal stress or the tensile hydrostatic pressure or the effective stress or a combination of these ? This doubt is present because the stress concentration of the tensile hydrostatic pressure is much higher than that of the other components. In fracture mechanics, it is commonly believed that the fracture may be determined by the stress intensity factor (or the normal stress intensity factor) for the case of an existing crack. But, in the hard particle reinforcement composite, the stress

around a particle does not always approach infinity as the trend of $1/\sqrt{r}$ would indicate. Can we still use the stress intensity factor to measure the damage initiation (or void initiation) from the stress concentration? Even if we are able to decide the stress intensity factor by some method, for example, by the $1/\sqrt{r}$ curve fitting, the physical meaning is very vague due to the different patterns of the stress concentration of the individual field variables. Fig. 3.6 supports the proposition that the tensile hydrostatic pressure plays an important role in the damage initiation (or void initiation) in two-phase materials.

Actually, the damage initiation is complex and is unlikely to be determined by only one field component. For instance, the stress state is uniquely defined by the three invariants and the three principal stress directions. If the damage initiation is determined by the stress state, it would depend on multiple factors. The different criteria for void initiation have been reviewed in Chapter 2. Among those, the stress and strain criteria are experimentally based. The consideration of the energy concentration is of interest in this present analysis.

Consider the elastic energy concentration. According to the derivation by Dieter[163], the total strain energy can be split into a term depending on change of volume and a term depending on distortion. In the present work, it will be expressed by the mean stress and the effective stress as follows.

$$U_0=\frac{1}{2k}\sigma^2_{mean}+\frac{1}{6\mu}\sigma^2_{eff} \tag{3.12}$$

where U_0 represents the elastic energy. The first term is related to the change of volume, the second term is related to the distortion; σ_{mean} is the mean stress (or the tensile

hydrostatic pressure), σ_{eff} the Mises effective stress. In accord with the formula, we consider two situations, the far field and the local field at the interface, to compare the energy variation between the two energy terms in a system comprised of an aluminium matrix and a spherical SiC particle.

By substituting the elastic constants of the aluminium matrix into the formula (k=68.6 GPa, μ=26 GPa). The first term becomes $7.3\times10^{-12}\sigma^2_{mean}$ and the second term becomes $6.4\times10^{-12}\sigma^2_{eff}$.

(a) The far field

For the far field, since $\sigma_{mean}=\sigma_{yy0}/3$ and $\sigma_{eff}=\sigma_{yy0}$, respectively, where σ_{yy0} is the tensile stress to which the system is subjected. The ratio of the two far field terms is 0.126 (about one eighth), i.e. the energy generated by the volume change is much smaller than that generated by the distortion.

(b) The elastic energy at the interface

At the interface, the first term increases to $7.85\times10^{-12}(\sigma_{yy0})^2$ ($\because \sigma_{mean}|_{local}=3.11\sigma_{mean}|_{far}=1.037\sigma_{yy0}$), while the second term is $5.42\times10^{-12}(\sigma_{yy0})^2$ ($\because\sigma_{eff}|_{local}=0.92\sigma_{eff}|_{far}=0.92\sigma_{yy0}$). The ratio increases to 1.446. The energy generated by the volume change increases rapidly as the interface is approached. At the interface, it exceeds the distortion energy.

The above analysis suggests that in the homogeneous matrix subjected to uniaxial tension, the energy generated by the distortion dominates, whereas in the two-phase system the energy generated by the volume change would also play a very important role, especially when the particle is much stiffer than the matrix. Practically, this implies

that the determination of the ductility of the two phase materials should not ignore considering the local concentration of the tensile hydrostatic pressure because of the energy generated by the volume change.

Fig. 3.7 presents the calculated circumferential perturbations in the relative elastic field of the effective stress, the normal stress, the tensile hydrostatic pressure, the normal strain, and the strain energy. It shows that:

(1) All the perturbations die away from the interface monotonically. The size of the disturbance is about the radius of the spherical SiC particle.

(2) Negative perturbations characterize the circumferential elastic field concentrations of the hard particle reinforcement.

(3) The rank of the relative perturbations is in the sequence of the hydrostatic pressure, strain energy, the normal stress, the normal strain, and the effective stress.

Fig. 3.8 illustrates the angular variation, on a longitudinal line along the interface, of the relative perturbations in the specific elastic fields of the effective stress, the normal stress, the tensile hydrostatic pressure, the normal strain, and the strain energy. It is noted that at angles from 0° to about 40° the elastic field concentrations of the different variables are scattered rather than varying together in the same direction as a group, i.e. the concentration factor for different components changes from 0.9 to 3.1 in this system of an aluminium matrix and a spherical SiC particle. Beyond 40° through to 90°, they decrease together as a group.

3.3.4 Dependence of the Interfacial Stress Concentration on Elastic Moduli

To emphasize that the pattern of the elastic field concentrations depends on the elastic constants of the inhomogeneity, two extreme cases have also been considered: a rigid sphere and a spherical cavity.

For the case of the rigid sphere, the longitudinal (or angular) character is illustrated in Fig. 3.9. The elastic field variables examined include the effective stress, the tensile hydrostatic pressure, the normal stress, the normal strain and the elastic energy. This angular character is similar to that for the case of the SiC sphere, i.e. this pattern is scattered up to 40° degrees.

What is different is that the perturbations are stronger, for example, the perturbation of the tensile hydrostatic pressure rises up to about 2.8 times as large as that of the far field at the interface, while for the case of the SiC sphere the perturbation is 2.11 times. Note that the stress concentration does not approach infinity as one might think due to the extreme rigidity of the sphere (or the severe discontinuity of the materials at the interface).

For the case of the spherical cavity, the longitudinal character is shown in Fig. 3.10. It is completely different from that of the rigid sphere and the SiC sphere. What is distinctive is that:

(1) The highest positive stress concentration occurs near the equator instead of along the pole.

(2) The perturbations of all the field variables near the equator, except for the strain energy, approximately match each other, i.e. they are not scattered. The highest elastic

field concentration is that of the strain energy at the equator.

The former feature, in (1), implies that the difference in the stress concentration pattern would produce a different failure mechanism in the two-phase materials depending on the type of the inhomogeneity, if we regard a cavity as the extreme of a soft inhomogeneity. It is noted that whether or not the plastic behaviour of the matrix is considered does not affect these results because the plastic deformation always starts from the pre-deformed elastic field, and failure initiation occurs when whatever critical state of the stress and deformation is exceeded. For the case of the spherical cavity, the failure initiates at the equator.

The latter, in (2), infers that for the case of the spherical cavity any stress component may be used to measure the stress concentration without large difference by choosing the effective stress component, the normal stress component, or the tensile hydrostatic pressure component, whereas for the case of the hard sphere the selection of the given stress component leads to a different measure of the stress concentration. The reason for the highest strain energy occurring at the equator is that both the tensile hydrostatic pressure and the effective stress are a maximum at the equator at the interface.

These results have practical significance for the nucleation and growth of voids near hard particles in MMCs:

(1) at the interface with perfect bonding, the local stress state would cause void initiation at the poles of the particles along the line of loading.

(2) for the growth of these voids once they are created, the local stress redistribution

after void initiation and during the void growth will tend toward that shown in Figure 3.10, and the potential for void linking will be due to the high dilatation energy (or the high triaxiality) and the high distortion (or the high effective stress) near the equators of the growing voids.

These explain why in Al/$(SiC)_p$ MMCs the void is commonly nucleated along the pole at the interface, while void linking usually occurs at a large angle from the pole (i.e. from the tensile loading direction).

To optimize the ductility of the hard particle reinforced composites, it is suggested that one should minimize the overlap of the tensile pressure field from neighbouring particles to avoid the strong triaxial stress at the pole (i.e. avoid particle clustering along the line of loading).

3.4 Stress Carrying Capability of Particle

In hard particle reinforced metal matrix composites, the stress transfer from the matrix to the particles is mainly determined by the misfit of the elastic constants between the two phases. In designing alloys and particulate composites, the questions of how effective the particles are at transferring load to themselves, and thereby providing reinforcement, is of interest.

The following attempts to get some insight on the dependence of the stress transfer on the elastic misfit based on Eshelby's analysis.

3.4.1 Definition

To measure the stress transfer to the particle in the inhomogeneity problem subjected to a tensile loading σ_{yy0}, the stress carrying capability of particle is defined as the ratio of the normal stress in the particle to that at the remote field, i.e. the ratio $=(\sigma_{yy}|_{\text{sphere}})/\sigma_{yy0}$.

3.4.2 Derivation

The expression for the stress carrying capability of a particle has been derived by the present author into the following form:

$$\frac{\sigma_{yy}}{\sigma_{yy0}}=\frac{k^*}{3k}(1+\alpha A)+\frac{2\mu^*}{3\mu}(1+\beta B) \tag{3.13}$$

$$\alpha=\frac{1}{3}\frac{(1+\nu)}{(1-\nu)}\ ;\ \beta=\frac{2}{15}\frac{4-5\nu}{1-\nu}\ ;\ A=\frac{k^*-k}{(k-k^*)\alpha-k}\ ;\ B=\frac{\mu^*-\mu}{(\mu^*-\mu)\beta-\mu}$$

where all the symbols have been defined previously.

To obtain these equations, consider the uniform elastic field within a sphere by means of Eshelby's analysis. These stresses may be written in the form of Hooke's law:

$$\sigma_{ij(in)}=k^*(e^c{}_{(in)}+e^A)\delta_{ij}+2\mu^*(e'^c_{ij(in)}+e'^A_{ij}) \tag{3.14}$$

where the constraint strains are associated with the far strains and the equivalent 'phase transformation' strains, which are:

$$e^c_{(in)}=\alpha e^T\ ;\ e'^c_{ij(in)}=\beta e'^T_{ij}\ ;\ e^T=Ae^A\ ;\ e'^T_{ij}=Be'^A_{ij} \tag{3.15}$$

Substitute Equation (3.15) into Equation (3.14), and the relationship of the

stresses and the far field strains is obtained straightforwardly:

$$\sigma_{ij(in)} = k^*(1+\alpha A)e^A\delta_{ij} + 2\mu^*(1+\beta B)e'^A_{ij} \tag{3.16}$$

and the tensile stress within the sphere becomes:

$$\sigma_{yy} = k^*(1+\alpha A)e^A + 2\mu^*(1+\beta B)e'^A_{yy} \tag{3.17}$$

Further, the relationship between the far field strain and the far field tensile stress can be determined by making use of the following:

$$\begin{cases} \sigma_{yy0} = ke^A + 2\mu e'^A_{yy} \\ 0 = ke^A + 2\mu e'^A_{xx} \\ 0 = ke^A + 2\mu e'^A_{zz} \end{cases} \tag{3.18}$$

Note that $e'_{xx}{}^A + e'_{yy}{}^A + e'_{zz}{}^A = 0$. Hence, we have

$$e^A = \frac{\sigma_{yy0}}{3k} \quad ; \quad e'^A_{yy} = \frac{\sigma_{yy0}}{3\mu} \tag{3.19}$$

Therefore, Equation (3.13) is obtained simply by substituting Equations (3.19) into Equation (3.17).

3.4.3 Dependence on the Elastic Constants

To evaluate the dependence of the stress transfer on the elastic constants of the two phases, we investigate the formula of the stress carrying capability, Equation (3.13).

In order to emphasise the effect of the stiffness, assume that the Poisson ratios of the two phases are the same. Later, it will be shown that the effect of Poisson ratio of the particle is minor at the high ratio of the stiffness (E^*/E). Note that $k=E/3(1-2\nu)$ and

$\mu = E/2(1+\nu)$. Equation (3.13) is simplified to:

$$\frac{\sigma_{yy}}{\sigma_{yy0}} = \frac{E^*}{3E}\left(1+\alpha\frac{E^*-E}{(E-E^*)\alpha-E}\right)+\frac{2E^*}{3E}\left(1+\beta\frac{E^*-E}{(E^*-E)\beta-E}\right) \qquad (3.20)$$

If the Poisson ratio is chosen as 1/3 (as that of the aluminium matrix), the further degeneration of the form (3.13) gives:

$$\frac{\sigma_{yy}}{\sigma_{yy0}} = \frac{9\left[\frac{E^*}{E}\right]\left(2+3\left[\frac{E^*}{E}\right]\right)}{\left(1+2\left[\frac{E^*}{E}\right]\right)\left(8+7\left[\frac{E^*}{E}\right]\right)} \qquad (3.21)$$

or if it is assumed that $x = E^*/E$, one gets:

$$f(x) = \frac{\sigma_{yy}}{\sigma_{yy0}} = \frac{9x(2+3x)}{(1+2x)(8+7x)} \qquad (3.22)$$

where f(x) represents the stress carrying capability as a function of the ratio of the stiffnesses.

Consider some specific cases, which are $x=0$, 1, and ∞. The particles correspond to those of the extremely soft, the identical, and the rigid compared with the elastic constants of the matrix. The values of the stress carrying capability are respectively zero, one and 27/14. Physically, these results indicate that

(1) the extremely soft particle is too soft to carry stress;

(2) the constraint by the surrounding matrix to the identical stiffness particle disappears;

(3) the stress transfer does not reach infinity when the particle is rigid.

Generally, the stress carrying capability increases with an increase of the stiffness

of the particle.

However, how is the stress carrying capability affected by the rate of increase of the stiffness of the particle ?

Consider the change in terms of the derivative of Equation (3.22), which may be derived as:

$$f'(x)=\frac{9[16+48x+41x^2]}{(1+2x)^2(8+7x)^2} \tag{3.23}$$

where f'(x) represents the increase rate of the stress carrying capability of the particle via the elastic misfit of the two phases.

Again, consider three cases at x=0, 1, and ∞, in which the rates are 2.25, 0.46, and 0. The results denote that at a large ratio of the misfit, the stress transfer can only be increased marginally by continuously increasing the stiffness of the particle, while at a low ratio of the misfit, the increase of the capability at stress transferring to the particle increases considerably with an increase in the Young's modulus of the particle.

In order to also consider the influence of the Poisson ratio on the stress transfer, Equation (3.13) is used to express the stress carrying capability of the inhomogeneity and graphics algorithms have been developed to illustrate the influence. Note that the elastic constants of the matrix are assumed to be those of aluminium.

Figure 3.11, which plots the relationship between the stress carrying capability and the ratio of the Young's moduli, represents the stress carrying capability of a hard particle, where E and E_0 are the Young's moduli of the spherical particle and the matrix, respectively. The ratio between the Young's moduli alters from one to ten.

It shows that the stress carrying capability of a hard particle does monotonically increase with the increase of the Young's modulus ratio, i.e. E^*/E. This increase appears to be a roughly parabolic curve. At a high ratio of Young's moduli, the stress carrying capability of a hard particle does not gain much by further increasing the stiffness of hard particles, whereas at the low ratio (e.g. 1-2), the stress transfer depends strongly on the misfit, i.e. the capability of the stress carrying capability increases dramatically. Beyond a ratio of about 6, the gain in stress transfer is relatively minor. Practically, this means that in order to find a 'optimum' reinforcement, a very high stiffness of hard particles is not always necessary, but rather a reinforcement with both stiffness and lightness is required.

Another feature of the stress transfer to the hard sphere is that the stress carrying capability changes only slightly with Poisson ratio as shown in Fig. 3.11, especially at the high ratio of Young's modulus.

Fig. 3.12 represents the stress carrying capability of soft particles, where the ratio of the Young's moduli, E^*/E, varies from zero to one.

Similar to Fig. 3.11, Fig. 3.12 shows there is an increase of the stress transfer with an increase of the ratio of Young's moduli. However, what is different is the sensitivity of the increase to the Poisson ratio of the particle. At the low ratio of Young's moduli, the stress carrying capability of the particle strongly depends on the Poisson ratio of the particle. The higher the Poisson ratio, the higher is the transfer of stress to the particle. An interesting inference from the results is that even if the stiffness of the reinforcement is slightly lower than the matrix, the stress transferred from the matrix

may still be greater than that within the far field matrix when the Poisson ratio of the reinforcement is higher than that of the matrix. For example, if for whatever reason the uniformity of the elastic constants within a material is changed, and if the Poisson ratio of the disturbed region is higher than the remainder (the stiffness may remain the same or be slightly changed), strengthening of the material may be achieved.

Furthermore, there is another interesting measure of the gathering capability of an inhomogeneity. Similar to the definition of the stress gathering capability, the gathering capability for strain energy density may be defined as the ratio of the strain energy density within the inhomogeneity to that at the far-field. It can be proven from Eshelby's theory that the strain energy density gathering capability may be written as the following formula:

$$\frac{SENER}{SENER_0} = 1 - \frac{x(1-x)}{(1+2x)(8+7x)} - \frac{2(1-x)^2(32+112x+105x^2)}{(1+2x)^2(8+7x)^2}$$

if it is assumed that both the matrix and the inhomogeneity have the same Poisson ratio (equal to 1/3) and that the variable x represents the ratio of the Young's modulus of the inhomogeneity and that of the matrix, E*/E (i.e. the ratio of Young's moduli). This factor varies with the misfit of moduli as shown in Fig.3.13. The transfer of the strain energy is zero in the cases of the rigid particle and the equivalent cavity, whereas the strain energy will be equivalently transferred to the particle which has matrix properties. In all other cases, the strain energy density will be lower in the particle than that in the far field. This obviously implies that whenever there exists a misfit of material moduli, there is a step in the stored energy at the interface. It must be remembered that the stored

energy is the product of the stress and strain. If particle fracture is to be a failure mechanism, then it appears that a substantial part of the energy loss driving the failure must come from the surrounding matrix.

3.5 Size effect

In the following, it will shown that the constraint stress concentration is scaled by the size of the spherical inhomogeneity, i.e. that the local constraint stress and strain is the same at a field point $\mathbf{r}_1$ and at a field point $\mathbf{r}_2$ if $\mathbf{r}_1/a_1=\mathbf{r}_2/a_2$ where:

(1) The field point $\mathbf{r}_1$ is a point in the matrix in which a spherical inhomogeneity with the radius a_1 is embedded.

(2) The field point $\mathbf{r}_2$ is a point in the matrix in which a spherical inhomogeneity with the radius a_2 is embedded.

Consider a system in which a matrix containing a spherical inhomogeneity is subjected to a far field. Assume the radius of the sphere is a and that the inhomogeneity has different elastic constants from the matrix. According to Eshelby's analysis, the calculation of the constraint field can be converted into an equivalent phase transformation problem (or the inclusion problem). The equivalent "phase transformation" strains (or stress-free strains) may be obtained from the far field, and the constraint strain terms may be written as:

$$u_{i,j}^{c}=\frac{1}{16\pi\mu(1-\nu)}p_{jk}{}^{T}\psi_{,ijkl}-\frac{1}{4\pi\mu}p_{ik}{}^{T}\phi_{,kl}$$
$$\psi=\int_{v}|r-r'|dv;\quad \phi=\int_{v}\frac{1}{|r-r'|}dv \tag{3.23}$$

where ϕ and ψ are the Newtonian potentials and biharmonic potentials, $\mathbf{r}$ is a field point, $\mathbf{r}'$ is a point within the volume v.

Let us examine the scaled feature starting from the derivatives of the potentials. Note that the coefficients are the same for any system if the only difference is the size of the inhomogeneity.

In the system, at the field point $\mathbf{r}$, the strains may be expressed using the derivatives of:

$$\psi_{,ijkl}=\left[\int_{v}|r-r'|dv\right]_{,ijkl}=\frac{\partial^{4}\psi}{\partial x_i\partial x_j\partial x_k\partial x_l};\quad \phi_{,kl}=\left[\int_{v}\frac{1}{|r-r'|}dv\right]_{,kl}=\frac{\partial^{2}\phi}{\partial x_k\partial x_l} \tag{3.24}$$

where v is a volume of a sphere in which the radius is a and the boundary equation of the sphere is $x_1^2+x_2^2+x_3^2=a^2$.

Consider the biharmonic potentials first. Assume $\mathbf{t}=\mathbf{r}/a$ and $\mathbf{t}'=\mathbf{r}'/a$, i.e. $\mathbf{t}=\mathbf{t}(x_1/a,x_2/a,x_3/a)$ and $\mathbf{t}'=\mathbf{t}'(x_1'/a,x_2'/a,x_3'/a)$, so that the boundary equation of the sphere becomes $t_1^2+t_2^2+t_3^2=1$. The forms are converted into:

$$\psi_{,ijkl}=\left[\int_{v_0}|at-at'|a^3dv_0\right]_{,ijkl}=\left[a^4\int_{v_0}|t-t'|dv_0\right]_{,ijkl} \tag{3.25}$$

where v_0 is a spherical volume with a unit radius.

If we define a normalized function $\psi_0(\mathbf{t})$, i.e.

$$\psi_0(t)=\int_{v_0}|t-t'|dv_0 \tag{3.26}$$

we obtain

$$\psi_{,ijkl}=\left[a^4\psi_0(t)\right]_{,ijkl}=a^4\left(\frac{\partial t_i}{\partial x_i}\frac{\partial}{\partial t_i}\left(\frac{\partial t_j}{\partial x_j}\frac{\partial}{\partial t_j}\left(\frac{\partial t_k}{\partial x_k}\frac{\partial}{\partial t_k}\left(\frac{\partial t_l}{\partial x_l}\frac{\partial\psi_0(t)}{\partial t_l}\right)\right)\right)\right) \tag{3.27}$$

Since $\partial t_i/\partial x_i=\partial t_j/\partial x_j=\partial t_k/\partial x_k=\partial t_l/\partial x_l=1/a$, the above strain terms eventually may be written in the ratio of the distance of a field point and the particle radius, that is to say,

$$\psi_{,ijkl}=\left(\frac{\partial^4\psi_0(t)}{\partial t_i\partial t_j\partial t_k\partial t_l}\right)\Bigg|_{t=\frac{r}{a}} \tag{3.28}$$

Equation (3.28) verifies that the fourth-order derivatives of the biharmonic potentials are scaled by the radius of the sphere; namely, for any value of the radius, the derivatives are decided only by the ratios of the field coordinates to the sphere radius.

Similarly, for the Newtonian potential terms

$$\phi_{,kl}=\left[\int_{v_0}\frac{a^3}{|at-at'|}dv_0\right]_{,kl}=\left[a^2\int_{v_0}\frac{1}{|t-t'|}dv_0\right]_{,kl} \tag{3.29}$$

where v_0 and a have been defined previously.

A normalized function $\phi_0(t)$ is defined as follows;

$$\phi_0(t)=\int_{v_0}\frac{1}{|t-t'|}dv_0 \tag{3.30}$$

By substituting this definition into the second-order derivatives. We get:

$$\phi_{,kl}=\left[a^2\phi_0(t)\right]_{,kl}=a^2\left(\frac{\partial t_k}{\partial x_k}\frac{\partial}{\partial t_k}\left(\frac{\partial t_l}{\partial x_l}\frac{\partial \phi_0(t)}{\partial t_l}\right)\right) \tag{3.31}$$

Again, because $\partial t_k/\partial x_k=\partial t_l/\partial x_l=1/a$, the derivatives of the Newtonian potentials may be written as:

$$\phi_{,kl}=\left(\frac{\partial^2\phi_0(t)}{\partial t_k\partial t_l}\right)\Bigg|_{t=\frac{r}{a}} \tag{3.32}$$

Equation (3.32) verifies that the second-order derivatives are also scaled.

Recall Equation (3.23), i.e.

$$u_{i,j}^{c}=\frac{1}{16\pi\mu(1-\nu)}p_{jk}{}^{T}\psi_{,ijkl}-\frac{1}{4\pi\mu}p_{ik}{}^{T}\phi_{,kl}$$
$$\psi=\int_v|r-r'|dv;\quad \phi=\int_v\frac{1}{|r-r'|}dv \tag{3.23}$$

in which the constraint strain field is expressed by the derivatives of the two potentials.

Hence, the constraint strain field is normalized by the size of the inhomogeneity. The practical meaning of this is that the stress and strain perturbation around the particle is determined by the ratio of the field-point distance and the particle size and the misfit of the elastic constants.

(Note that with respect to the constraint displacement field, the size of the inhomogeneity does not scale the value. Actually, the displacement field is amplified by by a factor of the radius a for the same distance-to-radius ratio.)

3.6 Summary

The elastic field around a SiC sphere within the aluminium matrix has been visualized by means of computer simulation applying Eshelby's model. The general interaction between the two phases can be summarized as:

(1) SiC particles carry higher tensile stresses than the aluminium matrix.

(2) All the stress and strain perturbations in the aluminium matrix are developed near the interface, and eventually they approach the far field at a rate which is proportional to $1/r^3$.

(3) The triaxial stress exhibits the strongest perturbation and compared with any other components it has the highest relative concentration along the pole at the interface.

(4) Matrix yielding would first occur along the pole a small distance away from the interface.

By examination of the matrix-inhomogeneity interfacial stress characteristics, it is found that:

For a hard particle, all the highest relative stress concentrations in the aluminium matrix are along the pole, though the degree of the concentration is different for different field variables. For the soft particle, the highest concentrations are near the equator. This indicates that there would exist different failure mechanisms with different types of particle reinforcement.

With respect to the causes of interfacial detachment, the analysis shows that the elastic energy consist of two terms: (a) that generated due to the specific volume change; (b) that generated due to the distortion. The consideration of the detailed results suggests

that in the homogeneous matrix subjected to uniaxial tension, the failure may be determined by the distortion energy (or the effective stress), while in the two-phase composites the tensile hydrostatic pressure also plays an important role on the material failure, especially when the volume fraction of the reinforcement is high.

With respect to the dependence of the stress transfer on the misfit of the elastic constants between the two phases, the results show that:

(1) The stress carrying capability increases monotonically with the increase of the ratio of the Young's moduli;

(2) The increase rate of the stress carrying capability is low at the high modulus ratio, but high at the low modulus ratio. These infer that it is not always necessary to obtain the effective stress transfer by choosing the very stiff reinforcement.

Finally, it has been shown that all the stress and strain perturbation fields are scaled by the particle size.

However, the work in this chapter is only that from the simplest prototype for the MMCs, in which the interaction between the particles, the plastic behaviour of the matrix and other aspects, have not been considered.

CHAPTER 4

STRESS CONCENTRATION AND INTERACTIONS

II. A New Approach Applicable to Arbitrary Particle Geometries

4.1 Introduction

Inhomogeneity problems[96,116,118] have been well defined as those in which the uniformity of an elastic medium is disturbed by a region within it which has elastic constants differing from its own. The determination of the stress concentration at an inhomogeneity, when the system is subjected to a far-field stress, is directly applicable to the role of the second phase particles in strengthening and in fracture initiation in two-phase materials and particle reinforced metal matrix composites (e.g. SiC reinforced metal matrix composites in the present work).

In the past few decades, advances on this subject have been manifested by many significant theoretical and experimental works. For instance, Eshelby[96,116,118] presented an elegant theoretical treatment to reveal the elastic constraint resulting from an ellipsoidal inhomogeneity, based on Love's point-force theory[164].

However, Eshelby's inhomogeneity theory[96,116,118] is limited in application because it is not able to deal with these problems in which the inhomogeneity has a shape other than ellipsoidal. His method requires the assumption of uniform stress-free strains, which would not be found in non-ellipsoidal particles, and finding closed forms of Green functions[118] which is difficult for non-ellipsoids. It should be noted that the models produced from the disiocation theory provide a clear physical picture, but they are based on experimental observation and analysis for systems with spherical particles only.

For the case of SiC particulate reinforced aluminium metal matrix composites, the particles are angular in character. The particle shape directly affects the material strengthening, failure and stress distributions. Neglecting shape seriously weakens the modelling of the behaviour of this material. Fan, Keer and Mura[122] (1992) proposed a modulus perturbation approach, which converted the inhomogeneity problem into a series of inclusion problems by using the eigenstrain concept. But, it requires that the difference between the moduli of the matrix and inhomogeneity be small compared to the matrix modulus itself. In the case with which we are concerned, the particles are much stiffer than the matrix; the ratio of Young's moduli is about 6:1. To examine the effect of particle shape on the stress distribution within and around a single particle subjected to an uniform remote stress field, the method of Fan et al. is therefore excluded.

The motivation of the present work is two-fold:

a) At a fundamental level, to study the interactions between the matrix and an arbitrary shape of particle.

b) At an application level, to provide an alternative method to solve the inhomogeneity problem without using the finite element method (FEM) in which a large number of elements are required to simulate the infinite matrix condition, especially when a high level of singularity in both the particle shape and material discontinuity is involved. A further application of the method is that it can be used as a verification method for other numerical results.

The approach in this chapter for arbitrary-shaped inhomogeneity problems combines boundary integral equations with a sequence of cutting, straining, and welding

procedures to numerically acquire stress and strain distributions at the inhomogeneity. Physically, the strain misfit is considered as the driving force to cause the stress concentration when the system is subjected to a far-field stress. The approach allows an large difference of modulus between particle and matrix. Also the effect of the inhomogeneity shape on fracture initiation will be discussed in general.

4.2 A BIE Formulation For Three-Dimensional Elastostatics

4.2.1 Description of the BIE

Generally, the boundary integral equation method consists of the transformation of the partial differential equations, describing the behaviour of the unknown inside and on the boundary of the domain, to an integral equation over the boundary.

In the case of the elastostatics, these partial differential equations are the equilibrium equations, which manifest the force balance at any local state. The BIE states that once the complete description of the boundary conditions, i.e. both the traction and the displacement on the boundary, is given, the displacement and the stress fields inside the boundary at any point are then uniquely determined.

However, what is the most important is that the BIE is a direct means for computing unknown boundary data from known boundary data. For instance, as shown in Fig. 4.1, a region $R^{(k)}$ is enclosed by two surface areas, $S_1^{(k)}$ and $S_2^{(k)}$. If on the $S_1^{(k)}$ surface the displacements are given while on the $S_2^{(k)}$ surface the traction forces are given, the BIE may be used to decide the traction on the $S_1^{(k)}$ and the displacement on the $S_2^{(k)}$, and the behaviour of the unknown inside fields may be solved afterwards with

the complete boundary data.

The advantages of the boundary integral equations have been summarized by Lachat[16] as follows:

(1) The system of equations resulting from discretization of the boundary integral equation is smaller than that obtained by, for example, the finite element method;

(2) The field equations are satisfied exactly everywhere inside the domain.

In addition, it is worth reiterating that the numerical solution of these equations is performed on the boundary alone and if values at interior points are required, they are calculated afterwards from the surface data.

4.2.2 Formulation of the BIE

In this part, Lachat's notation[16] is adopted. The body is divided into two regions, $R^{(k)}$ and $R^{(l)}$, i.e. the inhomogeneity region and the matrix region, each of which has different elastic constants, shown in Fig. 4.2.

Some corresponding mathematical descriptions on three dimensional elastostatics can be defined as follows:

The displacement field $u_i^{(k)}$ of $R^{(k)}$ is taken to be any function satisfying the equilibrium equations (if body forces are zero);

$$\frac{\partial \sigma_{ij}[u^{(k)}]}{\partial x_j}=0 \qquad (4.1)$$

for $x \in R^{(k)}$, in which x represents any field point with the coordinates of x_1,x_2,x_3, where $\sigma_{ij}[u^{(k)}]$ is the stress field corresponding to $u^{(k)}$ (or $u_1^{(k)},u_2^{(k)}, u_3^{(k)}$) .

At a point x on the surface of $R^{(k)}$,

$$t_i^{(k)}(x) = \sigma_{ij}[u^{(k)}]\, n_j^{(k)}(x) \tag{4.2}$$

$n_j^{(k)}(x)$ is the outward normal to $R^{(k)}$ at x; and $t_i^{(k)}(x)$ is the traction on the tangent plane.

At a point on the interface between subregions $R^{(k)}$ and $R^{(l)}$, the displacements should be continuous and the reaction forces of the traction should be the same in magnitude but with the opposite sign, if perfect bonding is assumed;

$$\begin{aligned} u_i^{(k)}(x) &= u_i^{(l)}(x) \\ t_i^{(k)}(x) &= -t_i^{(l)}(x) \end{aligned} \tag{4.3}$$

According to the theory of the boundary integral equation, which can be derived from the divergence theorem, the behaviour of the unknown inside and on the boundary, is:

$$c_{ij}^{(k)}(x)u_j^{(k)}(x) + \int_{S^{(k)}} T_{ij}^{(k)}(x,y)u_j^{(k)}(y)dS_y = \int_{S^{(k)}} U_{ij}^{(k)}(x,y)t_j^{(k)}(y)dS_y \tag{4.4}$$

In the formula, $U_{ij}^{(k)}(x,y)$ are the elementary solutions of the displacement at the field point x for the point load applied at a source point y on the boundary. Physically, it represents the displacement in the ith direction produced by a unit point body force in the jth direction, which is;

$$U_{ij}^{(k)}(x,y) = \frac{(1+\nu^{(k)})}{8\pi E^{(k)}(1-\nu^{(k)})r}\left\{(3-4\nu^{(k)})\delta_{ij} + \frac{(x_i-y_i)(x_j-y_j)}{r^2}\right\} \tag{4.5}$$

where $E^{(k)}$ and $\nu^{(k)}$ are the elastic constants of $R^{(k)}$, r is the distance between x and y, and δ_{ij} is the usual Kronecker delta.

The displacements can be differentiated according to strain-displacement relationship to obtain strains; these in turn are transformed through Hooke's law into stress. The traction along an arbitrary surface $S^{(k)}$ within $R^{(k)}$ are given by equation (2), such that the fundamental traction $T_{ij}^{(k)}(x,y)$ for three dimension is given.

$$T_{ij}^{(k)}(x,y)=\frac{1}{8\pi(1-\nu^{(k)})r^2}\left\{(1-2\nu^{(k)})\left[n_i^{(k)}(y)\frac{(x_j-y_j)}{r}-n_j^{(k)}(y)\frac{(x_i-y_i)}{r}\right]+\left[(1-2\nu^{(k)})\delta_{ij}+3\frac{(x_i-y_i)(x_j-y_j)}{r^2}\right]\frac{dr}{dn^{(k)}}\right\} \qquad (4.6)$$

When the field point x is a boundary point, the Cauchy principal value of the integral on the left side of Equation (4.4) is taken, and the coefficient of $c_{ij}^{(k)}$ gives the form of;

$$c_{ij}^{(k)}(x)=\lim_{\epsilon\to 0}\int_{S_\epsilon} T_{ij}^{(k)}(x,y)\,dS_y \qquad (4.7)$$

The well-known result for flat surfaces is that $c_{ij}^{(k)}(x)=\frac{1}{2}\delta_{ij}$. When the surface is not flat, the value of $c_{ij}^{(k)}(x)$ may be found by

$$c_{ij}^{(k)}(x)=-\int_{<S>} T_{ij}^{(k)}(x,y)\,dS_y \qquad (4.8)$$

where the principal value integral on S is denoted as $<S>$, i.e. S-S_ϵ when the size parameter ϵ is taken in the limit to zero.

When the field point x is an interior point, $c_{ij}^{(k)}(x)=\delta_{ij}$, an expression for the dispiacement is written as:

$$u_i^{(k)}(x)=-\int_{S^{(k)}} T_{ij}^{(k)}(x,y)u_j^{(k)}(y)dS_y+\int_{S^{(k)}} U_{ij}^{(k)}(x,y)t_j^{(k)}(y)dS_y \qquad (4.9)$$

Similarly, in the region $R^{(i)}$, the matrix medium, the behaviour of the unknown

inside $R^{(l)}$, (outside the inhomogeneity) and on the boundary can be expressed as:

$$c_{ij}^{(l)}(x)u_j^{(l)}(x)+\int_{S^{(l)}} T_{ij}^{(l)}(x,y)u_j^{(l)}(y)dS_y=\int_{S^{(l)}} U_{ij}^{(l)}(x,y)t_j^{(l)}(y)dS_y \qquad (4.10)$$

The components of $U_{ij}^{(l)}(x,y)$, $T_{ij}^{(l)}(x,y)$, $c_{ij}^{(l)}(x)$, $\sigma_{ij}[u^{(l)}]$, $u^{(l)}$ are the fundamental displacement, the fundamental traction, the Cauchy principal value, stress field in the tensor form, and displacement field in the vector form, respectively. The elastic constants are those of the matrix. However, what is substantially different is that the region $R^{(l)}$ is an infinite domain. Practically, the boundary operation of the above equation is difficult, since the remote fields exist and no known data is available for the inhomogeneity-matrix interface. The following approach offers a concise method for solution.

4.3 The Approach to the Inhomogeneity Problem with Arbitrary Shape of the Inhomogeneous Region

Consider an infinite solid, shown in Fig. 4.2, which has elastic constants $\lambda^{(k)}$, $\mu^{(k)}$ inside a region bounded by a closed surface $S^{(k)}$ (the 'inhomogeneity') and elastic constants $\lambda^{(l)}$, $\mu^{(l)}$ in the region outside $S^{(l)}$ (the 'matrix'). $S^{(k)}$ and $S^{(l)}$ are attached and perfect bonding is assumed. In order to provide the convenience in the analysis, the two are regarded as being separable.

The aim is to find the elastic field everywhere when the stress is required to reduce to the constant value $p_{ij}^{\wedge}$ far from $S^{(k)}$, which encloses the arbitrary form of the inhomogeneity.

The problem may reduced to the determination of the elastic field produced by

the strain misfit of the two phases at their interface by the following series of steps: (Fig.4.3 provides a simple illustration of the process.)

Step One (cutting):

The solid is cut mathematically into two parts, the inhomogeneity and the matrix, shown in Fig. 4.3(a). The solid is now in the unstressed states.

Step Two (straining):

Suppose that the remote uniform stress $p_{ij}^{\wedge}$ is imposed throughout the medium, i.e. within both the inhomogeneity and the matrix. The strains in the matrix are related to the stresses by Hooke's law,

$$p_{ij}^{\wedge}=\lambda^{(1)}e^{\wedge}\delta_{ij}+2\mu^{(1)}e_{ij}^{\wedge}$$

while the strain inside the surface of the inhomogeneity may be expressed as:

$$p_{ij}^{\wedge}=\lambda^{(k)}e^{in}\delta_{ij}+2\mu^{(k)}e_{ij}^{in}$$

where $e^{\wedge}$ and $e_{ij}^{\wedge}$ are the remote uniform strains, i.e. the trace of the strain tensor (volume change rate $e^{\wedge}=e_{11}^{\wedge}+e_{22}^{\wedge}+e_{33}^{\wedge}$) and the strain components, whereas e^{in} ($=e_{11}^{in}+e_{22}^{in}+e_{33}^{in}$) and e_{ij}^{in} are the uniform strains created by the remote stresses $p_{ij}^{\wedge}$ within the inhomogeneity.

The process can be shown in Fig. 4.3(b) and (c). Under the same stress field, the strain response from the two phases is different. The matrix strains more than the inhomogeneity does if the inhomogeneity is stiffer. The corresponding strains in the inhomogeneity can be expressed by the remote uniform stresses:

$$\begin{pmatrix} e_{11}^{in} \\ e_{22}^{in} \\ e_{33}^{in} \\ e_{12}^{in} \\ e_{13}^{in} \\ e_{23}^{in} \end{pmatrix} = \begin{pmatrix} \lambda^{(k)}+2\mu^{(k)} & \lambda^{(k)} & \lambda^{(k)} & 0 & 0 & 0 \\ \lambda^{(k)} & \lambda^{(k)}+2\mu^{(k)} & \lambda^{(k)} & 0 & 0 & 0 \\ \lambda^{(k)} & \lambda^{(k)} & \lambda^{(k)}+2\mu^{(k)} & 0 & 0 & 0 \\ 0 & 0 & 0 & 2\mu^{(k)} & 0 & 0 \\ 0 & 0 & 0 & 0 & 2\mu^{(k)} & 0 \\ 0 & 0 & 0 & 0 & 0 & 2\mu^{(k)} \end{pmatrix}^{-1} \begin{pmatrix} P_{11}^{A} \\ P_{22}^{A} \\ P_{33}^{A} \\ P_{12}^{A} \\ P_{13}^{A} \\ P_{23}^{A} \end{pmatrix} \qquad (4.11)$$

Consequently the difference of the strains between the matrix and the inhomogeneity makes the interfaces of the matrix $S^{(1)}$ and the inhomogeneity $S^{(k)}$ separate. Fig. 4.3(b) illustrates the straining process in both the matrix and the inhomogeneity relative to the unstrained states. Fig. 4.3(c) shows the uniform strain states after straining. It is the misfit of the strains that produces the stress perturbation around the inhomogeneity. These constraint fields are decided by the individual elastic constants of each phase and the form of the inhomogeneity. This part of the analysis procedure is called ´straining´.

Step Three (welding):

Now, assume that the matrix and the inhomogeneity has perfect bonding so that the constraint displacement of the inhomogeneity (excluding the displacement under the uniform strains) at any point on the boundary accommodates that of the matrix at the corresponding point (i.e. the originally attached point) to reach a static equilibrium state. The total magnitude of the constraint displacements of the two phases at the same point may be expressed by the difference of the strains of the two phases, i.e. $\tilde{u}_i(y) = |\tilde{u}_i^{(k)}(y)| + |\tilde{u}_i^{(1)}(y)| = |(e_{ij}^{(1)} - e_{ij}^{(k)})y_j| = |\Delta e_{ij} y_j|$, where $\tilde{u}_i^{(k)}(y)$ and $\tilde{u}_i^{(1)}(y)$ are the constraint

displacements of the inhomogeneity and the matrix on the boundary. The difference of the strains can be uniquely decided by the remote stress fields, that is,

$$\begin{pmatrix}\Delta\varepsilon_{11}\\ \Delta\varepsilon_{22}\\ \Delta\varepsilon_{33}\\ \Delta\varepsilon_{12}\\ \Delta\varepsilon_{13}\\ \Delta\varepsilon_{23}\end{pmatrix} = \left\{\begin{pmatrix}\lambda^{(1)}+2\mu^{(1)} & \lambda^{(1)} & \lambda^{(1)} & 0 & 0 & 0\\ \lambda^{(1)} & \lambda^{(1)}+2\mu^{(1)} & \lambda^{(1)} & 0 & 0 & 0\\ \lambda^{(1)} & \lambda^{(1)} & \lambda^{(1)}+2\mu^{(1)} & 0 & 0 & 0\\ 0 & 0 & 0 & 2\mu^{(1)} & 0 & 0\\ 0 & 0 & 0 & 0 & 2\mu^{(1)} & 0\\ 0 & 0 & 0 & 0 & 0 & 2\mu^{(1)}\end{pmatrix}^{-1} - \begin{pmatrix}\lambda^{(\infty)}+2\mu^{(\infty)} & \lambda^{(\infty)} & \lambda^{(\infty)} & 0 & 0 & 0\\ \lambda^{(\infty)} & \lambda^{(\infty)}+2\mu^{(\infty)} & \lambda^{(\infty)} & 0 & 0 & 0\\ \lambda^{(\infty)} & \lambda^{(\infty)} & \lambda^{(\infty)}+2\mu^{(\infty)} & 0 & 0 & 0\\ 0 & 0 & 0 & 2\mu^{(\infty)} & 0 & 0\\ 0 & 0 & 0 & 0 & 2\mu^{(\infty)} & 0\\ 0 & 0 & 0 & 0 & 0 & 2\mu^{(\infty)}\end{pmatrix}^{-1}\right\}\begin{pmatrix}P^{A}_{11}\\ P^{A}_{22}\\ P^{A}_{33}\\ P^{A}_{12}\\ P^{A}_{13}\\ P^{A}_{23}\end{pmatrix} \tag{4.12}$$

Fig. 4.3(d) and (e) illustrate the welding process. $S^{(1)}$ and $S^{(\infty)}$ are forced to join together producing the perturbation of the stress.

Step Four (calculation of the fields):

The process from Step One to Step Three implies that to find the perturbation fields, one should fully make use of the given constraint conditions, i.e. the strain misfit of the two phase at interfaces (or the given conditions of the accommodation displacements $\hat{u}_i(y)$). The calculation of the constraint fields may be performed by the BIE, operating on the boundary alone, which will be elucidated in the next section.

Step Five (verification):

In order to verify the approach, the criteria used are that:

(1) The displacement is continuous, which can easily be proved by the welding process;

(2) The reaction tractions are equal in amplitude;

During the analysis, the elastic fields are treated as the sum of the constraint fields and the uniform remote fields. The former is calculated by the BIE so that the

condition (2) is satisfied automatically. The latter is produced by the assumption that the uniform stress fields both in the inhomogeneity and the matrix are equal so that the condition is a natural consequence. Since the elasticity accepts the superposition law, the above condition (2) is met.

(3) The equilibrium equations are satisfied everywhere, within both the inhomogeneity and the matrix.

It can also be proved by the nature of the BIE and the uniformity of the uniform elastic fields, that these automatically satisfied[161,162]. Therefore, if the elastic fields calculated satisfy the equilibrium equations, the constitutive equations, and the boundary conditions, then this approach gives the correct results and the solution is unique.

4.4 Numerical Formulation for the Interface Data

4.4.1 Discretization of the Integral Equations

As mentioned in Section 4.1 and 4.2, the boundary integral equations are applied on the boundary alone, which can be expressed as

$$c_{ij}^{(k)}(x)u_j^{(k)}(x)+\int_{S^{(k)}} T_{ij}^{(k)}(x,y)u_j^{(k)}(y)dS_y=\int_{S^{(k)}} U_{ij}^{(k)}(x,y)t_j^{(k)}(y)dS_y \qquad (4.13)$$

To obtain the complete boundary data, assume that the interface of the matrix and the inhomogeneity is discretized into N (or M) small pieces of area (or planelets). Each piece itself may be regarded as being so small that the outward normal on the piece is approximately constant, i.e. does not change by the variation in position on that planelet. Also the displacement and the traction can be considered as approximately uniform

vectors. Now let us consider the displacements at the field point x(n) on the nth planelet. From the above formula, the displacements u(x(n)) will be determined by the whole contribution of the singularities on the boundary (or the other boundary data), which is

$$c_{ij}^{(k)}(x_n)u_j^{(k)}(x_n)+\int_{S^{(k)}} T_{ij}^{(k)}(x_n,y)u_j^{(k)}(y)dS_y=\int_{S^{(k)}} U_{ij}^{(k)}(x_n,y)t_j^{(k)}(y)dS_y \qquad (4.14)$$

The two integrals will represent the principal integral values on the boundary, i.e. without considering the value at the singularity point. Similarly, since the boundary has been discretized into small enough pieces, the integrals can be written in the form of a summation, that is,

$$c_{ij}^{(k)}(x_n)u_j^{(k)}(x_n)+\sum_{m=1}^{M} u_j^{(k)}(y_m)\int_{S^{(k)}} T_{ij}^{(k)}(x_n,y)dS_{y_m}=\sum_{m=1}^{M} t_j^{(k)}(y_m)\int_{S^{(k)}} U_{ij}^{(k)}(x_n,y)dS_{y_m} \qquad (4.15)$$

where it is assumed that the fundamental displacement and the fundamental traction varies rapidly because of the nature of these kernel functions, which are sensitive to the distance between the field point and the source point. It is necessary to consider the local integration of both the fundamental functions separately using the other sub-integrals.

The two sub-integrals consist of the fundamental functions, which are the given functions. Hence, the values of the subintegrals on each planelet may be known as the coefficients of the unknown displacement and the unknown traction on the corresponding planelet, that is, we may write:

$$a_{ij}^{(k)}(n,m)=\int_{S^{(k)}} T_{ij}^{(k)}(x_n,y)dS_{y_m} \quad ; \quad b_{ij}^{(k)}(n,m)=\int_{S^{(k)}} U_{ij}^{(k)}(x_n,y)dS_{y_m} \qquad (4.16)$$

Therefore, the expression becomes:

$$c_{ij}^{(k)}(x_n)u_j^{(k)}(x_n)+\sum_{m=1}^{M} a_{ij}^{(k)}(n,m)u_j^{(k)}(y_m)=\sum_{m=1}^{M} b_{ij}^{(k)}(n,m)t_j^{(k)}(y_m) \qquad (4.17)$$

where n represents the nth field point, m represents the mth source planelet. The integration of the coefficients will be treated in the next section.

Since the boundary has been divided into N (or M) planelets, each element will set up three equations because of the need to represent a vector in three dimensions. The above formula will generate 3N (or 3M) linear equations, which in detail are

$$\begin{aligned} &c_{ij}^{(k)}(1)u_j^{(k)}(1)+\sum_{m=1}^{M} a_{ij}^{(k)}(1,m)u_j^{(k)}(y_m)=\sum_{m=1}^{M} b_{ij}^{(k)}(1,m)t_j^{(k)}(y_m) \\ &\qquad\qquad \vdots \\ &c_{ij}^{(k)}(N)u_j^{(k)}(N)+\sum_{m=1}^{M} a_{ij}^{(k)}(N,m)u_j^{(k)}(y_m)=\sum_{m=1}^{M} b_{ij}^{(k)}(N,m)t_j^{(k)}(y_m) \end{aligned} \qquad (4.18)$$

where i=1,2,3 and n varies from n=1 to N.

Further, if we simplify the expression into a more general form, i.e. to set $u_j(y_m)$ as the unknowns, we obtain:

$$\sum_{m=1}^{M} c_{ij}^{(k)}(m)u_j^{(k)}(y_m)\delta_{nm}+\sum_{m=1}^{M} a_{ij}^{(k)}(n,m)u_j^{(k)}(y_m)=\sum_{m=1}^{M} b_{ij}^{(k)}(n,m)t_j^{(k)}(y_m) \qquad (4.19)$$

or in the other equivalent formula:

$$\sum_{m=1}^{M}\left[c_{ij}^{(k)}(m)\delta_{nm}+a_{ij}^{(k)}(n,m)\right]u_j^{(k)}(y_m)=\sum_{m=1}^{M} b_{ij}^{(k)}(n,m)t_j^{(k)}(y_m) \qquad (4.20)$$

where δ_{nm} is Kronecker delta, i.e. when n=m, $\delta_{nm}=1$, while $n\neq m$, $\delta_{nm}=0$.

To express the above formula into the concise linear equations, we assume

q=n+(i-1) × N, p=m+(j-1) × M, (N=M=the total number of nodes = the number of planelets). The labels, q, p will vary from 1 to 3N (or 3M) and represent the number of a specific equations and the number of specific unknowns. These can be converted to the form:

$$A\begin{pmatrix} [i=1,j=1] & [i=1,j=2] & [i=1,j=3] \\ [i=2,j=1] & [i=2,j=2] & [i=2,j=3] \\ [i=3,j=1] & [i=3,j=2] & [i=3,j=3] \end{pmatrix}\begin{pmatrix} \begin{bmatrix} u_1(1) \\ u_1(2) \\ \vdots \\ u_1(M) \end{bmatrix} \\ \begin{bmatrix} u_2(1) \\ u_2(2) \\ \vdots \\ u_2(M) \end{bmatrix} \\ \begin{bmatrix} u_3(1) \\ u_3(2) \\ \vdots \\ u_3(M) \end{bmatrix} \end{pmatrix} = B\begin{pmatrix} [i=1,j=1] & [i=1,j=2] & [i=1,j=3] \\ [i=2,j=1] & [i=2,j=2] & [i=2,j=3] \\ [i=3,j=1] & [i=3,j=2] & [i=3,j=3] \end{pmatrix}\begin{pmatrix} \begin{bmatrix} t_1(1) \\ t_1(2) \\ \vdots \\ t(M) \end{bmatrix} \\ \begin{bmatrix} t_2(1) \\ t_2(2) \\ \vdots \\ t_2(M) \end{bmatrix} \\ \begin{bmatrix} t_3(1) \\ t_3(2) \\ \vdots \\ t_3(M) \end{bmatrix} \end{pmatrix} \quad \textbf{(4.21a)}$$

or, the relationship between the unknown displacement and the unknown traction may be written as simply in the form:

$$A_{qp}^{(k)}\bar{u}_p^{(k)} = B_{qp}^{(k)}\bar{t}_p^{(k)} \quad \textbf{(4.21b)}$$

$$q=\{n+(i-1)\times N\} \quad ; \quad p=\{m+(j-1)\times M\}$$

Later, the vector of the displacement unknowns will be written as $\{\bar{u}\}$ and the vector of the traction unknowns as $\{\bar{t}\}$.

In addition, the coefficients ($A_{qp}^{(k)}$, $B_{qp}^{(k)}$) of the linear equations may described in detail.

(1) When i=1 and j=1, then, q=1,2,3,···,N, p=1,2,3,···,M. The coefficients of the

unknowns of the displacement A_{qp} and that of the traction B_{qp} are

$$A_{qp}^{(k)}=A_{nm}^{(k)}=c_{11}^{(k)}(m)\delta_{nm}+a_{11}^{(k)}(n,m)$$
$$B_{qp}^{(k)}=B_{nm}^{(k)}=b_{11}^{(k)}(n,m) \tag{4.22}$$

(2) When i=1 and j=2, then, q=1,2,3,···,N, p=(M+1),(M+2),···,2M. The coefficients of those become:

$$A_{qp}^{(k)}=A_{n(M+m)}^{(k)}=c_{12}^{(k)}(m)\delta_{nm}+a_{12}^{(k)}(n,m)$$
$$B_{qp}^{(k)}=B_{n(M+m)}^{(k)}=b_{12}^{(k)}(n,m) \tag{4.23}$$

(3) When i=1 and j=3, then, q=1,2,3,···,N, p=(2M+1),(2M+2),···,3M. The coefficients of those become:

$$A_{qp}^{(k)}=A_{n(2M+m)}^{(k)}=c_{13}^{(k)}(m)\delta_{nm}+a_{13}^{(k)}(n,m)$$
$$B_{qp}^{(k)}=B_{n(2M+m)}^{(k)}=b_{13}^{(k)}(n,m) \tag{4.24}$$

(4) When i=2 and j=1, then, q=(N+1),(N+2),···,2N, p=1,2,3,···,M. The coefficients of those become:

$$A_{qp}^{(k)}=A_{(N+n)m}^{(k)}=c_{21}^{(k)}(m)\delta_{nm}+a_{21}^{(k)}(n,m)$$
$$B_{qp}^{(k)}=B_{(N+n)m}^{(k)}=b_{21}^{(k)}(n,m) \tag{4.25}$$

(5) When i=2 and j=2, then, q=(N+1),(N+2),···,2N, p=(M+1),(M+2),···,2M. The coefficients of those become:

$$A_{qp}^{(k)}=A_{(N+n)(M+m)}^{(k)}=c_{22}^{(k)}(m)\delta_{nm}+a_{22}^{(k)}(n,m)$$
$$B_{qp}^{(k)}=B_{(N+n)(M+m)}^{(k)}=b_{22}^{(k)}(n,m) \tag{4.26}$$

(6) When i=2 and j=3, then, q=(N+1),(N+2),···,2N, p=(2M+1),(2M+2),···,3M. The

coefficients of those become:

$$A_{qp}^{(k)}=A_{(N+n)(2M+m)}^{(k)}=c_{23}^{(k)}(m)\delta_{nm}+a_{23}^{(k)}(n,m)$$
$$B_{qp}^{(k)}=B_{(N+n)(2M+m)}^{(k)}=b_{23}^{(k)}(n,m) \tag{4.27}$$

(7) When i=3 and j=1, then, q=(2N+1),(2N+2),···,3N, p=1,2,3,···,M. The coefficients of those become:

$$A_{qp}^{(k)}=A_{(2N+n)m}^{(k)}=c_{31}^{(k)}(m)\delta_{nm}+a_{31}^{(k)}(n,m)$$
$$B_{qp}^{(k)}=B_{(2N+n)m}^{(k)}=b_{31}^{(k)}(n,m) \tag{4.28}$$

(8) When i=3 and j=2, then, q=(2N+1),(2N+2),···,3N, p=(M+1),(M+2),···,2M. The coefficients of those become:

$$A_{qp}^{(k)}=A_{(2N+n)(M+m)}^{(k)}=c_{32}^{(k)}(m)\delta_{nm}+a_{32}^{(k)}(n,m)$$
$$B_{qp}^{(k)}=B_{(2N+n)(M+m)}^{(k)}=b_{32}^{(k)}(n,m) \tag{4.29}$$

(9) When i=3 and j=3, then, q=(2N+1),(2N+2) ··· 3N, p=(2M+1),(2M+2),···,3M. The coefficients of those become:

$$A_{qp}^{(k)}=A_{(2N+n)(2M+m)}^{(k)}=c_{33}^{(k)}(m)\delta_{nm}+a_{33}^{(k)}(n,m)$$
$$B_{qp}^{(k)}=B_{(2N+n)(2M+m)}^{(k)}=b_{33}^{(k)}(n,m) \tag{4.30}$$

At this point in the calculation, the relationship between the unknowns of the displacement and those of the traction at the boundary $S^{(k)}$ of the inhomogeneity has been determined.

However, it is not enough to solve the whole inhomogeneity problem because the constraint fields will also depend on the existence of the surrounding matrix. To obtain

this relationship at the boundary $S^{(l)}$ of the matrix, we may use similar procedures. The formula in the region of the matrix domain for the unknown displacements and the unknown tractions can be written as:

$$A_{qp}^{(l)}u_{p}^{(l)}=B_{qp}^{(l)}t_{p}^{(l)} \quad ; \quad q=\{n+(i-1)\times N\} \quad ; \quad p=\{m+(j-1)\times M\} \tag{4.31}$$

In terms of the discretization, the continuous integration has been converted into a set of linear equations.

4.4.2 The Determination of the Coefficients

As mentioned in the previous section, the determination of the coefficients of the unknowns is due to the integration of the kernel functions ($T_{ij}(x,y)$ and $U_{ij}(x,y)$), where the point x represents the field point and the point y represents the source point. Consider the interface which has been discretized into many planelets. The integrations will be performed on each planelet. Since the field point may be or may not be a point on the planelet involved, we examine the cases: $x_n \notin S_{ym}$ and $x_n \in S_{ym}$ separately.

Starting from the definition of the coefficients as the previous section, that is:

$$\begin{aligned} a_{ij}^{(k)}(n,m)&=\int_{S^{(k)}} T_{ij}^{(k)}(x_n,y)dS_{y_m} \\ b_{ij}^{(k)}(n,m)&=\int_{S^{(k)}} U_{ij}^{(k)}(x_n,y)dS_{y_m} \end{aligned} \tag{4.32}$$

For $x_n \notin S_{ym}$, shown in Fig. 4.4, since there is not a singularity existing in the formula, the regular numerical integral is performed, i.e. to discretize the planelet S_{ym} into F sub-planelets and to find the integration in the form of the sum of the integrand multiplied by the area of each subplanelet. We have

$$a_{ij}^{(k)}(n,m)=\sum_{f=1}^{F} T_{ij}^{(k)}(x_n,y(f))\Delta S_{y_m}(f)$$

$$b_{ij}^{(k)}(n,m)=\sum_{f=1}^{F} U_{ij}^{(k)}(x_n,y(f))\Delta S_{y_m}(f) \qquad (4.33)$$

$$f=1,2,3,\ldots,F$$

where y(f) means a point on the fth sub-planelet, F may be different than the number for N or M depending on the accuracy required. The term $\Delta S_{ym}(f)$ is the scale value of the fth area. Similarly, the calculation for the matrix domain will accept the above formula, except that the superscript $^{(k)}$ in the formula is changed to $^{(l)}$.

For $x_n \in S_{ym}$, i.e. the singularity exists at x_n on the planelet Sy_m, as shown in Fig.4.5. Though we are allowed to remove the singularity point from the calculation because of the need to only calculate the principle integral value, the distance between the field point and the source point might be very short, in which case the numerical value may be very unstable. Thus, the evaluation of the integral will strongly depend on the numerical treatment around the singularity. Now we consider the integration of:

$$a_{ij}^{(k)}(n,m)=\sum_{\substack{f=1 \\ x_n \neq y(f)}}^{F} T_{ij}^{(k)}(x_n,y(f))\Delta S_{y_m}(f)$$

$$b_{ij}^{(k)}(n,m)=\sum_{\substack{f=1 \\ x_n \neq y(f)}}^{F} U_{ij}^{(k)}(x_n,y(f))\Delta S_{y_m}(f) \qquad (4.34)$$

$$f=1,2,3,\ldots,F$$

where the symbols have the same meanings as the previous expression (4.33).

With respect to the integration of the coefficients for b_{ij}, the singular integration is generated by closing to the field point with the order of $1/\epsilon$, where ϵ is a infinitesimal quantity of the distance between the field point and the source point. Fortunately, the area component in the integration will approach the infinitesimal quantity with the order of ϵ^2. Thus, generally, the calculation of b_{ij} will not involve the singular values, if the procedures do not violate common rules for the numerical analysis, (for example, no definite value divided by zero, etc.). The accuracy of a computer operation is acceptable in these cases.

However, with respect to the integration of the coefficients for a_{ij}, the singular integration will be generated by closing to the field point with the order of $1/\epsilon^2$, the same order that area component might approach. The numerical treatment should be performed carefully due to the fact that the individual value of $(T_{ij}^{(k)}(x(n),y(f))\Delta S_{ym}(f)\,|_{x(n)=y(f)})$ may be close to same quantity as total summation integration itself.

In the integrand, $T_{ij}^{(k)}(x,y)$ is:

$$T_{ij}^{(k)}(x,y)=\frac{1}{8\pi(1-\nu^{(k)})r^2}\left\{(1-2\nu^{(k)})\left[n_i^{(k)}(y)\frac{(x_j-y_j)}{r}-n_j^{(k)}(y)\frac{(x_i-y_i)}{r}\right]\right.$$
$$\left.+\left[(1-2\nu^{(k)})\delta_{ij}+3\frac{(x_i-y_i)(x_j-y_j)}{r^2}\right]\frac{dr}{dn^{(k)}}\right\} \qquad (4.35)$$

Aiming to acquire an appropriate numerical treatment for the coefficients a_{ij}, let us choose a symmetric region on the planelet S_{ym}, shown in Fig. 4.5, say, a square in which the field point x(n) is located at its centre. Notice that the outward normal to the planelet is **n** and any source point y(f) on the planelet makes a unit vector **n**´ of the

distance from the field point x(n). The two unit vectors are perpendicular to each other, i.e. $\mathbf{n} \perp \mathbf{n}'$. One may prove the principal integral value on that square area is zero, because:

Firstly, $(dr/dn^{(\alpha)})$ equals zero since x(n) is on the planelet so that the above expression becomes:

$$T_{ij}=\frac{(1-2\nu)}{8\pi(1-\nu)r^2}\left[n_i\frac{x_j-y_j}{r}-n_j\frac{x_i-y_i}{r}\right]=\frac{(1-2\nu)}{8\pi(1-\nu)r^2}\left[n_i n_j'-n_j n_i'\right] \tag{4.36}$$

$$n(n_1,n_2,n_3)\perp n'(n_1',n_2',n_3')$$

Secondly, suppose there are two points (e.g. point 1 and point 4) in Fig. 4.5. Since $\mathbf{n}_1'=-\mathbf{n}_4'$, if the same value in area is chosen for each area element, the summation of $T_{ij}^{(\alpha)}(x(n),y(1))\Delta S_{ym}(1)+T_{ij}^{(\alpha)}(x(n),y(4))\Delta S_{ym}(4)$ equals zero, where the above expression has been used. It is the same for the summation from the point 2 and the point 3. Therefore, the integration on the square is zero. In the numerical analysis, one may remove a symmetric small area from the simulation to reach the appropriate numerical results.

4.4.3 Numerical Implementation of the Approach

From Section 4.4.1 and 4.4.2, the relationship of the unknown displacement and the unknown traction, and the coefficients of the linear equation have been achieved by the numerical analysis. Now, one may start to build up a general relation connecting the boundary unknowns of the inhomogeneity and those of the matrix. Comparing the apparent formula, we have for $S^{(\alpha)}$ and $S^{(m)}$:

$$A_{qp}^{(k)}\overline{u}_p^{(k)}=B_{qp}^{(k)}\overline{t}_p^{(k)}$$

$$(and) \qquad (4.37a)$$

$$A_{qp}^{(l)}\overline{u}_p^{(l)}=B_{qp}^{(l)}\overline{t}_p^{(l)}$$

that is,

$$[A^{(k)}]\{\overline{u}^{(k)}\}=[B^{(k)}]\{\overline{t}^{(k)}\}$$

$$(and) \qquad (4.37b)$$

$$[A^{(l)}]\{\overline{u}^{(l)}\}=[B^{(l)}]\{\overline{t}^{(l)}\}$$

where again the superscript $^{(k)}$ associates with the calculation corresponding to the inhomogeneity, and the superscript $^{(l)}$ associates with the calculation corresponding to the matrix. [A] and [B] are the tensors of the coefficients.

The constraint elastic fields may be uniquely determined by the misfit of the strains through the use of the sequence of the procedures given in Section 4.3, namely cutting, straining, and welding. The approach denotes that the available information will be provided by the relationship of $\hat{u}_i=\Delta e_{ij}\, x_j|_{\text{at boundary}}$, where u_i is the total displacement in the ith direction at the boundary point x, i.e. the sum of the displacement from $S^{(k)}$ and that from $S^{(l)}$; the amount required to weld the two surfaces together, Δe_{ij} is the misfit of the strains, which has been described in detail in the previous section. Thus, there is a need to convert the linear equations into the explicit forms of the displacement:

$$\{\bar{u}^{(k)}\}=[A^{(k)}]^{-1}[B^{(k)}]\{\bar{t}^{(k)}\}$$
$$\{\bar{u}^{(i)}\}=[A^{(i)}]^{-1}[B^{(i)}]\{\bar{t}^{(i)}\} \tag{4.38}$$

Then the traction unknowns are related to the displacement knowns in the form of:

$$\{u\}=\{\bar{u}^{(k)}\}-\{\bar{u}^{(i)}\}=[A^{(k)}]^{-1}[B^{(k)}]\{\bar{t}^{(k)}\}-[A^{(i)}]^{-1}[B^{(i)}]\{\bar{t}^{(i)}\} \tag{4.39}$$

By making use of the boundary conditions, the traction forces should be equal in amount but with the opposite sign, i.e. $\{\bar{t}^{(k)}\}=-\{\bar{t}^{(i)}\}$, which manifests the physical reaction between the bodies. Further, the formula is derived as:

$$\{u\}=\{\bar{u}^{(k)}\}-\{\bar{u}^{(i)}\}=(\,[A^{(k)}]^{-1}[B^{(k)}]+[A^{(i)}]^{-1}[B^{(i)}]\,)\ \{\bar{t}^{(k)}\} \tag{4.40}$$

Therefore, the traction unknowns on the boundary $S^{(k)}$ of the inhomogeneity are solved:

$$\{\bar{t}^{(k)}\}=\ (\,[A^{(k)}]^{-1}[B^{(k)}]+[A^{(i)}]^{-1}[B^{(i)}]\,)^{-1}\ \{u\} \tag{4.41}$$

The traction unknowns on the boundary $S^{(i)}$ of the matrix may inversely be obtained by obeying the rule of the reaction forces, i.e. equal in magnitude and opposite in sign. Furthermore, the displacements on the two surfaces are determined from Equation (4.38).

At this stage, the complete boundary data for both media, (the inhomogeneity and the matrix), has been ascertained through the numerical discretization and its corresponding physical connection with the inhomogeneity problem.

The behaviour of the unknown inside each medium will be described next. Before that, it is worth briefly reiterating the solutions of the complete boundary data for the tractions and the displacements from the present approach. They are:

$$\{\bar{t}^{(k)}\} = \{[A^{(k)}]^{-1}[B^{(k)}] + [A^{(l)}]^{-1}[B^{(l)}]\}^{-1}\{\bar{u}\}$$
$$\{\bar{t}^{(k)}\} = -\{\bar{t}^{(l)}\} \qquad \text{(A)}$$

$$\{\bar{u}^{(k)}\} = [A^{(k)}]^{-1}[B^{(k)}]\{\bar{t}^{(k)}\}$$
$$\{\bar{u}^{(l)}\} = [A^{(l)}]^{-1}[B^{(l)}]\{\bar{t}^{(l)}\} \qquad \text{(B)}$$

where

$\{\bar{t}^{(\alpha)}\}$, the constraint tractions at the boundary of the inhomogeneity;

$\{\bar{t}^{(m)}\}$, the constraint traction at the boundary of the matrix;

$\{\hat{u}\}$, the accommodation displacements at the interface or the displacements induced by the strain misfit, in which $\hat{u}_i(x(n)) = \Delta e_{ij}\, x_j(n)\big|_{\text{at boundary}}$ $(n=1,2,...,N)$, i.e. $\{\hat{u}\} = \{\hat{u}_1(1),\hat{u}_1(2),...,\hat{u}_1(N),\hat{u}_2(1),\hat{u}_2(2),...,\hat{u}_2(N),\hat{u}_3(1),\hat{u}_3(2),...,\hat{u}_3(N)\}^T$, Δe_{ij} is expressed by equation (4.12); (^{T} strands for the transpose of the displacement vector.)

$[A^{(\alpha)}]$, the coefficient tensor of the unknown displacement corresponding to the inhomogeneity;

$[A^{(m)}]$, the coefficient tensor of the unknown displacement corresponding to the matrix;

$[B^{(\alpha)}]$, the coefficient tensor of the unknown traction corresponding to the inhomogeneity;

$[B^{(m)}]$, the coefficient tensor of the unknown traction corresponding to the inhomogeneity;

$\{\bar{u}^{(\alpha)}\}$, the constraint displacements at the boundary of the inhomogeneity;

$\{\bar{u}^{(m)}\}$, the constraint displacements at the boundary of the matrix;

$[]^{-1}$, the inverse of the second-order tensor ([A] or [B]).

The complete boundary data will uniquely be determined by the accommodation

displacements produced by the misfit of the constraint strain. The coefficients are constants when the geometry of the inhomogeneity and the elastic constants are certain.

4.5 The Behaviour of the Elastic Fields within and outside the Inhomogeneity

In the previous section, the complete boundary data have been determined by the a sequence of the discretization procedures. To obtain the behaviour of the elastic fields within and outside the inhomogeneity, further numerical operations have to be performed.

Consider the elastic fields within and outside the inhomogeneity separately.

4.5.1 The Elastic Fields within the Inhomogeneity

Step One:

Express the constraint displacement fields inside the inhomogeneity. Suppose x $\in R^{(k)}$ and x $\notin S^{(k)}$, where $R^{(k)}$ is the domain of the inhomogeneity. The constraint displacements at the point x may be written generally in the form of:

$$u_i^{(k)}(x) = -\int_{S^{(k)}} T_{ij}^{(k)}(x,y)u_j^{(k)}(y)dS_y + \int_{S^{(k)}} U_{ij}^{(k)}(x,y)t_j^{(k)}(y)dS_y \qquad (4.42)$$

Step Two:

Calculate the constraint displacement fields. The complete boundary data of the inhomogeneity have been determined in Section 4.4. The displacements $u_j(y_m)$ and the tractions $t_j(y_m)$ are obtained by solving the linear equations (A) and (B) on the previous page. Thus, the constraint displacement values at the point x are

$$u_j^{(k)}(x) = -\sum_{m=1}^{M} u_j^{(k)}(y_m) \int_{S^{(k)}} T_{ij}^{(k)}(x,y) dS_{y_m} + \sum_{m=1}^{M} t_j^{(k)}(y_m) \int_{S^{(k)}} U_{ij}^{(k)}(x,y) dS_{y_m} \qquad (4.43)$$

where the point y_m is a point on the mth planelet Sy_m. The sub-integrals may also be expressed in the form of the summations in cases that the point x is close to the interface:

$$\int_{S^{(k)}} T_{ij}^{(k)}(x,y) dS_{y_m} = \sum_{f=1}^{F} T_{ij}^{(k)}(x,y(f)) \Delta S_{y_m}(f)$$

$$\int_{S^{(k)}} U_{ij}^{(k)}(x,y) dS_{y_m} = \sum_{f=1}^{F} U_{ij}^{(k)}(x,y(f)) \Delta S_{y_m}(f) \qquad (4.44)$$

$$f = 1,2,3,\ldots,F$$

where $T_{ij}(x,y(f))$

$$T_{ij}^{(k)}(x,y(f)) = \frac{1}{8\pi(1-\nu^{(k)})r^2} \left\{ (1-2\nu^{(k)}) \left[n_i(m)^{(k)}(y(f)) \frac{(x_j - y_j(f))}{r}(f) - n_j(m)^{(k)}(y(f)) \frac{(x_i - y_i(f))}{r} \right] \right. \qquad (4.45)$$

$$\left. + \left[(1-2\nu^{(k)})\delta_{ij} + 3\frac{(x_i - y_i(f))(x_j - y_j(f))}{r^2} \right] \frac{dr}{dn(m)^{(k)}} \right\}$$

and $U_{ij}(x,y(f))$

$$U_{ij}^{(k)}(x,y(f)) = \frac{(1+\nu^{(k)})}{8\pi E^{(k)}(1-\nu^{(k)})r(f)} \left\{ (3-4\nu^{(k)})\delta_{ij} + \frac{(x_i - y_i(f))(x_j - y_j(f))}{r(f)^2} \right\} \qquad (4.46)$$

Note that all the symbols have been described in Section 4.4.

Step Three:

Calculate the entire displacement fields. These fields, $\tilde{u}_i^{(k)}$, equal the sum of the constraint displacement fields, $\tilde{u}_i^{(k)}(x) = u_i^{(k)}(x)$ obtained from Step Two, and a uniform displacement fields $\hat{u}_i^{(k)}$ associated with the far fields, i.e.

$$\check{u}_i^{(k)} = \hat{u}_i^{(k)} + \tilde{u}_i^{(k)} \tag{4.47}$$

where $\hat{u}_i^{(k)} = e_{ij}^{in} x_j$, e_{ij}^{in} are the uniform strains which are found using (4.11).

Step Four:

Calculate the entire strain field. Suppose $\check{e}_{ij}^{(k)}$ represents the entire strain field, $\hat{e}_{ij}^{(k)}$ the uniform strains, and $\tilde{e}_{ij}^{(k)}$ the constraint strains inside the inhomogeneity. The relation from the superposition law of the elasticity shows:

$$\check{e}_{ij}^{(k)} = \hat{e}_{ij}^{(k)} + \tilde{e}_{ij}^{(k)} \tag{4.48}$$

where $\hat{e}_{ij}^{(k)} = e_{ij}^{in}$, $\tilde{e}_{ij}^{(k)} = \frac{1}{2}(\tilde{u}_{i,j} + \tilde{u}_{j,i})$.

Step Five:

Calculate the entire strain fields. Similarly, suppose $\check{p}_{ij}^{(k)}$ represents the entire stress fields, $\hat{p}_{ij}^{(k)}$ the uniform stress, and $\tilde{p}_{ij}^{(k)}$ the constraint stress inside the inhomogeneity. The relation will be:

$$\check{p}_{ij}^{(k)} = \hat{p}_{ij}^{(k)} + \tilde{p}_{ij}^{(k)} \tag{4.49}$$

where $\hat{p}_{ij}^{(k)} = p_{ij}^{\wedge}$, $\tilde{p}_{ij}^{(k)} = \lambda^{(k)}\tilde{e}\delta_{ij} + 2\mu^{(k)}\tilde{e}_{ij}$

By the above five steps, stress and strain distributions in the inhomogeneity can be determined.

4.5.2 The Elastic Fields outside the Inhomogeneity (or in the Matrix)

Step One:

Express the constraint displacement fields in the matrix, domain $R^{(1)}$. Suppose $x \in R^{(1)}$ and $x \notin S^{(1)}$. The constraint displacements at the point x may be written generally in the form of:

$$u_i^{(l)}(x) = -\int_{S^{(l)}} T_{ij}^{(l)}(x,y)u_j^{(l)}(y)dS_y + \int_{S^{(l)}} U_{ij}^{(l)}(x,y)t_j^{(l)}(y)dS_y \tag{4.50}$$

Step Two:

Calculate the constraint displacement fields by the complete boundary data of the inhomogeneity.

$$u_j^{(l)}(x) = -\sum_{m=1}^{M} u_j^{(l)}(y_m)\int_{S^{(l)}} T_{ij}^{(l)}(x,y)dS_{y_m} + \sum_{m=1}^{M} t_j^{(l)}(y_m)\int_{S^{(l)}} U_{ij}^{(l)}(x,y)dS_{y_m} \tag{4.51}$$

where the point y_m is a point on the mth planelet Sy_m , and the subintegrals may be written in the form of:

$$\begin{aligned}
&\int_{S^{(l)}} T_{ij}^{(l)}(x,y)dS_{y_m} = \sum_{f=1}^{F} T_{ij}^{(l)}(x,y(f))\Delta S_{y_m}(f) \\
&\int_{S^{(l)}} U_{ij}^{(l)}(x,y)dS_{y_m} = \sum_{f=1}^{F} U_{ij}^{(l)}(x,y(f))\Delta S_{y_m}(f) \\
&f=1,2,3,\ldots,F
\end{aligned} \tag{4.52}$$

where $T_{ij}(x,y(f))$

$$\begin{aligned}
T_{ij}^{(l)}(x,y(f)) = \frac{1}{8\pi(1-\nu^{(l)})r^2}\Bigg\{&(1-2\nu^{(l)})\left[n_i(m)^{(l)}(y(f))\frac{(x_j-y_j(f))}{r}(f) - n_j(m)^{(l)}(y(f))\frac{(x_i-y_i(f))}{r}\right] \\
&+\left[(1-2\nu^{(l)})\delta_{ij}+3\frac{(x_i-y_i(f))(x_j-y_j(f))}{r^2}\right]\frac{dr}{dn(m)^{(l)}}\Bigg\}
\end{aligned} \tag{4.53}$$

and $U_{ij}(x,y(f))$

$$U_{ij}^{(f)}(x,y(f))=\frac{(1+\nu^{(f)})}{8\pi E^{(f)}(1-\nu^{(f)})r(f)}\left\{(3-4\nu^{(f)})\delta_{ij}+\frac{(x_i-y_i(f))(x_j-y_j(f))}{r(f)^2}\right\} \qquad (4.54)$$

Note that all the symbols have been described in Section 4.4.

Step Three:

Calculate the entire displacement field, which equals the sum of the constraint displacement field, $\tilde{u}_i^{(f)}(x)=u_i^{(f)}(x)$ obtained from Step Two, and a uniform displacement field $\hat{u}_i^{(f)}$, i.e.

$$\check{u}_i^{(f)}=\hat{u}_i^{(f)}+\tilde{u}_i^{(f)} \qquad (4.55)$$

where $\hat{u}_i^{(f)}=e_{ij}^{\wedge}\, x_j$, $e_{ij}^{\wedge}$ are the remote uniform strains.

Step Four:

Calculate the entire strain field. Suppose $\check{e}_{ij}^{(f)}$ represents the entire strain field, $\hat{e}_{ij}^{(f)}$ the uniform strains, and $\tilde{e}_{ij}^{(f)}$ the constraint strains in the matrix. The relation from the superposition law of the elasticity shows:

$$\check{e}_{ij}^{(f)}=\hat{e}_{ij}^{(f)}+\tilde{e}_{ij}^{(f)} \qquad (4.56)$$

where $\hat{e}_{ij}^{(f)}=e_{ij}^{im}$, $\tilde{e}_{ij}^{(f)}=\frac{1}{2}(\tilde{u}_{i,j}^{(f)}+\tilde{u}_{j,i}^{(f)})$.

Step Five:

Calculate the entire stress field. Similarly, suppose $\check{p}_{ij}^{(f)}$ represents the entire stress field, $\hat{p}_{ij}^{(f)}$ the uniform stress, and $\tilde{p}_{ij}^{(f)}$ the constraint stress in the matrix. The relation will be:

$$\check{p}_{ij}^{(f)}=\hat{p}_{ij}^{(f)}+\tilde{p}_{ij}^{(f)} \qquad (4.57)$$

where $\hat{p}_{ij}^{(f)}=p_{ij}^{\wedge}$, $\tilde{p}_{ij}^{(f)}=\lambda^{(f)}\tilde{e}\delta_{ij}+2\mu^{(f)}\tilde{e}_{ij}$

The procedures provide the stress and strain distributions outside the

inhomogeneity in the matrix.

4.6 Examples

4.6.1 Materials and Element Arrangement

As examples, a system of an infinite aluminium medium and a cube-shaped inhomogeneity, subjected to a far-field tensile stress of 70 MPa, has been considered. The elastic constants of the cube are those of the SiC. In addition, an extreme case of the rigid cubic particle is also simulated.

In order to degenerate the linear equations to solve, only a quadrant of the cube has been taken into account. The element arrangement is shown in Fig.4.7, in which there are nine elements and nodes each sides. In total, it consists of 243 elements (or planelets) and the same number of nodes which are located at the centre of each planelet.

4.6.2 Numerical Simulation

Equation (A) and Equation (B) in Section 4.4.3 represent the formulation of solving the numerical approximation values of the boundary data, i.e. the traction forces and the displacements. The procedures for the nun al approach are summarized as Figure 4.6.

First of all, the elastic constants of the matrix and the inhomogeneity are input to the program. The geometric arrangement is also defined. Then to obtain the assembled set of linear equations, one needs to determine the following:

(1) the accommodation displacements induced by the strain misfit;

Since the strain misfit is represented in Equation 4.12(a), the accommodation displacement may be simply determined by:

$$\hat{u}_i(x) = \Delta e_{ij}\, x_j \big|_{\text{at boundary}}$$

i.e. the accommodation displacement may be expressed as the function of the boundary coordinates.

For the case of the SiC cube, these misfit strains are:

$$\Delta e_{11} = \Delta e_{33} \approx -0.030\% \quad ; \quad \Delta e_{22} \approx 0.084\% \quad ; \quad \Delta e_{ij} = 0 \quad (i \neq j)$$

The accommodation displacements may be converted into the form of the given vector of the linear equations in the same order as in Equation 4.21(a).

For the case of the rigid cubic particle, these misfit strains are simply determined by the far-field strains, i.e.

$$\Delta e_{11} = \Delta e_{33} \approx -0.033\% \quad ; \quad \Delta e_{22} \approx 0.1\% \quad ; \quad \Delta e_{ij} = 0 \quad (i \neq j)$$

since the particle resists any deformation due the rigidity.

(2) the coefficient tensors of the displacement and the traction in the inhomogeneity;

The components of the coefficient tensors are expressed in Equation 4.21b. In detail, they can be found in the Equations 4.22 to 4.30. Keep in mind that the Cauchy principal value is $c_{ij} = \frac{1}{2}\delta_{ij}$ for the flat surfaces. The components a_{ij} and b_{ij} in Equations 4.22 to 4.30 are obtained by the procedures in given Section 4.4.2. The application of Equation 4.33 or Equation 4.34 is determined by noting the distinction of the integral interior and the integral exterior point.

(3) the coefficient tensors of the displacement and the traction in the matrix.

Similar to (2), the components are determined through the same procedures. What is different is only that the elastic constants are those of the aluminium matrix and the direction of the normal outward changes.

4.6.3 Results

By solving 729 linear equations in terms of the Gauss-Jorden technique[150], the traction and the displacement at the interface are obtained. For instance, the tensile traction forces at the interfaces of the aluminium-SiC and the aluminium-rigid are shown in Fig. 4.8, in which the centre line and diagonal line have been defined as in Fig.4.7. It is noticed that at the sharp corner there is a stronger perturbation of the traction forces than that at the smooth interface, e.g. the top centre of the particle. Note that the type of the stress concentration is obviously different from that of a system with a spherical particle as was examined in Chapter 3. This difference would determine the difference feature of the damage initiation, i.e. starting at the sharp corner for particulate particles and at the top for spherical particles. Actually, the experimental evidence has proved these prediction results (e.g. the former for the case of angular particles[55,56,63] and the latter for the case of spherical particles[29,42]). In addition, it is noticeable that the rigid particle causes the very strong constraint at the corners, e.g. a few times higher than the far-field stress at the corner along the diagonal line shown in Fig.4.7 and in Fig.4.8. It implies that if the strength and the stiffness of the particle are high and the interface has strong bonding, the stress carrying capability of the particle would increase by the

constraint in the sense of the average stress that the particles carry, while if the strength of the particle is low, the situation would be different due to the possibility of the particle cracking. To optimize the design of the MMCs, both the shape and the strength of the reinforcement are of importance.

A comparison of the results from the BIE approach with that from the linear finite element analysis (FEA) has also been made in order to distinguish the differences and the advantages of each approach. The FEA is a powerful tool to investigate the general interaction between particles and the surrounding matrix. In general, FEA can be used to investigate the plastic behaviour of metals to study the interactions between particles, whereas the present BIE approach cannot deal with more than one particle. Also the FEA can cope with the linear elastic problem with little effort once the geometry is defined. However, a difficulty of FEA is to simulate a system with an infinite domain. This indicates that a large number of the 3D elements are needed to obtain fairly accurate results, especially if there exist the sharp corners. The usual response is to refine the mesh near the singularity, but the increase of the elements increases the computation cost and actually can also increase the errors generated during the computation. For example, a model has been created using FEA, in which the volume fraction of the particles is about 2.0%. This model may be approximately assumed to satisfy the infinite matrix condition. In the finite element model, there are about 3,000 nodes and the 9,000 unknowns, while in the BIE model the number of the surface nodes is far less than that in the FE model. A comparison of the two results (for 9,000 unknowns and 729 unknowns respectively) is shown in Fig.4.9. The predictions are close to each other in

value showing that the present approach, based on combining the BIE method with a series of operating procedures, is essentially correct.

It is believed by the present author that, for certain types of calculation such as for the cube-shaped particle, the BIE method is more accurate than finite element model. A fundamental problem with use of the finite element method arises in the calculation of stresses and displacements at interfaces, or other singularities. Ordinarily, the stresses are reported for a set of Gaussian points located within the elements, and so values at the surface of the elements must be extrapolated through these points to the element faces. Alternatively, one can increase the accuracy by using a hybrid type of element, but this doubles the number of unknowns. Because of the solution methods used, as the number of equations increases, the absolute error in the calculation of a given unknown also increases. The solution process causes some error. By refining the mesh, the extrapolation errors are reduced, but the number of equations that must be solved simultaneously increases. It is therefore clear that for certain types of calculations, the present approach is a new and useful tool.

4.7 Applications and Extension

The above approach, Sections 4.1 to 4.6, has been based on the assumption that the inhomogeneity and the matrix are perfectly bonded.

However, recently, there has been increasing interest in imperfect interface conditions, which involves the investigation of the interfacial sliding and debonding. Some models for spherical[123](1991), ellipsoidal[126](1985), and circular inhomogeneity[131] (1991) have been presented. For instance, Mura, Jasiuk and Tsuchida[126] presented a "no

shear traction at interface" model. Mura and Furuhashi[100] claimed that they found that when an ellipsoidal inclusion undergoes a shear and the inclusion is free to slip along the interface, the stress field vanishes everywhere in the inhomogeneity and the matrix. As may be appropriate in the case of thin coatings on a hard second phase particle, a model of an imperfect elastic string-type interface was proposed by Hashin[123]. The interface spring constants are expressed in terms of interphase elastic properties and thickness outside a spherical inhomogeneity. Levy[131] (1991) suggested that inhomogeneity interacts with the matrix through a prescribed interface law which depends on the displacement jump at the interface.

To extend the approach to the imperfect bonding problem, the author believes that the strain misfit is physically related to the interface law because it is the driving force producing the stress perturbation around the inhomogeneity. This indicates that whatever interface law we choose, (shear free[126], spring type[123], traction-displacement jump[131] or other types), the traction force and the displacement (or displacement jump) would be expressed as functions of the strain misfit or the commodation displacement.

If the interface law is given, the numerical simulation may be performed starting from the Equations ((4.38) or (B)), which reflect the elastostatic equilibrium condition in each phase. By introducing the interface law, the boundary date of each phase may uniquely be obtained. (This part of work will be pursued after the author finishes her graduate study.)

In general, there is potential to extend the approach to problems of contact (including sliding, interface friction), the thin coating, and debonding.

4.8 Summary

In the present chapter, a new numerical approach to the inhomogeneity problem with arbitrary shape has been proposed. Physically, the approach has been completed using a sequence of cutting, straining, and welding procedures. The advantages of the method may be summarized as follows:

(1) Compared with FEA for the inhomogeneity problem, the approach requires fewer nodes to reach the same accuracy of calculation, because it converts a three dimensional computation problem into a two-dimensional one (a surface integral). It takes far less computer time and computer power (CPU) to obtain reasonably accurate results.

(2) The approach reduces the inhomogeneity problems to the determination of the elastic perturbation field induced by the strain misfit. It distinguishes the perturbation field from the uniform stress field and emphasises that the strain misfit is the driving force to cause stress concentration at inhomogeneity.

(3) The approach is sensitive to the variation of the stress fields near interface, meets the equilibrium equations everywhere, and reflects the nature of the force action and reaction at the boundary of the two different mediums;

(4) It may be used as an absolute verification method for other computation methods for inhomogeneity problems.

(5) It is a useful method to examine the effect of inhomogeneity shape on the stress concentration.

However, it should be noted that, although one may get a basic view of the interaction between the matrix and the particle from the analysis in Chapters 3 and 4,

these approaches are only based on elasticity theory and the treatment is only for the single particle problem without considering the interaction between particles and the plastic behaviour of the matrix. These topics will be studied in the next two chapters.

CHAPTER 5

STRESS CONCENTRATION AND INTERACTIONS

III. Development of Plastic Deformation around Particles

5.1 Introduction

The elastic solution for the inhomogeneity problems allows, to some extent, a basic understanding of the interaction between a particle and a matrix, as has been described in Chapters 3 and 4. However, the limitation of ignoring the plastic behaviour of the metal matrix and the interaction between particles is still a challenge.

Fortunately, the availability of several approximation methods, such as the finite element method, overcomes the limitation to simulate the nonlinear behaviour of materials and interaction. Using FEM, the early investigation of the two-phase materials was largely done using two-dimensional calculations of real microstructures[133,135,136] and of one spherical particle[44,137]. But the former[133,135,136] suffered significantly from the lack of the fine meshes.

In practice, due to CPU requirement, cost, and the storage capacity required for FEM, modelling of the actual microstructure in three dimensions is extremely difficult. To extract key factors in studying the interactions between particles, a unit cell model was proposed by Flower & Watt[139,140] to simulate the tensile properties of two phase materials. The unit cell model allows the strong interaction between particles to be considered with a reasonable number of finite elements. This concept has been adopted in the present work.

The other recent works on modelling micromechanics of the MMCs using FEM

has been reviewed in Chapter 2.

This chapter will be concerned with using FEA for modelling the three dimensional micromechanical interactions in 6061-T4 Al/$(SiC)_p$ metal matrix composites subjected to a tensile loading. The work in the chapter will be classified into two main parts:

(A) Utilization of the FEM in modelling the micromechanics of the MMCs

It will describe:

(1) the utilization of a FEM software package, ABAQUS, as well as a mesh generation package, I-DEAS, to model three dimensional micromechanics in the MMCs;

(2) the concept of unit cell presented by Flower-Watt to model the interaction between particles;

(3) the FE calculation to ensure that the correct mechanical response in the MMCs was obtained by means of an appropriate mesh because of the singularity at the interface of particle and matrix. The results are verified by comparison with Eshelby's model.

(B) Stress concentration and ductility in the MMCs

This will focus on the following questions:

(1) How does the plastic behaviour of the aluminium matrix affect the stress gathering capability of the particles?

(2) Does the relative stress concentration in Al/$(SiC)_p$ MMCs increase with the increase in plastic strain?

(3) What factors are responsible for the low ductility of Al/$(SiC)_p$ MMCs?

5.2 Methodology of the FEA Modelling the MMCs

5.2.1 FEM and Utilization of the FEA package (ABAQUS)

Based on discretization, the finite element method is an approximate method to solve the differential equations, which reflects a piecewise application of a variational method. In micromechanics, this method is used to solve the equilibrium equations, whose solution satisfies the corresponding loading and restraint conditions at a boundary. The equilibrium statement is written as the Virtual Work Principle:

$$\int_V \sigma:\delta D dV = \int_S t^T \cdot \delta v dS + \int_V f^T \cdot \delta v dV \qquad (5.1)$$

where σ is the stress, $\delta\mathbf{D}$ the virtual deformation, $\mathbf{t}$ the traction at boundary, $\mathbf{f}$ the specific body force, $\delta\mathbf{v}$ the virtual displacement. Physically, the left-hand side of this equation is the internal virtual work, which equals the external virtual work. In general, a detailed description of the method can be found references[158,155,156,157].

In the present work, ABAQUS, a FEM software package[182] with the feature of solving non-linear problems, has been employed to calculate the stress concentration and interaction within the MMCs. The package allows modelling of finite deformation due to the application of Lagrangian updated system, incremental plasticity theory and an iteration process by the quasi-Newton method. Specifically, to interpret correctly the outputs, the basic usage in ABAQUS for measurements of deformation, strain, stress and other aspects is shown as follows:

(a) Deformation and Strain

ABAQUS employs the fact that any motion can be represented as a pure rigid

body rotation, followed by a pure stretch of three orthogonal directions. The decomposition theorem allows one to distinguish the straining part of the motion from the rigid body rotation, i.e. if two neighbouring material particles initially are located at some position $\mathbf{X}$ and $\mathbf{X}+d\mathbf{X}$, and after deformation new position $\mathbf{x}$ and $\mathbf{x}+d\mathbf{x}$, the deformation gradient matrix, $\mathbf{F}(=\partial\mathbf{x}/\partial\mathbf{X})$, completely defines the relative motions of materials by the relationship of $\mathbf{F}=\mathbf{V}\cdot\mathbf{R}$, where the stretch matrix, $\mathbf{V}$, completely defines the deformation of materials particles at $\mathbf{X}$, and the rotation matrix, $\mathbf{R}$, defines the rigid body rotation of the principal directions of strain.

Total strains in ABAQUS are reported in terms of nominal values $\epsilon=V-I$, where I is a unit matrix. Thus, a simple way of interpreting the total strain output from ABAQUS is to look at the principal values of the strain and the corresponding principal directions. Then recognizing that the principal strain values are the change in length per unit of original length, of material lines along the principal strain directions in the current configuration.

(b) Stress

ABAQUS always reports the stress as the Cauchy ("true") stress, i.e. the traction being carried per unit area by any internal surface in the body under study.

(c) Selection of the type of Solid Elements

The present work in ABAQUS uses first order isoparametric elements with reduced integration, i.e. eight-node bricks. These elements are chosen, because:

(1) at the Gauss points corresponding to reduced integration the strains are most accurately predicted as long as the elements are well shaped;

(2) when the constitutive model is nonlinear, then the strains passed into the constitutive routines are a better representation of the actual strains;

(3) in plasticity calculations there is an assumption of no volume change, which can cause elements to "lock" (i.e. be too stiff) when full integration is used.

(4) Reduced integration lowers the cost of forming a element.

Additionally, experience suggests that when discontinuities are expected in the solution, first order elements are usually recommended[182]. Therefore, considering the discontinuities between SiC particles and aluminium matrix and other aspects, in the present work first order isoparametric elements with reduced integration have been chosen.

(d) Selection of calculation model

In the present work, the elastic-plastic model in ABAQUS has been employed to consider the elastic and plastic response of the aluminium matrix. In the elastic-plastic model provided in ABAQUS, the elastic and plastic responses are distinguished by separating the deformation into recoverable (elastic) and non-recoverable (plastic) parts, i.e. this separation is $\epsilon=\epsilon^{el}+\epsilon^{pl}$, where ϵ is the total strain, ϵ^{el} is the elastic strain, and ϵ^{pl} is plastic strain. It is true as long as the elastic strains remain small. For a metal like aluminium, this condition is usually satisfied.

(e) Stress Potentials

The metal plasticity models in ABAQUS use the Mises stress potential for isotropic metal behaviour. These potentials depend only on the deviatoric stress, so that the plastic part of the response is incompressible.

(f) Convergence

The finite element models generated in ABAQUS may involve several thousand degrees of freedom. In terms of these variables, the equilibrium equations obtained by discretizing the virtual work equation may be written symbolically as: $F_i^N(u_j^M)=0$, where F_i^N is the force component to the N^{th} variable in the problem, and u_j^M is the value of the M^{th} variable. The basic problem is to solve the equation for the variables throughout the deformation by means of a series of "small" increments. At each increment, convergence is measured by ensuring that all entries in F_i^N are sufficiently small. The equations are checked against the prescribed force PTOL, which has values chosen in the analysis to be 0.1% of actual loads.

(g) The Process of FE modelling

Another software, I-DEAS Engineering Analysis, has been used to mesh geometries of the MMCs and generate an ABAQUS input file. The process contains geometry creation definition, generating elements through nodes, imposing the loads and restraints, unifying the case set, and transferring the case into the ABAQUS input file to perform the further FEA.

Then the corresponding model was analyzed by running the ABAQUS program on a SiliconGraphics, IRIS-4D Series workstation (IRIX operating system).

To display the FE results, the ABAQUS post-processing program was used. A Seiko Instruments Inc, CH 5504 colour printer was connected to the computer to plot the contours for the model.

(h) Materials used in the Elastic-Plastic Model

To investigate the stress concentration within SiC particle reinforced 6061-T4 aluminium metal matrix composites and the interaction between SiC particle and aluminium, as mentioned, the elastic-plastic model is used, in which the material elastic properties are shown in Table 3.1. Note that it is assumed that the SiC particle within the MMCs only experiences the elastic deformation, and the aluminium matrix may undergo elastic deformation and/or plastic deformation depending on the amount of loading. This elastic-plastic behaviour of 6061-T4 aluminium will be modelled using Alcan supplied experimental data.

When dealing with two different materials in ABAQUS, the elastic plastic data for each material has to be supplied separately. The plastic behaviour is supplied as a table of the effective stress vs. the effective plastic strain for aluminium. Since it is assumed that there is a perfect bonding between the matrix and the particle during simulation, to avoid the local stress state and the local strain magnitude beyond the experimental data, the stress strain curve fitting has been performed for extrapolation purposes.

To obtain a well-fit extrapolation data, an empirical equation for describing stress-strain curve proposed in the theses of by Jain[183] and Abduluwayed[184] has been used, which is:

$$\sigma = c_0 \varepsilon^{B+A\ln\varepsilon} \tag{5.2}$$

where σ, ϵ are true stresses (MPa) and true strains and c_0, A and B are constants.

The values of constants c_0, A and B can be obtained from the curve fitting procedures[150] and the corresponding accuracy analysis, since the empirical equation can

written as:

$$\ln\sigma = A(\ln\varepsilon)^2 + B(\ln\varepsilon) + C \tag{5.3}$$

or

$$y = Ax^2 + Bx + C \tag{5.4}$$

if set $y=\ln(\sigma/100)$ and $x=\ln(100\epsilon)$, where $C=\ln(c_0)$.

Using nonlinear curve fitting techniques[150], the constants are found to be A=0.015, B=0.221, and C=0.3054. The Alcan experimental data for 6061-T4 aluminium and its extrapolated curve are shown in Figure 5.1. The fitting accuracy is set to have a calculation error of less than 0.00856 for y.

5.2.2 Flower-Watt Unit Cell

As mentioned, the purpose of the unit cell is to model interaction within the MMCs with a reasonable number of elements created. The concept of the unit cell will be used in the present FEA work, which can be described as follows.

The model of a "unit cell" type was presented by Flower and Watt[139,140]. It comprises of one or more particles set in a brick shaped "unit cell", as in Figure 5.2. Deformation of the cell is achieved by constraining the six surfaces of the cell to the flat planes during the tensile loading, allowing the free contraction on each surface, and satisfying the conditions of:

$$u_x(0,y,z)=0;\ u_y(x,0,z)=0;\ u_z(x,y,0)=0$$

$$u_x(x_0,y,z)=u_{x0};\ u_y(x,y_0,z)=u_{y0};\ u_z(x,y,z_0)=u_{z0}$$

where u_{x0}, u_{y0}, u_{z0} are the displacements at the corresponding planes depending on tensile loading and material properties of each phase. Since the loading of a tensile specimen is modelled, a further requirement is that there be no net force in the direction normal to side planes, i.e. $\int t_x(x_0,y,z)dydz=0$; $\int t_z(x,y,z_0)dydx=0$, to match the external loads. Finally, on all six planes, shear stress normal to that plane must be zero everywhere on that face.

Physically, the model of 5.2(a) and 5.2(b) reflects out infinitely into space, simulating a tensile test on whatever distribution of particle size and shape is chosen in the given model (as in Figure 5.2(c)). The net force acting on the upper and lower faces represents the local tensile force required to stretch the cell. Note that the model is not truly a unit cell analogue, because it is extended infinitely into space through reflection rather than translation. From this one can fairly easily obtain the stress-strain curve for the model involved upon calculating the average stress response.

5.2.3 Verification of the FE Calculation

There may exist the calculation singularities caused by the high level of material discontinuities within the MMCs. To ensure that the results from the FEA are relatively reasonable, a verification of the linear FEA, including the fineness of the mesh, and the use of unit cell has been performed in this section. The verification compares the results from the FEA for a low volume fraction of particles with those from Eshelby's theory. The analysis will calculate the stress concentration and interactions between SiC particles and matrix. The composite is subjected to a 0.2% engineering strain.

(a) Configuration

The simulation has applied a "unit cell" concept. The model adopts the six-sided, eight-node, three dimensional brick element with the total of 2195 elements and 2744 nodes. The volume fraction of spherical SiC particles is 1.94% so that the particles are considered relatively isolated. Because of the symmetry, only an octant of the particle is to be modelled. The matrix possesses the mechanical properties of 6061-T4 condition aluminum shown in Table 3.1. Both the matrix and the particles deform elastically.

(b) Stress Concentration within SiC/Al

The field concentrations at SiC particles have been shown in Fig.5.3(a)-(e). The results from FEA confirm those of Eshelby (see Chapter 3), namely that:

(1) Significant perturbation is only developed near the matrix-particle interface due to the discontinuities and the high level of the misfit of the moduli.

(2) As expected, the SiC particle carries a higher effective stress than aluminium matrix (Fig.5.3(a)). The stress transfer to the particles is evident (also see Fig.5.3(c))

(3) The maximum variations of Von Mises stress (or effective stress) (Fig.5.3(a)), the normal stress (Fig.5.3(c)), the normal strain (Fig.5.3(d)) occur along the pole and a small distance away from the interface.

(4) The greatest stress concentration of the tensile hydrostatic pressure happens in the matrix along the pole and at the interface (Fig.5.3(b)).

In addition, the strain energy density contour in the particle apparently shows a lower level than the far field. Actually, it implies that whenever there exists a misfit of material moduli, a loss of energy at the interface is expected. This has been indicated

from Eshelby's theory (see Chapter 3).

(c) Verification

For any numerical calculation, the accuracy obtained, the type of elements chosen and the physical model used are of importance. Basic verification of the calculation is necessary.

A comparison of the tensile hydrostatic pressure contours and the tensile stress contours are shown in Fig.5.4 and Fig.5.5, respectively. It confirms that with the present mesh arrangement, the calculation results of FEA fit with those of Eshelby's theory. Specifically, their polar characteristics are shown in Fig.5.6. The slight differences of the two at a distance away from the interface are because the FEM approach is not an ideal single particle model. The boundaries are mirror symmetry planes. Therefore the constraint interaction between distant particles has been taken into account so that the stress concentration is slightly higher than the analytic single particle calculation.

The results infer that:

(1) the present mesh is reasonably fine enough to obtain accurate stress concentration and interactions within the MMCs, although the misfit of the mechanical properties of the two phases are severe.

(2) the first order isoparametric elements with reduced integration may be used to model three dimensional unit cell without the "locking" phenomenon and that they produce reasonable results.

(3) the unit cell is able to reflect correctly the interaction between the particles.

(4) good accuracy can be expected by controlling PTOL values for the further elastic-

plastic FEA. In the further work presented, the values are 0.1% of actual loads.

5.3 Plastic Relaxation

This section focuses on the start of the plastic behaviour of the MMCs. The motivation is to know:

(1) how the stress concentration changes when the aluminium matrix starts to deform plastically.

(2) if the stress transfer capability varies due to the plastic behaviour of the matrix.

In the present work, a comparison between elastic analysis and elastic-plastic deformation has been examined at the overall engineering stress 94.2 MPa, which is the tensile stress at 0.2% strain offset for the MMCs. For the elastic case, an aluminium matrix with a very high yield strength has been assumed to emphasize the effects of plastic flow. Actually, the analysis simulates an early loading process within a composite when both the matrix and the particle deform elastically. The linearity of the elastic analysis makes the stress and strain perturbation field scaled and the stress concentration pattern remains the same till the plastic deformation of the matrix starts to take place.

The contrast between the effective stress contours for the elastic and elastic-plastic cases is shown in Fig.5.7. As the loading is first applied, both the SiC particle and the aluminium matrix deform elastically. The stress concentration is expected to have the pattern as Fig. 5.7(a). However, when the local effective stress in the matrix reaches the yield point, the matrix starts to deform plastically. Then the consequence is that the stress concentration is released or relaxed towards that shown in Fig.5.7(b) at the yield strain

of the composite. The perturbation range becomes smaller and more localized, but the maximum of the concentration is still along the pole and a small distance away from the interface. The results imply that the concentration of the local distortion energy decreases when the plastic deformation starts.

The release and localization of the stress concentration has also been found in the contours of the tensile hydrostatic pressure in Fig.5.8. The concentration pattern varies from Fig.5.8(a) to Fig.5.8(b) while the loading starts to be exerted on the MMCs from the beginning to the yield strain. Similar to the elastic analysis, the highest concentration of pressure occurs at the interface, but the peak value compared with the far field value decreases and the relaxation is also high at values more than one radius above and below the particles. As a result, the concentration of the energy density related to the local volume change decreases.

However, the stress gathering capability of particles decreases at the same time because of the plastic relaxation of the matrix (see Fig.5.9). The contour (Fig.5.9(b) of the normal stress from the elastic plastic analysis again shows localization of the volume of stress concentration and the release (or relaxation) of the peak value of the stress concentration. The plastic behaviour of the metal matrix reduces the severity of the constraint at an early loading stage, so that the stress cannot be effectively transferred to the particle.

Figure 5.10 clearly summarizes the results of plastic relaxation above. Comparing elastic with elastic plastic the polar perturbations of stress components, i.e. mean stress, normal stress and Von Mises stress, die away from interface, while the concentrations

of components reduce before the MMC reaches yielding. These perturbations of stresses at yielding drop dramatically such that the stress concentrations beyond a radius away from the interface may be neglected. Furthermore, it is noted that there is a strong perturbation of the stress triaxiality at the interface during the loading before yield. As discussed in Chapter 3, it plays an important role of initiating the voids around the particles because of its raising the local strain energy density.

Figure 5.11 shows the normal strain contours. It is natural that, in the elastic-plastic case, the local strain level along the pole is very high because of the development of the effective stress fields. The plastic behaviour of the matrix weakens the stress gathering capability of the particle at early loading because the matrix can supply the required strain at much lower stresses than the particle. The high local plastic deformation and the strong fluctuation of the strain distribution within the matrix apparently imply that the movement of a large amount of dislocations would be involved during the loading process. It is interesting to think that the further work hardening is achieved by two parts: an average back stress, and a stress related to the fluctuation of the dislocation microstructure[106].

The contours of the strain energy density and the effective plastic energy density are shown in Fig.5.12 and Fig.5.13, respectively. The densities of the maximum strain energy stored and the maximum plastic energy dissipated have the same order when the MMC is at the yield strain.

So, in general, the plastic behaviour of the matrix decreases the stress concentration around the particle by plastic relaxation at an early loading stage. In turn,

the stress gathering capability of particle is lowered. The particles act as if they are becoming softer in that their stress levels do not increase proportionally, but the tensile stress carried by particle is still higher than the overall stress.

It implies that the stress carried by a composite at its yield strain will be smaller than that predicted through elastic analysis.

5.4 Accumulation of Plastic Deformation

This section focuses on the accumulation of the plastic deformation. An elastic plastic FEM analysis has been performed by imposing overall engineering strains of 0.2%, 2%, and 5%. The motivation of the work is to know:

(1) how the stress gathering capability of the particle changes with the increase of the loading;

(2) how the stress concentration within the MMC varies with the accumulation of plastic deformation.

The contours of Von Mises stress, the hydrostatic pressure, and the tensile stress during the accumulation of the plastic deformation are shown in Fig.5.14, Fig.5.15, and Fig.5.16, respectively. As expected, the levels of stress distributions increase monotonically with the increase of the overall strains imposed. It is noted that the mean stress constraint (hydrostatic pressure) from the misfit and plastic behaviour of matrix still causes the highest perturbation.

However, the most striking results about these stress distributions are that the stress concentrations of all these components increase with the increase of the overall

strain, which are shown in Fig.5.17 in terms of the pole characteristics. These stress concentrations may even exceed those calculated by elastic analysis, but they are expected to reach upper-limits for each stress variable (see Section 3.3.4 in Chapter 3). The change of the stress concentration is worth mentioning. At the very beginning of the loading, when both the matrix and the particles deform elastically, the relative stress concentration ($F-F_0/F_0$) depends on the elastic moduli of the two phases, but it is independent of the change in the overall (elastic) strain level. It is at a relatively high level in Al-SiC_p. When the matrix starts to deform plastically, the relative stress concentration is lowered because of the plastic relaxation. But with further deformation the relative stress concentration increases. In practice, the consequence of the change of the relative stress concentration leads to a lower yield stress of the MMC due to plastic relaxation and a potential for early failure of the composite due to the high stress concentration with continuing plastic strain. At the same time, the stress gathering capability of the particles becomes higher with continuing strain as manifested by value the tensile stress S_{22} at the interface. Recall that equilibrium requires that S_{22} be balanced across the interface, and that the stress remains relatively constant in an ellipsoidal particle. This reflects the interaction between the particles and the matrix at the interface.

Further evidence on the effects of plastic accumulation is shown in Fig.5.18 (the effective plastic strain), in Fig.5.19 (the strain energy density), and in Fig.5.20 (the plastic energy density). As the overall strain increases, all the components increase rapidly along the pole and at a small distance from the interface. A striking result is that

the local values of the plastic energy density may be 1-2 orders of magnitude greater than those of the elastic strain energy at 5.0% overall strain. This means that even at these low levels of particulate, most of the external work is dissipated as plastic deformation, and relatively little goes to the increase in stored elastic energy.

5.5 Discussion on the Ductility of Particulate Composites

The ductility of a material is defined as the capability of a material to undergo a deformation. In practice, the reduction in area and the elongation of a material sample are commonly used as the measure of ductility. The factors that affect the ductility of the two phase materials have been reviewed in Chapter 2.

However, one contradictory fact to the practical measure of ductility should be noted. As Chen et al.[28] and Palmer et al.[29] reported, at low temperature the elongation was greater than that at higher temperature, while the reduction in area had the opposite dependence, i.e. lower at low temperature. It implies that factors of the reduction in area and the elongation are physically vague to measure the ductility of the two phase materials.

Consider a material under loading. Certainly, strain energy would be stored within the material to resist the external loading and plastic energy would be dissipated if the external loading exceeds the yield stress of the material to produce the permanent plastic deformation. It is reasonable to think that the capabilities of a material storing the strain energy and dissipating nonrecoverable energy are the measure for material failure. It is believed by the present author that there exists a competition mechanism of the

failure modes. For any type of material, two energy tolerance values (strain energy limit and plastic energy limit) are important to determine the ductility of the material whether the material fails in brittle type of fracture or in material exhaustion, if the self-healing mechanism[40,41], which may exist for compressive hydrostatic stresses, can be neglected. Applying this to the MMC, due to the high level of the non-uniformity of the stress distribution, the concept may be introduced as the "local" ductility criterion.

As discussed in Chapter 3, the total strain energy comprises a term depending on change of volume and a term depending on distortion. It may be expressed by the mean stress and the effective stress, i.e.

$$U_0=\frac{1}{2k}\sigma^2_{mean}+\frac{1}{6G}\sigma^2_{eff} \tag{5.5}$$

According to the elastic plastic FEA above, the high stress concentrations (Fig.5.17) of the effective stress (Fig.5.14) and the tensile hydrostatic pressure (Fig.5.15) occur near interface. Especially, the dramatic change of the mean stress at and near the interface contributes a great deal to the increase of the strain energy density. This situation is completely different to that within the uniform materials, in which the contribution from the mean stress may be neglected. It is this difference that gives MMCs low ductility. The high and localized stress concentrations are responsible for the early void initiation and growth.

On the other hand, the process of the work hardening within materials cannot be endless. Therefore, the local and high accumulation of the plastic deformation would lead to the matrix exhaustion if this limit is reached.

Finally, as far as the particle cracking is concerned, although it helps stress relaxation at an early stage of strain, the later accumulation of plastic deformation actually raises stress concentration. The consequence is to increase the stress gathering capability of the particles, but at the same time the possibility for the particle cracking also increases, if the particles do not possess high breaking resistance.

In general, the stress concentration and the accumulation of the plastic deformation within the MMC elevates the stress transfer to the particles, but degrades the ductility of the MMCs.

5.6 Summary

The utilization of the FEA to model the micromechanical interactions around spherical particles in 6061-T4 Al/$(SiC)_p$ metal matrix composites subjected to a tensile loading has described the following:

(1) the use of ABAQUS and I-DEAS software packages;

(2) making use of the Flower-Watt unit cell to model the interaction between particles;

(3) the verification of the FEA by classical analysis.

An elastic plastic FEA has been performed at low particle volume fraction (1.94%). By examining the plastic relaxation and the plastic accumulation in the MMC, the following conclusions are reached:

(1) Plastic deformation helps stress relaxation at early strain stage. The relative stress concentration is relaxed and the stress gathering capability of the particles is reduced.

(2) During further plastic accumulation due to the increasing tensile loading, strain

hardening overcomes the plastic relaxation effects and the relative stress concentration then increases. This concentration may even exceed that caused by the misfit of the elastic moduli. Concurrent with this, the stress gathering capability of the particle also increases.

The ductility of a MMC depends not only on the elastic stored energy, but also on the plastic deformation accumulated. It is therefore proposed that the following should be considered in explaining the low ductility of Al/$(SiC)_p$ MMCs.

(1) The elastic stored energy has two terms; a distortion term and a hydrostatically driven volume change term. Near the interface, the hydrostatic pressure increases the strain energy dramatically, and will be partially responsible along with the effective stress for the early void initiation by interfacial detachment and later void growth within the MMC;

(2) the localized high accumulation of the plastic deformation near particles may lead to the matrix exhaustion;

(3) the high stress gathering capability of the particles will be partially responsible for the particle cracking, if the particles do not possess high breaking resistance. Note that the non-uniformity of the stress distribution within non-ellipsoidal particles is another reason for the particle cracking, as will be described in the next chapter.

CHAPTER 6

EFFECTS OF PARTICLE MORPHOLOGY ON THE DEFORMATION CHARACTERISTICS WITHIN Al/$(SiC)_p$ MMCs

6.1 Introduction

In the previous chapters, we have focused on:

(1) visualizing the stress-strain distribution around a spherical SiC particle using Eshelby's theory, and examining stress transfer as a result of the misfit of moduli between the matrix and the particle, interfacial characteristics, and the effect of particle size.

(2) developing a method to find the stress-strain distribution at an arbitrary shaped particle and examining the non-uniformity of the distribution and the interfacial characteristics.

(3) examining the effects of plastic relaxation and plastic accumulation on the stress transfer and the stress concentration using the elastic plastic FEA, and discussion of their effects on the ductility of the MMCs.

The above investigations dealt with inhomogeneity problems (i.e. the case of a system of a single particle and an infinite domain) or problems of isolated particles embedded in the matrix (i.e. cases of low volume fraction of reinforcement). These results help us to understand the way in which an isolated particle carries stress.

However, multiphase discontinuous composites, such as Al/$(SiC)_p$ MMC, achieve high yield stress and high stiffness by incorporating a large amount of particles (or reinforcements) into the metal matrix. The investigation complexity increases not only

because of the strong interactions between particles, but also because of real particle morphologies and thermally induced stresses. Optimizing composite development ought to include considerations of all the fundamental aspects of particles including their shape, size, volume fraction, spacing and thermally induced stresses to predict the mechanical response of composites.

The use of FEA to study micromechanics for Al/(SiC) has shown considerable promise. This can be shown by many recent works[141-9,152,154,170,176,177], which have been reviewed in Chapter 2. Most of these studies focused on the prediction of the deformation characteristics of the Al/$(SiC)_w$ MMCs.

However, using three dimensional FEA to model Al/$(SiC)_p$ MMCs within which either spherical particles or angular particles are embedded, is a new area of practical importance (see Chapter 1 and Chapter 2). The objective is to provide a reasonable guide to improve actual material performance.

The present chapter will examine the effects of volume fraction, particle shape, and spacing on the deformation characteristics, and predict the mechanical response of Al/$(SiC)_p$ MMCs using FEA. The FEA will also adopt an elastic-plastic model and a three dimensional Flower-Watt unit cell model. In detail, the study attempts to increase an understanding of:

(1) how the increase of the volume fraction affects the interactions between particles and the intervening matrix in terms of the mechanical response, including the overall stress strain curve, the yield strength, the work-hardening rate, local stress concentrations and the ductility within the MMCs;

(2) how strongly the particle shape is related to the stress concentration and the failure process within the MMCs;

(3) if and how the clustering of the particles is responsible for local failure within the MMCs.

Note that the effects of thermally induced stresses will be studied in Chapter 7.

6.2 Effects of Volume Fraction

6.2.1 Configuration

The three-dimensional elastic-plastic FE models adopted assume that the SiC particles only deform elastically, while the matrix deforms elastically or elastic-plastically depending on the external load. The non-linear behaviour of 6061 aluminum alloy in the T4 condition was obtained from Alcan experimental data (see Table 3.1 and Fig.5.1).

In this section, the calculations were carried out with models changing in volume fraction from 5% to 25% (in 5% steps). The particles with spherical shape were uniformly dispersed, and were centred in each unit cell. The mesh arrangement is shown in Table 5.1 (a table for the element number at each volume fraction) and the subsequent geometry is given in the individual figures. The computation procedures and considerations of FEA details have already been introduced in Chapter 5.

6.2.2 Interactions vs Volume fraction

The interactions between particles and the matrix and between particles themselves strongly depend on the volume fraction of the reinforcement, as has been shown in some

experiments and/or FE analyses[76,82,141,144,146,147]. In general, the higher volume fraction, the stronger the perturbations of the local stress and strain state within the MMCs and the greater the interactions. Practically, using three dimensional FEA, these interactions are modelled by means of the unit cell concept. A typical non-uniform stress distribution within a unit cell is shown in Figure 6.4, which is the effective stress contour at 25% volume fraction at 5% overall engineering strain. The present FE calculations provide a means to quantitatively represent these perturbations. The results, with volume fractions from 5% to 25%, and at 5.0% overall engineering tensile strain are exhibited as follows.

Three components, namely Von Mises stress, the hydrostatic pressure, and the effective plastic energy density, were chosen to display the local perturbations within the MMCs. Their contours reflect respectively the physical quantities of the local distortion, the local mean stress state (although there is a change in sign between hydrostatic pressure and the mean stress), and the local dissipated energy density (work of plastic deformation). The Von Mises stress contours are shown in Figure 6.1. Comparing the contours, what is common is that in both volume fractions the particles carry high stresses as expected, the stress distributions within the particles are relatively uniform within the spherical particle reinforcement, and the highest values occur along the loading direction and a small distance away from the interface. What is different is that the local perturbations increase with the increase of the volume fraction. The region between particles at 25% volume fraction shows the highest level of constraint. Since physically Von Mises stress measures the distortion energy[163], one anticipates that the strain energy stored within the MMCs at higher volume fraction is higher, unless the perturbations of

the hydrostatic pressure contour show the opposite.

Actually, the perturbations of the hydrostatic pressure also increase with the increase of the volume fraction, shown in Figure 6.2. The distinguishing difference between the two components is that at the interface the hydrostatic pressure concentration is very high. Although the mean stress component does not affect the plastic deformation according to the assumptions of plasticity theory, this concentration contributes significantly to that of the local total strain energy density along with Von Mises stress concentration (see Chapter 3). Due to the high triaxiality at the interface, the hydrostatic pressure has been proved to be a non-negligible factor in the local stored energy density in Chapter 3 and Chapter 5. The behaviour of the high triaxiality in the composites would play an important part in the process of the plastic flow and the void nucleation, as will be discussed later. Another mechanical feature in addition to the stored strain energy in composites is the effective plastic energy density which represents the energy dissipated in the matrix, shown in Figure 6.3. Again, its local concentration increases with increasing volume fraction. It indicates that if the local material exhaustion is one of the failure modes of the composites, the ductility of the composites would strongly depend on the volume fraction. The higher the volume fraction is, the lower the expected ductility is, as has been proved by experiments (e.g.Ref.[82]). On the other hand, the higher the level of the local clustering, the higher the possibility of early local failure becomes due to the high local volume fraction, which leads to both high local strain and plastic energy density.

In general, the constraint between the matrix and particles within composites

increases with increasing the volume fraction. The consequence of the interactions is that:
(1) the external stresses exerted on composites may be largely transferred to the particles so that the strength and the stiffness of composites apparently can be superior to those of unreinforced aluminium alloys, especially at high volume fractions;
(2) the misfit of the mechanical properties between the phases leads to high local stress and energy density concentration. As a result, an enhancement of the work hardening rate within the matrix is expected, while at the same time the increasing strength and stiffness of the composites would be obtained at the cost of decreasing the ductility.

6.2.3 Overall Mechanical Response vs Volume Fraction

Figure 6.5 shows the predicted stress-strain curves for volume fractions from 5% to 25% (5% steps) of SiC particles for 6061-T4 condition Al/(SiC)$_p$ composites, in which an overall strain range from 0.0 to 0.05 and a lower overall strain range from 0.0 to 0.005 are plotted separately in (a) and (b). Also the experimental measured stress-strain curve of the unreinforced aluminium alloy is given (i.e. 0% volume fraction of reinforcement). In these calculations, the same matrix microstructure is assumed at all volume fractions. The results show that an increase in the particle content promotes an increase in the stiffness and the flow strength of the composites (see Figure 6.5(b)), as has been ascertained by experiments for particulate reinforced aluminium composites. According to some previous FEA works[141], it was proposed that a major contribution to this increase in flow strength with increased reinforcement arises from the increase of hydrostatic tension in the matrix due to constrained plastic flow. The increased

hydrostatic tension also leads to an apparent increase in work hardening rate. However, the present author believes that the major contributions to the elevation in the stiffness and the flow strength with increased particle content comes from the stress transfer to the particles as well as an increase of the work hardening within the matrix (see Section 6.3.5 for further discussion). In Figure 6.5, another interesting phenomenon should be noted. The increase in load carrying ability at a given strain level for a 5% change from 5% to 10% particles is less than that on going from 20% to 25% particle volume fraction. Intuitively one might have thought that in doubling the particle content, the former change might produce a bigger effect than the latter. In fact, it is the opposite. Again, this is closely related to the process of the work hardening and the stress transfer within composites. With increasing volume fraction, the increase of the work hardening and the stress transfer vary with the volume fraction at a given strain level and appear as a high level at high volume fraction. The strong interactions between particles elevates the work hardening in the matrix such that at a given strain, the matrix at higher volume fraction carries a higher average stress. The similar effect of volume fraction would happen to the particles. The stress transferred to the particles would increase with increasing volume fraction due to this work hardening effect (the effect of the work hardening on the stress transfer has been studied in Chapter 5). Also, the work hardening rates show similar results, especially at low strain levels (Figure 6.6). In order to estimate the increase of the strength within the composites, Figure 6.7 has been plotted to illustrate the relationship of the strength to the volume fraction. In this figure, the strength at three different overall engineering strain levels, i.e. 0.2% (flow strength),

2%, and 5%, has been examined. The predicted strength shows an increase of ~25 MPa at 0.2% strain level on increasing the volume fraction to 25%, an increase of ~61 MPa at 2.0% strain level, and an increase of ~85 MPa at 5.0% strain level. This figure clearly exhibits the nonlinear rate of increase for strength vs volume fraction.

By examining the predicted stress-strain curves, the following conclusions can be reached:

(1) the stiffness and the strength of the composites increases with increasing volume fraction as expected;

(2) the work hardening rate of composites increases with increasing volume fraction and the effect is strongest at low strain levels;

(3) at a given strain level, the rate of increase in the strength vs. volume fraction is higher at higher volume fraction levels.

To further understand the effect of volume fraction on the strengthening and void nucleation mechanisms within the composites, the next section will focus on the effect of volume fraction on the local stress concentration.

6.2.4 The Local Stress and Strain Concentration vs Volume Fraction

The peak level of stress variables in composites is one of the factors which are related to the strengthening and failure mechanisms. Figure 6.8 shows the relationship of the maximum stress value to the applied strain at several volume fractions (i.e. 5%, 15%, 20%, 25% vol pct) in 6061-T4 aluminium. For the stress state in the matrix, these figures reveal that:

(1) The components of the effective stress, the mean stress, and the normal stress vary with a parabolic type of the increase with increasing overall strain for a given volume fraction.

(2) As anticipated, the peak level of the work hardening in the matrix, which is expressed by the effective stress, is increased with an increase of the external strain. Also, an increase of this level with increasing volume fraction is evident. This rate of increase vs. volume fraction is high at high volume fraction. It indicates that the interaction between particles becomes an important contribution to the peak work hardening at high volume fraction.

(3) Comparing the composites with the unreinforced alloys under tension, the distinguishing difference is the existence of a high maximum hydrostatic tension in composites, which has the order of the effective stress or higher than the effective stress at high volume fraction, while in unreinforced alloys the value is about one third of that of the effective stress. Its significance has been analyzed in Chapter 3 and Chapter 5. Again, the rate of increase vs. volume fraction is high at high volume fraction, which shows the contribution of the interaction between particles.

(4) The peak normal stress is the highest local value among the three. Actually, it implies a high stress gathering capability of the particles. To reach static force balance, the fibre-like pattern of the normal stress is developed.

With respect to the relationship of the local stresses to the applied strain in the particles, Figure 6.9 shows that:

(1) A parabolic increase in local stresses with increasing applied strain at a given volume

fraction is similar to that found in the matrix.

(2) The level of the peak effective stress is the highest, compared to the other two stress components. This is reasonable if one considers a stress state of tension in the loading direction and compression in the direction normal to the loading due to the force imposed on the particles within composites (also see Chapter 3).

(3) Because of the stress state described in (2), the hydrostatic tension within the particles becomes insignificant.

Figure 6.10 converts the above results into the relationship between the peak local stresses and volume fraction at strain levels of 2.0% and 5.0%, both for the matrix and for the particles. The effect of volume fraction on the peak local stresses clearly indicates that in the matrix, the peak hydrostatic tension has the same order or is even higher than the effective value at the relatively high volume fraction, which would play an important role in the void formation, an initiation stage of failure process. In the particles, the high deviatoric stress and high normal stress denote the stress transfer to the particles due to the stiffer elastic modulus, which could lead to the particle failure.

The peak local strain (E22) is plotted vs. strains both in the matrix and the particles in Figure 6.11. It is noted that:

(1) In the matrix, the peak local strain increases almost linearly with the increase of the overall strain for a given volume fraction.

(2) In the matrix, an interesting phenomenon is that the peak local strain increases at an increasing rate with the increase of the volume fraction for a given strain level. The higher the strain level is, the higher is the rate of increase with the volume fraction.

Actually, it indicates that at a low strain level, the interaction between particles is insignificant so that the peak strain value apparently increases nearly linearly, while at a high strain level, this interaction becomes extremely dominant and leads to an extra contribution to the local plastic flow.

(3) Particles deform very little due to their high elastic modulus. The increase of the peak local strain with increasing strain level appears as a declining parabolic curve, because of plastic relaxation in the matrix.

(4) Also, in the particles, the peak local strain increases at an increasing rate with the increase of the volume fraction at a given strain level because of the increase of the interaction between particles at high volume fraction.

6.2.5 Synopsis

Generally, the characteristics in composites subjected to tensile loading that distinguishes them from unreinforced alloys are:

(1) the stress transfer to the particles due to the misfit of the two phases;

(2) the increase of the work hardening around particles;

(3) a dramatic increase of the tensile hydrostatic stress around particles.

These characteristics provide an increase in the strength and the stiffness of composites. At the same time, this leads to a degradation in the ductility due to the high concentration of stress.

Furthermore, the strength and the ductility of composites vary with volume fraction. With increasing volume fraction:

(1) the overall strength of composites increase nonlinearly as shown in Figure 6.7 due to an increase of both stress transfer and work hardening in composites.

(2) the peak value of the tensile hydrostatic stress increases nonlinearly, compared with a nearly linear increase of the peak effective stress (see Figure 6.10), which leads to a rapid decrease of the ductility in composites because of the major contribution of the tensile hydrostatic stress to the strain energy density, especially that at high volume fraction.

6.3 Effects of Particle Shape

6.3.1 Effect of Particle Shape at Low Volume Fraction

In order to investigate the effect of the particle shape on deformation characteristics within composites, the present section will focus on:

(1) comparing the difference of the deformation characteristics in both the matrix and the particles for two extreme cases; spherical particle reinforced MMC and cubic particle reinforced MMC at 1.94% volume fraction. Unlike previous FEA studies from literature, the stress state within the particles will be examined.

(2) presenting the effect of the aspect ratio of particles on stress concentration.

The former mentioned in (1) comprises two three-dimensional models. One model was meshed by incorporating a spherical particle in an aluminium matrix using a unit cell with 2195 nodes and 2744 elements. The other was generated by assuming uniformly dispersed cubic particles in composites with 3375 nodes and 2744 elements. Since the analysis is aimed at understanding the general effect of the particle shape, this part of the

work uses the linear FE analysis, in which the overall engineering strain is set to be 0.1%. Figure 6.12 (a)-(e) shows the component distributions within the composite. These components are the effective stress, the hydrostatic pressure, the normal stress, the normal strain, and the strain energy density. These indicate that:

(1) The distributions are relatively uniform within spherical particles as proposed by Eshelby, while they are strongly non-uniform within cube-shaped particles.

(2) For cubic particles, the striking results are that the highest normal stress occurs at the side wall of cubic particles and the highest hydrostatic tension occurs at the midpoint of the side wall of cubic particles, which denotes the highest possibility of the particle cracking starting at the midlength of the particles, which is in accordance with the experimental results[30,31]. In fact, if perfect bonding holds, the stretch of the side interface along tensile direction is required to be equal in both particle and matrix at the side interface. This constraint forces the matrix at the interface to stretch less than the rest of the matrix medium, but it also exerts an extra tensile reaction force on the side wall of the particle so that the side wall of the particle stretches the same as the matrix next to the side wall. As a result, a strong tensile stress in the particle at the side wall is found. The high tensile hydrostatic pressure at midpoint of the particle is also due to the perfect bonding constraint. All this suggests that the particle cracking is governed by stress control.

(3) Figure 6.12(a) and 6.12(d) show that the composites with spherical particle reinforcements have much higher local plastic deformation in the matrix compared with those with cubic particle reinforcement for a given strain level. The highly concentrated

locations are at the pole a small distance away from interface of the spherical particles and are at the corners for cubic particles. The stress concentrations shown in Figure 6.12(a),(b), and (c) also display a similar pole and corner effect for the different particle shapes. Compare this with experimental results shown in Figure 2.12 and Fig. 2.14, where the void nucleates at the corners of angular particles or whiskers. Which component in Figure 6.12 is the critical one to determine the initiation of the void formation in the matrix? Is it Von Mises stress, hydrostatic pressure, normal stress, normal strain, strain energy density or some other component or combination of components? Since in each plot, a strong corner effect is developed, it becomes difficult to decide which component is suitable to set the criterion for void nucleation. Consider the elastic-plastic feature of the matrix. It seems that it is reasonable to choose the tensile hydrostatic pressure from the comparison of the analyses of plane strain and plane stress state in Chapter 2 or the strain energy density from the change of the stress state within composites in Chapter 3 and Chapter 5. If any process for the void growth is involved, it is believed that the work hardening will continue until either material exhaustion or the material strength is reached.

Figure 6.13 shows the effect of the particle aspect ratio on stress concentration. The models are generated to have a bar shaped particle within the unit cell. The aspect ratio here are defined as l (the length of particle along the tensile direction): w (the width of particle normal to the tensile direction):t (the thickness of particle normal to the tensile direction and the plane of the page). For the long particle model, the particle aspect ratio is 1:0.61:0.61 with a volume fraction of 1.84%; the model comprises of

2942 nodes and 2366 elements. For the short particle model, the mesh arrangement is the same except that the particle is rotated 90° degrees, which makes the aspect ratio become 0.61:1:0.61. The cubic model is arranged exactly as that in Figure 6.12. Since volume fractions of particles involved in these models are small, the interaction between particles is negligible. Then, the shape effect can be calculated by the FEA. The comparison of the hydrostatic pressure contours in Figure 6.13 shows that the high aspect ratio induces a high tensile hydrostatic pressure at midpoint of the particle during tensile loading, which implies that the longer the particle is, the higher the possibility of particle cracking. A similar indication is also found in the matrix, i.e. the tensile hydrostatic pressure is elevated at top interface and at corners simply by increasing the aspect ratio.

The above results reveal that:

(1) At a low volume fraction and a given strain, if no particle cracking is involved, the ductility of composites with spherical particles would be expected to be inferior, because all components, including the effective stress, the hydrostatic pressure, the normal stress, the normal strain and the strain energy density, in the matrix are higher (Figure 6.12). However, angular particles experience a strong non-uniform stress concentration, which increases the possibility of particle cracking. Such particle cracking will likely degrade the ductility of composites with angular particles.

(2) The possibility of particle cracking would increase with increasing the aspect ratio.

(3) Early void nucleation at the particle corners will more likely occur at particles with a high aspect ratio.

6.3.2 Effect of Particle Shape with Non-uniformly Dispersed Particles

Again, the behaviour of two extreme shapes, cubic particles and spherical particles has been modelled, as shown in Figure 6.14. In both cases, the particle volume fraction is 6.18 vol.%, the centre-to-centre distance for the particles in the upper right of the unit cell is 1.33 times the spherical particle diameter, and the overall engineering strain is 0.05 for the contour plots. The particles in the lower left represent isolated particles.

Figure 6.14(b) compares the distribution and magnitude of σ_{yy} in and around these two particle shapes. Firstly, the stresses in the matrix are highest directly above and below the particles, as would be expected from Eshelby's analysis. In isolated spherical particles, we have found the stress to be uniform, as predicted by Eshelby. For isolated cubic particles the stress within these non-ellipsoidal particles is not uniform. Both isolated and clustered cubic particles carry a much higher stress than their spherical equivalents. The σ_{yy} stress is especially high along the side walls of the particle, not just down the corners of the particle. It is common to observe SiC particles which have fractured on the plane normal to the load axis; a result consistent with the stress levels seen in these cubic particles. In the matrices, the stress levels are highest along the line of loading between closely spaced particles, but the σ_{yy} stress levels observed in the matrix between the cubic faces is much higher (629.2 MPa) than that developed between the spherical particles (530.5 MPa), even though the distance of closest approach between the spherical particles is a bit smaller than that of the cubes.

Figure 6.14(a) shows the hydrostatic stress developed in and around these same

particles. This stress is much higher at the top of the cubic particles (647.2 MPA) than the highest hydrostatic stress developed at the spherical particles (361.6 MPa). This dramatic increase due to the clustering (or the high local volume fraction) could largely change the evaluation of the effect of shape on the composite ductility because this stress is important in that it plays an important role in interfacial failure between the particles and matrix, resulting in void nucleation at the interface, as discussed in Chapter 3 and Chapter 5.

The comparison of the stress-strain curves for the two extreme shape models (shown in Figure 6.14) is plotted in Figure 6.15. As expected, the composites with cubic particles display higher work hardening at any given tensile strain because of the higher stress carried. The non-uniformity of the particle dispersion may affect a great deal of the deformation characteristics in composites during tensile loading. It is anticipated that the non-uniformity of the angular particles would effect a more sensitive control on the ductility of composites and the stress state in and around particles. In general, composites which have spherical particles should give better ductility than those with angular particles, if highly clustered particles are involved, regardless of the failure mechanism. The composite material with the cubic SiC particles did have a higher strain hardening rate in non-uniform case compared with non-uniform spherical particles, and so supported a somewhat higher load for a given strain level. But the 15 MPa gain in load carrying capacity at the engineering strain of 0.05 is achieved at a cost of about double increase in the tensile hydrostatic stress developed at the interface in the matrix and a 482.3% increase within the cubic particles, as well as a 767.3% increase in the σ_{yy} stress

tending to fracture the cubic particle. Keep in mind that this is equivalent to about a four times increase of volume change strain energy density in the matrix at the highest hydrostatic stress position and about twenty four times increase for that in the cubic particles (see Chapter 3). The contribution could be a significant increase in the strain energy density. Although the above calculation still needs to have its accuracy improved due to the relatively coarse mesh, it does not stop one concluding that the increase in load carrying capacity given by non-uniformly dispersed angular particles may not be worth the probable decrease in ductility.

6.3.3 Effect of Particle Shape at High Volume Fraction

The sensitivity of the mechanical response to particle shape with increasing volume fraction is of interest. This is because it is helpful in a practical sense to determine whether there is a preference to optimize the composite ductility and strength by choosing a certain particle shape for a given volume fraction. In the previous section, it has been shown that due to the non-uniformity of the particle dispersion, the stress state in the composite would be strongly affected at locations where the local volume fraction is high. To further examine the effect at higher volume fraction with a uniform dispersion of particles, the present section will deal with the particle shape effect at 25% volume fraction and compare these results with those at low volume fraction. Two models have been used for this purpose, as shown in Figure 6.16, in which there are 2197 nodes and 2728 elements meshed in the cubic particle model, and 1126 nodes and 875 elements in the spherical particle model.

Figures 6.16(a)-(e) show the component contour plots at 0.05 engineering strain. The most noticeable result is that at high volume fractions in aluminum matrices, the tensile hydrostatic stress (Figure 6.16(a)), the normal stress (Figure 6.16(b)), and the strain energy density (Figure 6.16(d)) at 25 vol% shift to the much higher level in the cubic particle compared with those in the spherical particle model. This is not seen at low volume fractions. The normal strain (Figure 6.16(c)) and the plastic energy density (Figure 6.16(e)) remain at a higher level in the spherical particle model, similar to what is observed at low volume fraction. As a result, at high volume fraction, if the failure process in the composites is controlled by the stress state or the strain energy density state, the composites with spherical particles should provide higher ductility. If the failure process is controlled by the matrix plastic deformation or the effective plastic energy density, then the composites with cubic particles should provide better ductility. It is worth noting that the experimentally observed appearance of void initiation in Figure 2.12 and Figure 2.13 is displayed in cubic model, i.e. a maximum tensile hydrostatic stress or maximum strain energy density is found at the corners of the cubic particle. The strong constraint between closely spaced cubic particles elevates the tensile hydrostatic stress. Therefore it is suggested that at high volume fraction, void nucleation in Al/(SiC) is controlled the tensile hydrostatic pressure or by the strain energy density if one considers the significant contribution of the tensile hydrostatic pressure to the strain energy density, especially when the composite is subjected to a large amount of overall tensile strain. In the cubic particles, the strong triaxiality at the midpoint of particle side also suggests that particle cracking in angular particles is controlled by the value of the

tensile hydrostatic pressure. This consequence remains the same as that found at low volume fraction.

To further examine the shape effect on the process of the void nucleation, we compare the maximum local stress relationships in the two models. It is found that in the matrices, the maximum stress states (see the tensile hydrostatic stress and the normal stress components) shown in Figure 6.17(a) are much higher in the composite with cubic particles than those in the composites with spherical particles shown in Figure 6.8. In the particles, this elevation of stress state due to the difference of the particle shape is even more striking, comparing Figure 6.17(b) to Figure 6.9. For example, at 0.02 overall engineering strain, the maximum normal stress in cubic particles may exceed 2.0 GPa, while the same component in spherical particles it is less than 0.5 GPa. If it is assumed that the particle tensile strength is 2.0 GPa, then particle cracking would occur at this given strain level. But for spherical particles this particle cracking would only occur at a larger applied strain levels. Figures 6.17(c) and (d) show the comparison of the maximum normal strain relationships in the two extreme cases of the shape. In the matrices, the maximum strain in the composite with spherical particles is slightly larger than that in the composite with cubic particles, as shown in Figure 6.17(c). However, in the particles, it is quite the opposite, i.e. the maximum strain is much higher in the cubic particles of the composites. Actually, it is the consequence that the stress and strain states are relatively uniform in the elliptical particles as proposed by Eshelby, whereas it is non-uniform for the non-elliptical particles. The high level of the gradient in the angular particles may be another reason to cause the particle cracking.

Summarizing the effects of the particle shape on the mechanical response in the composites, the conclusions are:

(1) At very low volume fractions, angular particle reinforced composites may give the better ductility compared with the spherical particle reinforced composites, because of the lower stress and strain state in the matrix.

(2) For one interfacial failure, it is expected that the void would be initiated at the pole of the spherical particle, while being initiated at the corners of the angular particle.

(3) The local stress state in angular particle reinforced composites would be much more strongly affected by the non-uniform dispersion of the particles, compared with the spherical particle reinforced composites. This indicates that in the material processing for the angular particle reinforced composites, the uniformity of the particle dispersion is an important requirement to avoid degrading the ductility and the strength expected in the final product.

(4) The aspect ratio of the particles affects the maximum stress state in the composites. The higher the aspect ratio, the higher is the stress concentration, which would lead to low ductility in the composites caused by early particle cracking and/or void nucleation at the corners of the particles.

(5) At high volume fractions, it is suggested that spherical particle reinforced composites should give a better compromise between ductility and strength because the rapid elevation of the local stress states within the angular particle reinforced composites with increasing the volume fraction would lead to early failure processes in the composite, such as particle cracking and/or the void nucleation. The concomitant increase in the

global stress-strain curve attained by angular particles is not as significant.

6.4 Effects of the Particle Clustering

The effects of volume fraction and particle clustering on the mechanical response of composites are, in fact, closely related subjects. Clearly, when the level of the particle clustering is high, it means that the local volume fraction in the clusters must be higher than the average volume fraction in the composites. Section 6.2 and Section 6.3.2 have introduced and examined these subjects. The present section will specifically and separately characterize the effects of the tensile clustering (i.e. where the particles are clustered in the tensile loading direction) and the effects of the side clustering (i.e. where the particles are clustered in the direction normal to the tensile loading) on the mechanical response. Also, comparison of the effects of tensile clustering at different volume fractions will be made.

6.4.1 Configuration

To clarify the difference between tensile clustering and side clustering, several models with 10% volume fraction of particles have been adopted. Figure 6.18 and Figure 6.19 show two models, in which there are 2606 nodes and 2137 elements for the clustering models, and 1910 nodes and 1479 elements for the uniformly dispersed model.

Figure 6.20 shows the tensile clustering models at different volume fraction, in which the mesh arrangement at 10 vol% is the same as that in the Figure 6.18, and there are 1910 nodes and 1479 elements at 20 vol%.

Elastic-plastic FEA has been used to obtain the component contours at 0.05 overall engineering strain shown in Figure 6.18-6.19 in 18 incremental steps for both the models and to predict the stress strain curves for the effect of the clustering at different volume fractions.

6.4.2 The Effect of the Tensile Clustering

In the present study, the effect of the tensile clustering is demonstrated in Figures 6.18. Figure 6.18(a) compares the hydrostatic stress distribution in a uniform distribution of particles with that of a distribution with closer spacing along the line of loading. In the left figure of Figure 6.18(a), where the particle spacing is 0.736 times of the particle diameter, the stress is approximately consistent with that predicted by Eshelby, and visualized in Chapter 3, in that the highest values for the hydrostatic stress would occur directly above and below the particle along the line of loading and the stress within the particle is uniform. When the particle spacing is reduced to 0.279 times of the diameter, then the hydrostatic stress is significantly increased along the line of loading between particles closely spaced along the line of loading, and is significantly higher near the particle interface (463.3 MPa compared with 284.6 MPa for the left figure of Fig 6.18(a).

This effect is even more strikingly demonstrated in Figures 6.18(b) for the same particle spacings. It shows the strong concentration of σ_{yy} between the particles closely spaced along the line of loading. The Von Mises effective stress reaches a maximum along the line of loading, but at a small distance from the particle-matrix interface. This

displacement of the maximum from the interface is a result of the high tensile σ_{xx} and σ_{zz} stresses at the interface. Plastic deformation would therefore be most intense midway between the particles, when the particles are closely spaced. If failure were to occur by material exhaustion in the matrix, then this would be the expected site, as has sometimes been observed.

In general, the results are in accordance with those by Flower and Watt[139,140,145] that the effect of putting a distribution of particles in the material is to cause zones of high stress between the particles linking them together in a fibrous-like stress distribution, oriented along the line of loading.

6.4.3 The Effect of the Side Clustering

For particle spacing changes in the direction perpendicular to the line of loading, the effects on the stress distribution are much less sensitive. In detail, the maximum values of the effective stress (Figure 6.19(a)), the tensile hydrostatic stress (Figure 6.19(b), the normal stress (Figure 6.19(c)) and the transverse stress (Figure 6.19(d)) in the uniform and side clustering cases are not changed much as shown for the tensile clustering. The uniformity of the stress state is slightly affected by side clustering (see Figure 6.19(c) and (d)), but it is not as dramatic as shown for tensile clustering. Generally, the particle spacing in this direction (i.e. in the fracture plane) will no doubt play an important role in void linking. However, it would appear to be not significant in void nucleation, based on the present results and similar results from other models examined as part of the present study.

6.4.4 The Effect of Tensile Clustering vs Volume Fraction

Figure 6.20 displays the effective stress and the normal stress contours for the tensile clustering at 5.0% engineering strain with 10% and 20% volume fractions, in which the close spacings between particles are the same. It is shown that increasing the volume fraction also elevates the stress level between the closely spaced particles as expected. This would further degrade the ductility of the composites at a higher volume fraction due to the tensile clustering. Another interesting result is found in that the effect of the clustering on the overall stress strain curve of the composites varies with the average volume fraction. The lower the volume fraction is, the higher the effect of the tensile clustering as shown in Figure 6.21.

In summary, for materials with large hard particles, one should aim to distribute these particles as evenly as possible to avoid the very high stresses developed along the line of loading between closely spaced particles. Specifically, the clustering at low volume fraction would significantly change the mechanical properties, such as the ductility and the strength. Compared with side clustering, the tensile clustering would be significant in void nucleation. Therefore, generally well control on fabrication processes would be of practical importance, because of a tendency for particle clustering in the fabrication processes for real materials.

6.5 Effects of Particle Size

The results for varying particle size are in agreement with those of other continuum treatments, including Eshelby's analysis; namely that the stresses scale with

the particle diameter. Therefore for a given particle shape and spacing (relative to the diameter), the maximum stresses of whatever type are independent of the particle size according to these continuum models, including the FEA. As well the overall stress-strain curve is independent of the relative particle size. But what does change is the elastic stored energy around individual particles, and this may be the controlling factor in local fracture initiation. It is an experimental observation that composites with larger particles have poorer ductility[19,71,172]. This can be reconciled with the present calculations if energy release is the governing factor leading to fracture.

This particle size scaling effect holds for spherical and cubic inclusions, and for all spatial distributions of the particles, according to our FE calculations.

6.8 Summary

The work in this chapter has examined the influence of the aspects of particle shape, size, volume fraction, and distribution on deformation characteristics of $(SiC)_p$/Al MMC by using FE models and applying the concept of the Flower-Watt unit cell. It has focused on the understanding of interactions between the two phases in terms of the close examination of stress states within and around particles.

Summarizing the results above, the following conclusions can be drawn:

(1) The external stresses exerted on composites may be largely transferred to the particles such that the stiffness and the strength of the composites increases with increasing volume fraction. The work hardening rate also increases. The increasingly high constraint between particles at high volume fraction leads to the effect that for a given strain level,

the rate of increase in the strength vs. volume fraction is higher at higher volume fraction levels.

(2) At high volume fraction, discontinuous composites reinforced with spherical particles should give better ductility than those with angular particles. The increase in load carrying capacity given by cubic particles is not worth the probable decrease in ductility.

(3) For materials with large hard particles, one should aim to distribute these particles as evenly as possible to avoid the very high stresses developed along the line of loading between closely spaced particles.

(4) The particle size scaling effect holds for spherical and cubic inclusions, and for all spatial distributions of the particles, according to our continuum calculations.

(5) The mechanical response of two phase materials may be predicted and understood, if the interface strength and mechanical behaviours of two individual phases can be described accurately.

CHAPTER 7

EFFECTS OF THERMALLY INDUCED STRESSES ON THE DEFORMATION CHARACTERISTICS WITHIN Al/$(SiC)_p$ MMCs

7.1 Introduction

There exists another type of stress concentration which is generated due to the discontinuity of the coefficient of the thermal expansion (CTE) in a material. For instance, residual stresses are inherent in Al/$(SiC)_p$ composites after any cooling process because of the great difference of the CTE between aluminum and silicon carbide. These stresses cannot completely be eliminated by plastic relaxation, interface sliding, or other micromechanisms during the thermal processing of materials. Thus the effect of the thermally induced residual stresses on the mechanical properties and ductility of Al/$(SiC)_p$ should be taken into account.

Academic interest in the subject has been reflected by many recent works[73,79,80,89,143,152,174,175,176,177,179]. It has commonly been recognized that the incorporation of SiC platelets in aluminium matrices results in increased values of the elastic modulus and yield strength not only because of the back stress, but also because of an increase in the dislocation density in the Al matrix due to the differences in the CTEs (which corresponds to the thermally induced stresses).

The results from this dissertation have produced a new viewpoint with respect to the role of particles in the strengthening process. Fundamentally, the strengthening mechanisms by particles have traditionally been related to the consequence of the creation and movement of the "geometrically necessary" dislocations. However, this work-

hardening effect within the metal matrix alone is unlikely to represent the entire strengthening role of the second phase particles within the Al/(SiC)$_p$ MMCs, because the role of the particle gathering the stress to itself also makes an important contribution. This strengthening mechanism macroscopically offers the superior gain of the strength in the Al/(SiC)$_p$ MMCs to that in the aluminium alloys. In the alloys, the precipitates developed from phase transformations are responsible for the strengthening. The second phases are considered as small particles, i.e. as point hardening agents, which interfere with the dislocation movement to affect the work hardening process. Their own mechanical properties are neglected or are assumed to be close to that of the matrix. In most commercial precipitation strengthened Al alloys, the precipitate volume fraction is small. In this situation, it is reasonable to estimate the strength of the alloys only by the dislocation interference within the alloys. In contrast, in the MMCs, the SiC particles are large and strong particles (the size is >1 μm and the Young's modulus is as about 6.4 times as great as that of the aluminium matrix), and a large volume fraction of particles are incorporated within the matrix. The mechanical response of the particles is no longer an ignorable part during deformation of the MMCs. The stress transfer to particles becomes an important issue.

In the rest of this chapter, the way in which the stress transfer is affected by the thermally induced stresses will be examined.

As a useful tool, FEA allows us to investigate the effect of the thermally induced stresses by continuum mechanics. The previous works on Al/(SiC)$_w$ MMCs[89,152,170,177] have shown the applications of FEA for whisker reinforcements. In the present chapter,

the thermo-elastic-plastic FEA will be used to simulate the thermally induced residual stresses (TIRS) and the effect of the TIRS on deformation characteristics in the Al/$(SiC)_p$ particle MMCs. It will focus on:

a) displaying and investigating the TIRS after cooling processing;

b) analyzing the process of the stress redistribution during uniaxial loading and emphasising the influence of the TIRS on the stress transfer to particles.

c) examining the effects of the TIRS on mechanical responses compared with those when the material is initially free of residual stresses.

7.2 Configuration

In the present chapter, thermo-elastic-plastic FE models in ABAQUS have been adopted. During cooling, the three dimensional unit cell, namely the Flower-Watt cell, allows all the side walls to be free to move due to the thermal contraction, but the individual walls are kept planar. The computation assumes that the material is taken to be stress-free at a uniform temperature of 350°C. According to some works[89,177], at or above this temperature, the flow strengths of aluminium alloys are so low that a negligible dependence of computed residual stresses is expected for temperature changes above 350°C. Some other works[39] also showed that the stresses became effective at 300°C on the basis of the marked decrease of strength of aluminium and its alloys near this temperature. In the present simulation the thermally induced residual stresses were computed using a temperature drop from 350°C to 20°C (room temperature) in 10 increments. The CTE of the aluminium used was 2.0×10^{-5} m/(m·°C) and that of the SiC

particles was 4.0×10^{-6} m/(m·°C). The mechanical properties of both the matrix and the particle are shown in Table 3.1. The plastic behaviour of the matrix is represented in Figure 5.1.

The present work further attempts to examine the effect of thermally induced residual stresses on the deformation characteristics in the MMCs at different volume fractions during the tensile loading. The volume fractions chosen were 5% and 25% of SiC spherical particles. The former model contained 1750 eight-node elements with 2241 nodes. The latter model contained 875 eight-node elements with 1126 nodes. To monitor the stress redistribution during the tensile loading, the computation involved 20 increments in the engineering strain range of 0.0%-0.5% and 12 increments in the engineering strain range of 0.2-5.0%. These were chosen so as to consider the rapid change in stress concentrations which occur at low strain levels.

7.3 Thermally Induced Residual Stresses after Cooling

The misfit of the CTEs in the Al/$(SiC)_p$ generates the stress concentration after the cooling process. The higher the misfit, the stronger are the thermally induced residual stresses. Many experimental works[73,80,175] have revealed the local high concentration of the dislocation density near the SiC particles in Al/(SiC) composites, which corresponds to the inherent local residual stresses.

At the relatively low volume fraction 5%, the effective stress, i.e. the Von Mises stress, appears as strong interactions between the particle and the matrix near interface in the matrix, shown in Figure 7.1(a). A plastic zone was developed around the particles

within the matrix, extending to about half particle radius. However, the distortion within the particle occurs at a very low level, which is opposite to the case after tensile loading. The reason for this is that during the thermal contraction the matrix exerts a nearly isotropic and relatively uniform compressive pressure onto the particles because the particles are harder and contract less, and also because plastic relaxation outside of the particles partially releases the stress concentration within the particles. These processes make the bulk volume decrease dominant within the particles, so that the distortion with respect to the deviatoric stress component becomes insignificant within the particles. Additionally, in the matrix, the mean stress becomes tensile at regions far away from the particle and compressive near the particles, as shown in Figure 7.1(b). Furthermore, as expected, due to the constraint between particles, a strong stress fluctuation of the normal stress (S22) occurred at the equatorial plane (Figure 7.1(c)). In the particles the compressive stress is created by squeezing from the matrix and also at the top of the particle by the reaction of the particles resisting the squeezing. In contrast, the constraint from the particles did not allow the matrix to be free to contract along the tensile direction near the equatorial plane so that the tension appears there. With respect to the normal strain (E22) contour, the largest compressive strains were obtained at the tops of the interface, shown in Figure 7.1(d). Since there is no external stress, then by symmetry the S11 and E11 contours would appear identical with Figures 7.1(c)-(d) except for a 90° rotation of the figures. In these contours, these initial compressive zones are particularly interesting, as will be discussed in further sections. Furthermore and similarly, the strain energy density stored (Figure 7.1(e)) and the plastic energy density dissipated (Figure

7.1(f)) in the MMCs displayed the strong layers at the interface in the matrix. Especially, noteworthy is that the plastic zone was formed only at the region near the interface in the matrix.

In general, at low volume fractions, the thermally induced residual stresses are localized around the particles. The existence of an initial plastic zone and the initial compressive stress region is of interest.

At a relatively high volume fraction, 25%, the effective stress experiences a much stronger constraint from the particles and the matrix, shown in Figure 7.2(a). The matrix yields almost everywhere, compared with the partial yielded region at lower volume fractions. The Mises distortion within the particle still occurs at a lowest level, but the uniformity within the particles no longer holds due to the constraints from the neighbouring particles. Strikingly, the mean stress almost exclusively exhibits tensile values in the matrix and compressive values in the particles, as shown in Figure 7.2(b). Again the strong plastic constraint between the neighbouring particles exists. Figure 7.2(c) illustrates the tensile stress component of the thermal induced residual stresses, in which the initial compressive zone remains as in the case at low volume fraction and a fibre-like pattern linking the particles in the y direction is formed. Concurrently, the strong S22 tension at the equator of the particles is due to the constraint of the thermal contraction in the matrix causing the hydrostatic pressure to exhibit tensile character. Thus at high volume fractions the mean stress in the matrix is positive and in the particles it is opposite, as has been shown in some neutron diffraction results[68]. Another feature of the thermal residual stresses at high volume fraction that should be noted is

that the maximum initial compressive strain moves to the midpoint between the particles due to the plastic flow constraint, shown in Figure 7.2(d), as compared with the zone which is at the interface at low volume fraction as seen in Figure 7.1(d).

If one bears in mind two facts: (a) there is no externally applied stress; (b) these results are not dependent on the absolute size of the particle. Then it becomes clear that the residual stresses shown in Figure 7.1 and 7.2 represent the stress field that would be created between any two particles of equal size with the equivalent ratio of separation distance to radius. In viewing these figures, the reader can then transpose these stress fields to a random particle array, and expect to find something like the stress fields from Figure 7.2 between closely spaced particles, whereas Figure 7.1 represents what would be found between particles with a greater separation distance. The trends as particles get farther apart are made clear from these two sets of figures.

In summary, comparing the thermal residual stresses at different volume fractions, it was noted that the higher the volume fraction of particles, the stronger is the plastic flow due to CTE constraints. Examining the individual components, the results show that:

(1) In the matrix the initial plastic zone is larger and the constraint is stronger at higher volume fractions, the peak value shifts from the interface at low volume fraction to the midpoint for closely spaced particles. In the particle, the distortion remains at a low level. (See Figure 7.1(a) and Figure 7.2(a))

(2) In the matrix, due to the strong constraint, the initial compressive mean stress zone reduces in size with increasing the volume fraction so that at high volume fraction the

matrix displays a tensile mean stress on average. In the particle, the compressive mean stress also decreases with increasing the volume fraction, but it remains at a relatively high level compared with that in the matrix. (See Figure 7.1(b) and Figure 7.2(b))

(3) Surprisingly the compressive tensile stress in the particle decreases rapidly with the increase of the volume fraction. It is believed that this is a consiquence of the strong constraint between the particle and the matrix. In the matrix the fibre-like pattern of the initial compressive stress forms at high volume fraction, whereas at low volume fraction the pattern is more localized. (See Figure 7.1(c) and Figure 7.2(c))

(4) Due to the plastic flow constraint, as increasing volume fraction the largest zone of the initial compressive strain moves from the interface of the particles (with isolated particles) to the centre of the line between the particles.

The above details may be related fairly directly to interpret the possible strengthening mechanisms resulting from the thermally induced residual stresses in the Al/$(SiC)_p$ MMCs subjected to subsequent tensile loading.

7.4 The Redistribution of the Stress Concentration during Tensile Loading

The way in which the stresses within MMCs with thermally induced residual stresses are redistributed during the uniaxial loading is of interest. To explore how the thermally induced residual stresses affect the stress transfer to particles, the present section analyzes the evolution of the mechanical response for materials with 5% volume fraction of SiC.

The changes in the effective stress with increasing overall tensile strains from

0.0% to 0.5% (0.1% increase step) is shown in Figure 7.3. In the particles, as the strain increases, their stress gathering capability increases starting from carrying less than 10.6 MPa at the initial state to carrying greater than 208 MPa at 0.5% overall strain. The particles gradually become the major stress bearer compared with the matrix, which carries a stress less than 157 MPa. The process of stress redistribution in the matrix indicates that local unloading takes place along the loading direction to release the initial compressive zone until the local stress overcomes the thermal residual stress. Then as the loading continuously increases, a stable stress concentration pattern starts to build up. Comparing this with an identical model without thermal stresses, the consequence is that the local yielding is delayed by the presence of the thermal stresses. Hence, at low loading the matrix along the loading line deforms elastically so that this elastic stress field is superimposed on the thermal residual stress. According to the analysis in Chapter 5, this change may rapidly increase the effective stress gathering capability of the particles through the delay of the plastic relaxation.

As shown in Section 7.3, the hydrostatic pressure component of the thermally residual stresses is amazingly large within the particles (with the compressive pressure greater than 167 MPa). This amount of pressure is of interest because it is equivalent to that when a 500 MPa uniaxial compressive stress is exerted on the particles. This pressure may contribute an increase of the strength within the MMCs. Subsequently, with the increase of tensile strain, the pressure in the particles is released to a small tensile value at the overall engineering strain 0.5%, shown in Figure 7.4. The release of the pressure may play a role in avoiding particle cracking. On the other hand, in the matrix,

the evolution of the stress redistribution reveals a stress concentration built-up towards the interface. Generally the hydrostatic pressure becomes less concentrated at the poles of the particles with thermal stresses. If one considers the fact that the stress concentration in both the effective stress and the hydrostatic pressure drops due to the existence of the thermal stresses, it leads one to conclude that the process of the void formation at the poles of the particles may be delayed because the strain energy density required to generate voids near the interface is lower compared with that where there are no thermal stresses.

The evolution of the tensile stress component has been shown in Figure 7.5(a)-(f). The change of the stress within the particles spans from about 166 MPa compressive stress at 0.0% strain to about the same value of the tensile stress at 0.5%. Combined with the suppression of the effective stress, it is anticipated there would be a rapid increase in the stress gathering capability of the particles due to the superposition of a quasi-elastic stress field. In the matrix, with the increase of the externally applied strain, the redistribution of the tensile stress shifts the highest stress concentration from the equator to the poles of the particle to reach a relatively stable pattern.

Since the stored strain energy density is one of the factors controlling void formation in the matrix and particle cracking, its change with external tensile loading is also of interest, as shown in Figure 7.6(a)-(f) in which the overall engineering strain varies from 0.0% to 0.5%. The strong fluctuation at low strain levels is expected due to the gradual elimination of the compressive zone at the poles of the particles. At 0.5% strain, the pattern tends to be stable, but the highest value is seen to be lower than that

without the thermal stresses.

Figure 7.7(a)-(f) exhibits the evolution of the plastic energy density. It should be noted that the initial and nearly isometric plastic zone first spreads near the equatorial plane because the increase of the tensile stress near the equatorial plane keeps elevating the effective stress. Then with increasing loading, the plastic zone is developed at the poles along the loading direction.

Having examined the stress redistribution during the tensile loading from initial residual stress state to 0.5% strain at low volume fraction, the most significant results are that the existence of the thermal residual stresses retards the accumulation of stress concentration for both the effective stress and the hydrostatic pressure. This would lead to the rapid increase of the stress gathering capability of the particles and the retardation of void formation within the matrix.

7.5 A Comparison with and without Thermal Stresses

In the previous section, it was found that the existence of thermally induced residual stresses affects the overall mechanical properties of the composites and also the stress gathering capability of the particles. The following will compare the difference at 0.5% external strain with and without thermal stresses to further understand the effect of the thermal stresses on the mechanical properties of the MMCs.

Figure 7.8 shows the effective stress contours with and without thermal stresses at 0.5% engineering strain. It is noted that the plastic zone is more highly developed around the equator of particles with thermal stresses, in contrast to the stress contour

forming a fibre-like pattern along the direction of loading in the absence of thermal stresses. A comparison of the hydrostatic pressure contours at 0.5% engineering strain is shown in Figure 7.9. With thermal stresses, the tensile pressure is lower (about 20 MPa) in the particle and this concentration at the poles of particle is expectingly reduced. Significantly, along with the tensile pressure, the tensile stress contours at 0.5% engineering strain show obviously that the gradient of the stress concentration in the matrix reduces due to thermal stresses as displayed in Figure 7.10. This is important because the effect actually implies that due to the decrease of the gradient of the stress concentration, an increase in the strength of the MMCs with thermal stresses is mainly due to the increase of the matrix stress gathering capability. This increase in the strength is directly related to the retardation of the effective stress. It needs a higher external tensile strain to reach the same polar effective stress than the case without thermal stresses.

At the higher strain level of 5%, the differences in the stress concentration become smaller. A comparison is made in Figures 7.11 to 7.13, which are the effective stress, the hydrostatic pressure and the tensile stress contours with and without thermal stresses. However, it still can be noted that the stress gathering capability of the particles is slightly higher with thermal stresses than that without thermal stresses, but the effect would disappear with continuing increase in the tensile strain through the further movement of the plastic flow. Eventually at a high enough strain level, the response of the MMCs would not be affected by the misfit of the CTEs, namely the difference in CTE's.

By comparing the difference with and without thermal stresses, it is readily demonstrated that the misfit of the CTEs would strongly affect the initial stiffness, the yield stress and the beginning tensile loading stage of the MMCs. It is expected that at high volume fraction, the effect of the thermal residual stresses on the overall mechanical response would be similar to that at low volume fractions.

7.6 Effect of the Thermally Induced Stresses on Overall Stress Strain Curves

Figure 7.13(a) and Figure 7.13(b) are the stress-strain curves of a 25% volume fraction particle composite model with and without heat treatment. As expected it was found that there is an increase in the 0.2% yield strength of composite because of thermally induced residual stresses. The process leading to the increase in strength of the MMCs may be classified into the following stages:

(1) The initial loading stage (strain $< \sim 0.15\%$)

An interesting FEA result is that for both the tensile loading and compressive loading, the apparent stiffness of the MMCs is reduced, if one considers the thermal stresses compared with the case with no thermal stresses. By reviewing the redistribution during the uniaxial loading, this result seems reasonable. At the beginning of tension, the initial plastic zone near the equatorial plane decreases the rate of stress the increase in the matrix and therefore its ability to carry the stress during tensile loading. On the other hand, in the case of the compression, the initial compressive plastic zone at the poles of the particles would decrease the efficiency of the rate of increase for the particle to carry compressive stress. In both cases, the initial plastic zone generated within the matrix

makes the apparent overall stiffness lower. Note that, without considering the residual stresses, the matrix and the particle deform elastically at the initial loading.

(2) The initial yielding stage (strain between 0.15%-0.3%)

Recall that when substantial plastic flow takes place in particulate reinforced materials, this plastic flow occurs above and below the poles of the particle. The effect of the thermal stresses is to leave a residual compressive stress along the polar direction at these locations.

In the early stages of plastic flow in tension then, the effect of the residual stress at the poles is to retard the development of the Mises effective stresses there. The net effect is to cause a delay in general yielding. For compressive loading, the further accumulation of the plastic deformation within the matrix would increase the stress concentration in the MMCs and at the same time increase the stress gathering capability of the particles. Note that the initial compressive stresses exist in the particle after cooling process. Again, an increase in the strength of the MMCs is anticipated.

The results above suggest that the effect of the thermal residual stresses on the yield strength should not be considered simply as the half difference of the tensile yield strength and the compressive strength as some works did.

(3) The stable stage of the increase in the strength (strain between 0.3%-2.0%)

At the stage, the increase in strength predicted with thermal stresses in both cases exhibits a stable value ~ 8 MPa. In real materials, this value is expected to be larger because of the effects of the particle shape and the tensile clustering.

(4) The large strain stage

At this stage, the plastic deformation is sufficiently accumulated within the matrix that any effects from the initial residual stress are negligible. The stress concentration also increases as shown in Chapter 5. The influence of the thermal stresses on the stress concentrations is expected to be decreased gradually as increasing tensile or compressive loading. From the present results, this phenomenon has been shown for the case of the tensile loading.

In general, the overall stress and strain behaviour is expected to be sensitive to the effect of the thermal residual stresses at the initial strain levels. The yield strength would be strongly dependent on the cooling process. The strength determining mechanisms of MMCs are those of the stress transfer to particles and work hardening in the matrix. The former mechanism distinguishes MMCs from ordinary alloys.

It is found that the prediction from the therm-elasto-plastic FEA confirms a experimental result[179], that the tensile yield stress is slightly larger than the compressive yield stress for composites containing spherical SiC particles. If one considers another interesting result, in this case for whisker composites, a higher compression yield stress than tensile yield stress is expected, which has also been found by experiments[179] and FEA[152]. It can be suggested that for the particulate composite, if the particle shape is other than spherical, the effect of the thermal stresses on the yield stress may be minor.

7.7 Discussion

The prominent advantages in using FEA to investigate the mechanical properties of microstructures are that:

(1) it is able to reveal the evolution of the plastic deformation and stress redistribution with and without thermal stresses within the MMCs subjected to a tensile loading;

(2) it is able to reveal the levels of the local work hardening within the matrix so that the contribution of the work hardening in material strengthening is included during the analysis;

(3) it is also able to reveal the contribution of the stress transfer to the particles in materials strengthening; this is information which cannot be provided by the observation of dislocations.

The above processes can be modelled for Al/$(SiC)_p$ MMCs, if the material behaviour, such as the work hardening, the thermal response, and the elastic response, are described correctly, and if appropriate particle shape and distribution are used.

To explore the influence on work hardening with and without residual stresses, of various contributions including the stress transfer to the particles, a general discussion is given as follows.

A. Strengthening by work hardening within the matrix

It is well established that the plastic deformation is physically manifested by the movement of the dislocations generated within the matrix, when the external forces exceed the yield stress. As a result of the movement of the dislocations, work hardening is achieved due to the interference of these dislocations. In general, for two phase materials, the work hardening comprises two parts. One part is the work hardening caused by the creation and the movement of the 'statistically stored' dislocations, which are created from the intrinsic matrix defects. The other part is the work hardening caused

by the creation and the movement of the 'geometrically necessary' dislocations, which are created as a result of the existence of the hard second phase. The latter practically involves two contributions, the movement of dislocations generated from the thermal contraction due to the misfit of the CTEs and the movement of dislocations generated from the tensile loading due to the misfit of the elastic or elastic-plastic properties of the matrix and the particles. The common characteristic of these two contributions is that the misfit causes a high stress concentration accumulation and plastic zone (i.e. intensified dislocations) around the particles. The strengthening process is directly related to this increase of dislocation density due to the misfits. However, it should be clarified that the strengthening process actually is that of the multiplication of the unmovable dislocations, which has been shown by Stobbs, Watt and Brown[99]. By examining the fatigue behaviour in copper-silica, they found that there was little or no fatigue-hardening in spite of the increase of dislocation density during the process. It suggested that the increase of the dislocation density is a necessary condition, but is not a sufficient condition. The multiplication of a high density of unmovable dislocations is of essential importance.

Through the use of the FEA in continuum mechanics, work hardening has been shown to be related to the local fluctuation of the stress concentration and the plastic deformation within the aluminium matrix. It is assumed that the behaviour of the work hardening in the matrix is isometric and it follows the Prandtle-Reuss flow law, i.e. the direction of flow is the same as the direction of the outward normal to the yield surface. As with any other existing composite model, the present model uses the mechanical properties of each constituent, independently. However, one question proposed by Taya,

Lulay and Lloyd[80] is worth consideration, that is, are the mechanical properties of the matrix metal in a MMC the same as those of the unreinforced metal? To increase the accuracy of the prediction from continuum mechanics, what kind of additional input data is required and how can one get them? Actually, the prediction of FEA using the behaviour of the work hardening of the unreinforced metal leads to a softer stress-strain response for MMCs than is observed in real materials. For instance, Vogelsang et al.[15] found that the yield strength for 6061 Al/$(SiC)_w$ MMCs at 20 vol pct is increased by more than a factor of two compared with that of annealed powder compacted 6061 Al alloy. Furthermore, FEA predicted an ultimate strength of only 186 MPa for 20 vol pct SiC composite, whereas the measured value of ultimate strength for this materials is 448 MPa. Arsennault and Fisher[178] proposed that the increased strength could be accounted for by a high dislocation density in the Al matrix after cooling process due to the misfit of the CTEs of Al and SiC. But further FEA[152] with consideration of the residual stresses predicted an increase in strength of less than 50 MPa with 480 degrees cooling. It is still a much lower value than that of the experiments. These results suggested that this increase in strength cannot be explained directly by continuum mechanics theories if the work hardening of the matrix metal in the MMCs the same as those of the unreinforced metal.

Therefore, to clarify the strengthening mechanisms in the MMCs, the details about the cooling process and the tensile loading within the MMCs should be reexamined closely. According to the observation on the dislocation density and the strengthening by Stobbs et al.[99], the multiplication of the unmovable dislocations results in the work

hardening or strengthening within the matrix.

In the MMCs, the dislocations generated from the thermal contraction and the tensile loading process cannot as freely move through the matrix medium as through the unreinforced matrix medium. Especially, when the volume fraction is high, some of dislocations would be pinned or impeded by the particles so that the unmovable dislocations would be increased compared with those within the unreinforced metal. Therefore, the apparent work hardening of the matrix in the MMCs is expected to be higher than that in the unreinforced uniform metal. It implies that the behaviour of the work hardening of the matrix within the MMCs is different from that within the unreinforced matrix. The consequence of the difference is that the matrix within the MMCs is apparently stiffer.

B. Strengthening due to the stress concentration

Brown and Clarke[106] have proposed that the local fluctuating stresses act essentially as barriers to make it more difficult for successive glide dislocations to bypass the particles. The present author believes that the high stress concentration of hydrostatic pressure within the MMCs is one of the major factors responsible for the impedance to the plastic flow. This is because the significant difference of the mechanical response between the unreinforced aluminium and the MMCs is the accumulation of a high stress concentration of the hydrostatic pressure near the particles in the MMCs. The contribution of the tensile hydrostatic pressure to the local strain energy becomes an important part of the total strain energy, which has been discussed in Chapter 3, 5 and 6. The opposite gradient of the strain energy density physically represents a resistant

force to the movement of the dislocations. The higher the strain energy density concentration is, the larger the resistant force or the stronger is the impedance to the plastic flow. It is reasonable to modify the flow potential within the matrix in the MMCs by considering the effect of the hydrostatic pressure or even its gradient.

C. Strengthening by the stress transfer to the particles

In the previous chapters (Chapters 3 to 6), the analytical and FE analyses revealed that the particles carries higher stresses than the matrix. The stress gathering capability of the particles depends on the misfit of the material properties of Al and SiC. Since the incorporation of the large SiC particles into the aluminium matrix usually involves a finite volume fraction of the reinforcements, this part of contribution to the strengthening of the MMCs is not ignorable.

With consideration of the thermal residual stresses, in the present chapter, the results shows that the effect of the misfit of the CTEs does provide an increase in the strength of the MMCs at a low tensile loading level due to the increase of the stress gathering capability of the particles because of the retardation of the local yielding point, but this effect would decrease with increasing tensile loading.

However, using the thermo-elasto-plastic FEA, the prediction of the strength of the MMCs is less than the measured values. It suggested that a modification of the constitutive equations and the description of the flow potentials of the matrix will be required because of the above considerations about work hardening in the MMCs, namely the stress concentration, and stress transfer to the particles. It is anticipated that if the behaviour of the work hardening within the matrix in the MMCs can be correctly

described, the FEA can be used to predict a reasonable increase in the strength in the MMCs similar to the measured values. That is to say, the matrix in the MMCs is expected to carry higher stresses due to the stiffer work hardening, and so also would the particles corresponding to their stress gathering capability. This magnification of the stress carried within both the matrix and the particles actually leads to doubts that these are among the reasons responsible for the low ductility of the MMCs and the particle cracking.

7.8 Summary

The effect of thermally induced residual stresses on the mechanical responses of Al/SiC composites was investigated by applying thermo-elasto-plastic FEA. The results have shown that:

(1) the residual stresses resulting from the thermal contraction during the heat treatment do provide an increase in the strength of the MMCs.

(2) the effect of the thermal stresses on the mechanical properties decreases with increasing the tensile plastic strain.

(3) the yield strength for the tensile loading is higher than that for the compressive loading in spherical SiC particle reinforced aluminium metal matrix composites.

(4) the accurate prediction from FEA requires additional input data on the work hardening within the matrix of the MMCs and a modification of the description of the constitutive equations and the flow potential.

CHAPTER 8

GENERAL SUMMARY AND CONCLUSIONS

This chapter summarizes the new observations that have been found in this modelling study.

Part I: Basic Role of a Hard Particle

(1) By visualizing the elastic field around a SiC sphere within the aluminium matrix applying Eshelby's model, the following characteristics of a hard particle embedded in a soft matrix subjected to tensile loading has been confirmed:

(a) SiC particles carry higher tensile stresses than the aluminium matrix, which corresponds to stress transfer to the hard particle. The author has coined the term "stress gathering capability" to express the relative ratio of theses stresses and to emphasize its importance in the strengthening of MMC's.

(b) All the stress and strain perturbations in the aluminium matrix are developed near the interface. Matrix yielding would first occur along the pole a small distance away from the interface, which leads to a higher global level of work hardening in the matrix, compared with the unreinforced matrix.

(c) The triaxial stress exhibits the strongest perturbation and compared with any other components it has the highest relative concentration along the pole at the interface.

(2) By analyzing the dependence of the stress transfer on the relative misfit of the elastic

constants, it is found that:

(a) The stress carrying capability increases monotonically with the increase of the ratio of the Young's moduli;

(b) The increase rate of the stress carrying capability is high at low modulus ratios, but low at high modulus ratios. This infers that it is not always necessary to obtain the effective stress transfer by choosing extremely stiff reinforcement.

(3) By studying the stored strain energy density, it can be concluded that this energy density consists of two terms:

(a) that generated due to the specific volume change, which may be expressed as a function of the mean stress;

(b) that generated due to the distortion, which may be expressed through the effective stress.

Hence, the failure process in two phase materials would be strongly affected by the local value of the tensile hydrostatic pressure.

(4) All the stress and strain perturbation fields are scaled by the particle size.

Part II: A New Approach to Inhomogeneity Problems with Arbitrary Shape Particle

A new method for solving arbitrary-shaped inhomogeneity problems has been developed.

(1) The approach combines boundary integral equations, based on Betti's principle, with a sequence of cutting, straining, and welding procedures to numerically acquire stress and

strain distributions at an inhomogeneity with an arbitrary shape.

(2) The approach reduces the inhomogeneity problems to the determination of the elastic perturbation field induced by the strain misfit. It distinguishes the perturbation field from the uniform stress field and emphasises that the strain misfit is the driving force to cause stress concentration at inhomogeneity when a system comprised of an infinite domain and an inhomogeneity is subjected to a far-field stress.

(3) The approach converts a three dimensional computation problem for a singularity into a two-dimensional one (a surface integral). It takes far less computer time than for FEA to obtain reasonably accurate results.

(4) The approach is sensitive to the variation of stress fields near a singularity and meets the equilibrium equations everywhere within both matrix region and the inhomogeneity region.

(5) It may also be used as an absolute verification method for other computation methods for inhomogeneity problems.

(6) The stress states both in the matrix and in the inhomogeneity are non-uniform.

Part III: Plastic Relaxation and Plastic Accumulation

An elastic plastic FEA has been performed at low particle volume fraction. By examining the plastic relaxation and the plastic accumulation in the MMCs. It can be concluded that:

(1) Plastic deformation helps stress relaxation at an early strain stage. The relative stress concentration is relaxed and the stress gathering capability of the particles is reduced.

(2) During further plastic accumulation due to the increasing tensile loading, strain hardening overcomes the plastic relaxation effects and the relative stress concentration in the matrix then increases. This concentration may even exceed that caused by the misfit of the elastic moduli. Concurrently with this, the stress gathering capability of the particle also increases.

The ductility of an MMC depends not only on the elastic stored energy, but also on the plastic deformation accumulated. It is therefore proposed that the following should be considered in explaining the low ductility of Al/$(SiC)_p$ MMCs.

(1) Along with the effective stress, the tensile hydrostatic pressure is responsible for the early void initiation at the interface within the MMC;

(2) The localized high accumulation of the plastic deformation near particles may lead to matrix exhaustion;

(3) the high stress gathering capability of the particles will be partially responsible for the particle cracking.

Part IV: Effects of Particle Morphology on Mechanical Response in Al/$(SiC)_p$ MMCs

The influence of the aspects of particle shape, size, volume fraction, and distribution on deformation characteristics of $(SiC)_p$/Al MMCs were examined using FE models and applying the concept of the Flower-Watt unit cell. The conclusions are:

(1) The external stresses exerted on composites may be largely transferred to the particles such that the stiffness, the strength and the work hardening rate of the composites increases with increasing volume fraction as expected. The high constraint between

particles at high volume fraction leads to the result that at a given strain level, the rate of increase in the strength vs. volume fraction is higher at higher volume fraction levels.

(2) At high volume fraction, discontinuous composites reinforced with spherical particles should give better ductility than those with angular particles. The increase in load carrying capacity given by cubic particles compared with spherical particles is not worth the probable decrease in ductility.

(3) For materials with large hard particles, one should aim to distribute these particles as evenly as possible to avoid the very high stresses developed along the line of loading between closely spaced particles.

(4) The particle size scaling effect holds for spherical and cubic inclusions, and for all spatial distributions of the particles, according to our continuum calculations.

(5) The mechanical response of two phase materials may be predicted and understood, if the interface strength and mechanical behaviours of two individual phases are described accurately.

Part V: Effect of Residual Stresses on Mechanical Response in Al/$(SiC)_p$ MMCs

The effect of thermally induced residual stresses on the mechanical responses of Al/SiC composites has been investigated by applying thermo-elasto-plastic FEA. The conclusions are:

(1) the residual stresses resulting from the thermal contraction during the heat treatment does provide an increase in the strength of the MMCs.

(2) the effect of the thermal stresses on the mechanical properties decreases with

increasing the tensile plastic strain.

(3) the yield strength for the tensile loading is higher than that for the compressive loading in spherical SiC particle reinforced aluminium metal matrix composites.

(4) accurate prediction from FEA requires additional input data on the work hardening within the matrix of the MMCs and a modification of the description of the constitutive equations and the flow potential.

CHAPTER 9

SUGGESTIONS FOR FURTHER WORK

The new results presented in this dissertation suggest a number of ways in which the research could be extended. The following are those which the author believes to be promising.

9.1 Modification of Constitutive Equations and Plastic Flow Potentials in Modelling Two-phase Composite Materials

In Chapter 7, it has been found that new appropriate constitutive equations and/or flow potentials in modelling composite materials are needed, because the hardening behaviour of the matrix material is strongly affected by the existence of the second phase particles. The behaviour of the work hardening in the matrix of composites would be distinguished from unreinforced alloys due to the increase of the immovable dislocations. This change requires that the constitutive equations and plastic flow potentials be modified before they can be used in real material modelling.

The present author believes that the modification will take the gradient of the stress state and the high triaxial stress into account, because these characterize the difference between unreinforced alloys and composites. A large amount of experimental work is needed to construct an accurate description of the elastic-plastic behaviour of the matrix of composites.

9.2 Extension of the Method Developed in Chapter 4

The extension of the method developed in Chapter 4 will include the following:

(1) developing more sophisticated and versatile computer programs for solving the inhomogeneity problems with an arbitrary shaped particle.

(2) investigating the possibility whether the method can be extended to an elastic-plastic analysis.

(3) examining the stress field at the particle when the interface does not have perfect bonding and the real interface force law is given.

(4) extending the method to applications in two-dimensional cases.

9.3 Modelling Ductility of Composites

The prediction of the ductility of composites is another important subject apart from the study on key parameters and residual stresses in Chapter 6 and Chapter 7. It is believed that using FEA and applying the concept of unit cell, the ductility can be calculated in an average sense, if the criteria for local material failure are accurately described. In addition to this, statistical analysis is also a promising method to simulate the failure process.

9.4 Modelling Other Two-phase Composites and/or Multiphase Composites

The present study can be easily extended to that of the deformation characteristics in other two-phase composites and/or multiphase composites, such as $Al/(Al_2O_3)_p$ MMCs and aluminium composites reinforced by $(Si)_p$ and $(SiC)_p$ or $(SiC)_w$. The stress transfer

to particles, the stress distribution in composites, the overall stress strain curves, and other mechanical responses can be predicted.

REFERENCES

[1] Feest, E.A., Metal matrix composites for industrial application, Materials and Design, Vol. VII (2), pp. 58-64, 1986.

[2] Lloyd, D.J., Metal matrix composites ——— An overview, Proceeding of the International Symposium on "Advanced Structural Materials", Vol. 9, (Edited by D. S. Wilkinson), Pergamon Press, pp.1-21, 1989.

[3] Kelly, A., Metal matrix composites ——— An overview, Conference Proceedings, "Cast Reinforced Metal Composites", (Edited by S. G. Fishman, A. K. Dhingra) ASM International, pp. 1-5, 1988.

[4] Feest, E. A., Exploitation of the metal matrix composites concepts, Metals and Materials, Vol. 4, p. 273, 1988.

[5] Srivatsan, T. S. and Lavernia, E.J., Use of spray techniques to synthesize particulate-reinforced metal-matrix composites (Review), Journal of Materials Science, Vol. 27, pp. 5965-5981, 1992.

[6] Gilman, P. S., The spray deposition of metals and composites, The Journal of the Minerals, Metals & Materials Society, P.41, July 1993.

[7] Sampath, S. and Herman, H., Plasma spray forming metals, intermetallics, and composites, The Journal of the Minerals, Metals & Materials Society, pp. 42-49, July 1993.

[8] News & Updates, Materials design & manufacturing technology ——— Plasma-activated sintering densifies powder metals and ceramics in seconds, The Journal of the Minerals, Metals & Materials Society, p. 6, March 1993.

[9] Mortensen, A. and Koczak, M. J., The status of metal-matrix composite research and development in Japan, The Journal of the Minerals, Metals & Materials Society, pp. 10-18, March 1993.

[10] Varley, P.C., "The Technology of Aluminium and its Alloys", London, Newnes-Butterworths, pp.1-8, 1970.

[11] Pehlke, R.D., "Unit Processes of Extractive Metallurgy", American Elsevier Publishing Company INC., New York, London, Amsterdam, pp.195-196 and pp.208-211, 1973.

[12] Nicol, M. J., Progress in electrometallurgy research and applications, The Journal of the Minerals, Metals & Materials Society, , pp.55-58, April 1993.

[13] Brimelow, E. I., The use of aluminium alloys in building, Metallurgia, Vol. 39, pp.195-200, 1949.

[14] News & Updates, Vehicle weight-reduction goals spur use of aluminum in automobiles, The Journal of the Minerals, Metals & Materials Society, p. 5, March 1993.

[15] Petty, E. R., "Physical Metallurgy of Engineering Materials", American Elsevier Publishing Company, INC, New York, p.2, 1968.

[16] Kannikeswaran, K. and Lin, R. Y., The interaction between various Al alloys and SiC, Proceeding of the International Symposium on "Advanced Structural Materials", Vol. 9, (Edited by D. S. Wilkinson), Pergamon Press, pp. 79-86, 1989.

[17] Corbin, S., Stress-strain curve of 6061-T4 unreinforced aluminum alloys, (Alcan material sample), 1991.

[18] Lloyd, D. J. and Morris, P. L., The fracture behaviour of particulate metal matrix composites, Report, Kingston, 1991.

[19] Lloyd, D. J. and Morris, P. L., Some factors influencing the ductility and properties of particulate reinforced MMCs, "Fabrication of Particulate Reinforced Metal Composites", Proceedings of an International Conference, pp.235-244, Sept. 1990.

[20] Edelson, B. I. and Baldwin, W. M. Jr., The effect of second phases on the mechanical properties of alloys, Transactions of the ASM, Vol. 55, pp. 230-250, 1962.

[21] Gurland, J. and Plateau, J., The mechanism of ductile rupture of metals containing inclusions, Transactions of the ASM, Vol. 56, pp. 442-454, 1963.

[22] Tipper, C.F., The fracture of metals, Metallurgia, Vol.39, pp.133-138, 1949.

[23] Puttick,K.W., Ductile fracture in metals, Phil. Mag., Vol.4, p.964, 1959.

[24] Liu, D.S., Manoharan, M., and Lewandowski, J.J., Effect of supperimposed hydrostatic pressure on the fracture properties of particulate reinforced metal matrix composites, Scripta Metallurgica, Vol.23, pp.253-256, 1989.

[25] Liu, D.S., Manoharan, M, and Lewandowski, J.J., Effects of microstructure on the behaviour of an aluminium alloy and an aluminium matrix composite tested under low levels of superimposed hydrostatic pressure, Metallurgical Transactions

A, Vol.20A, pp.2409-2417, 1989.

[26] Rosenfield, A.R., Criteria for ductile fracture of two-phase alloys, Metall. Rev., Vol. 13, pp.29-40, 1968.

[27] Gurland, J. and Parikh, N.M., Microstructural aspects of the fracture of two-phase alloys, "Fracture of Metal-Matrix Particulate Composites, Modern Composite Materials", (Edited by L.J. Broutman and R.H.Krock, Addison-Wesley), pp.841-878, 1969.

[28] Chin, G.Y., Hosford, W.F.Jr., and Backofen, W.A., Ductile fracture of aluminium, Transactions of the Metallurgical Society of AIME, Vol.230, pp.437-449, 1964.

[29] Palmer, I.G., Smith, G.C., and Warda, R.D., Some aspects of ductile fracture in metals, "Physical Basis of Yield and Fracture", Conference Proceedings, Institute of Physics and Physical Society, Conference Series No.1, pp.53-59, Sept. 1966.

[30] Lindley, T.C., Oates, G. and Richards, C.E., A critical appraisal of carbide cracking mechanisms in ferrite/carbide aggregates, Acta Metallurgica, Vol.18, pp.1127-1136, 1970.

[31] Broek, D., "Elementary Engineering Fracture Mechanics", Martinus Nijhohoff Publishers, p.38-48, 1982.

[32] Berg, C.A., Plastic dilation and void interaction, "Inelastic Behaviour of Solids", (Edited by Kanniner, M.F. et al), p.171, 1969.

[33] Evans, A.G., The mechanical properties of reinforced ceramic, metal and intermetallic matrix composites, Materials Science and Engineering, A143, pp.63-76, 1991.

[34] Lloyd, D.J., Aspects of fracture in particulate reinforced metal matrix composites, Acta metall. Mater., Vol.39, No.1, pp.59-71, 1991.

[35] Rogers, H.C., Tensile fracture of ductile metals, Trans. Metallurgical Society of AIME, Vol.218, pp.498-506, 1960.

[36] Beachem, C.D., A electron fractographic study of the influence of plastic strain conditions upon ductile rupture precesses in metals, Transactions of the ASM, Vol.56, pp.318-326, 1963.

[37] McClintock, F.A., A criterion for ductile fracture by the growth of holes, J. of

Appl. Mechanics, p.363, 1968.

[38] Masuda, C. and Tanaka, Y., Tensile and fatigue properties of SiC whiskers and SiC particulate reinforced aluminium composites, "Advances in Fracture Research", Vol.4, International Conference on Fracture, ICF7, University of Houston, p.3089, 1989.

[39] Liu, C.T. and Gurland, J., Thermally induced residual stresses in silicon phase of Al-Si alloys, Trans. of the ASM, Vol.58, pp.66-73, 1965.

[40] Bridgman, P.W., "Studies in Large Plastic Flow and Fracture", Harvard University press, Cambridge, Massachusetts, pp.74-86, 1964.

[41] Bridgman, P.W., Fracture and hydrostatic pressure, "Collected Experimental Papers", Harvard University press, Cambridge, Massachusetts, Vol.7, (Paper 163) p.3856, 1964. (or "Fracturing of Metals" Cleveland: American Society for Metals, pp.246-261, 1948.)

[42] Tanaka, K., Mori, T. and Nakamura, T., Cavity formation at the interface of a spherical inclusion in a plastically deformed matrix, Phil. Mag., Vol.21, p.267, 1970.

[43] Manoharan, M., Liu, C., and Lewandowski, J.J., Microstructure and particle size effects on fracture in aluminium metal matrix composites, "Advances in Fracture Research", (Edited by Salama, K.) Vol.4, International Conference on Fracture, ICF7, University of Houston, p.2977, 1989.

[44] Argon, A. S. and Im, J., and Safoglu, R., Cavity formation from inclusions in ductile fracture, Metallurgical Transactions A, Vol.6A, p.825, 1975.

[45] Rice, J.R., and Tracey, D.M., On the ductile enlargement of voids in triaxial stress fields, J.Mech. Phys. Solids, Vol.17, p.201, 1969.

[46] Thomason, P.F., A theory for ductile fracture by internal necking of cavities, Inst. Metals, Vol.96, p.360, 1968.

[47] Brown, L.M. and Embury, J.D., The initiation and growth of voids at second phase particles, Proc. 3rd Int. Conf. on Strength of Metals and Alloys, Inst. of Metal. London, pp.164-169, 1973.

[48] Argon, A.S. and Im, J., Separation of second phase particles in spheroidized 1045 steel, Cu-0.6pct Cu alloy, and maraging steel in plastic strain, Metallurgical Transactions A, Vol.6A, P.83, 1975.

[49] Broek, D., The role of inclusions in ductile fracture and fracture toughness, Eng. Fracture Mechanics, Vol.5, pp.55-66, 1973.

[50] Goods, S.H. and Brown, L.M., The nucleation of cavities by plastic deformation, Acta metallurgica, Vol.27, pp.1-25, 1979.

[51] Van De Kasteele, J.C. and Broek, D., The failure of large second phase particles in a cracking aluminum alloy, Engineering Fracture Mechanics, Vol.9, pp.625-635, 1977.

[52] Mott,G. and Liaw,P.K., Correlation of mechanical and ultrasonic properties of Al-SiC Metal-Matrix composites, Metall. Transactions A, Vol.19A, Sept., p.2233, 1988.

[53] Hertzberg, R.W., "Deformation and Fracture mechanics of Engineering materials", John Wiley & Sons, (Third Edition), p.300, 1989.

[54] Nardone, V.C., Prewo, K.M., On the strength of discontinuous silicon carbide reinforced aluminum composites, Scripta Metallurgica, Vol.20, pp.43-48, 1986.

[55] Nutt, S.R. and Dura, J.M., A failure mechanisms in Al-SiC composites, Scripta Metallurgica, Vol.20, pp.1055-1058, 1986.

[56] Nutt, S.R., and Needleman, A., Void nucleation at fibre ends in Al-SiC composites, Scripta metallurgica, Vol.21, pp.705-710, 1987.

[57] Dignard, L.M., Malis, T.F., Boyd, J.D. and Embury, J.D., Characterization of interfaces in metal-matrix composites, Proceeding of the International Symposium on "Advanced Structural materials", (Edited by D.S.Wilkinson), Pergamon Press, pp.87-95, 1989.

[58] Iricibar, R., LeRoy, G. and Embury, J.D., Relationship of strain hardening and damage in ductile fracture, Metal Science, Aug-Sept., p.337, 1980.

[59] LeRoy, G., Embury, J.D., Edward, G. and Ashby, M.F., A model of ductile fracture based on the nucleation and growth of voids, Acta Metallurgica, Vol.29, pp.1509-1522, 1981.

[60] Brownrigg, A., Spitzig, W.A., Richmond, O., Teirlinck, D., and Embury, J.D., The influence of hydrostatic pressure on the flow stress and ductility of a spheroidized 1045 steel, Acta Metall., Vol.31, No.8, pp.1141-1150, 1983.

[61] Teirlinck, D., Ashby, M.F., and Embury, J.D., Damage accumulation during ductile rupture and the development of failure maps, "Advances in Fracture

Research", Proceeding of the 6th International conference on Fracture, New Delhi, India, (Edited by Valluri, S.T. et al), pp.105-125, 1984.

[62] Teirlinck, D., Zol, F., Embury, J.D., Ashby, M.F., Fracture mechanism maps in stress space, Acta Metall., Vol.36, No.5, pp.1213-1228, 1988.

[63] Lewandowski, J.J., and Liu, C., Effects of matrix microstructure and particle distribution on fracture of an aluminium metal matrix composite, Materials Science and Engineering, A107, pp.241-255, 1989.

[64] Lloyd, D.J., Lagace, H., McLeod, A. and Morris, P.L., Microstructural aspects of aluminium-silicon carbide particulate composites produced by a casing method, Materials Science and Engineering, A107, pp.73-80, 1989.

[65] You, C.P., Thompson, A.W. and Bernstein, I.M., Proposed failure mechanism in a discontinuously reinforced aluminium alloy, Scripta Metallurgica, Vol.21, pp.181-185, 1987.

[66] Liu, C. and Lewandowski, J.J., Microstructural effects on fracture microstructure in lightweight metal matrix composites, Proceeding of the International Symposium on "Advanced Structural materials", (Edited by D.S.Wilkinson), Pergamon Press, pp.23-31, 1989.

[67] Davidson, D.L., The growth of fatigue cracks through particulate SiC reinforced aluminium alloys, "Advances in Fracture Research", (Edited by Salama, K.), Vol.4, International Conference on Fracture, ICF7, University of Houston, p.3021, 1989.

[68] Lloyd, D.J. and Chamberlain, B., Properties of shape cast Al-SiC metal matrix composites, "Cast Reinforced Metal Composites", Conference Proceeding, ASM International, pp.263-269, 1988.

[69] Skibo, M., Morris, P.L., Lloyd, D.J., Structure and properties of liquid metal processed SiC reinforced aluminum, "Cast Reinforced Metal Composites", Conference Proceeding, ASM International, p.257, 1988.

[70] Tuler, F.R., Beals, J.T., Demetry, C., Zhao, D., and Lloyd, D.J., Deformation mechanism mapping of SiC/Al metal matrix composite materials, "Cast Reinforced Metal Composites", Conference Proceeding, ASM International, p.321, 1988.

[71] Mochida, T., Taya, M. and Lloyd, D.J., Fracture of particles in a particle/metal composites under plastic straining and its effect on the Young's Modulus of the composite, Materials Transactions, JIM, Vol.32, No.10, pp.931-942, 1991.

[72] Zhao, D., Tuler, F.R., Lloyd, D.J., Processing stability and microstructure evolution of SiC particle-reinforced aluminium 6061 alloys during high temperature deformation, Scripta Metallurgica, Vol.27, pp.41-44, 1992.

[73] Nardone, V.C., Assessment of models used to predict the strength of discontinuous silicon carbide reinforced aluminum alloys, Scripta Metallurgica, Vol.21, pp.1313-1318, 1987.

[74] Lloyd, D.J., Factors influencing the properties of particulate reinforced composites produced by molten metal mixing, "Metal Matrix Composites ——— processing, Microstructure and Properties", Proceedings of the 12th Risφ International Symposium on Materials Science, (Edited by N. Hansen, et al) p.81, 1991.

[75] Flom,Y. and Arsenault,F.J., Effect of particle size on fracture toughness of SiC/Al, Composite Material, Acta Metall., Vol.37, No.9, pp.2413-2423, 1989.

[76] Kamat,S.V., Hirth,J.P. and Mchrabian,R., Mechanical properties of particulate reinforced aluminum matrix composites, Acta Metall., Vol.37, No.9, pp.2395-2402, 1989.

[77] Shang,J.K. and Ritchie,R.O., On the particle-size dependence of fatigue-crack propagation thresholds in SiC-particulate-reinforced aluminum-alloy composites: Role of crack closure and crack trapping, Acta Metall., Vol.37, No.8, pp.2267-2278, 1989.

[78] Barlow,C.Y. and Hansen,N., Deformation structures in aluminium containing small particles, Acta Metall., Vol.37, No.5, pp.1313-1320, 1989.

[79] Kim,C.T., Lee,J.K. and Plichta,M.R., Plastic relaxation of thermoelastic stress in aluminum/ceramic composites, Metallurgical Transactions A, Vol. 21A, March p.673, 1990.

[80] Taya,M., Lulay,K.E. and Lloyd,D.J., Strengthening of a particulate metal matrix composite by quenching, Acta Metall. Mater., Vol.39, No.1, pp.73-87, 1991

[81] Corbin,S.F. and Wilkinson,D.S., The onset of yielding in a SiC reinforced Al alloy, Proceedings of the 12th Risφ International Symposium on Materials Science, p.283, 1991.

[82] Embury,J.D., Newell,J. and Tao,S., Damage accumulation in an Al-SiC composite, Proceedings of the 12th Risφ International Symposium on Materials Science, p.317, 1991.

[83] Healy, J.C. and Beevers, C.J., A study of fatigue crack growth in a particulate-reinforced Al-Si alloy at 23 and 220 C, Materials Science and Engineering, Vol.A142, pp.183-192, 1991.

[84] Dutta, I., Allen, S.M. and Hafley, J.L., "Effect of reinforcement on the aging response case 6061 Al-Al_2O_3 Particulate Composites", Metallurgical Transactions A, Vol.22A, p.2553, 1991.

[85] Bayha, T.D. and Wawner, F.E., Reaction kinetics of an Al-Co intermetallic in Al-9Ti/SiC particle-reinforced composites, Metallurgical Transactions A, Vol. 23A, pp.1607-1608, 1992.

[86] Allen, A.J., Bourke, M.A., Dawes, S. and M.T.Hutchings, The analysis of internal strains measured by neutron diffraction in Al/SiC metal matrix composites, Acta Metall. Mater., Vol.40, No. 9, pp.2361-2373, 1992.

[87] McLeod,A.D. and Gabryel,C.M., Kinetics of the Growth of spinel, $MgAl_2O_4$, on alumina particulate in aluminum alloys containing magnesium, Metallurgical Transactions A, Vol. 23A, p.1279, 1992.

[88] Pandey,A.B., Mishra,R.S., and Mahajan,Y.R., Steady state creep behaviour of silicon carbide particulate reinforced aluminium composites, Acta Metall. Mater. Vol.40. No. 8, pp.2045-2052, 1992.

[89] Povirk,G.L.,Stout,M.G.,Bourke,M., Goldstone,J.A., Lawson,A.C., Lovato,M., Macewen,S.R., Nutt,S.R. and Needleman,A., Thermally and mechanically induced residual strains in Al-SiC Composites, Acta Metall. Mater. Vol.40, No. 9, pp.2391-2412, 1992.

[90] Sehitoglu,H. and Karayaka,M., Prediction of thermomechanical fatigue lives in metal matrix composites, Metallurgical Transactions A, Vol. 23A, p. 2029, 1992.

[91] Wang,N., Wang,Z. and Weatherly,G.C., Formation of magnesium aluminate (spinel) in cast SiC particulate-reinforced Al(A356) metal matrix composites, Metallurgical Transactions A, Vol. 23A, p.1423, 1992.

[92] Shannon,R.E., Liaw,P.K. and Harrigan,W.C., Jr., Nondestructive Evaluation for large-scale metal-matrix composite billet processing, Metallurgical Transactions A, Vol.23A, p.1541, 1992.

[93] Liu,Y.L., Jensen,D.J. and Hansen,N., Recovery and recrystallization in cold-rolled Al-SiCw composites, Metallurgical Transactions A, Vol.23A, p.807, 1992.

[94] Bao, G., Hutchinson, J.W. and McMeeking, R.M., Particle reinforcement of

ductile matrices against plastic flow and creep, Acta Metall., Vol. 39, No.8, pp.1871-1882, 1991.

[95] Vasudevan, A.K., Richmend, O., Zok, F. and Embury, J.D., The influence of hydrostatic pressure on the ductility of Al-SiC composites, Materials Science and Engineering, A107, pp.63-69, 1989.

[96] Eshelby, J.D., The elastic field outside and ellipsoidal inclusion, Proc. Roy. Soc., A252, p.561, 1959.

[97] Ashby, M.F., Work Hardening of Dispersion-hardened Crystals Phil. Mag., Vol. 14, p.1157, 1966.

[98] Ashby, M.F., Gelles, S.H. and Tanner, L.E., "The stress at which dislocations are generated at a particle-Matrix interface", Phil. Mag. Vol.19, p.757, 1969.

[99] Stobbs, W.M., Watt, D.F. and Brown, L.M., The fatigue hardening and softening of copper containing Silica particle, Phil. Mag., Vol.23, p.1169, 1971.

[100] Brown, L.M. and Stobbs, W.M., The work-hardening of copper-silica I. A model based on internal stresses, with no plastic relaxation, Phil. Mag., Vol.23, p.1185, 1971.

[101] Brown, L.M. and Stobbs, W.M., The work-hardening of copper-silica II. The role of plastic relaxation, Phil. Mag., Vol.23. p.1202, 1971.

[102] Stobbs, W.M., The work-hardening of copper-silica III. Diffusional stress relaxation, Phil. Mag., Vol.27, p.1073, 1973

[103] Brown, L.M., "Back stresses, image stresses, and work hardening", Acta Metallurgica, Vol.21, p.879, July, 1973.

[104] Atkinson, J.D., Brown, L.M. and Stobbs, W. M., The work-hardening of copper-silica IV. The Bauschinger effect and plastic relaxation, Phil. Mag., Vol. 30, p.1247, 1974.

[105] Morimoto, T. and Taya M., Thermal cycling damage of high temperature metal matrix composites, "Advances in Fracture Research", (Edited by Salama, K.), Vol.4, International Conference on Fracture, ICF7, University of Houston, p.2987, 1989.

[106] Brown, L.M. and Clarke, D.R., Work hardening due to internal stresses in composite materials, Acta Metallurgica, Vol.23, p.821, 1975.

[107] Brown, L.M. and Stobbs, W.M., The work-hardening of copper-silica V. Equilibrium plastic relaxation by secondary dislocations, Phil. Mag., Vol.34, No.3, pp.351-372, 1976.

[108] Brown, L.M., "Orowan's explanation of the Bauschinger effect", Scripta Metallurgica, Vol.11, pp.127-131, 1977

[109] You, C.P. and Allison, J.E., Fatigue crack growth and closure in a SiC_p - reinforced aluminum composites, "Advances in Fracture Research", (Edited by Salama, K.), Vol.4, International Conference on Fracture, ICF7, University of Houston, p.3005, 1989.

[110] Chapman, P.F. and Stobbs, W.M., The measurement of local rotation in the electron microscope, Phil. Mag., Vol.19, pp.1015-1030, 1969.

[111] Fisher, J.C., Hart, E.W. and Pry, R.H., The hardening of metal crystals by precipitates, Acta Metallurgica, Vol.1, pp.336-339, 1953.

[112] Ashby, M.F., The deformation of plastically non-homogeneous materials, Phil. Mag., Vol.21, pp.399-424, 1970.

[113] Gensamer, M., Strength and ductility, Transactions of the ASM, Vol.36, p.30, 1946.

[114] Argon, A.S., "Physics of Strength and Plasticity", The M.I.T. Press, 1969.

[115] Robinson, K., Elastic energy of an ellipsoidal inclusion in an infinite solid, J. of Applied Physics, Vol.22, No.8, p.1045, 1951.

[116] Eshelby,J.D., "The determination of the elastic field of an ellipsoidal inclusion, and related problems", Proc.Roy.Soc., A241, 376, 1957.

[117] Sternberg, E., Three-dimensional stress concentrations in the theory of elasticity, Applied Mechanics Reviews, Vol.11, No.1, p.1, Jan.1958.

[118] Eshelby, J.D., "Elastic inclusions and inhomogeneities", Progress in Solid Mechanics, Vol.2, p.88, 1961.

[119] Chiu, Y.P., On the stress field due to initial strains in cuboid surrounded by an infinite elastic space, J.Appl.Mech., pp.587-590, 1977.

[120] Mura,T. and Cheng, P.C., The elastic field outside an ellipsoidal inclusion, J.Appl.Mech., p.591, 1977.

[121] Mura, T., Inclusion problems, Appl Mech. Rev. Vol.41, No.1, Jan. 1988, p.15

[122] Fan,H., Keer,L.M. and Mura,T., Inhomogeneity problem revisited via the modulus perturbation approach, J. Solids structures, Vol. 29, No.20, pp.2583-2594, 1992

[123] Hashin, Z., The spherical inclusion with imperfect interface, Transactions of the ASME, Vol.58, pp.444-449, 1991.

[124] Kwon, D., Interfacial decohesion around spherical carbide particles, Scripta Metallurgica, Vol.22, pp.1161-1164, 1988.

[125] Mura, T., "Micromechanics of defects in solids", Nartinus Nijhoff Publishers, 1982.

[126] Mura, T., Jasiuk, I. and Tsuchida, B., The stress field of a sliding inclusion, Int. J. Solids Structures, Vol.21, No.12, pp.1165-1179, 1985.

[127] Withers,P.T., Stobbs, W.M. and Pedersen, O.B., The application of the Eshelby method of internal stress determination to short fibre metal matrix composites, Acta Metall., Vol.37, No.11, pp.3061-3084, 1989

[128] Isida,M. and Igawa,H., Analysis of a zig-zag array of circular inclusions in a solid under uniaxial tension, Int. J.Solids Structures, Vol.27, No.12, pp.1515-1535, 1991.

[129] Ritter, A.M., Jackson, M.R. and Wright, R.N., Fracture of steel/carbide particulate composites, "Advances in Fracture Research",, (Edited by Salama, K.), Vol.4, International Conference in Fracture, ICF7, University of Houston, p.2997, 1989.

[130] Bao,G., Hutchinson,J.W. and McMeeking, J.R., The flow stress of dual-phase, non-hardening solids, MECH-163, September 1990

[131] Levy,A.J., The debonding of elastic inclusions and inhomogeneities, J.Mech.Phys.Solids, Vol.39, No.4, pp.477-505, 1991.

[132] Needleman, A., A numerical study of necking in circular cylindrical bars, J.Mech.Phys. Solids, Vol.20, pp.111-127, 1972.

[133] Karlsson, B. and Sundstrom, B.O., Inhomogeneity in plastic deformation of two-phase steels, Materials Science and Engineering, Vol.16. p.161, 1974.

[134] Jinoch,J., Calculations of stress-strain curve and stress and strain distributions for

an alpha-beta Ti-8Mn alloy, Materials Science and Engineering, Vol.34, pp.203-211, 1978.

[135] Ankem, S. and Margolin, H., Finite element method calculations of stress-strain behaviour of alpha-beta Ti-Mn alloys: Part I. Stress-strain relations, Metallurgical Transactions A Vol.13A. p.595, 1982

[136] Ankem, S. and Margolin, H., Finite element method calculations of stress-strain behaviour of alpha-beta Ti-Mn alloys: Pat II. Stress and strain distributions, Metallurgical Transactions A, Vol.13A, p.603, 1982

[137] Thomson, R.D. and Hancock, J.W., Local stress and strain fields near a spherical elastic inclusion in a plastically deforming matrix, Int. J. Fract. Vol. 24, pp.209-228, 1984.

[138] Ankem, S. and Margolin, H., A rationalization of stress-strain behaviour of two-ductile phase alloys, Metallurgical transactions A, Vol.17A, p.2209, 1986.

[139] Flower, E.C. and Watt, D.F., Three dimensional finite element modelling of plasticity in a two-phase ductile material, University of Windsor Internal Report, Nov.14, 1988.

[140] Flower, E.C. "Modelling plasticity in a two-phase ductile material", Energy and Technology Review, Lawrence Livermore National Laboratory, pp.1-5, Sept. 1988

[141] Christman, T., Needleman,A., and Suresh, S., An experimental and numerical study of deformation in metal-ceramic composites, Acta Metall., Vol.37, No.11, pp.3029-3050, 1989.

[142] Christman, T., Needleman, C.A., Nutt,S. and Suresh,S., On microstructural evolution and micromechanical modelling of deformation of a whisker-reinforced metal-matrix composite, Materials Science and Engineering, Vol. A107, pp.49-61, 1989.

[143] Levy,A. and Papazian,J.M., Tensile properties of short fibre-reinforced SiC/Al composites: Part II. Finite-element analysis, Metallurgical Transactions A, Vol.21A, p.411, 1990

[144] Tvergaard,V., Analysis of tensile properties for a whisker-reinforced metal-matrix composite, Acta Metall. Mater. Vol. 38. No. 2, pp.185-194, 1990

[145] Flower,E.C. and Watt,D.F, Modelling plasticity in a two-phase ductile material, Cray Channels, pp.12-14, Spring 1990.

[146] Llorca,J., Needleman,A. and Suresh,S., An analysis of the effects of matrix void growth on deformation and ductility in metal-ceramic composites, Acta Metall. Mater., Vol.39, No.10, pp.2317-2335, 1991

[147] Levy,A. and Papazian,J.M., Elastoplastic finite element analysis of short-fibre-reinforced SiC/Al composites: Effects of thermal treatment, Acta Metall. Mater., Vol.39, No.10, pp.2255-2266, 1991.

[148] Hom,C.L., Three-dimensional finite element analysis of plastic deformation in a whisker-reinforced metal matrix composite, J. Mech. Phys. Solids, Vol.40, No.5, pp.991-1008, 1992

[149] Wang,Z., Chen,T.K. and Lloyd,D.J., Stress Distribution in particulate reinforced metal matrix composites subjected to external load, Metall. Trans., 24A, pp.197-207, 1993.

[150] Chapra, S.C. and Canale, R.P., "Numerical Methods for Engineers" (Second Edition), McGraw-Hill Book Company, p.248, 1988.

[151] Leitch,B.W. and Puls,M.P., Finite element calculations of the accommodation energy of a misfitting precipitate in an elastic-plastic matrix, Metall. Transactions A, Vol.23A, p.797, March 1992.

[152] Shi,N., Wilner,B. and Arsenault,R.J., An FEM study of the plastic deformation process of whisker reinforced SiC/Al composites, Acta Metall. Mater., Vol.40, No.11, pp.2841-2854, 1992.

[153] Brockenbrough,J.R., Hunt,W.H., Jr. and Richmond,O., A reinforced material model using actual microstructural geometry, Scripta Metallurgica, Vol.27, pp.385-390, 1992.

[154] Llorca,J., Suresh,S. and Needleman,A., An experimental and numerical study of cyclic deformation in metal-matrix composites, Metall. Transaction A, Vol.23, p.919, March 1992.

[155] Bathe, K.J., "Finite Element Procedures in Engineering Analysis", Prentice-Hall, Inc., Englewood Cliffs, New Jersey, 1982.

[156] Hsu, T.R., "The Finite Element Method in Thermomechanics", Allen & Unwin, 1990.

[157] Reddy, J.N., "An Introduction to the Finite Element Method", McGraw-Hill Book Company, 1984.

[158] Zienkiewicy, O.C. "The Finite Element Method", McGraw-Hill Book Company (UK) Limited, 1977.

[159] Prager, W., Introduction to Mechanics of Continua, Dover, Publications Inc., New York, N.Y., 1973.

[160] McMeeking, R.M. and Rice, J.R., Finite-element formulations for problems of large elastic plastic deformation, Int.J. Solids Structure, Vol.6, pp.1069-1086, 1970.

[161] Lachat, J.C. and Watson, J.O., Effective numerical treatment of boundary integral equations: A formulation for three-dimensional elastostatics, Int. J. Num. Meth. in Engineering, Vol.10, pp.991-1005, 1976.

[162] Cruse, T.A., "Boundary Element Analysis in Computational Fracture Mechanics", Kluwer Academic Publishers, 1988,

[163] Dieter, G.E., "Mechanical Metallurgy", (Second Edition) McGraw-Hill Series in Materials Science and Engineering, 1976.

[164] Love, A.E.H., "A Treatise on the Mathematical Theory of Elasticity", Fourth Edition, Cambridge At The University Press, 1952.

[165] Goodier, J.N., On the integration of the thermo-elastic equations, Phil. Mag., Ser. 7, p.1017, 1937.

[166] Bhargava, R.D., The inclusion problem, Appl. Sic. Res., Section A, Vol.11, p.80, 1961.

[167] Walpole, L.J., The analysis of the overall elastic properties of composite materials, "Fundamentals of Deformation and Fracture", (Edited by Bilby, B.A.et al) p.91, 1985.

[168] Hill, R., A self-consistent mechanics of composite materials, J. Mech. Phys. Solids, Vol. 13, pp.213-222, 1965.

[169] Mura, T. and Furuhashi, R., The elastic inclusion with a sliding interface, J. Appl. Mech., Vol.51, p.308, 1984.

[170] Povirk, G.L., Stout, M.F., Bourke, M., Goldstone, J.A., Lawson, A.C., Lovato, M., MacEwen, S.R., Nutt, S.R. and Needleman, A., Mechanically induced Residual stresses in Al/SiC composites, Scripta Metallurgica, Vol.25, pp.1883-1888, 1991.

[171] Taya, M. and Arsenault, R.J., "Metal Matrix Composites——Thermomechanical Behaviour", Pergamon Press, 1989.

[172] Lewandowski, J.J., Liu, D.S. and Liu, C., Observations on the effects of particulate size and superposed pressure on deformation of metal matrix composites, Scripta Metallurgica, Vol. 25, pp. 21-26, 1991.

[173] Kamat, S.V., Rollett, A.D. and Hirth, J.P., Plastic deformation in Al-alloy matrix-alumina particulate composites, Scripta Metallurgica, Vol.25, pp.27-32, 1991.

[174] Miller, W.S. and Humphreys, F.J., Strengthening mechanisms in particulate metal matrix composites, Scripta Metallurgica, Vol.25, pp.33-38, 1991.

[175] Vogelsang, M., Arsenault, R.J. and Fisher, R.M., An in situ HVEM study of dislocation generation at Al/SiC interfaces in metal matrix composites, Metall. Trans., A, Vol.17A, p.379, 1986.

[176] Povirk, G.L., Needleman, A. and Nutt, S.R., An analysis of the effect of residual stresses on deformation and damage mechanisms in Al-SiC composites, Mater. Sci. Eng., A132, pp. 31-38, 1991.

[177] Povirk, G.L., Needleman, A. and Nutt, S.R., An analysis of residual stress formation in whisker-reinforced Al-SiC composites, Mater. Sci. Eng., A125, pp.129-140, 1990.

[178] Arsenault, R.J. and Fisher, R.M., Microstructure of fibre and particulate SiC in 6061 Al composites, Scripta Metallurgica, Vol. 17, pp.67-71, 1983.

[179] Arsenault, R.J. and Taya, M., Thermal residual stress in metal matrix composite, Acta Metall., Vol.35, No.3, pp.651-659, 1987.

[180] Rack, H.J. and Krenzer, R.W., Thermomechanical treatment of high purity 6061 aluminum, Metall. Trans. A, Vol.8A, p.335, 1977.

[181] Hsu, T.R., "The Finite Element Method in Thermomechanics", Allen & Unwin, 1990.

[182] Hibbitt, Karlsson & Sorensen, Inc., "ABAQUS User's Manual & Theory Manual".

[183] Jain, M., "Structure-Property Relationships in Dual Phase Steels", M.A.Sc. Thesis, University of Windsor, 1984.

[184] Abduluyahed, A.A.O., "Tensile Stress-Strain Analysis of Multiphase Alloys", M.A.Sc. Thesis, University of Windsor, 1986.

LIST OF PUBLICATIONS/PRESENTATIONS

Resulting from this work

1. X.Q.Xu and D.F.Watt, Basic role of a hard particle in a metal matrix subjected to tensile loading, Submitted to Acta Metallurgica Et Materiallia in Nov. 1993, and accepted in March, 1994.

2. X.Q.Xu, D.F.Watt and N.Zamani, A new approach to find the stress distribution for an arbitrary shape of inhomogeneity, Submitted to Acta Metallurgia Et Materiallia, Nov. 1993.

3. D.F.Watt, X.Q.Xu and N.Zamani, Effects of particle morphology and spacing on the strain fields in a plastically deforming matrix, International Seminar on Micromechanics of Materials, Paris, July 1993.

4. X.Q.Xu and D.F.Watt, Interaction between hard particles and the surrounding matrix, 5th Canadian Materials Science Conference, Royal Military College of Canada, Kingston, Ontario, June 1993.

5. D.F.Watt and X.Q.Xu, Design of particles to extend the ductility limit of MMC's, University-Industry Consortium on Metal Matrix Composites, Workshop, Kingston, June 1993.

6. D.F.Watt, J.R.Dryden, J.Barfuss and X.Q.Xu, Elastic plastic strain fields around hard second-phase particles, University-Industry Consortium on Metal Matrix Composites, Workshop #4, "Internal Stress In MMC's", University of Alberta, Edmonton, Alberta, Aug. 1992.

7. X.Q.Xu, D.F.Watt and N.Zamani, Stress fields around clustered particles in a plastically deformed matrix, 4th Canadian Materials Science Conference, Royal Military College of Canada, Kingston, Ontario, June 1992.

8. D.F.Watt and X.Q.Xu, Computer modelling of Particle-matrix interactions in SiC reinforced aluminum metal matrix composites, 121st TMS Annual Meeting & Exhibition, San Diego, March 1992.

VITA AUCTORIS

The author was born in 1960 in Xi'an, P.R.China. She graduated from Nanking University where she obtained a B.Sc. in Physics in 1982. From there she went to Tongji University in Shanghai, P.R.China where she obtained an M.Sc. in Physics in 1984, specializing in Acoustics. Then, she had served as a lecturer in the same university for 5 years before she came to Canada in 1989. She is currently a candidate for the Ph.D in Engineering Materials at the University of Windsor and hopes to graduate in June 1994.

VOLUME II

LIST OF FIGURES

LIST OF TABLES

FIGURES

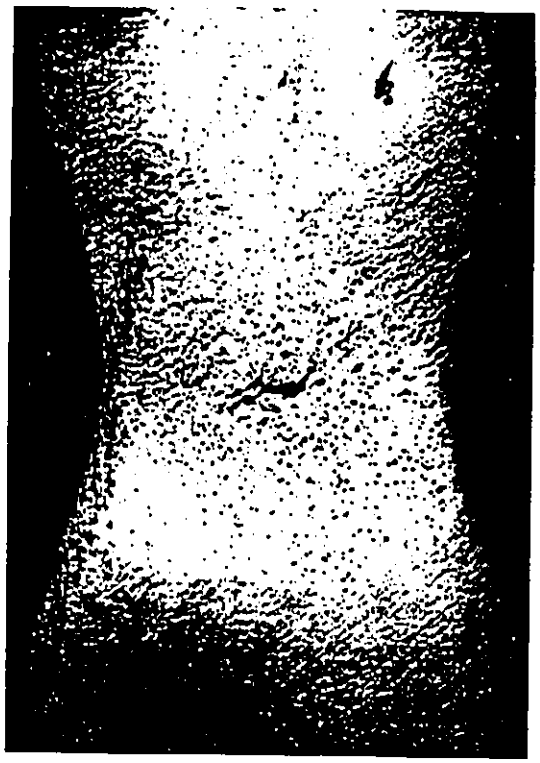

(a)

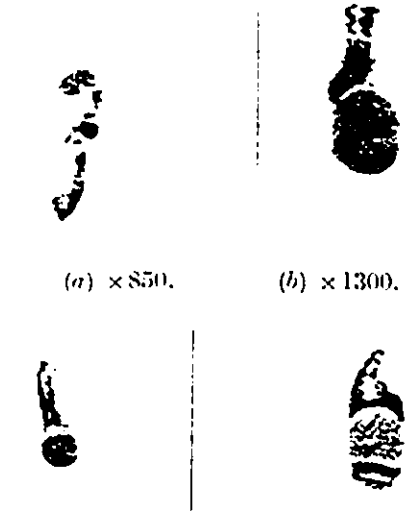

(b)

(c)

Figure 2.1 Necking of tensile specimen (after Puttick). (a) Section through neck; (b) Cavities forming at inclusions; (c) Cavities coalescing in central region of (a).

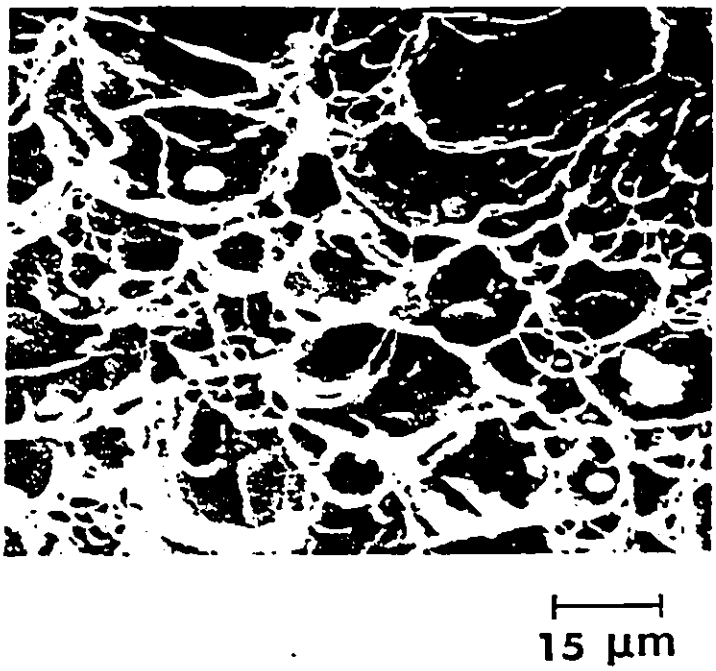

Figure 2.2 Ductile fracture surface of spheroidized steel with carbides present within the dimples (after Eiselstein).

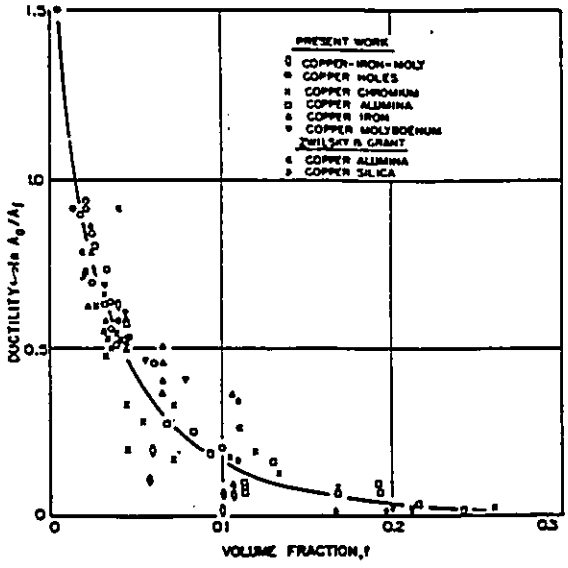

Figure 2.3 Ductility of several copper dispersion alloys vs volume fraction (after Edelson & Baldwin).

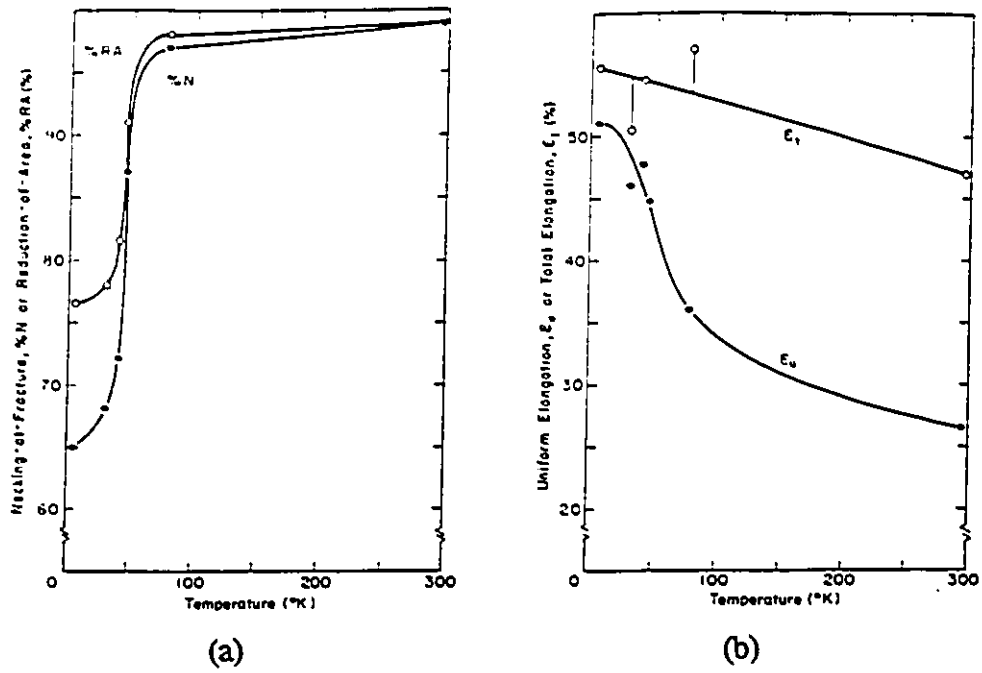

Figure 2.4 (a) Variation with temperature of percent necking-at-fracture and percent reduction-of-area; (b) Variation with temperature of uniform elongation and of total elongation. Both (a) and (b) are for the same fine-grained aluminium material (after Chin, Hosford & Backofen).

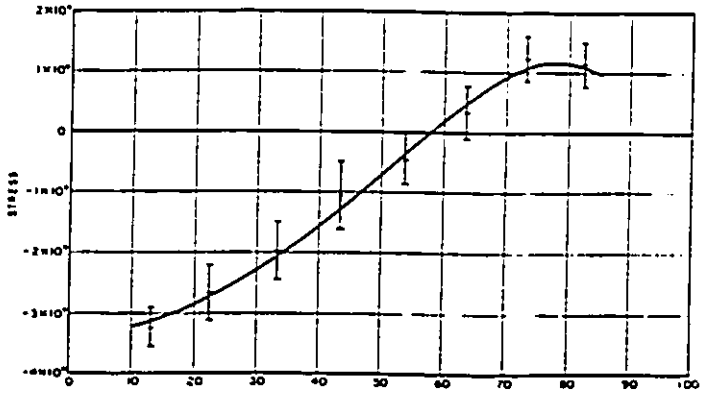

Figure 2.5 Residual stress in the Si phase of the Al-Si alloys (after Liu & Gurland).

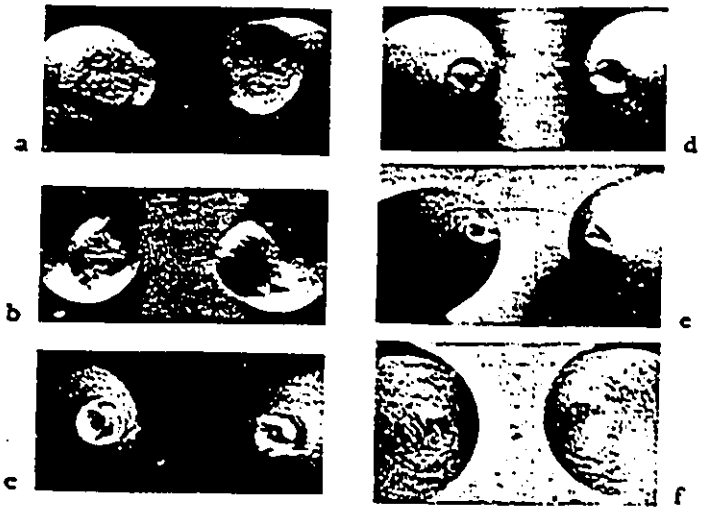

Figure 2.6 The progressive change in the character of the fracture for increasing hydrostatic pressures. (a) Broken at atmospheric pressure; (b) Broken under 34,000 psi; (c) Broken under 145,000 psi; (d) Broken under 186,000 psi; (e) Broken under 268,000 psi; (f) Broken under 387,000 psi.

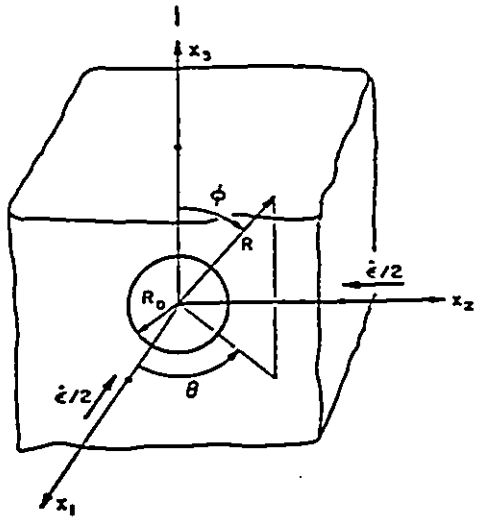

Figure 2.7 Spherical void in a remote simple tensile strain rate field.

Figure 2.8 Slip involving non-primary dislocations at large SiO_2 particle in a copper crystal, after a shear strain of 4% (after Stobbs and Brown).

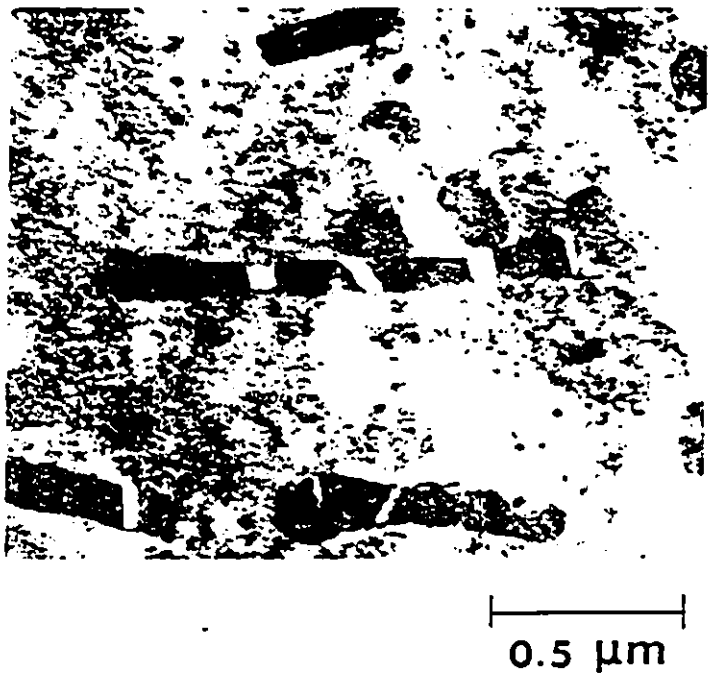

Figure 2.9 Multiple internal fracture of a particle with a large aspect ratio in an aluminium based alloy (after Broek).

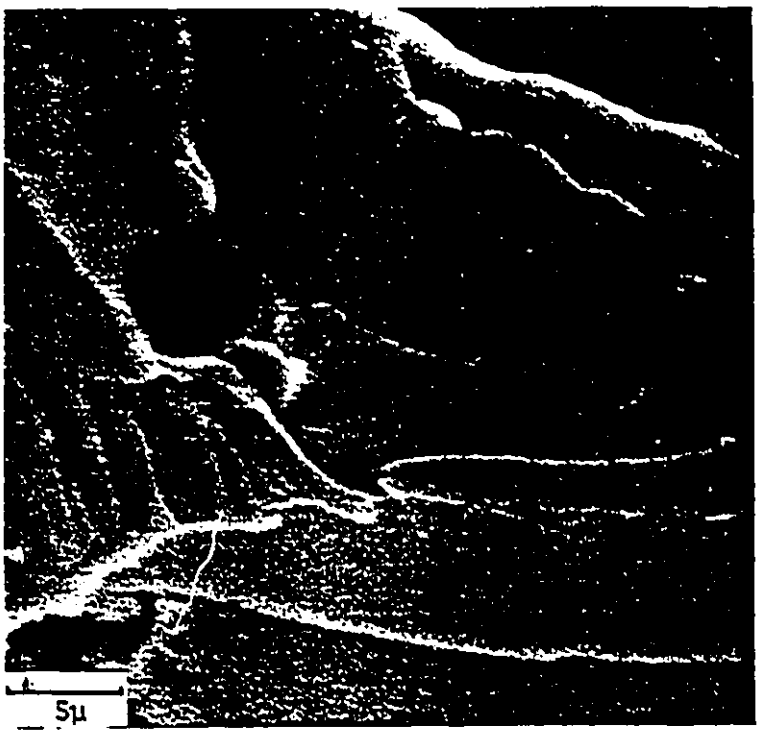

Figure 2.10 The elongated voids caused by a 50% strain to a iron sample in the direction of the tensile axis at room temperature (after Tanaka).

Figure 2.11 Multiple fracture modes in the Al/$(SiC)_p$ (after Lewandowski et al).

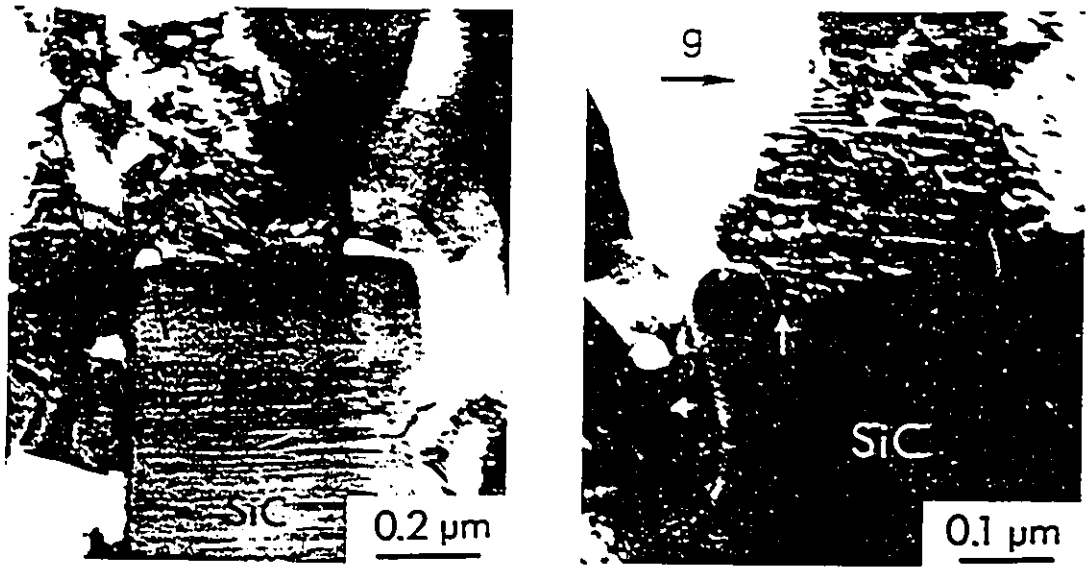

(a)

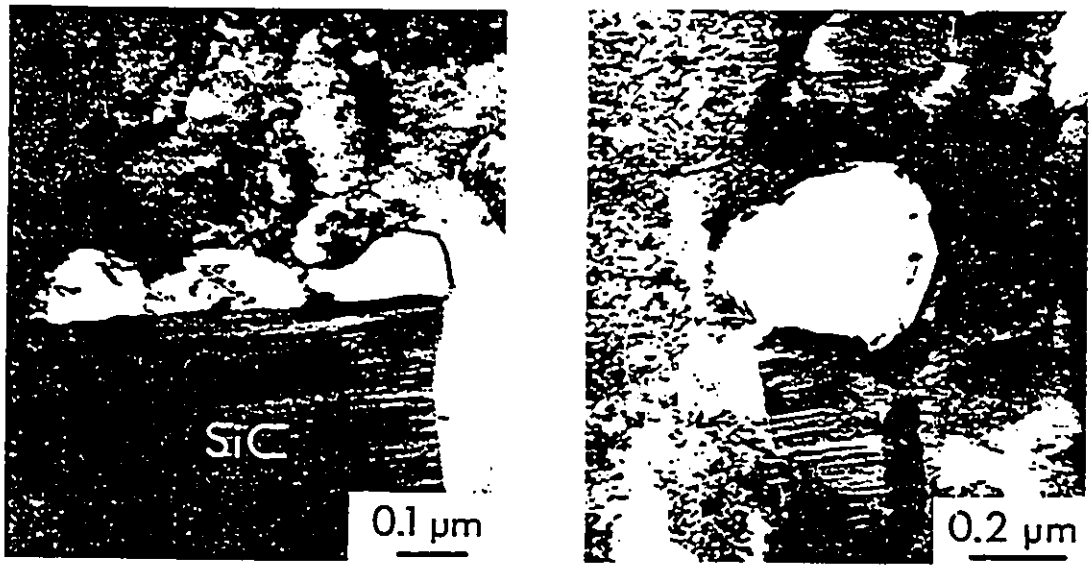

(b)

Figure 2.12 Void initiation and growth in tensile fracture specimen of 6061 Al-SiC composite. (a) void initiation at whisker end; (b) Void growth (after Nutt & Dura).

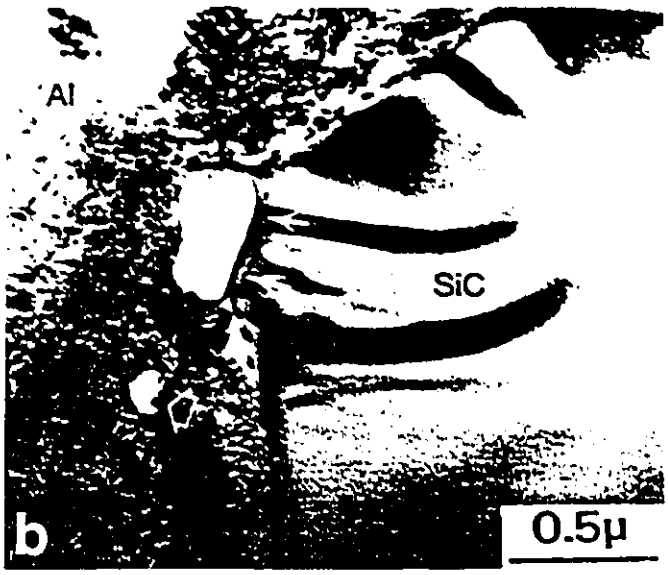

Figure 2.13 Void nucleation observed at and near interfaces in overaged specimen (after Lewandowski).

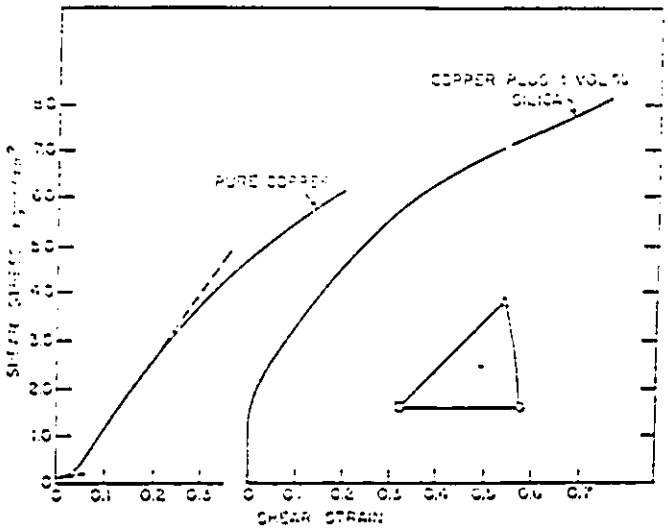

Figure 2.14 The shear stress/shear strain curves of a pure copper single crystal and a second crystal, identical with the first except for the inclusion of 1 volume % of SiO_2 particles whose mean diameter was 900Å (after Ashby).

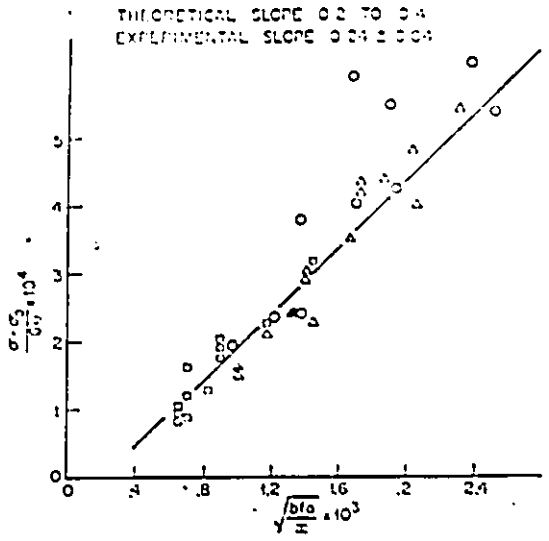

Figure 2.15 The increment of flow stress due to work hardening (after Ashby).

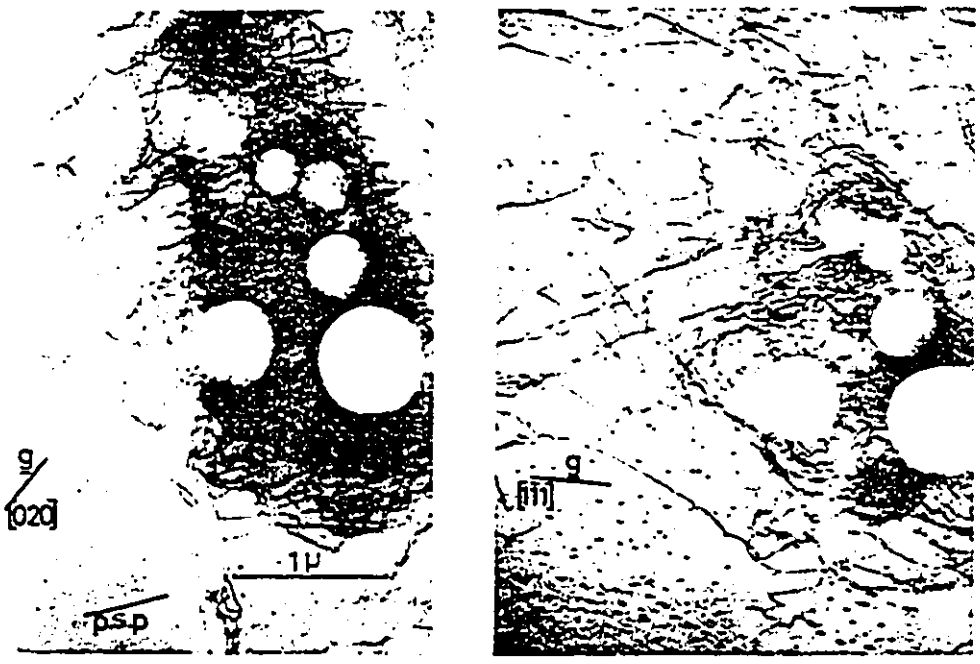

Figure 2.16 The dislocation structure around a cluster of particles (after Brown and Stobbs).

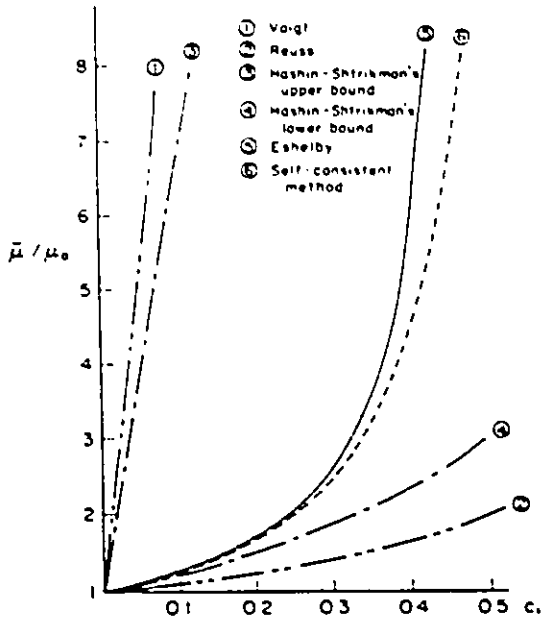

(a)

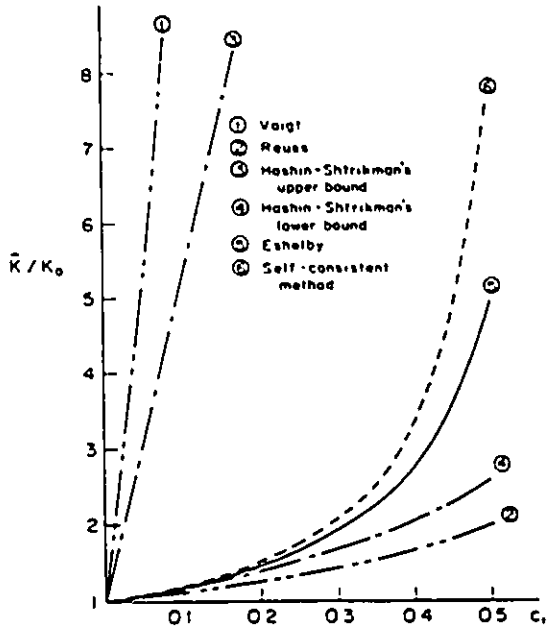

(b)

Figure 2.17 (a) The effective shear modulus versus the volume fraction of spherical inhomogeneities, $\mu^*/\mu = 100$; (b) The effective modulus versus the volume fraction of spherical inhomogeneities, $k^*/k = 100$ (after Mura).

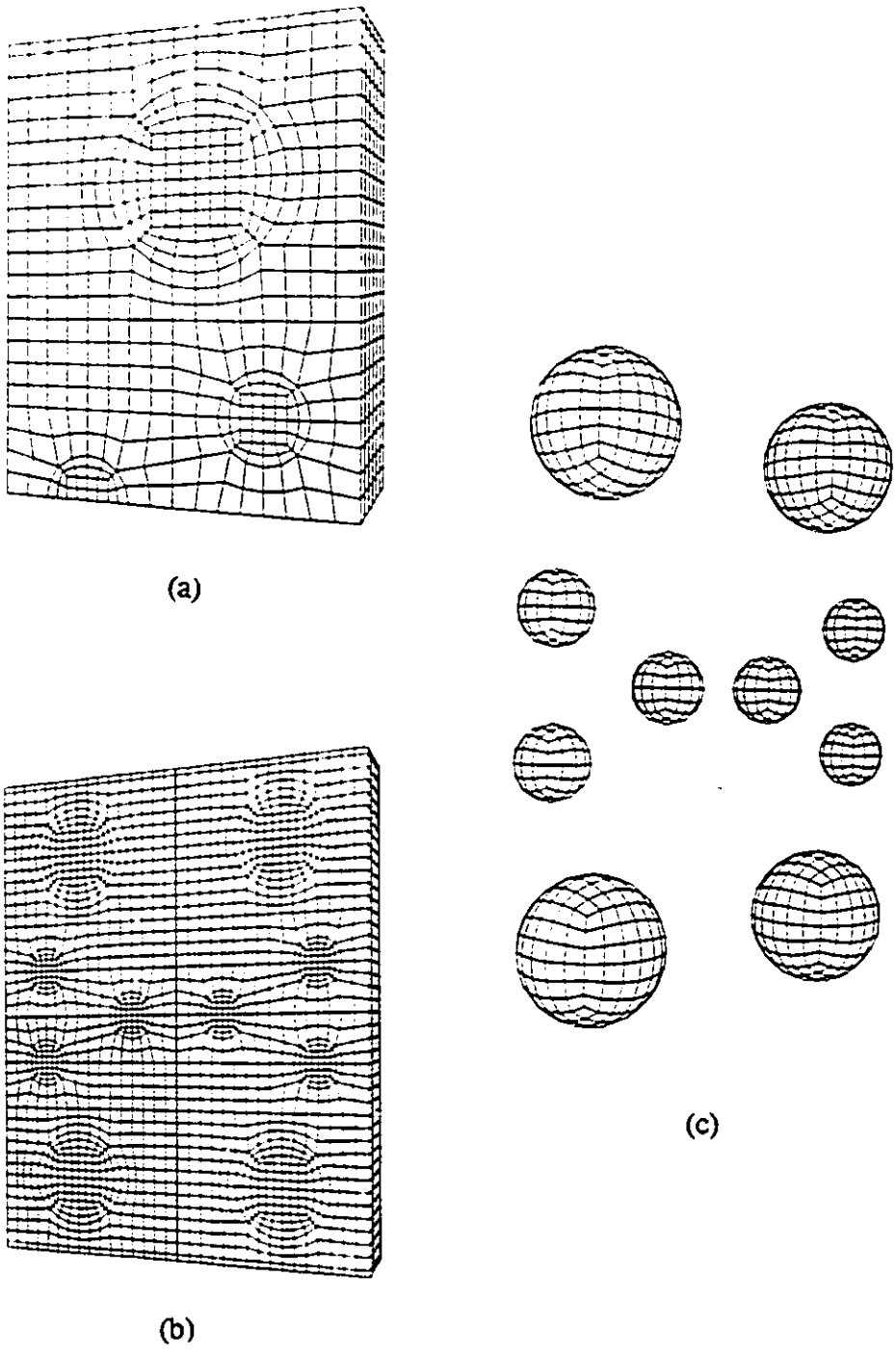

Figure 2.18 The unit cell model (after Flower & Watt). (a) Unit cell; (b) Reflected cells; (c) The array of spherical hard particles.

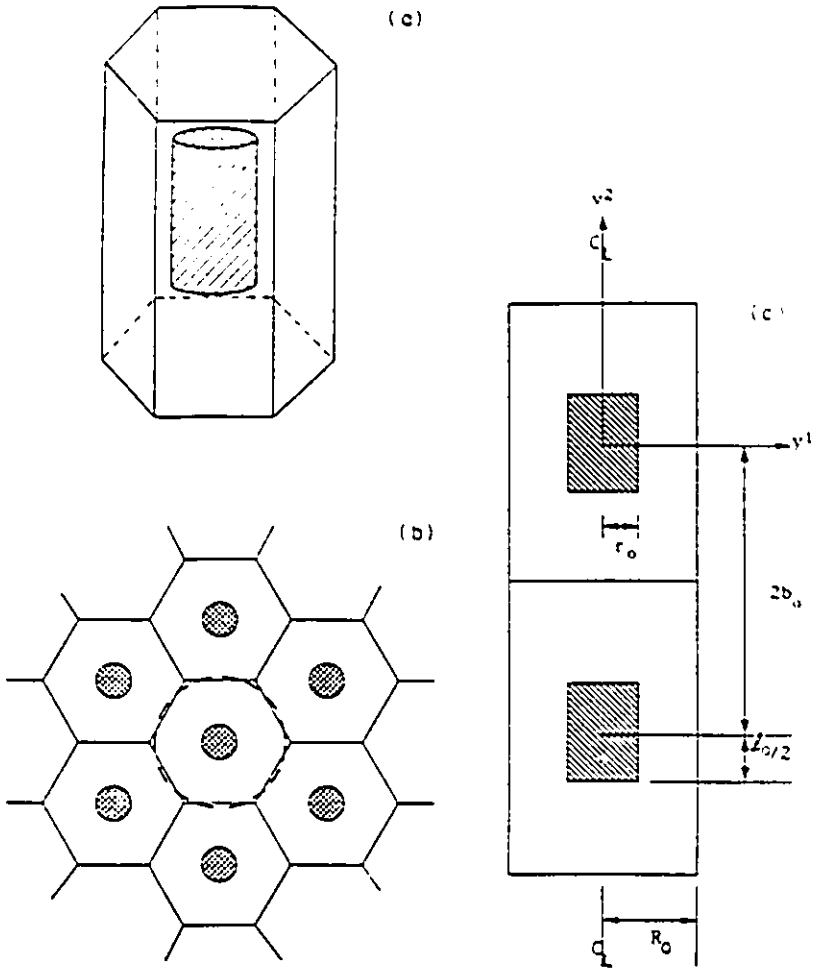

Figure 2.19 (a) A perspective of a single unit cell; (b) A projection in the loading direction; (c) A plane parallel to the loading axis (after Christman et al).

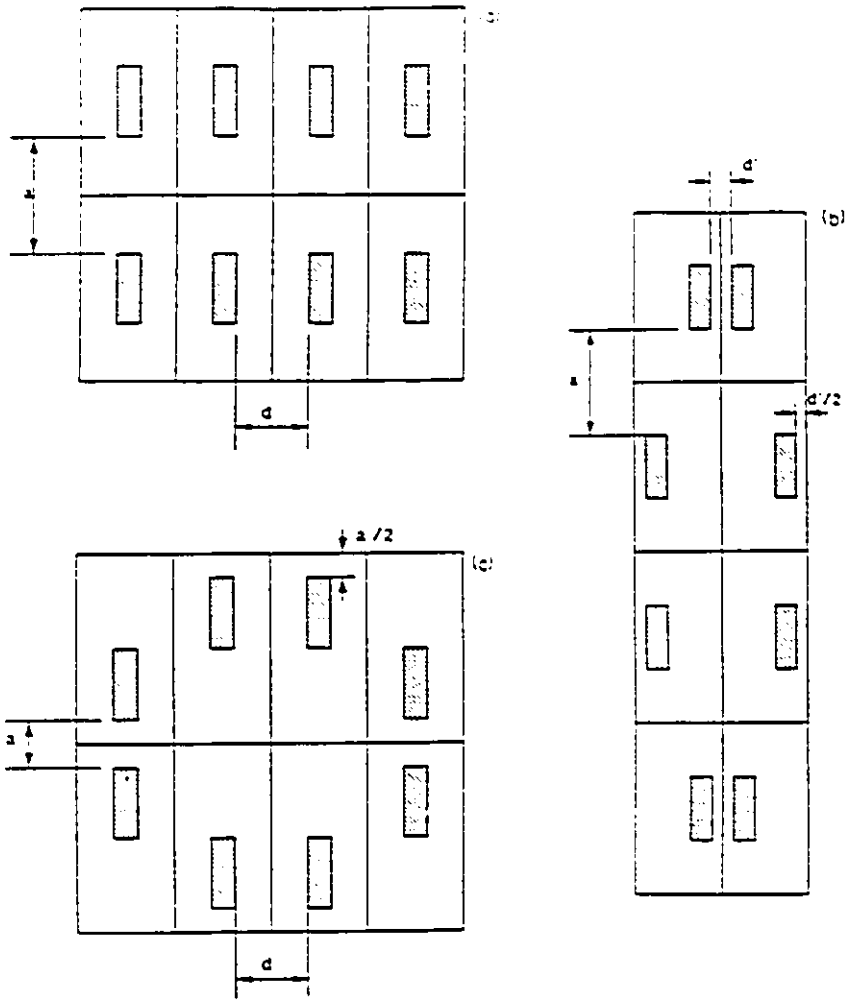

Figure 2.20 2D unit cell models used for the clustering calculations (after Christman et al).

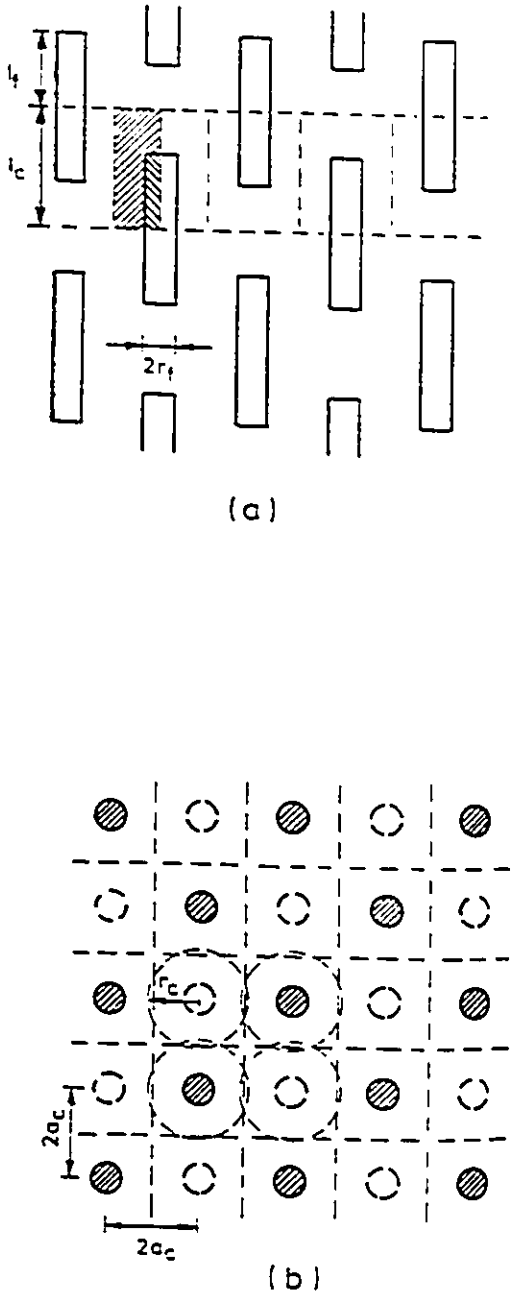

Figure 2.21 Periodic array of aligned whiskers. (a) Cross-section along fibres. (b) Cross-section normal to fibres (after Tvergaard).

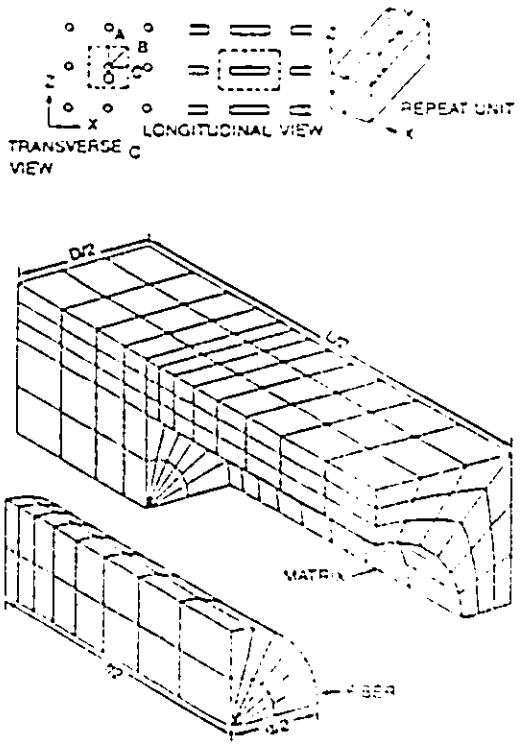

(a)

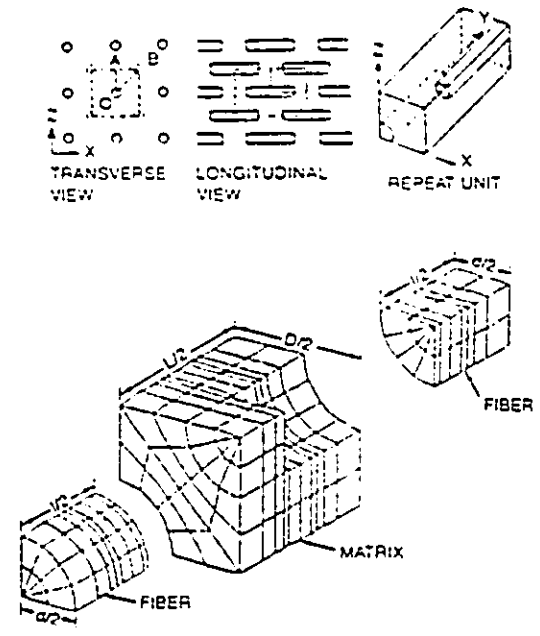

(b)

Figure 2.22 Models of short-fibre reinforced composites. (a) aligned fibre model; (b) staggered fibre model (after Levy).

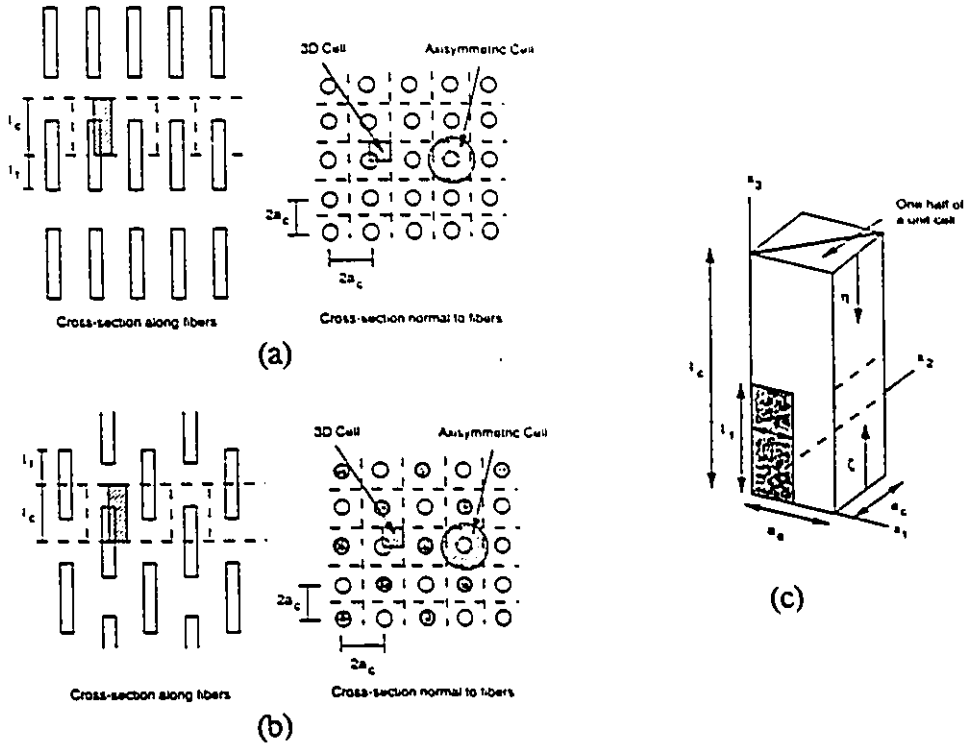

Figure 2.23 Unit cell containing one-eighth of a whisker used to model a periodic array of aligned whiskers (after Hom). (a) Aligned side-by-side whiskers; (b) Aligned overlapping whiskers; (c) one-eighth unit cell.

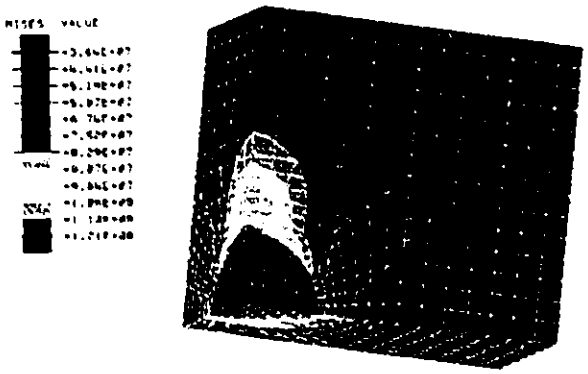

(a)

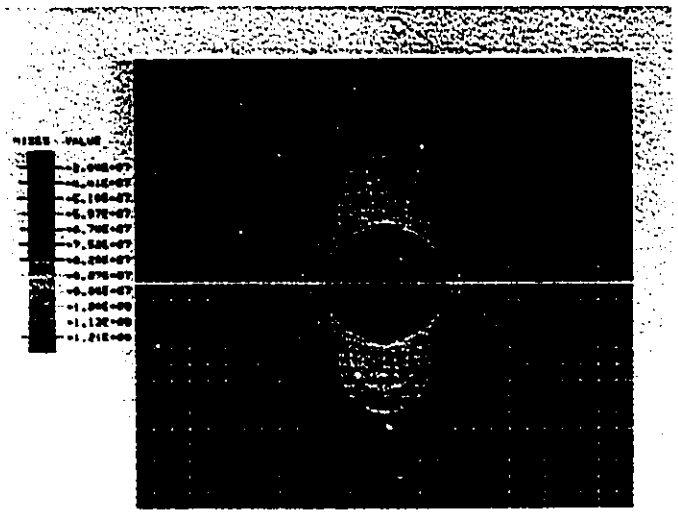

(b)

Figure 3.1 Von Mises stress contour (in units of Pa) in a system of an aluminium matrix and a SiC inhomogeneity subjected to 0.1% far field tensile strain using Eshelby's model. (a) Three dimensional view; (b) Front view.

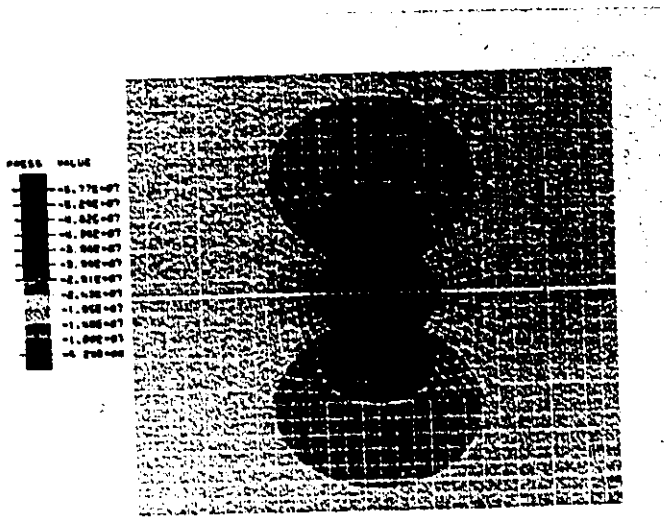

Figure 3.2 Hydrostatic pressure (PRESS) contour (in units of Pa).

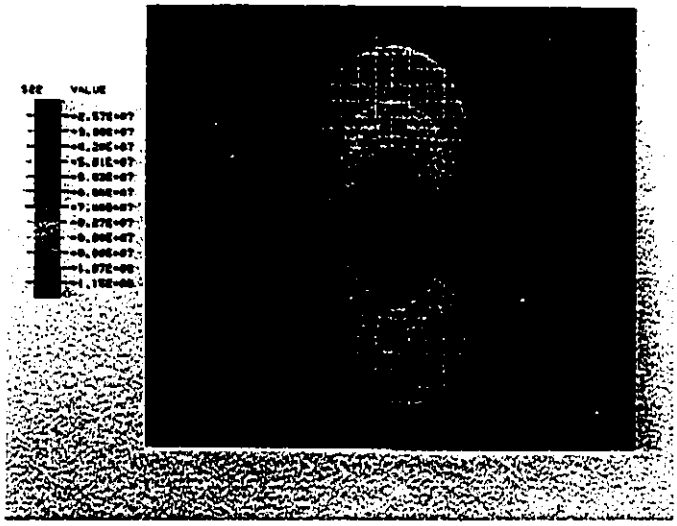

Figure 3.3 Tensile stress (S22) contour (in units of Pa).

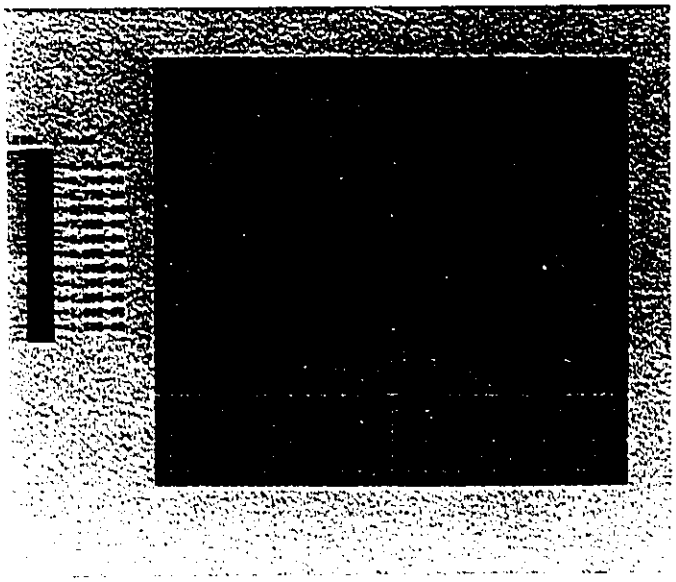

Figure 3.4 Tensile strain (E22) contour (in units of % m/m).

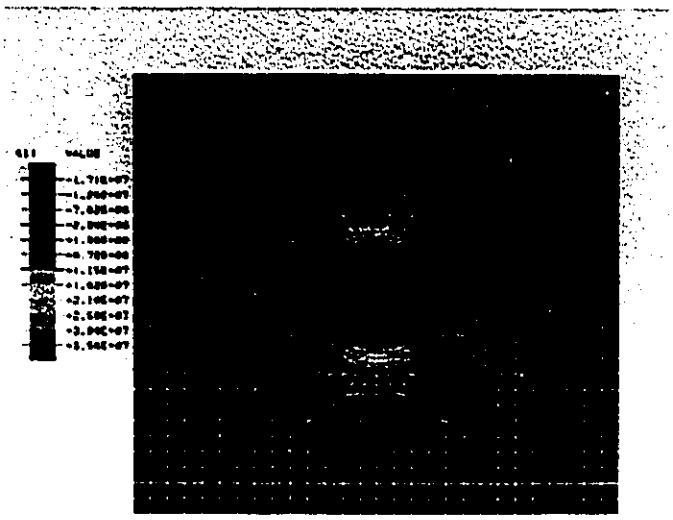

Figure 3.5 The transverse stress (S11) contour (in units of Pa).

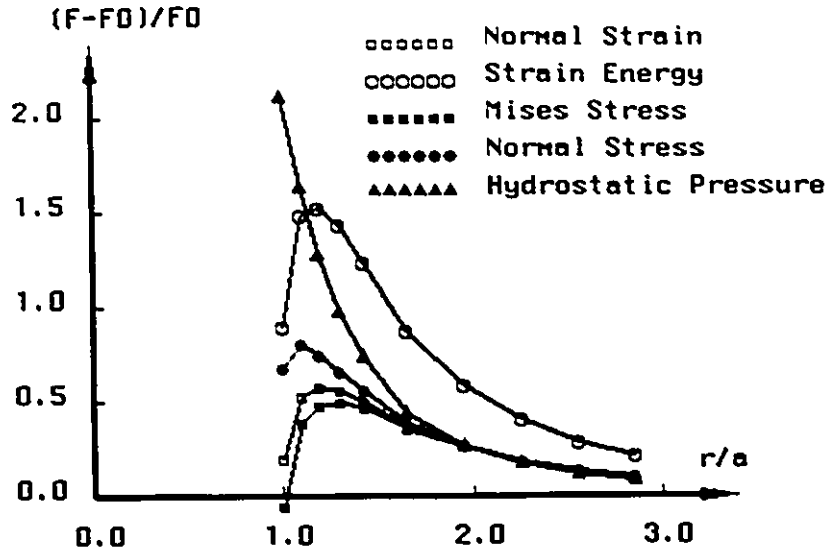

Figure 3.6 Characteristics of various parameters in the matrix along the line of loading through the pole.

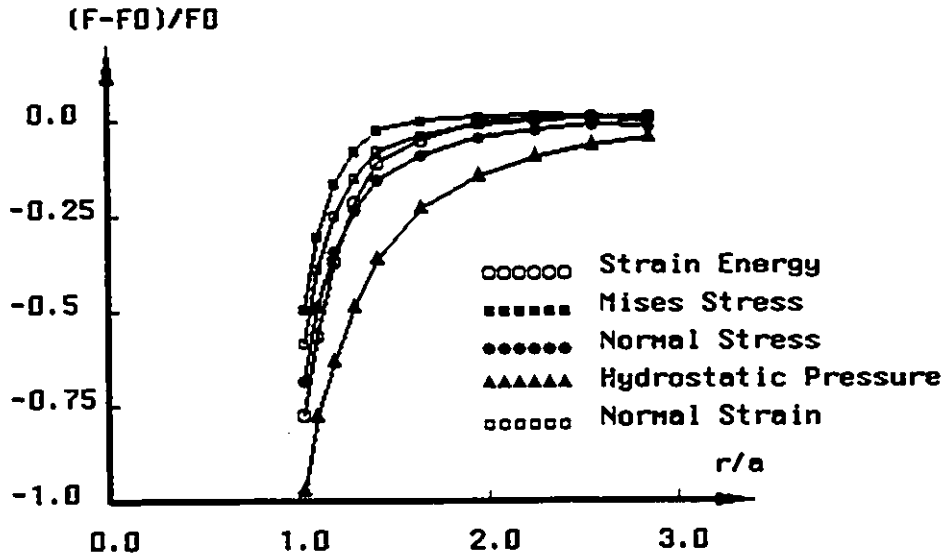

Figure 3.7 Parametric characteristics in the equatorial plane.

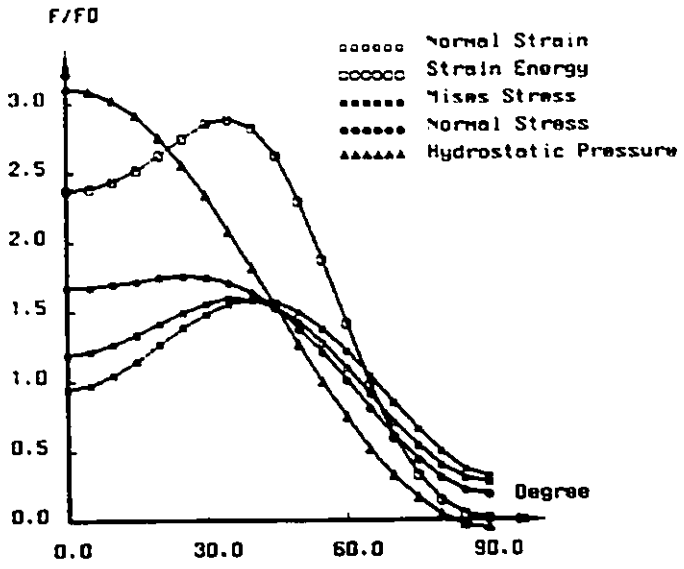

Figure 3.8 Angular variation of parameters along a longitudinal line for an Al/SiC system.

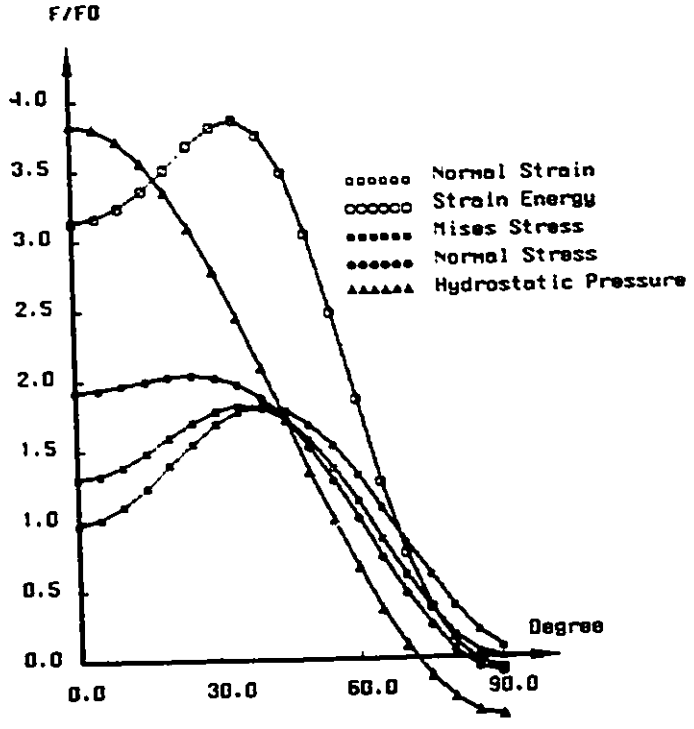

Figure 3.9 Angular variation of parameters along a longitudinal line for an Al/rigid system.

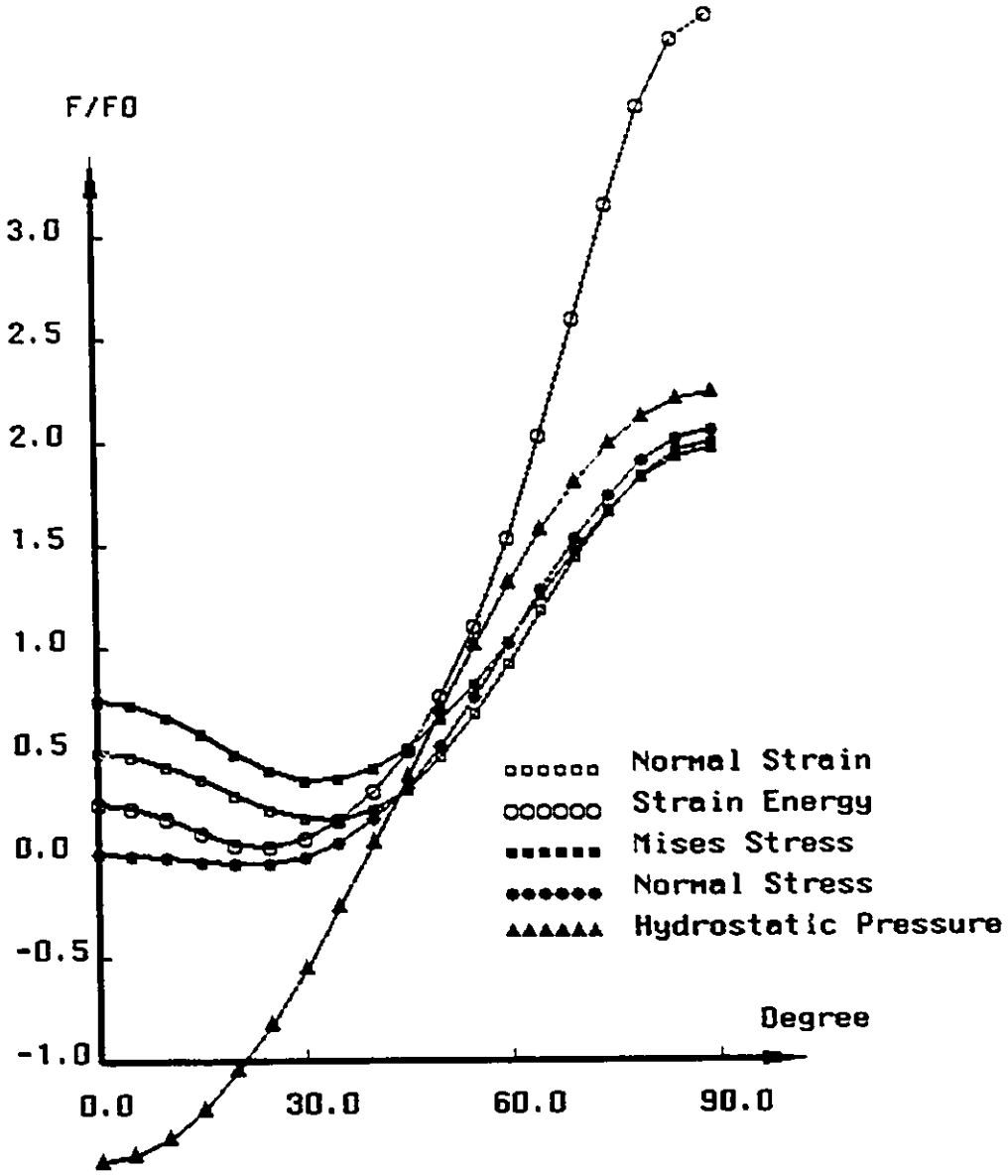

Figure 3.10 Angular variation of parameters along a longitudinal line for an Al/cavity system.

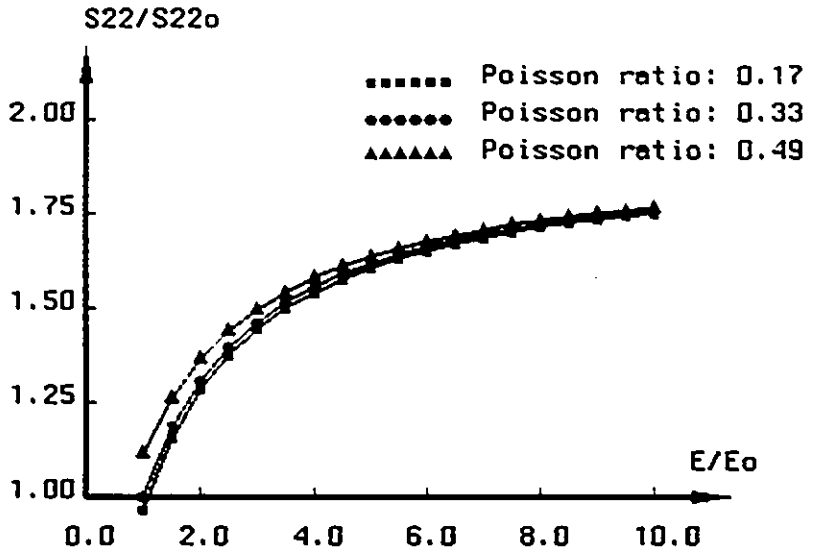

Figure 3.11 Stress gathering capability of a hard inhomogeneity, where S22 is the normal stress value in the inhomogeneity and $S22_0$ is that at the far-field.

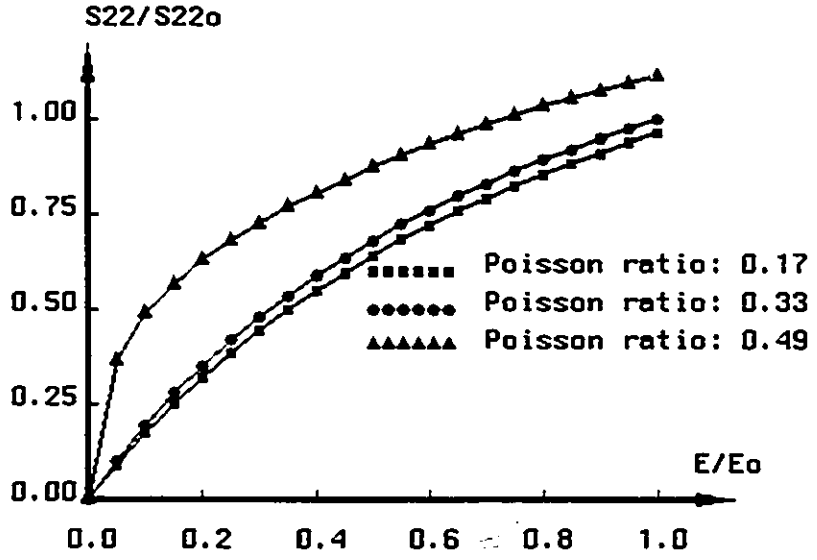

Figure 3.12 Stress gathering capability of a soft inhomogeneity, where S22 is the normal stress value in the inhomogeneity and $S22_0$ is that at the far-field.

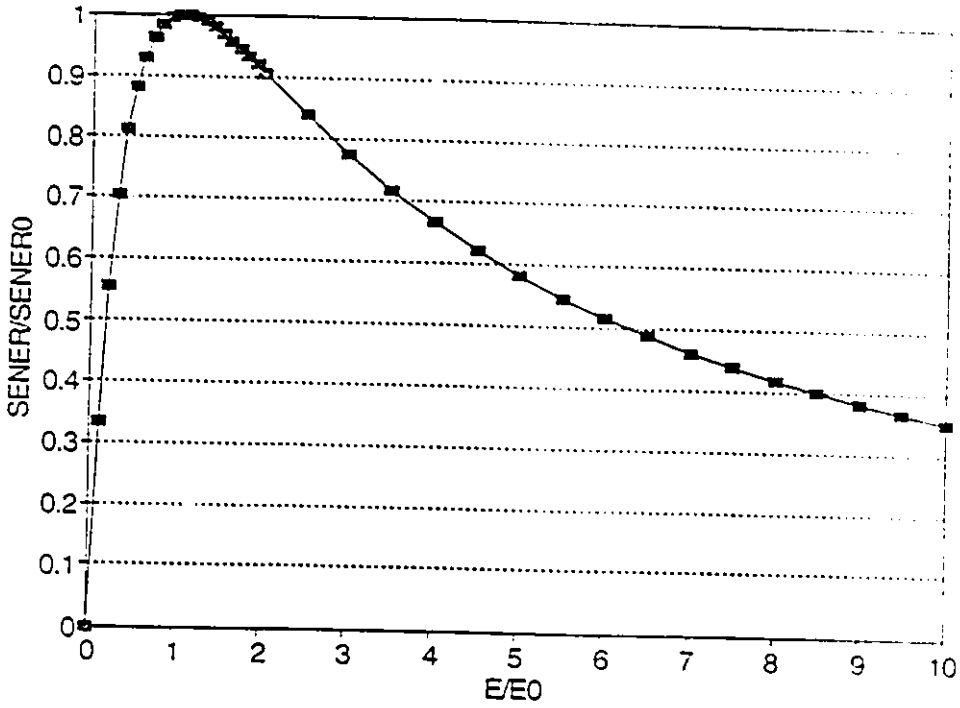

Figure 3.13 Strain energy gathering capability of an inhomogeneity.

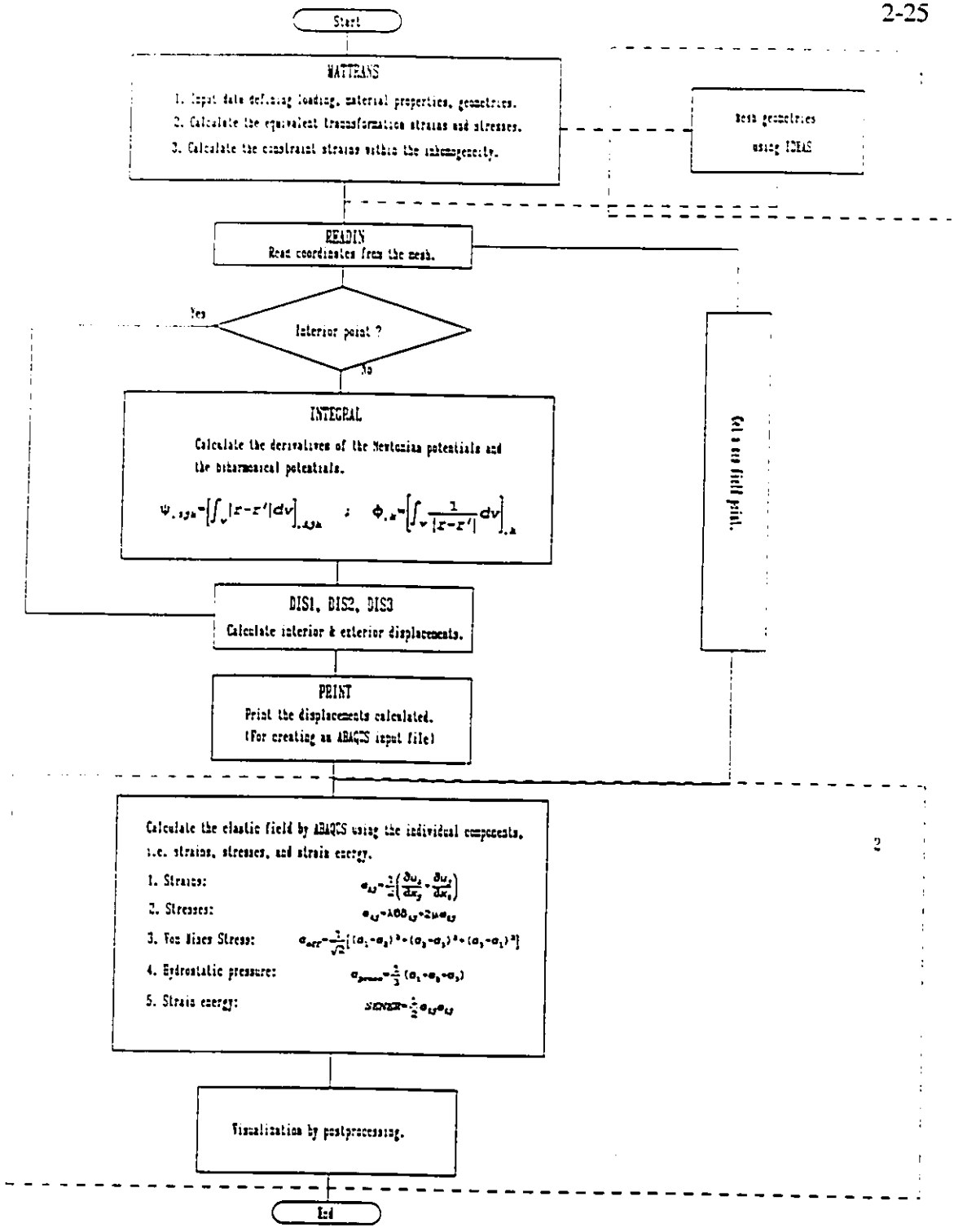

Figure 3.14 Programming procedures for visualizing the elastic fields around a spherical particle using Eshelby's method.

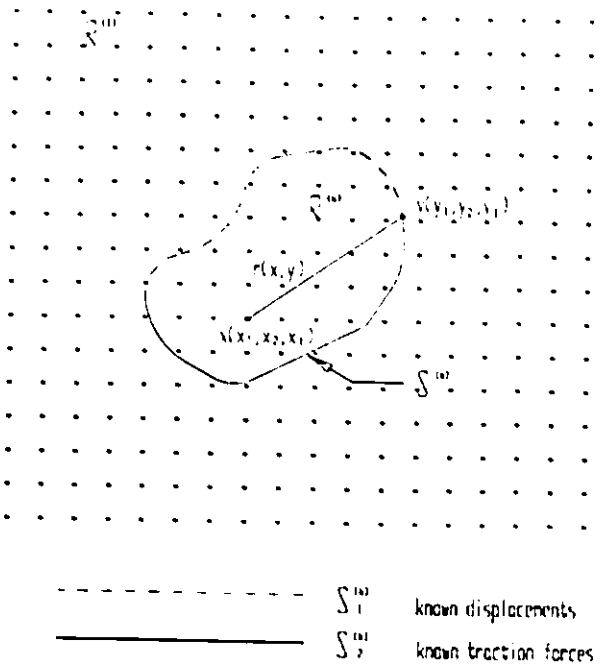

Figure 4.1 Geometry definition for the boundary description.

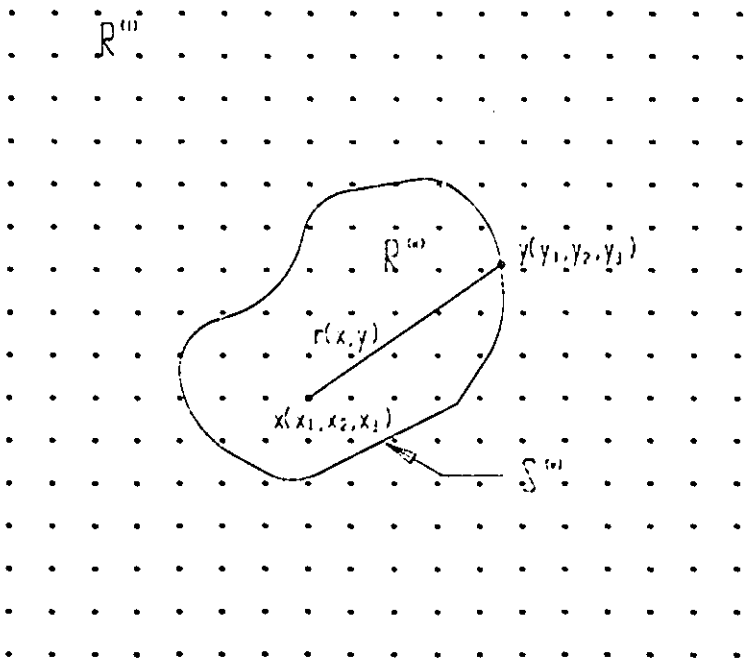

Figure 4.2 Geometry definition in general.

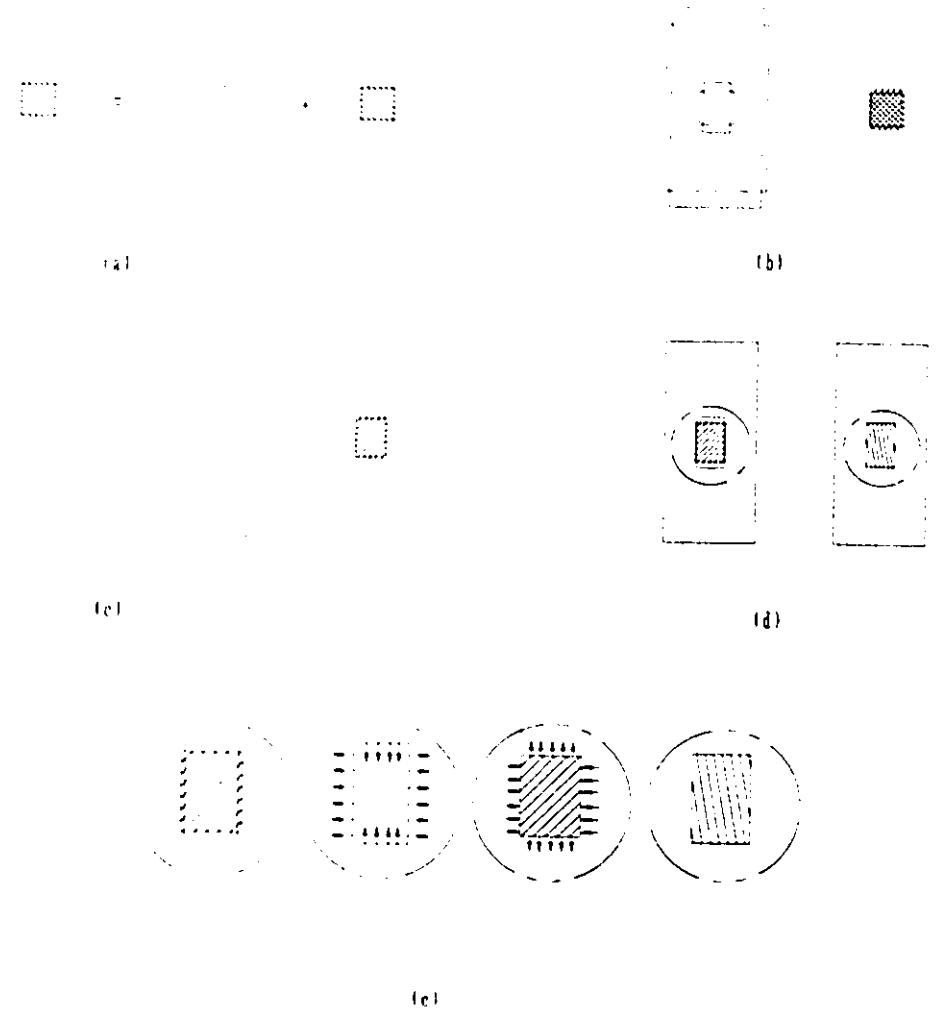

Figure 4.3 A illustration for the approach of the inhomogeneity problem by the process of: (a) cutting; (b) to (c) straining; (d) to (e) welding.

Figure 4.4 Geometry for the integrand platelet on which the field point is not contained.

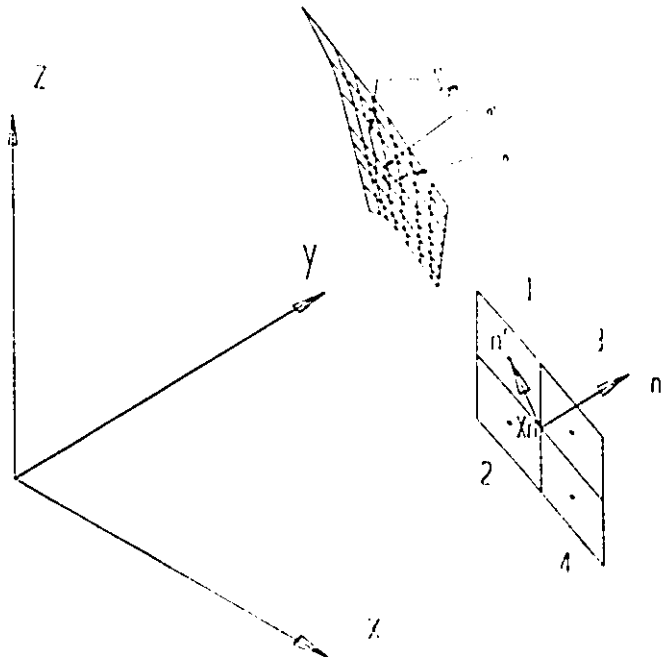

Figure 4.5 Geometry for the integrand platelet on which the field point is contained.

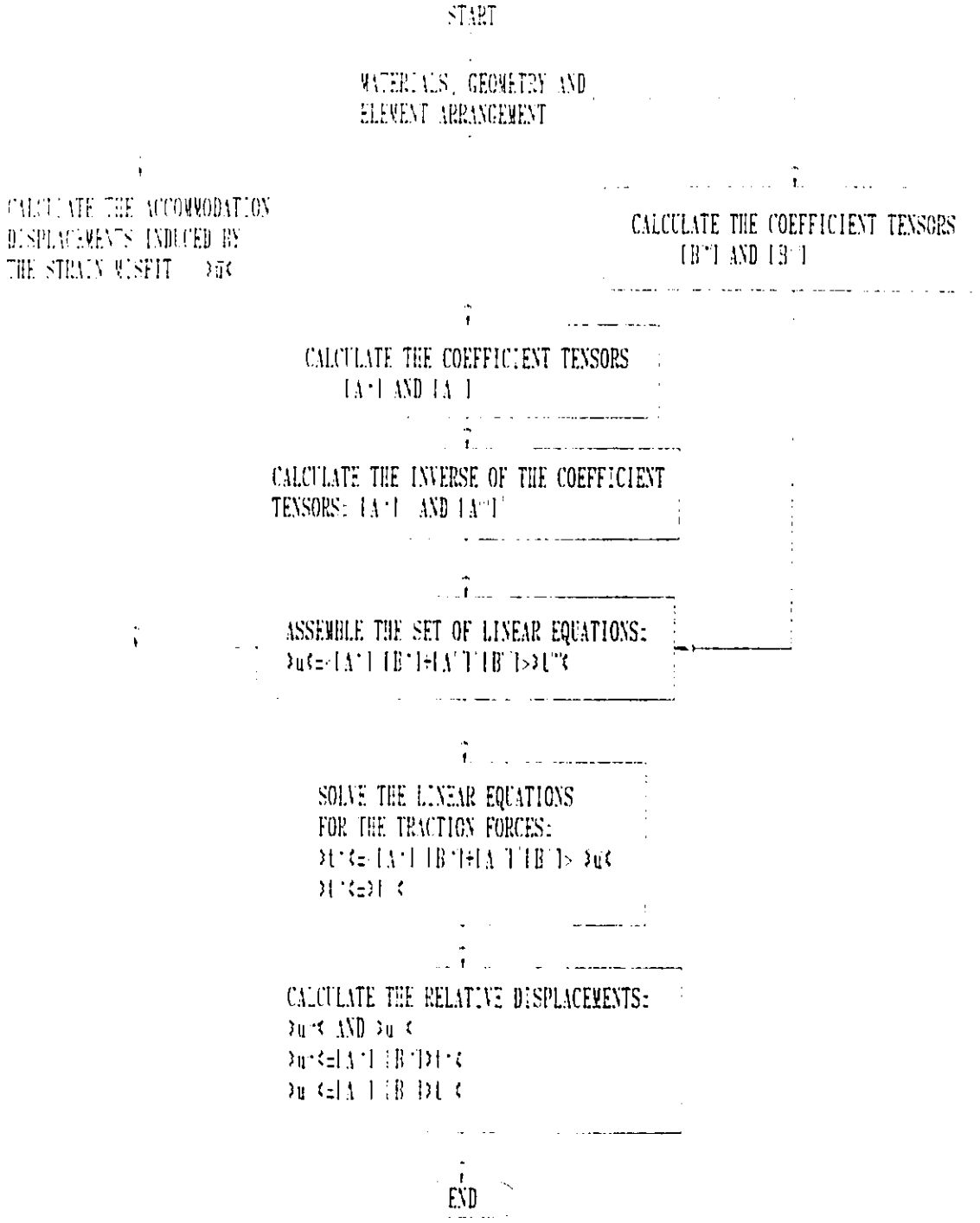

Figure 4.6 Programming procedures.

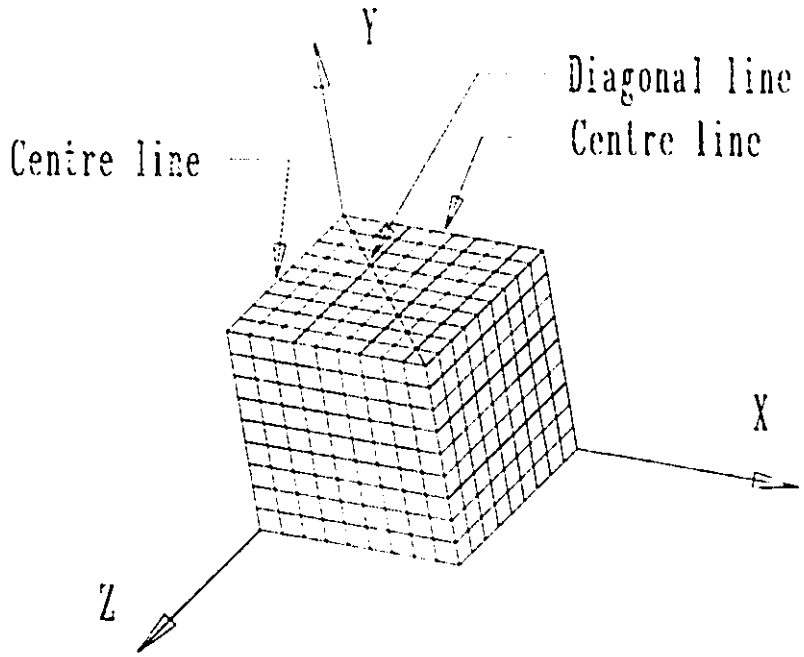

Figure 4.7 Element arrangement, and definition of centre line and diagonal line.

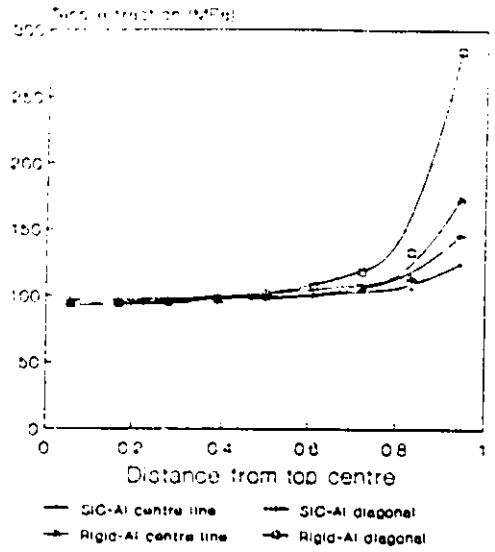

Figure 4.8 Interactions in a system of aluminium matrix and a cubic inhomogeneity subjected to 70 MPa far field stress.

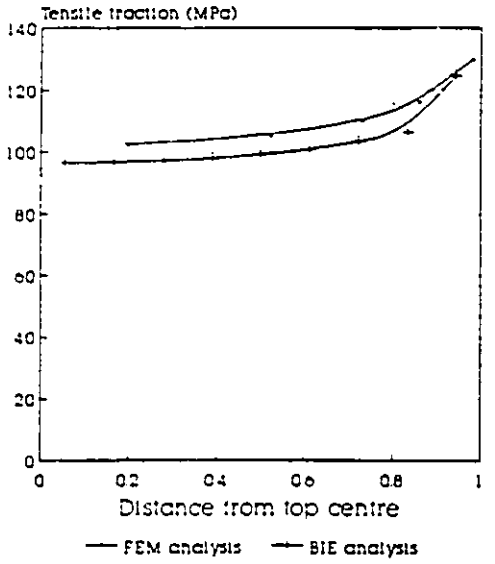

Figure 4.9 A comparison between the FEA and BIE predictions for the traction t_2 at SiC-Al interface centre line.

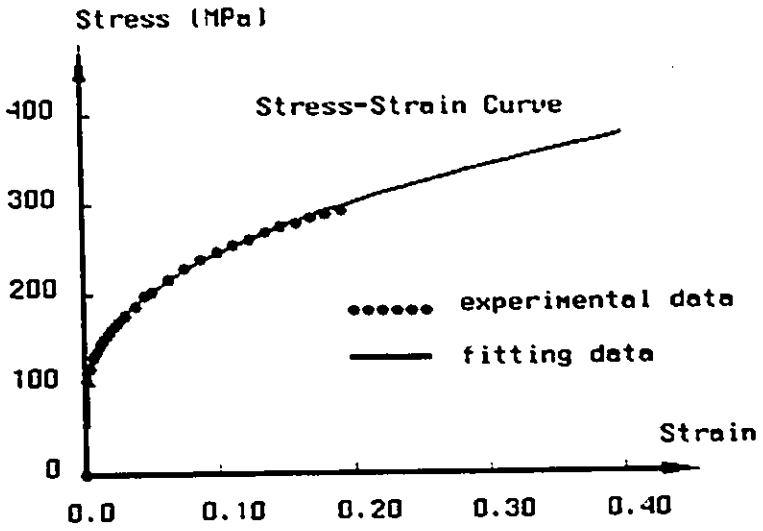

Figure 5.1 Stress strain curve of 6061-T4 aluminium.

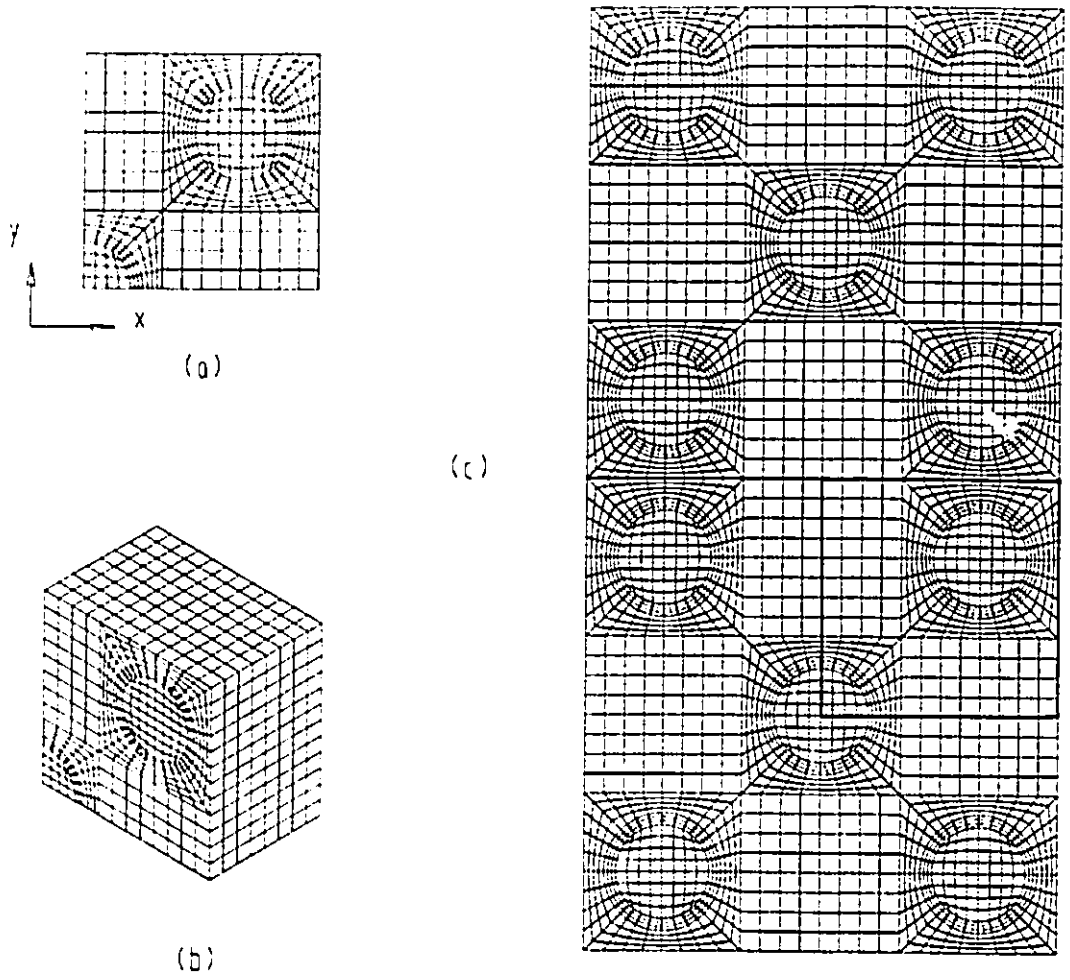

Figure 5.2 Unit cell model. (a) front view; (b) isometric view; (c) front reflecting view.

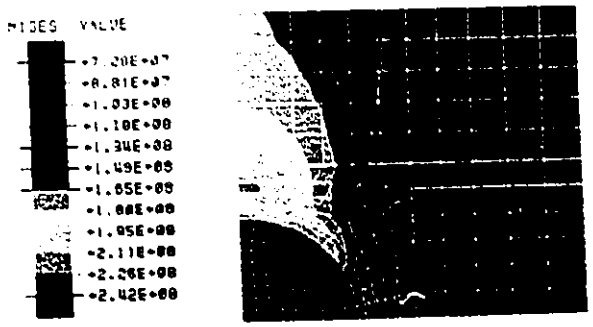

(a) The Von Mises stress contour.

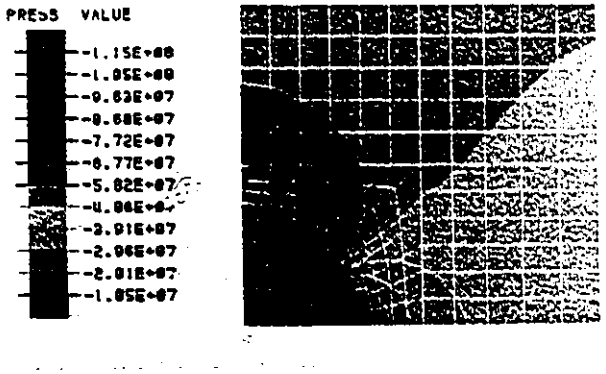

(b) The hydrostatic pressure contour.

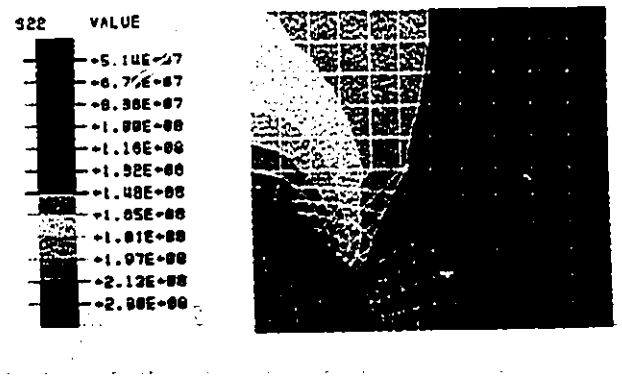

(c) The tensile stress contour.

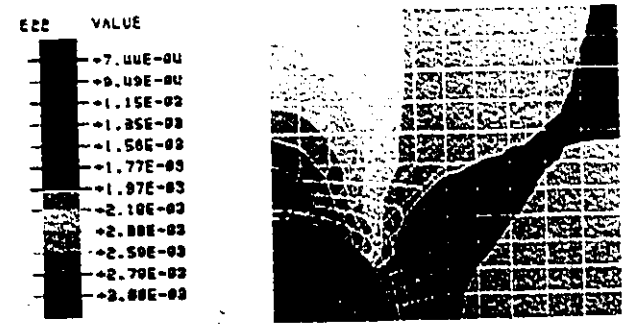

(d) The tensile strain contour.

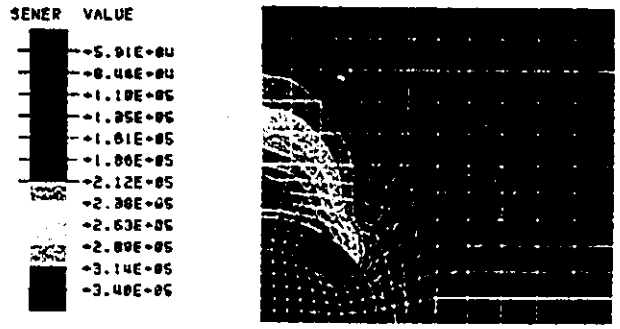

(e) The strain energy density contour.

Figure 5.3 The variable concentration contours calculated from linear FEM in a Al/$(SiC)_p$ MMC (Vol. Fract.=1.94%) subjected to a tensile strain of 0.2%.

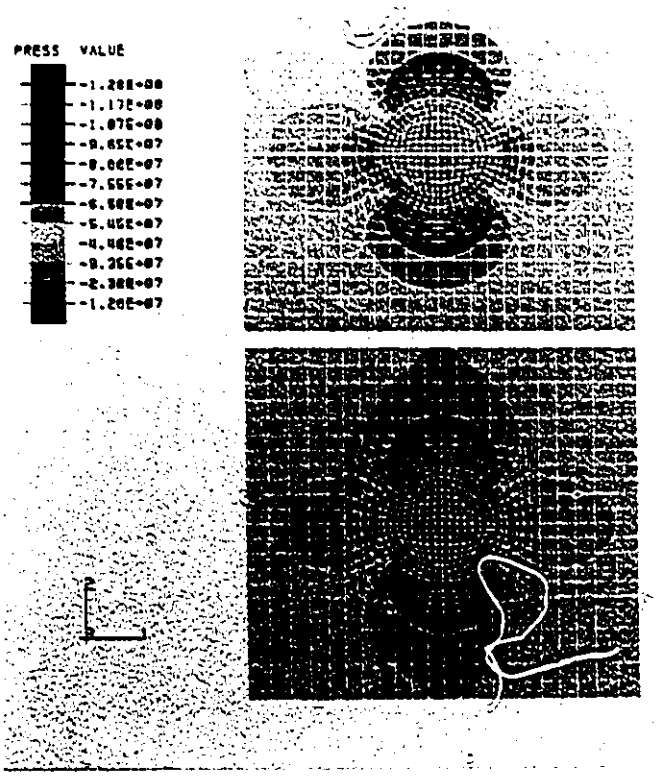

Figure 5.4 The effective hydrostatic pressure contours calculated from: (a) Eshelby's theory (upper figure) (b) elastic FEM (lower figure).

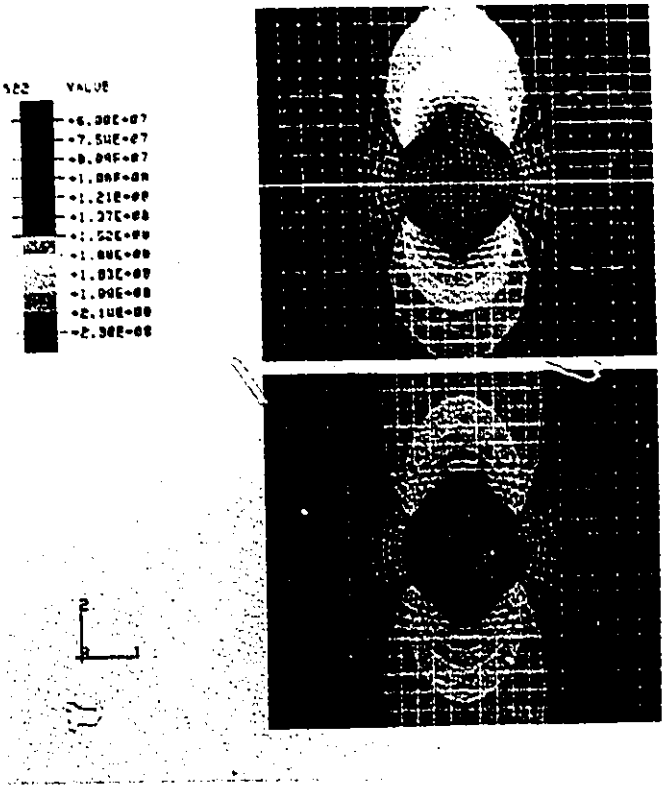

Figure 5.5 The normal stress contours calculated from: (a) Eshelby's theory (upper figure); (b) elastic FEM (lower figure).

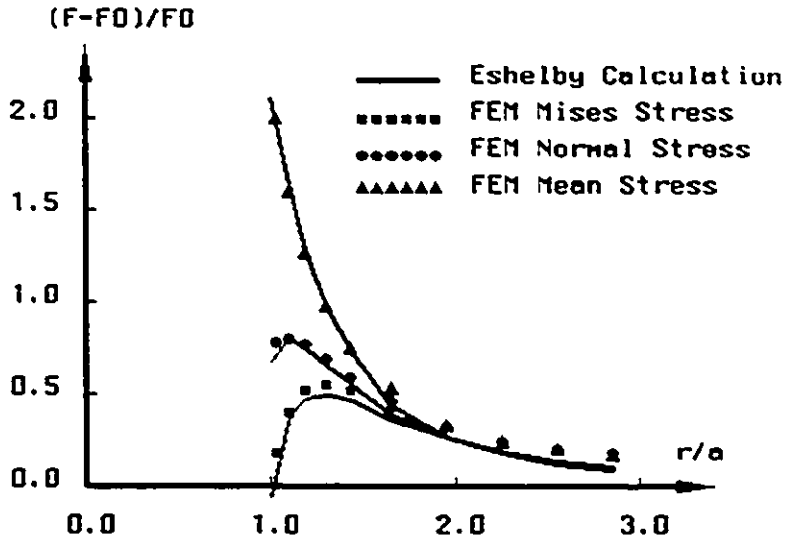

Figure 5.6 A comparison of polar characteristics calculated from Eshelby's theory and elastic FEM.

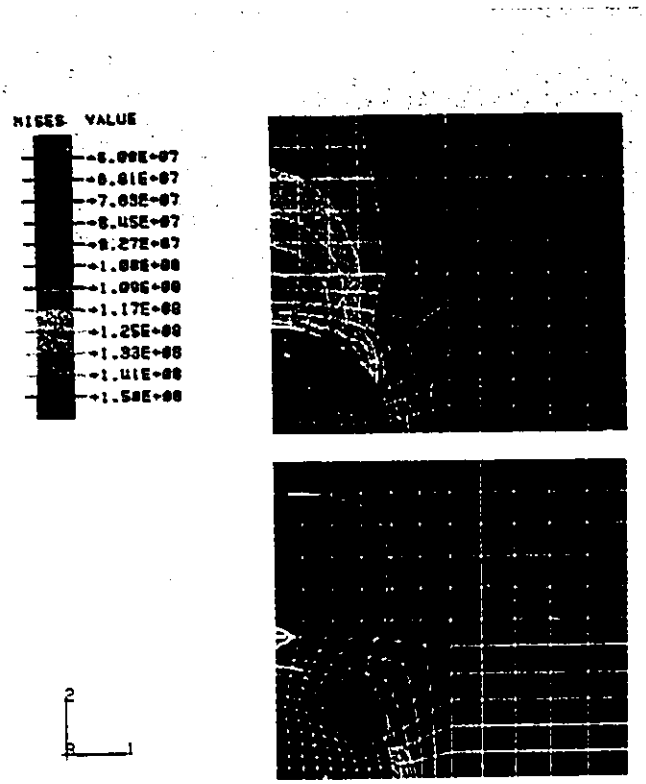

Figure 5.7 The influence of plastic behaviour of matrix on Von Mises stress concentration in 6061-T4 Al/$(SiC)_p$ subjected to a low tensile loading of 94.2 MPa (Vol. Fract.=1.94%). (a) elastic matrix (upper); (b) elastic plastic matrix (lower figure).

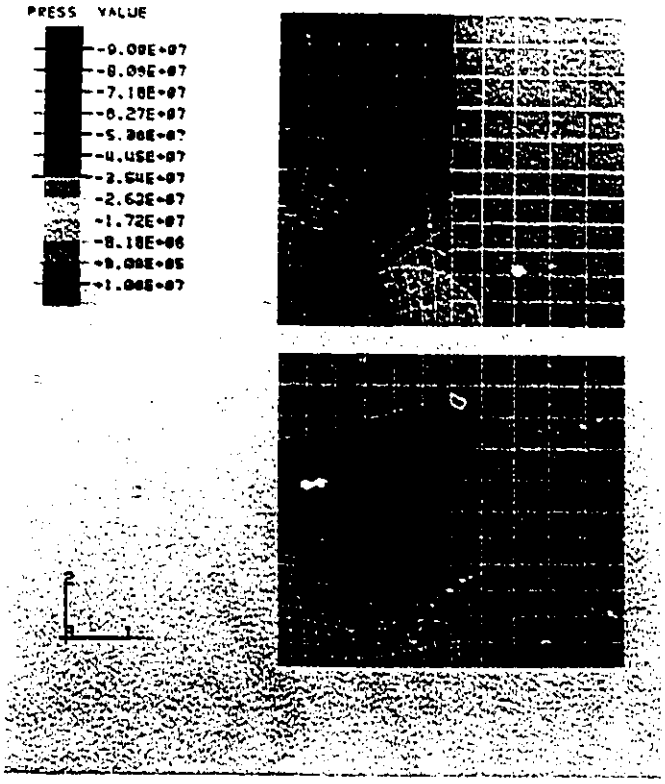

Figure 5.8 The influence of plastic behaviour of matrix on the effective hydrostatic pressure concentration. (a) elastic matrix (upper); (b) elastic-plastic matrix (lower figure).

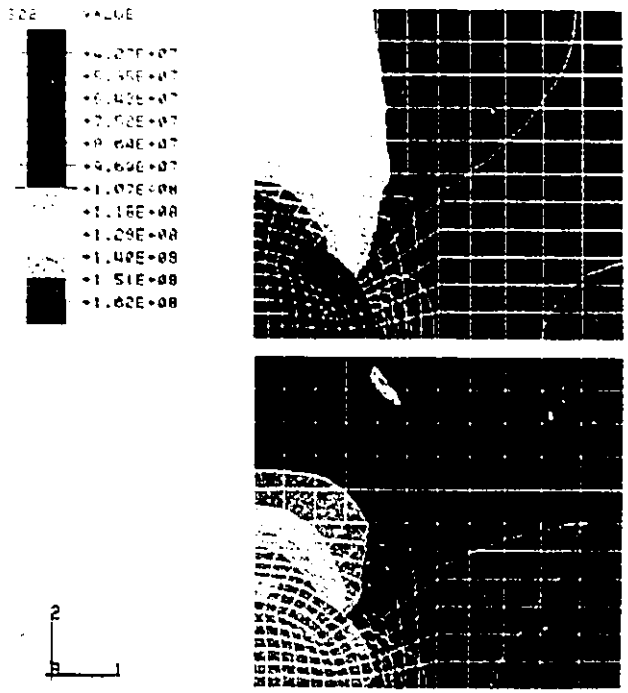

Figure 5.9 The influence of plastic behaviour of matrix on the normal stress concentration. (a) elastic matrix (upper); (b) elastic-plastic matrix (lower figure).

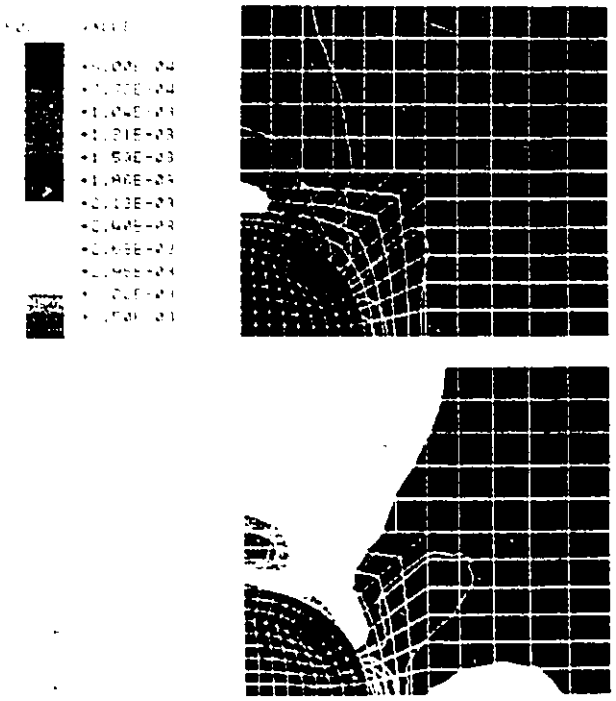

Figure 5.10 The influence of plastic behaviour of matrix on the normal strain concentration. (a) elastic matrix (upper figure); (b) elastic-plastic matrix (lower figure).

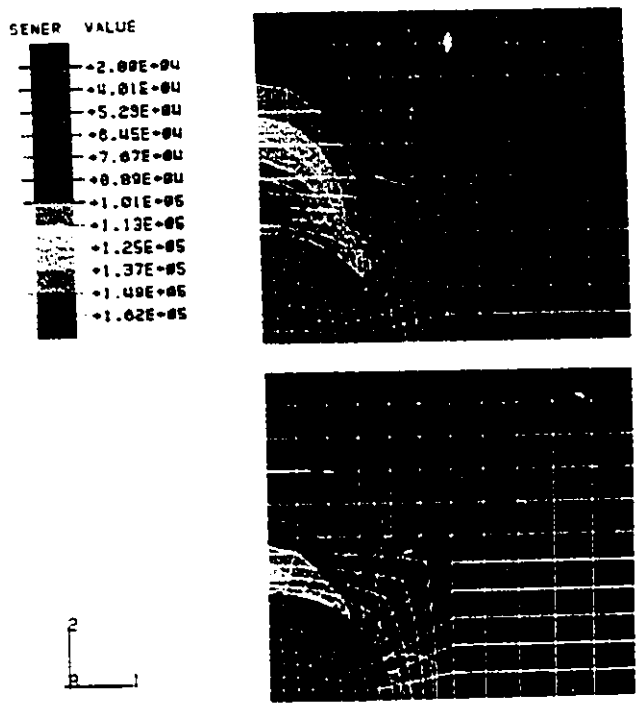

Figure 5.11 The influence of plastic behaviour of matrix on the strain energy concentration. (a) elastic matrix (upper figure); (b) elastic-plastic matrix (lower figure).

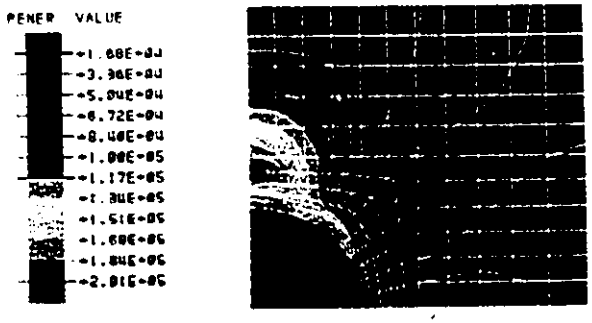

Figure 5.12 The influence of plastic behaviour on the effective plastic energy density concentration.

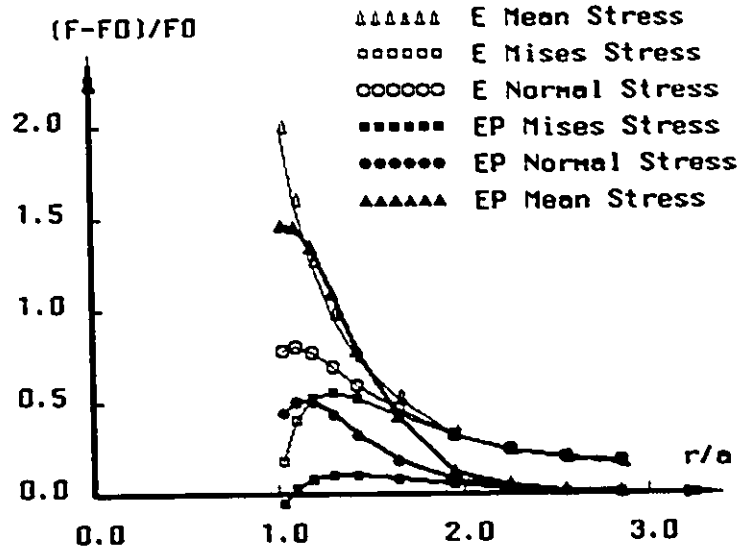

Figure 5.13 A comparison of polar characteristics with and without considering plastic behaviour of matrix.

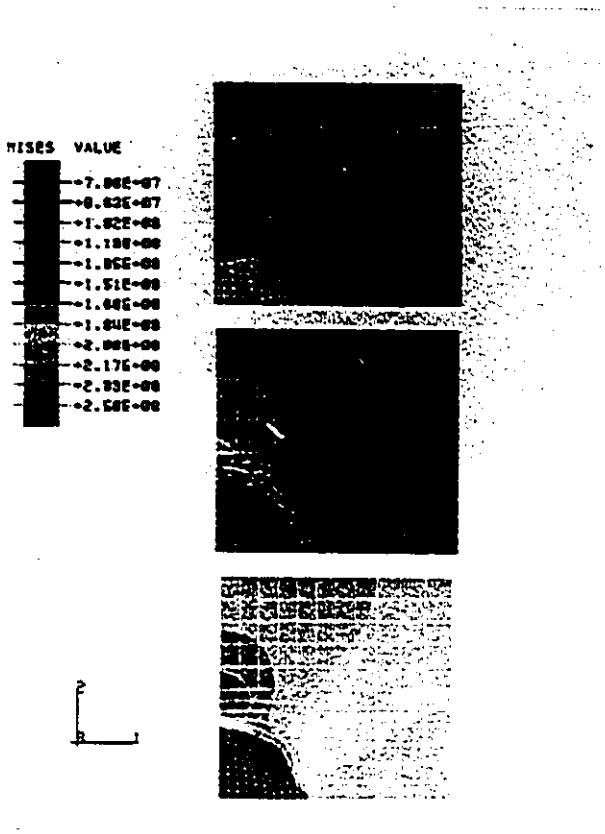

Figure 5.14 Development of Von Mises stress concentration at engineering strains of: (a) 0.2% (top figure); (b) 2.0% (middle figure); (c) 5.0% (bottom figure).

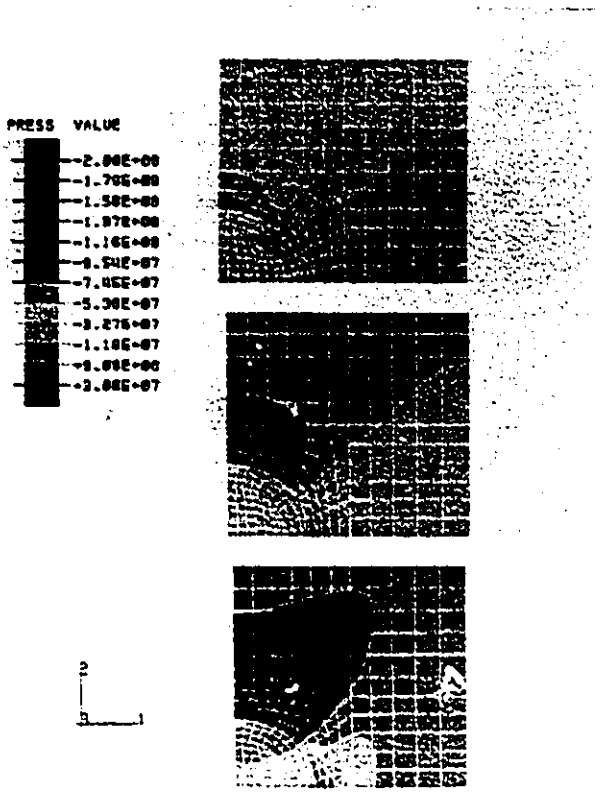

Figure 5.15 Development of the effective hydrostatic pressure concentration at engineering strains of: (a) 0.2% (top figure); (b) 2.0% (middle figure); (c) 5.0% (bottom figure).

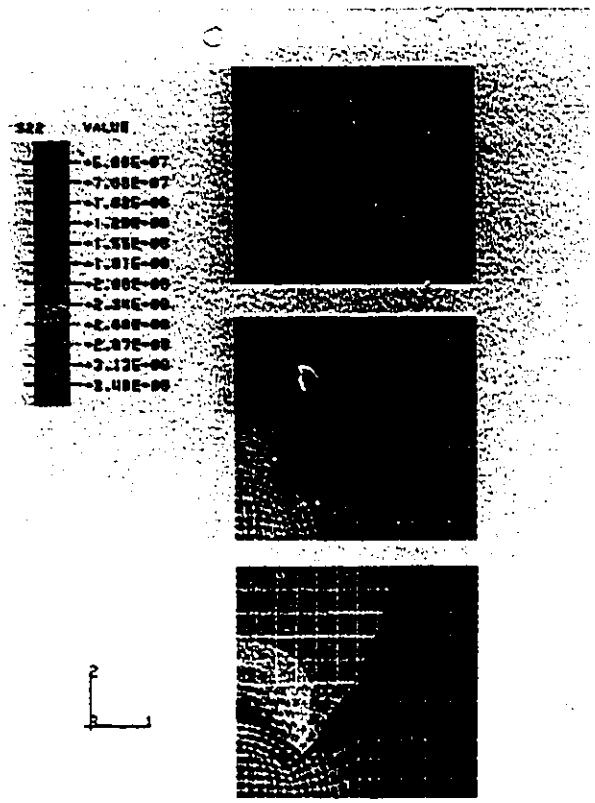

Figure 5.16 Development of the normal stress concentration at engineering strains of: (a) 0.2% (top figure); (b) 2.0% (middle figure); (c) 5.0% (bottom figure).

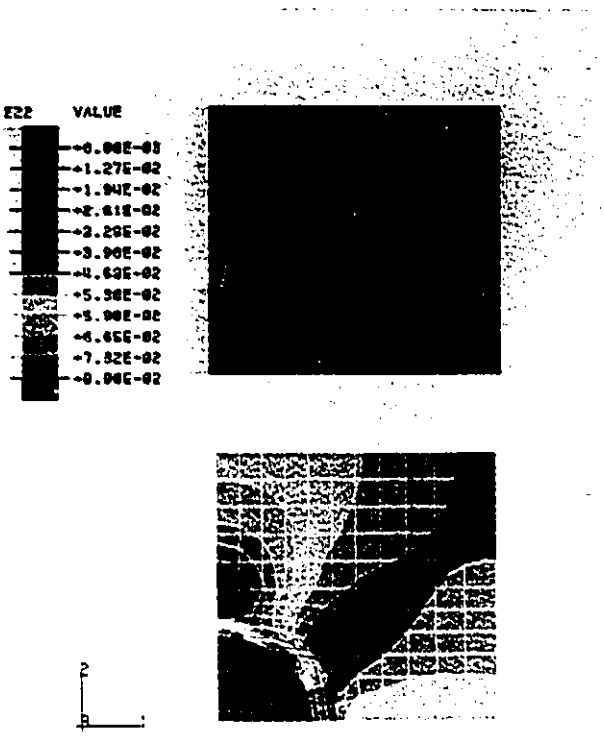

Figure 5.17 Development of the normal strain concentration at engineering strains of: (a) 2.0% (upper figure); (b) 5.0% (lower figure).

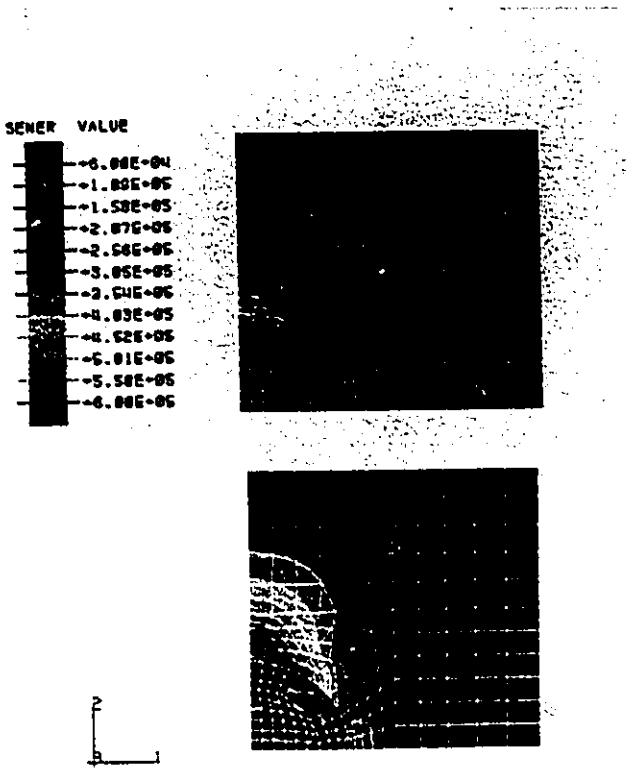

Figure 5.18 Development of the strain energy density concentration at engineering strains of: (a) 2.0% (upper figure); (b) 5.0% (lower figure).

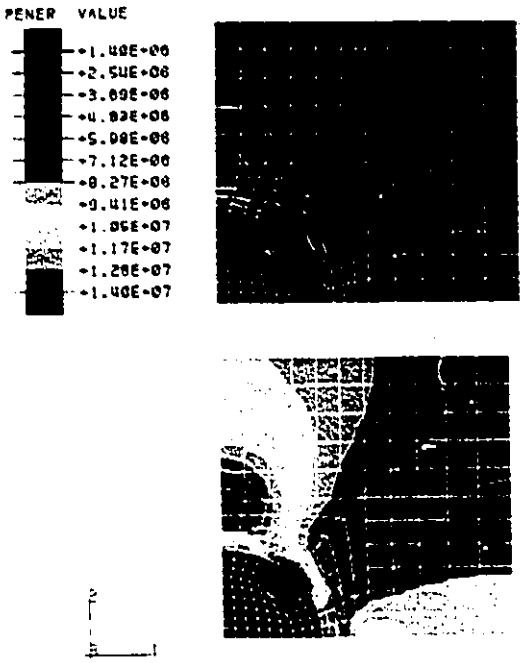

Figure 5.19 Development of the plastic energy density concentration at engineering strains of: (a) 2.0% (upper figure); (b) 5.0% (lower figure).

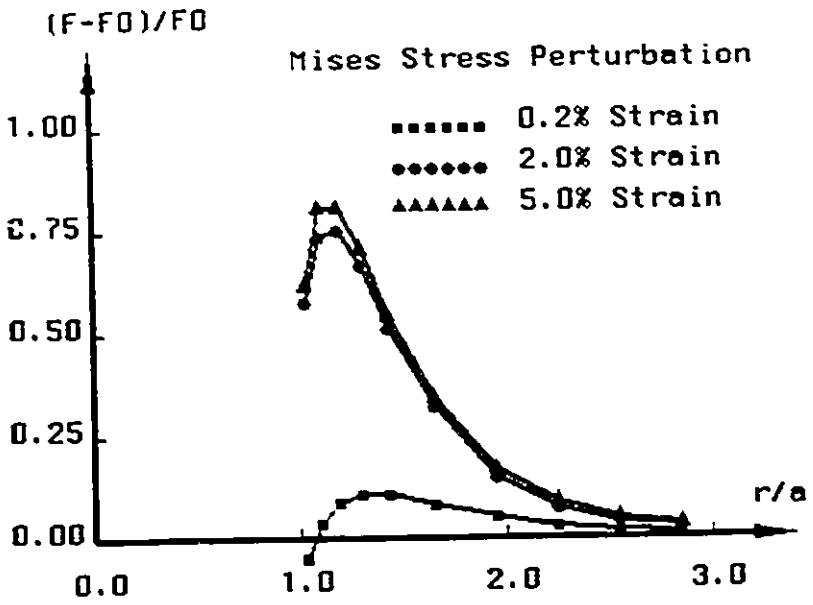
(F-F0)/F0
Mises Stress Perturbation
0.2% Strain
2.0% Strain
5.0% Strain
1.00
0.75
0.50
0.25
0.00
r/a
0.0
1.0
2.0
3.0

(a)

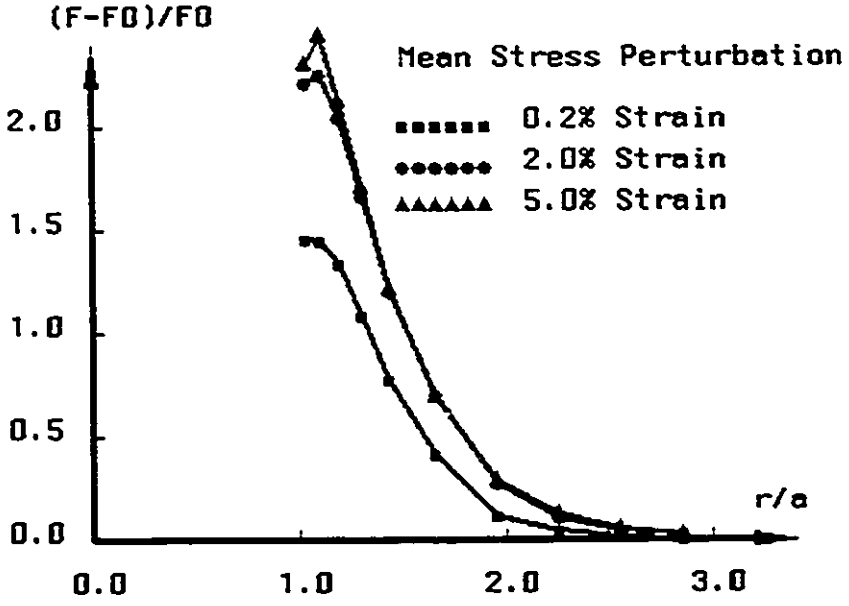
(F-F0)/F0
Mean Stress Perturbation
0.2% Strain
2.0% Strain
5.0% Strain
2.0
1.5
1.0
0.5
0.0
r/a
0.0
1.0
2.0
3.0

(b)

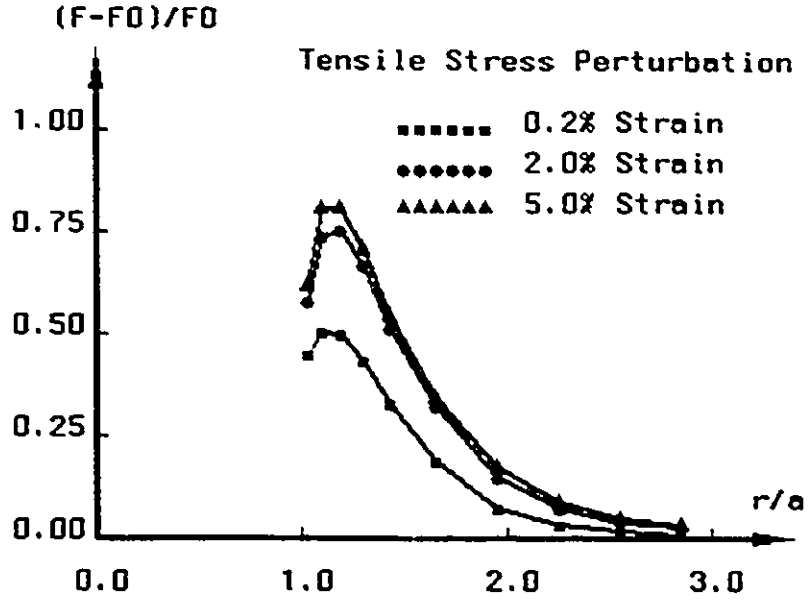

(c)

Figure 5.20 Polar characteristics at different strain levels. (a) Von Mises stress; (b) the mean stress; (c) the tensile stress.

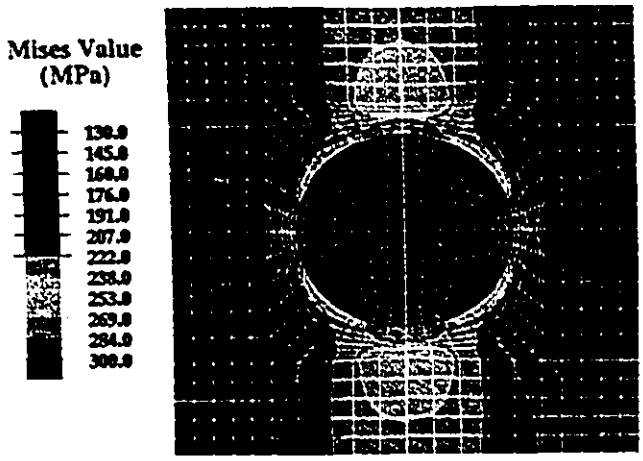

Von Mises Stress Contour
Uniform Distribution of Particles
Total Strain: 5% Volume Fraction: 5%
6061-T4 condition Al-(SiC)p MMC
92/08/14

(a)

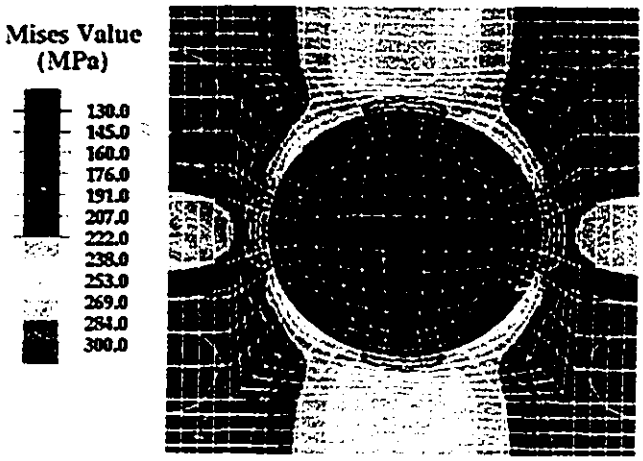

Von Mises Stress Contour
Uniform Distribution of Particles
Total Strain: 5% Volume Fraction:
6061-T4 condition Al-(SiC)p MMC
92/08/14

(b)

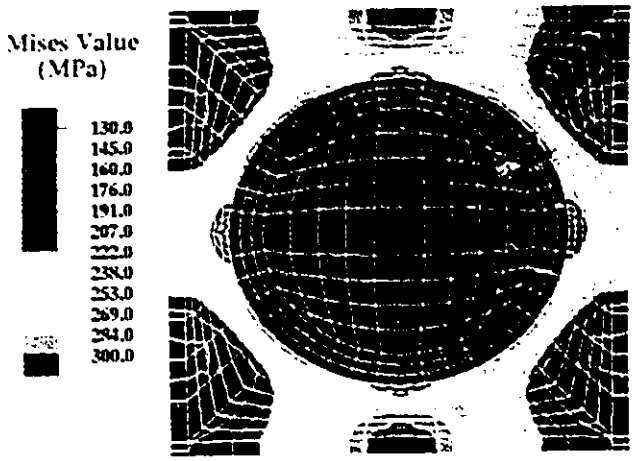

(c)

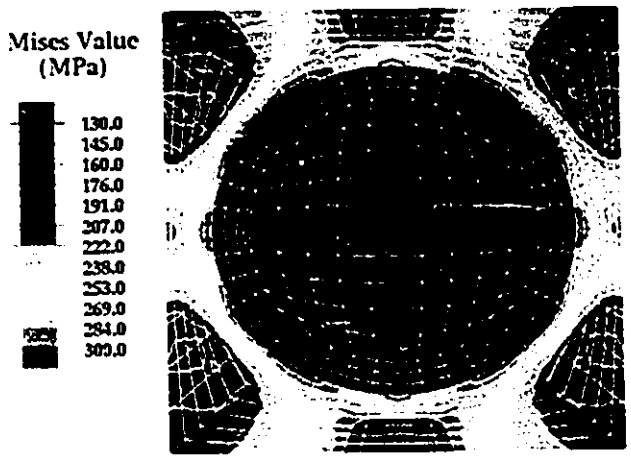

(d)

Figure 6.1 Von Mises contours in 6061-T4 Al/$(SiC)_p$ MMCs at 5.0% overall engineering strain with: (a) 5% volume fraction; (b) 10% volume fraction; (c) 20% volume fraction; (d) 25% volume fraction.

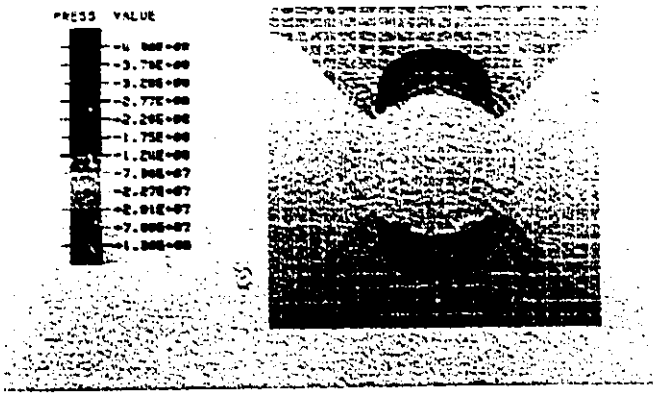

(a)

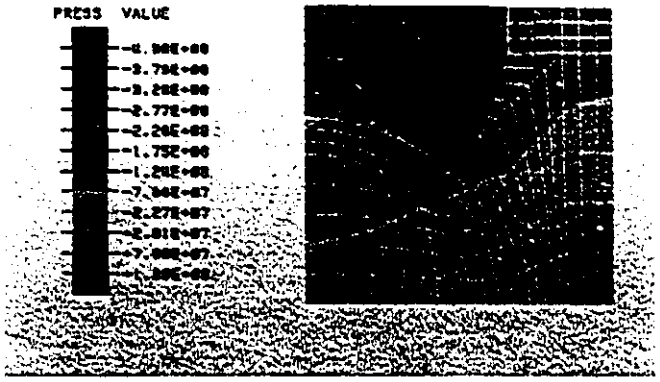

(b)

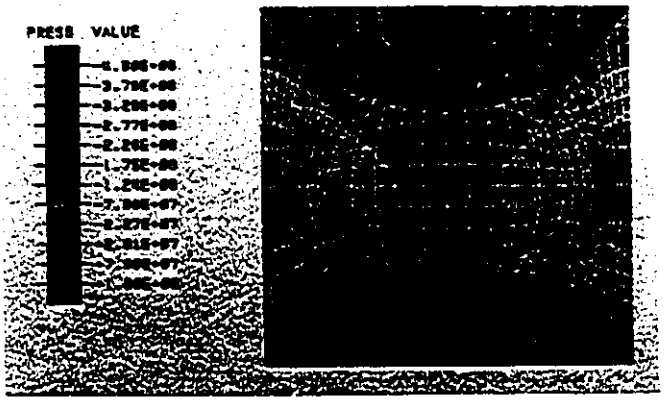

(c)

Figure 6.2 The hydrostatic pressure contours with: (a) 5% volume fraction; (b) 15% volume fraction; (c) 25% volume fraction.

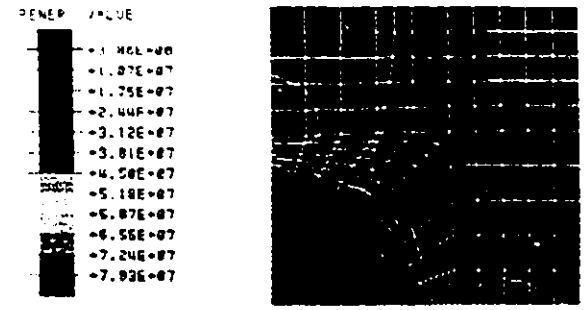

(a)

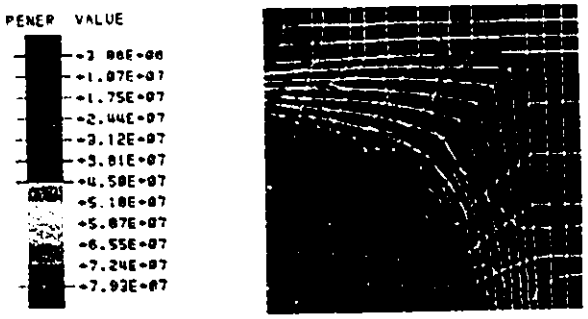

(b)

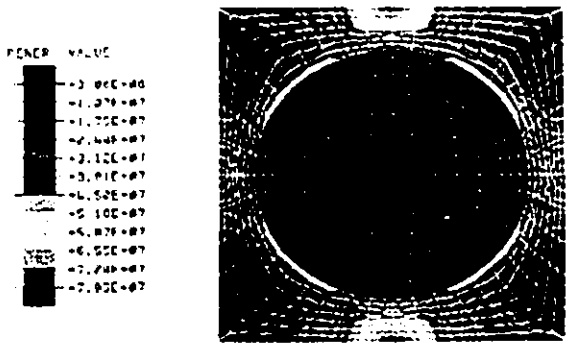

(c)

Figure 6.3 The effective plastic energy density contours with: (a) 5% volume fraction; (b) 15% volume fraction; (c) 25% volume fraction.

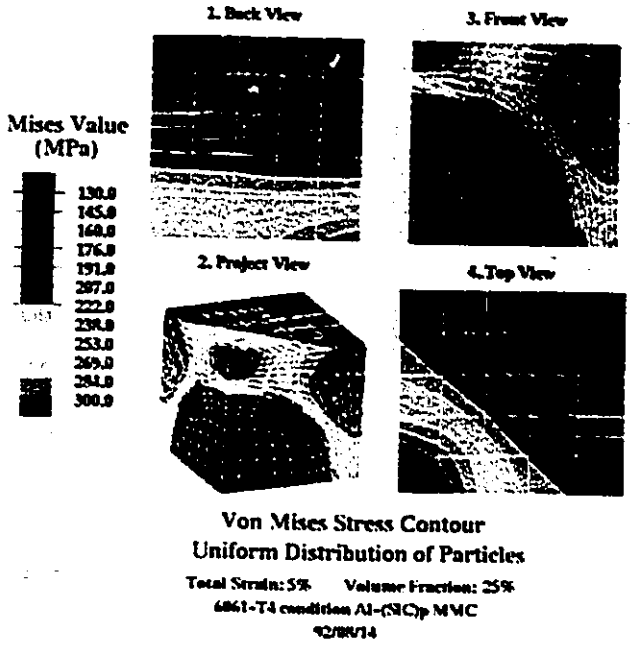

Figure 6.4 The effective stress concentration within the unit cell.

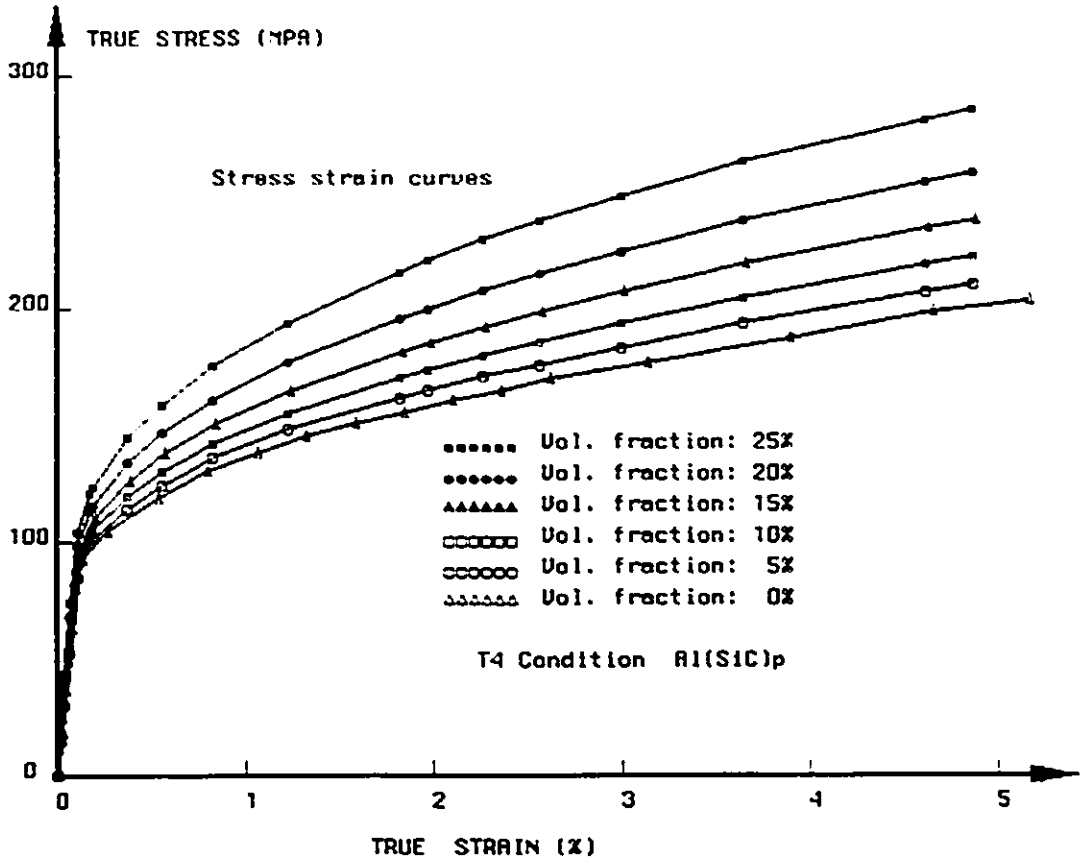
TRUE STRESS (MPA)
300
200
100
0
Stress strain curves
Vol. fraction: 25%
Vol. fraction: 20%
Vol. fraction: 15%
Vol. fraction: 10%
Vol. fraction: 5%
Vol. fraction: 0%
T4 Condition Al(SiC)p
0
1
2
3
4
5
TRUE STRAIN (%)

(a)

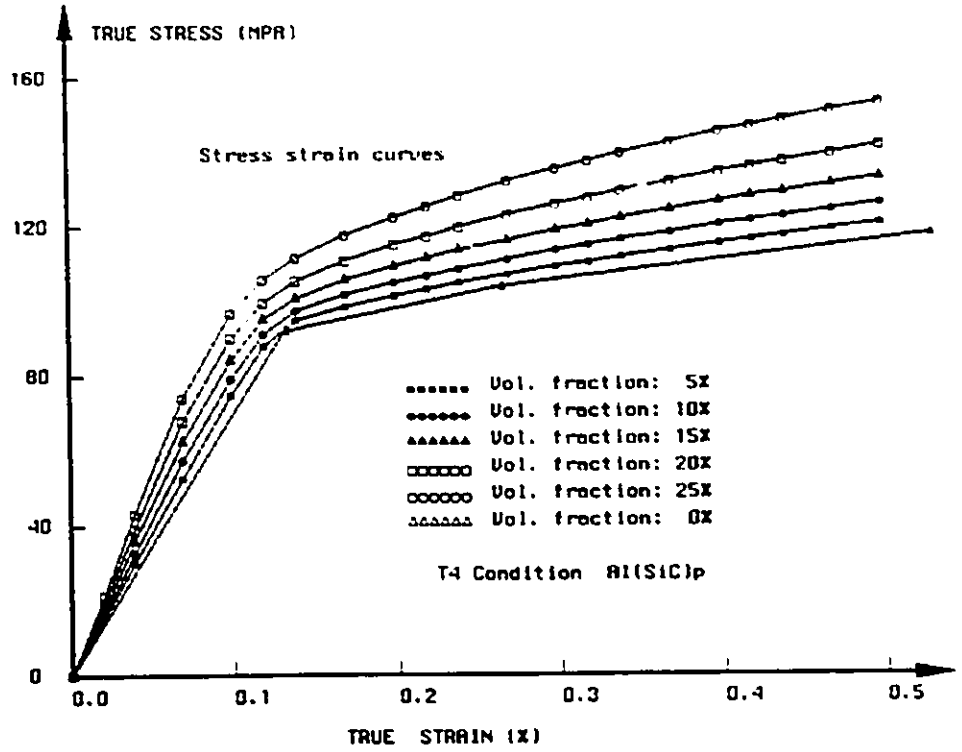

(b)

Figure 6.5 The stress strain curves predicted at different volume fractions. (a) 0%-5% overall strain; (b) 0%-0.5% overall strain.

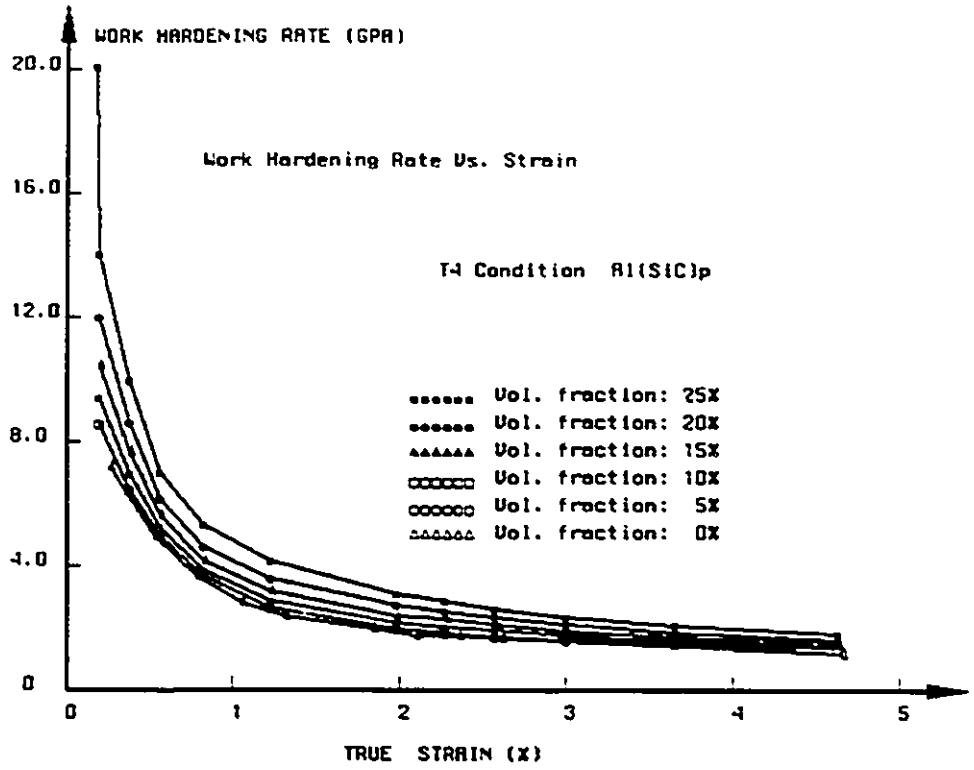

Figure 6.6 The work-hardening curves predicted at different volume fractions.

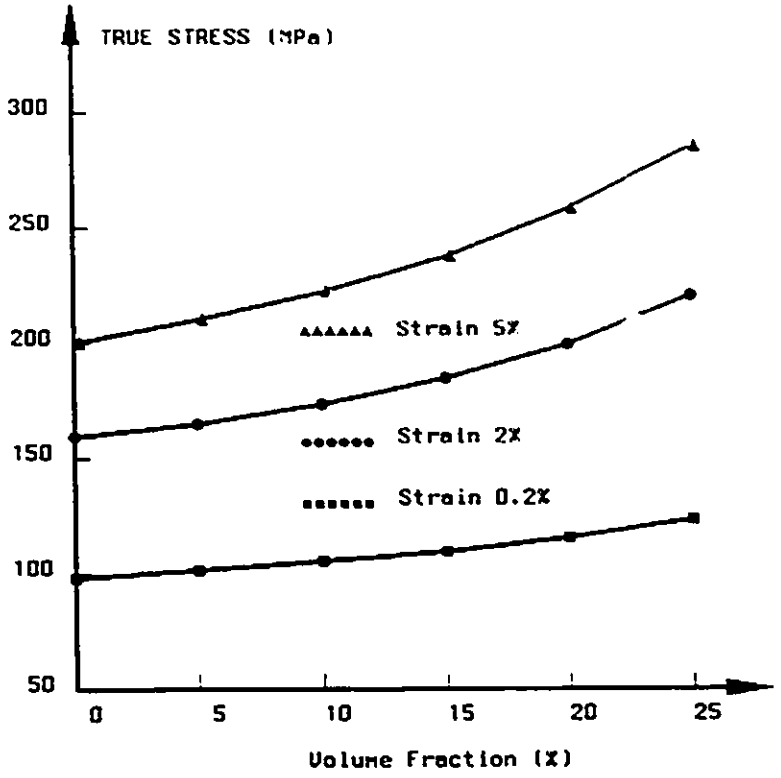

Figure 6.7 The overall stress-volume fraction curves at different overall strain levels.

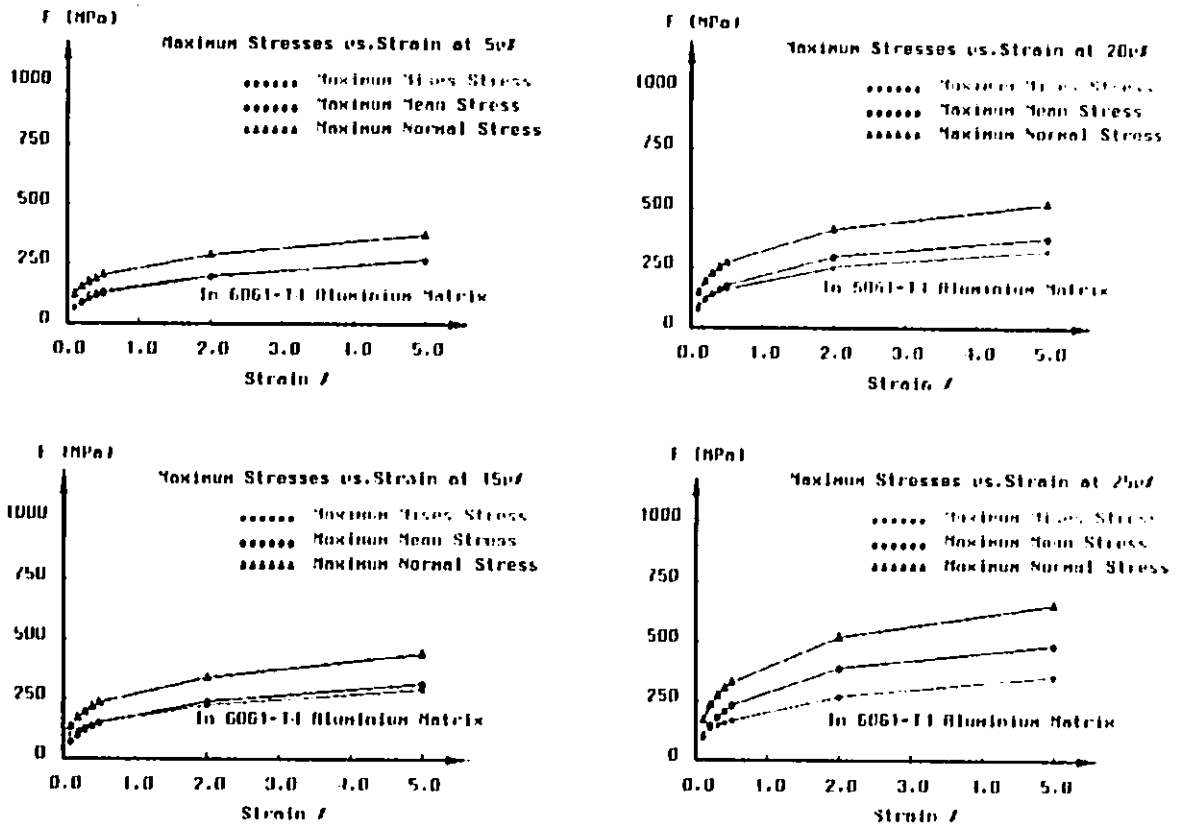

Figure 6.8 The relationship of the maximum local stresses within the aluminium matrix to the overall strain at different volume fractions.

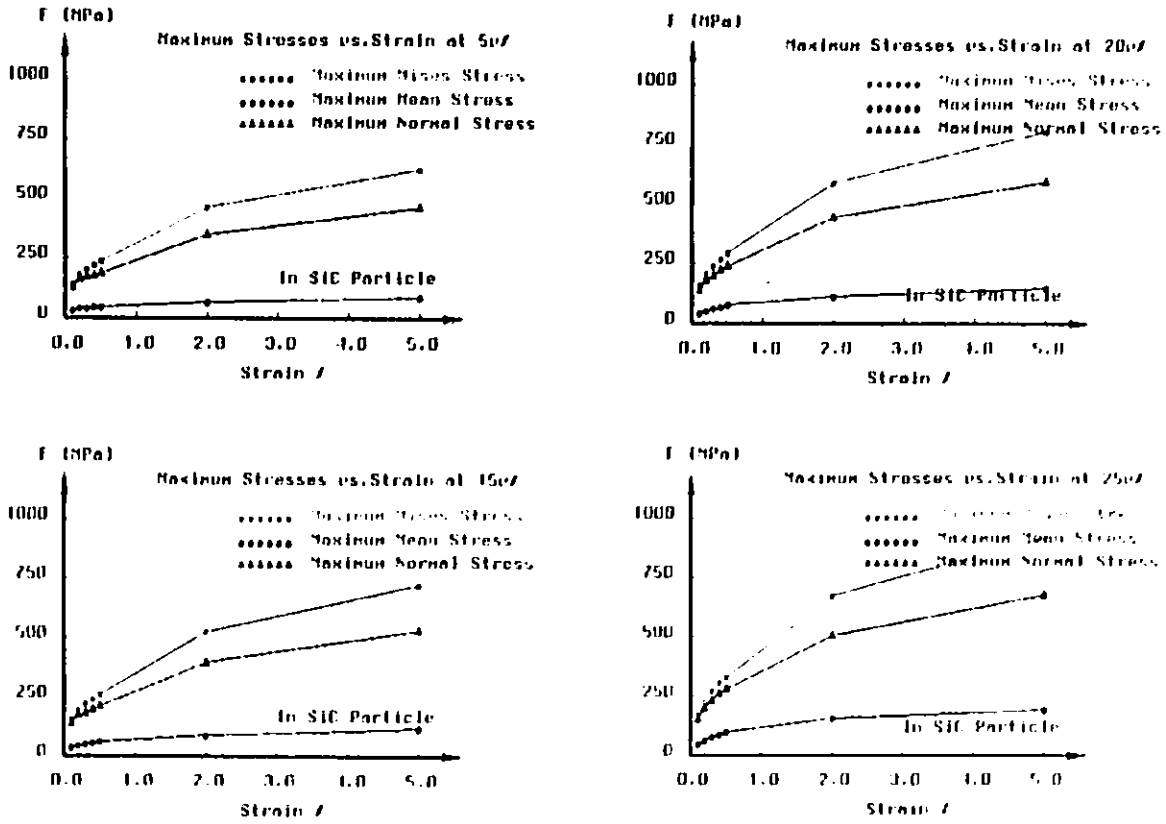

Figure 6.9 The relationship of the maximum local stresses within the SiC particles to the overall strain at different volume fractions.

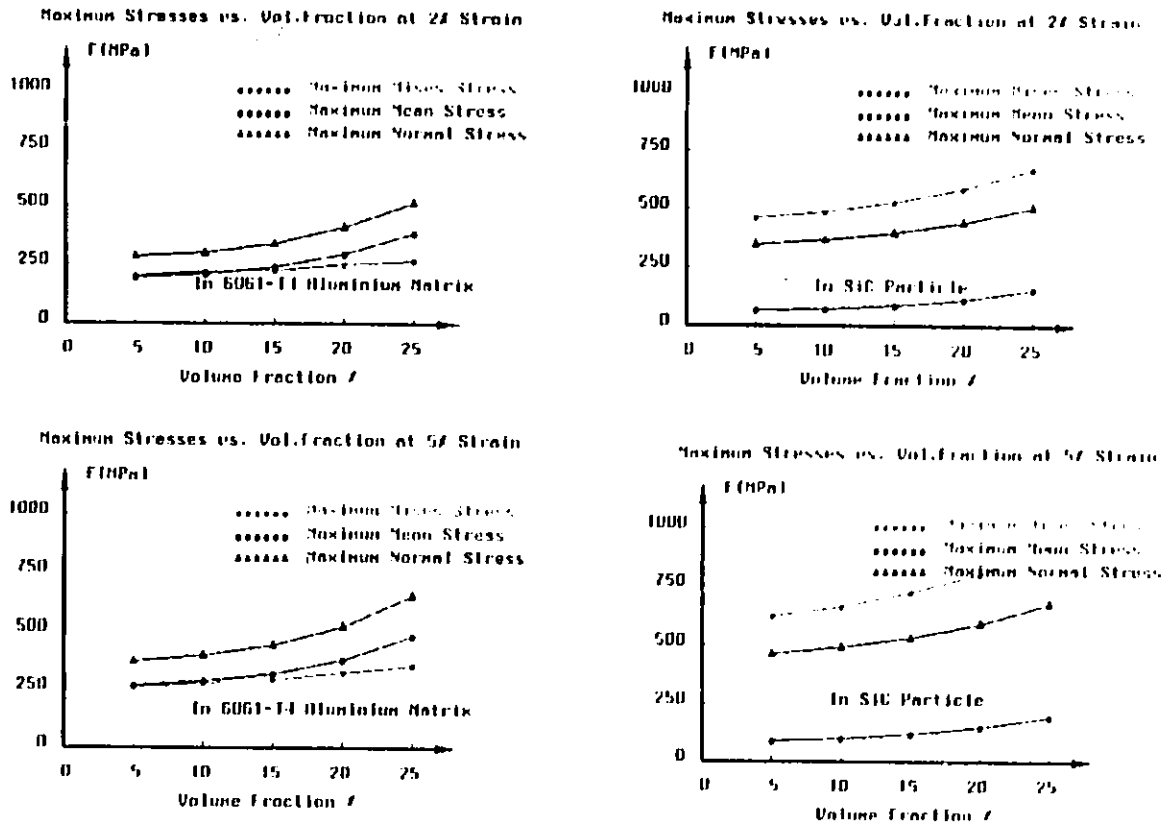

Figure 6.10 The relationship of the maximum local stresses to volume fraction at different overall strains.

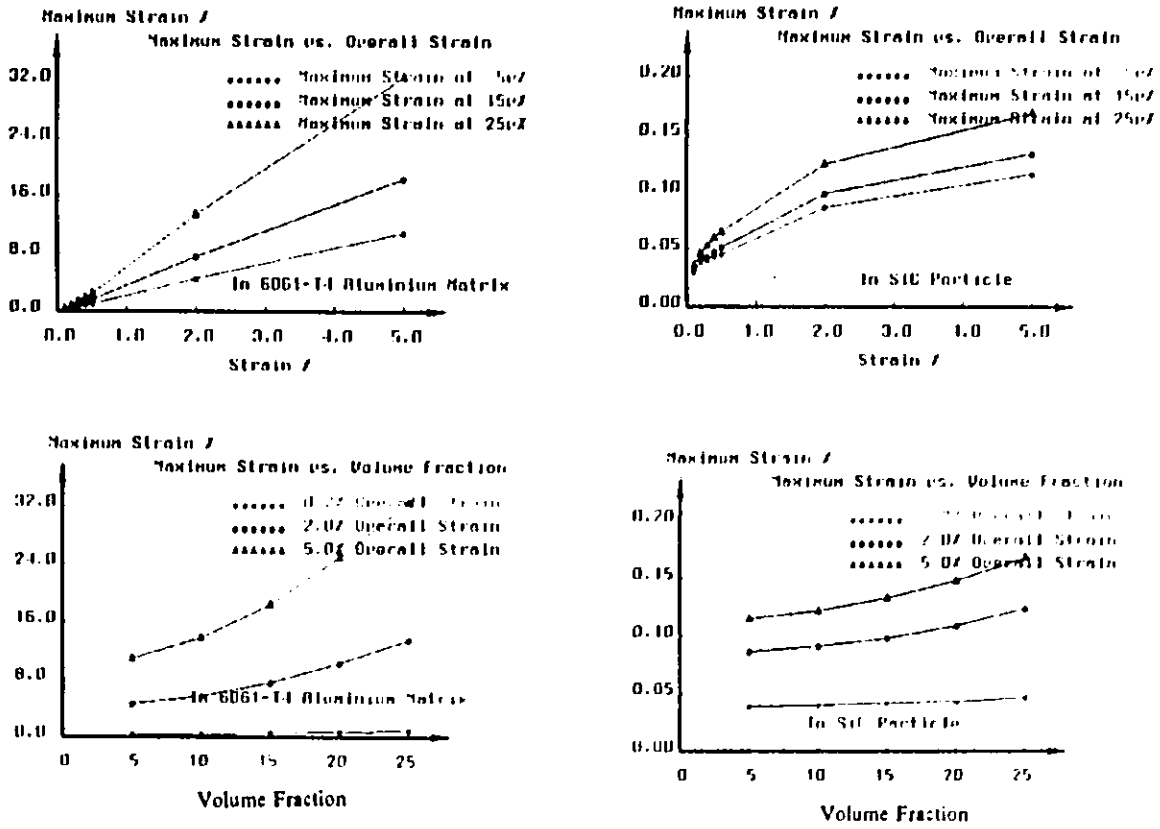

Figure 6.11 The relationships of the maximum local tensile strain to the volume fraction and to the overall strain.

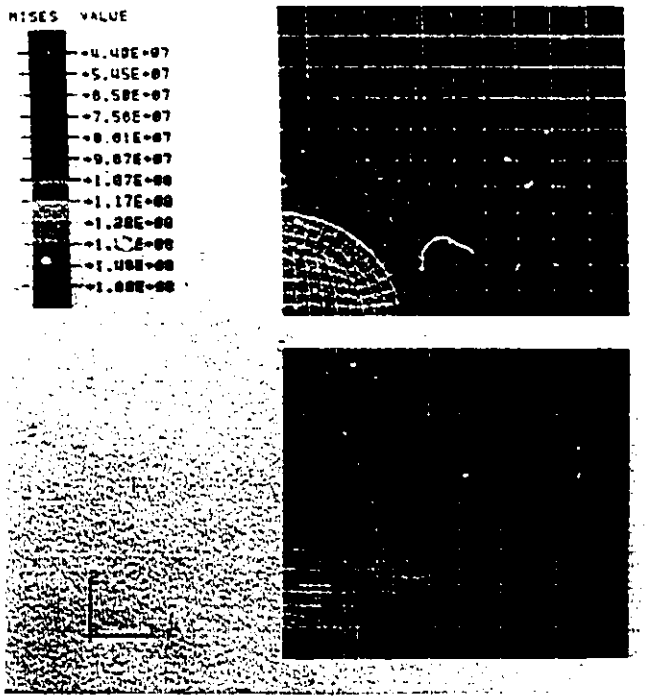

(a) The Von Mises contours.

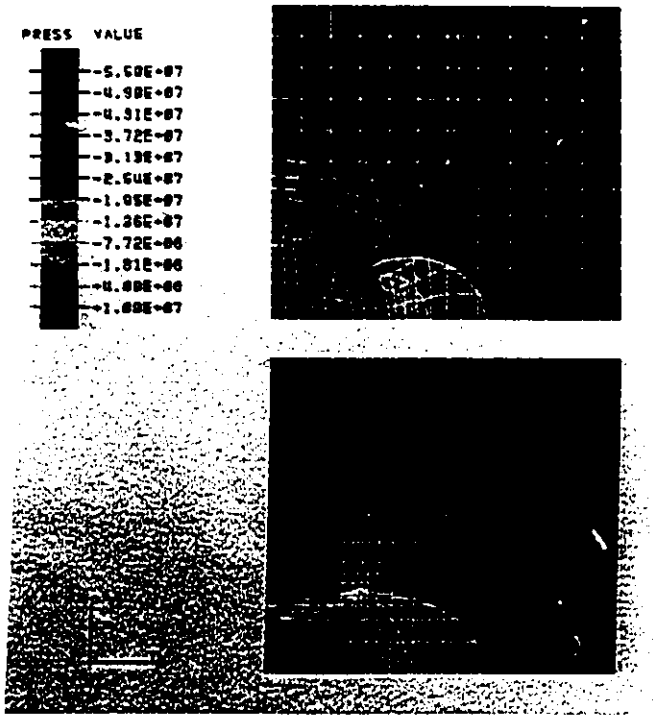

(b) The hydrostatic pressure contours.

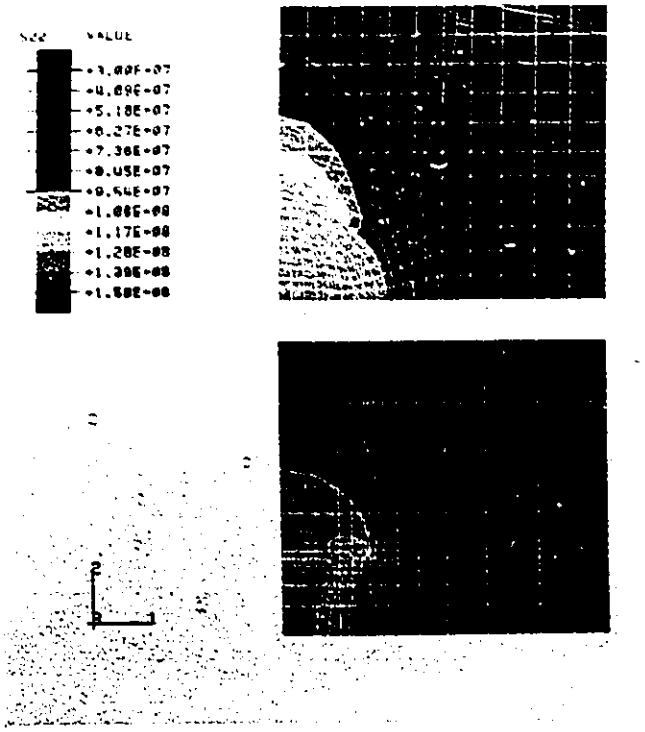

(c) The tensile stress contours.

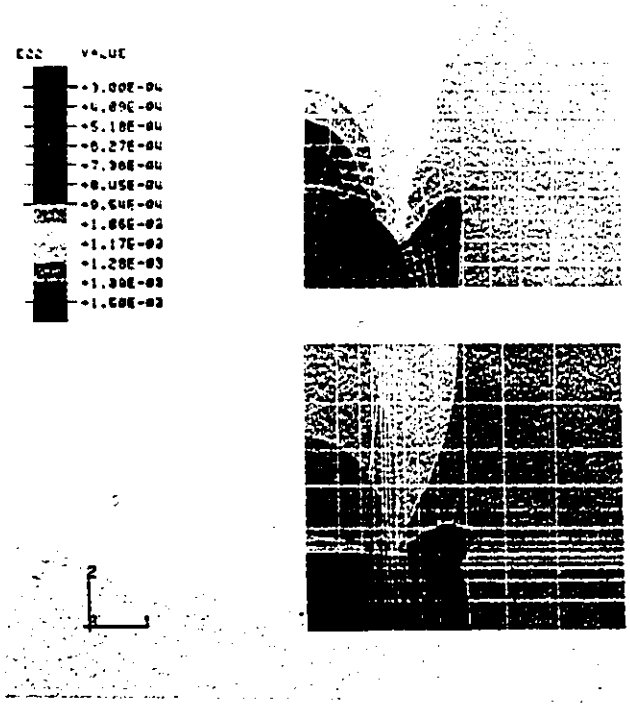

(d) The tensile strain contours.

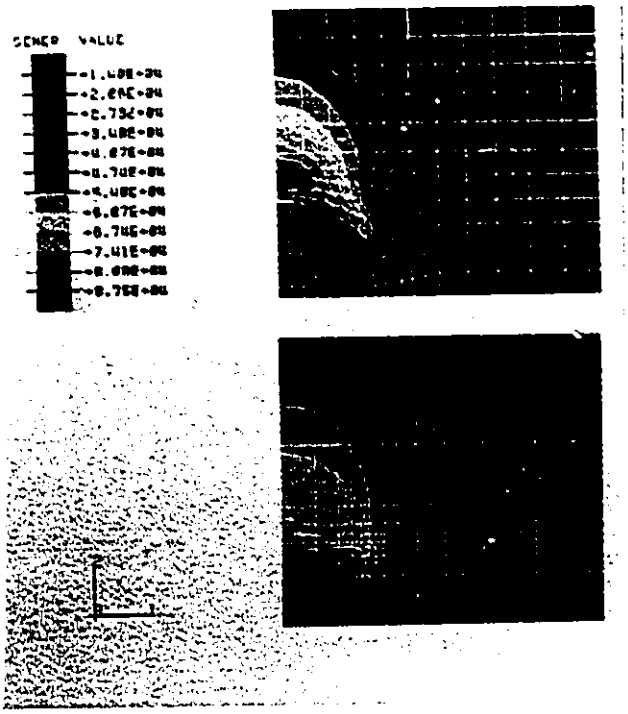

(e) The strain energy density contours.

Figure 6.12 A comparison of the component contours in 6061-T4 Al/$(SiC)_p$ MMCs with 1.94% volume fraction of particles: (i) spherical particles (upper figure); (ii) cubic particles (lower figure).

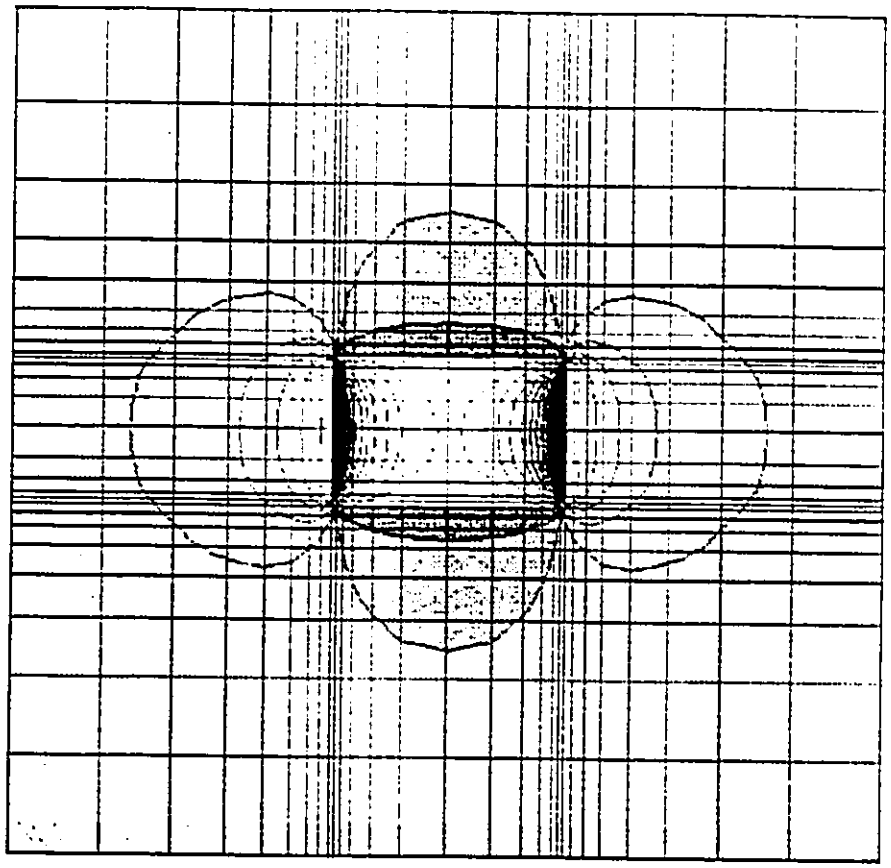

(a) long particles.

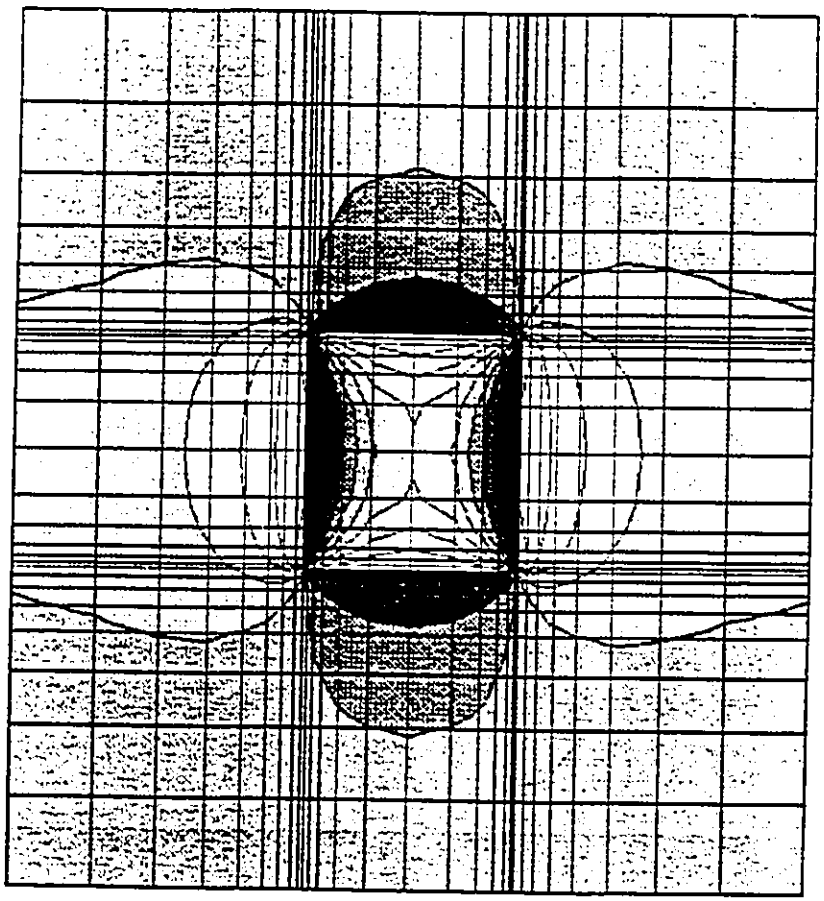

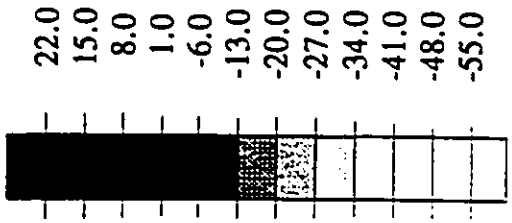

(b) cubic particles.

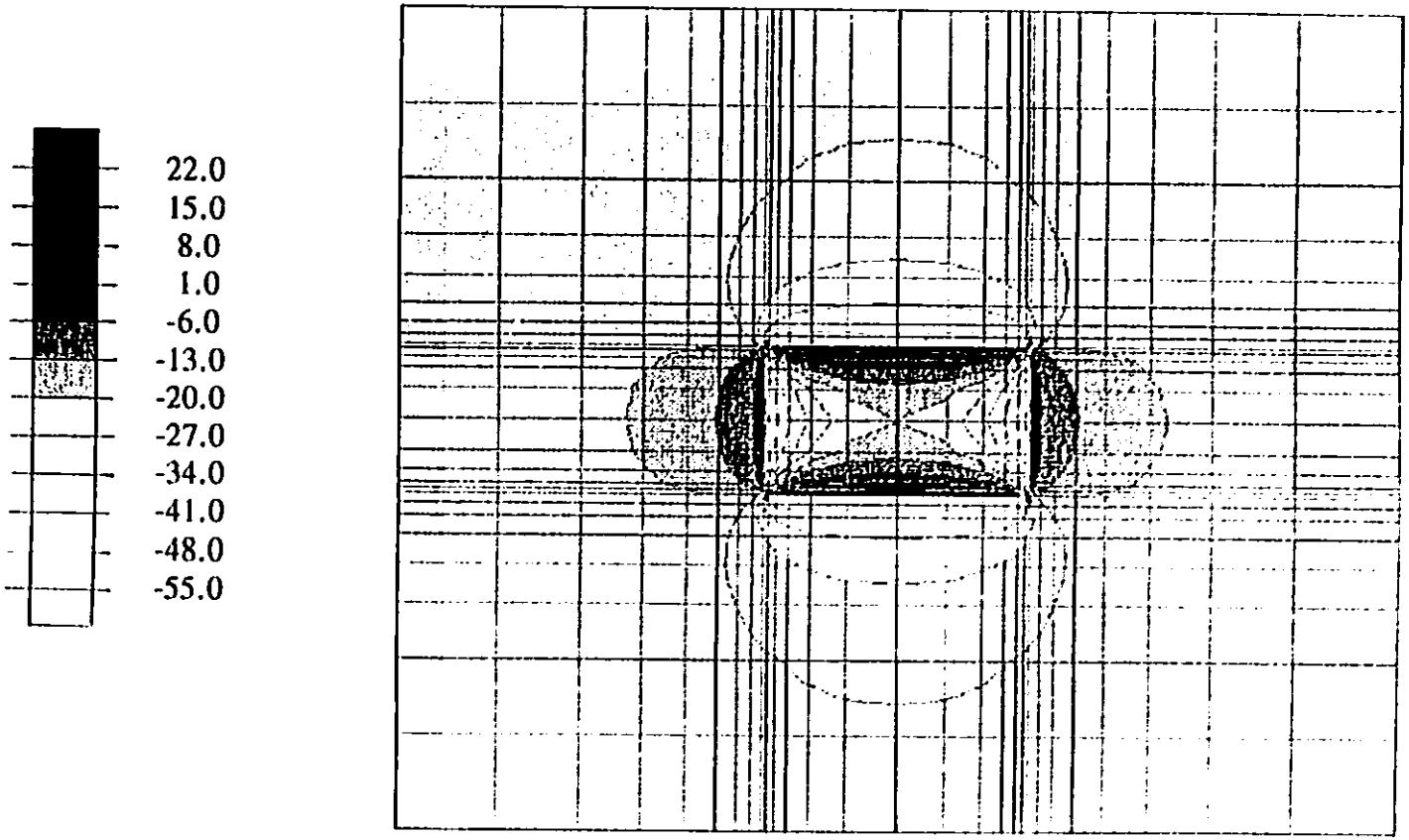

(c) short particles.

Figure 6.13 A comparison of the hydrostatic pressure contours in 6061-T4 Al/$(SiC)_p$ with different aspect ratios.

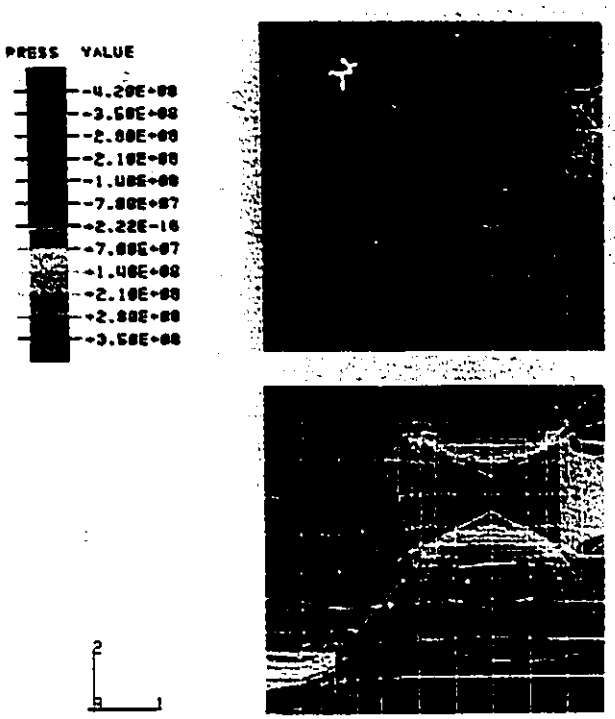

(a) The hydrostatic pressure contours.

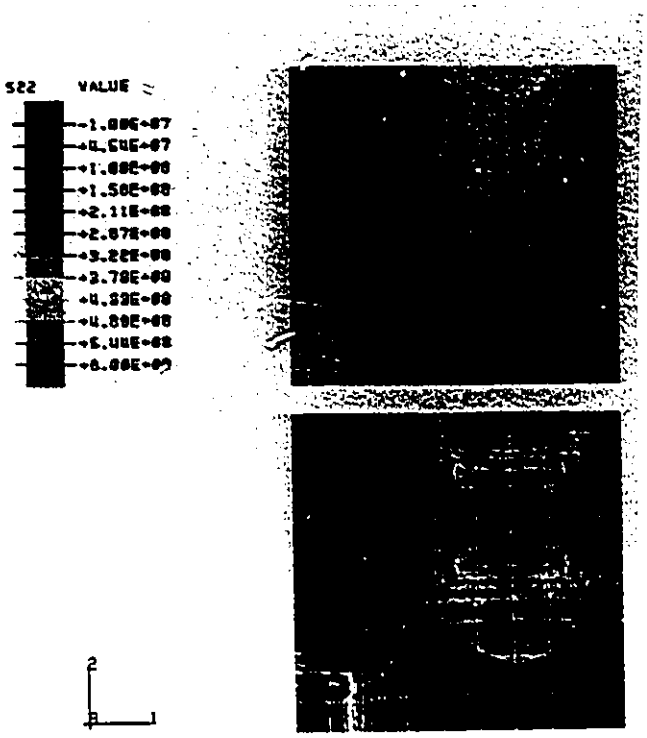

(b) The tensile stress contours.

Figure 6.14 A comparison of the component contours in 6061-T4 Al/$(SiC)_p$ with 6.18% volume fraction of particles: (i) spherical particles (upper figure); (ii) cubic particles (lower figure).

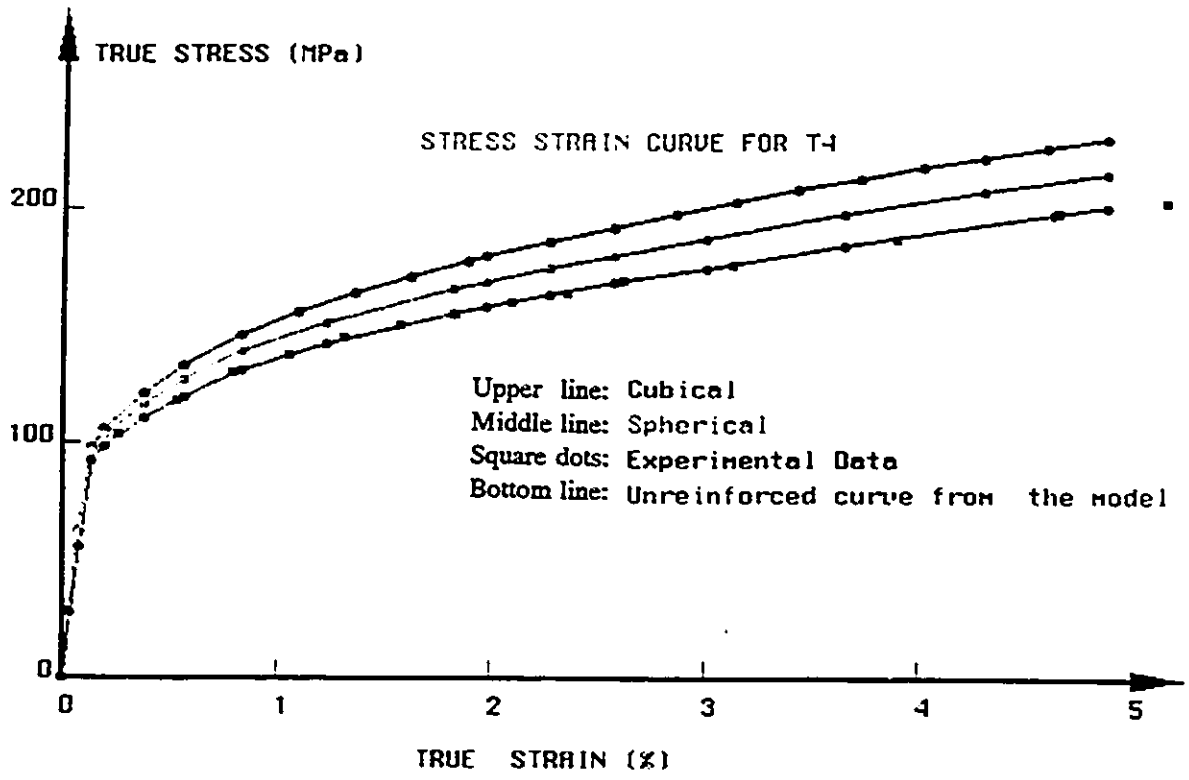
TRUE STRESS (MPa)
STRESS STRAIN CURVE FOR T-4
200
100
0
Upper line: Cubical
Middle line: Spherical
Square dots: Experimental Data
Bottom line: Unreinforced curve from the model
0
1
2
3
4
5
TRUE STRAIN (%)

(a)

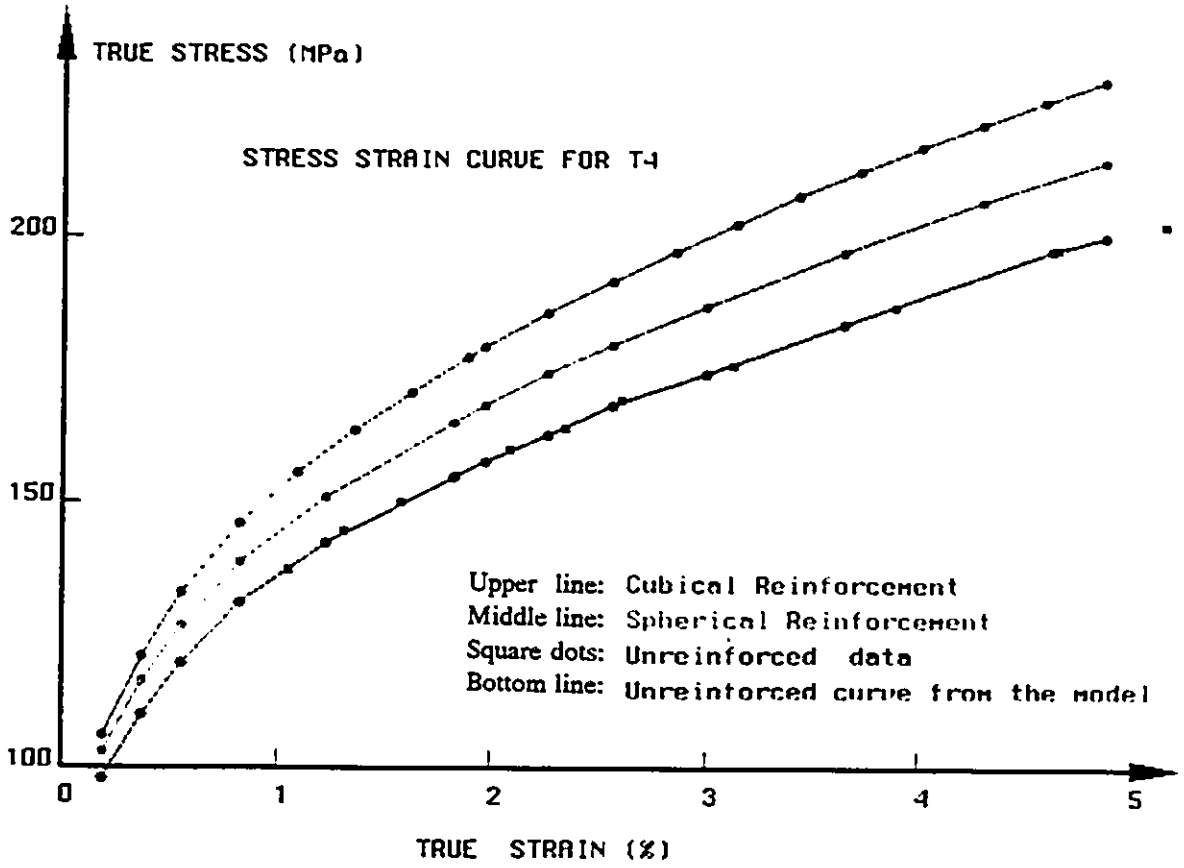

(b)

Figure 6.15 The overall stress strain curves with different particle shape: (a) entire stress range; (b) partial stress range.

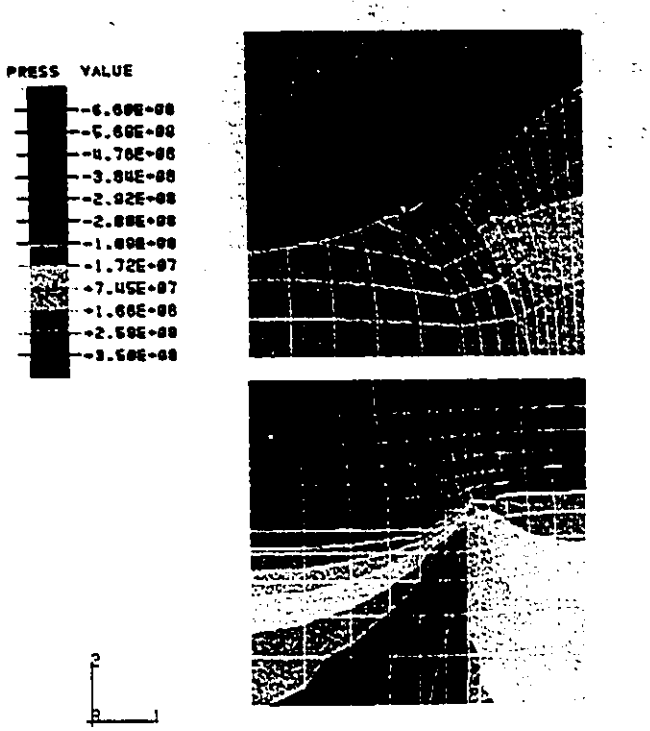

(a) The hydrostatic pressure contours.

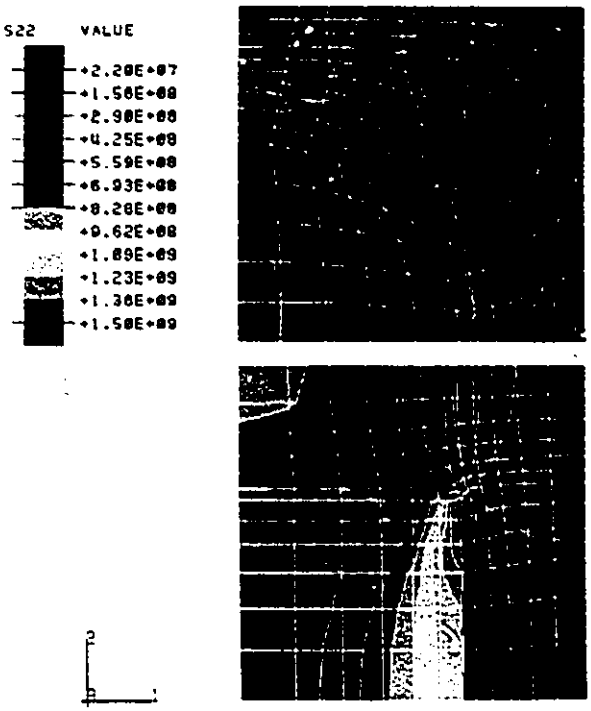

(b) The tensile stress contours.

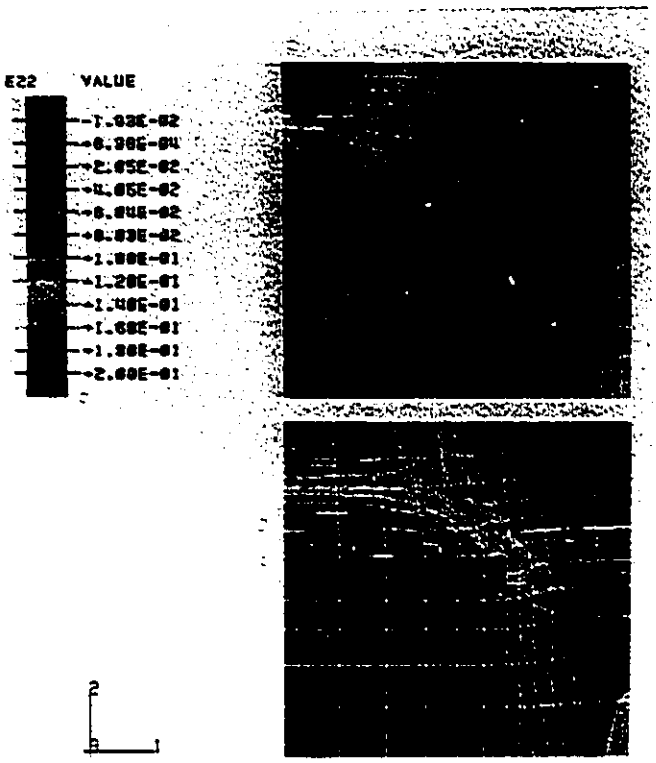

(c) The tensile strain contours.

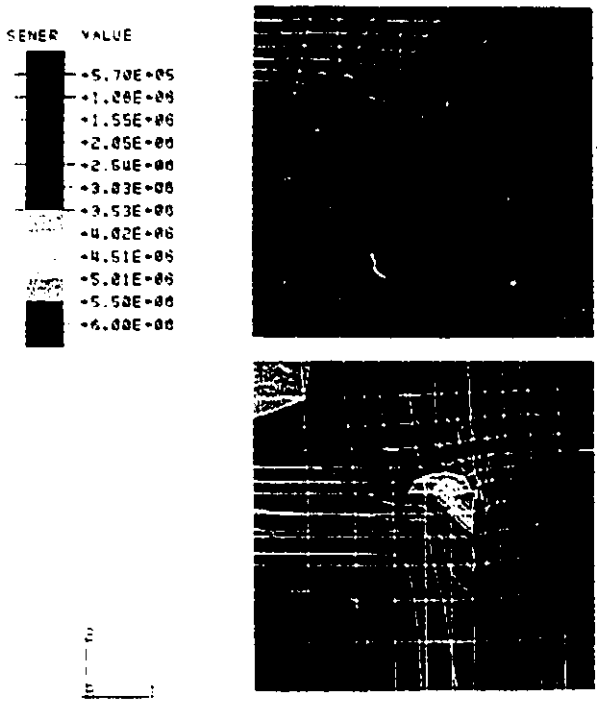

(d) The strain energy density contours.

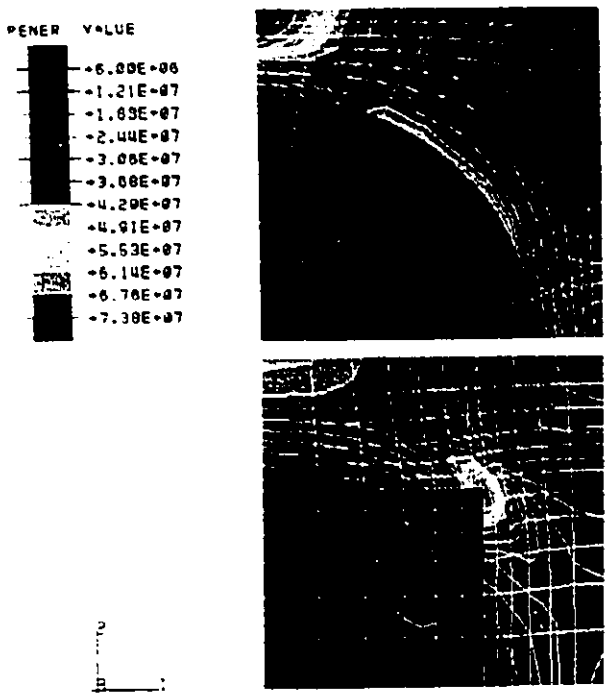

(e) The plastic energy density contours.

Figure 6.16 A comparison of the component contours in 6061-T4 Al/$(SiC)_p$ with 25% volume fraction of particles: (i) spherical particles (upper figure); (ii) cubic particles (lower figure).

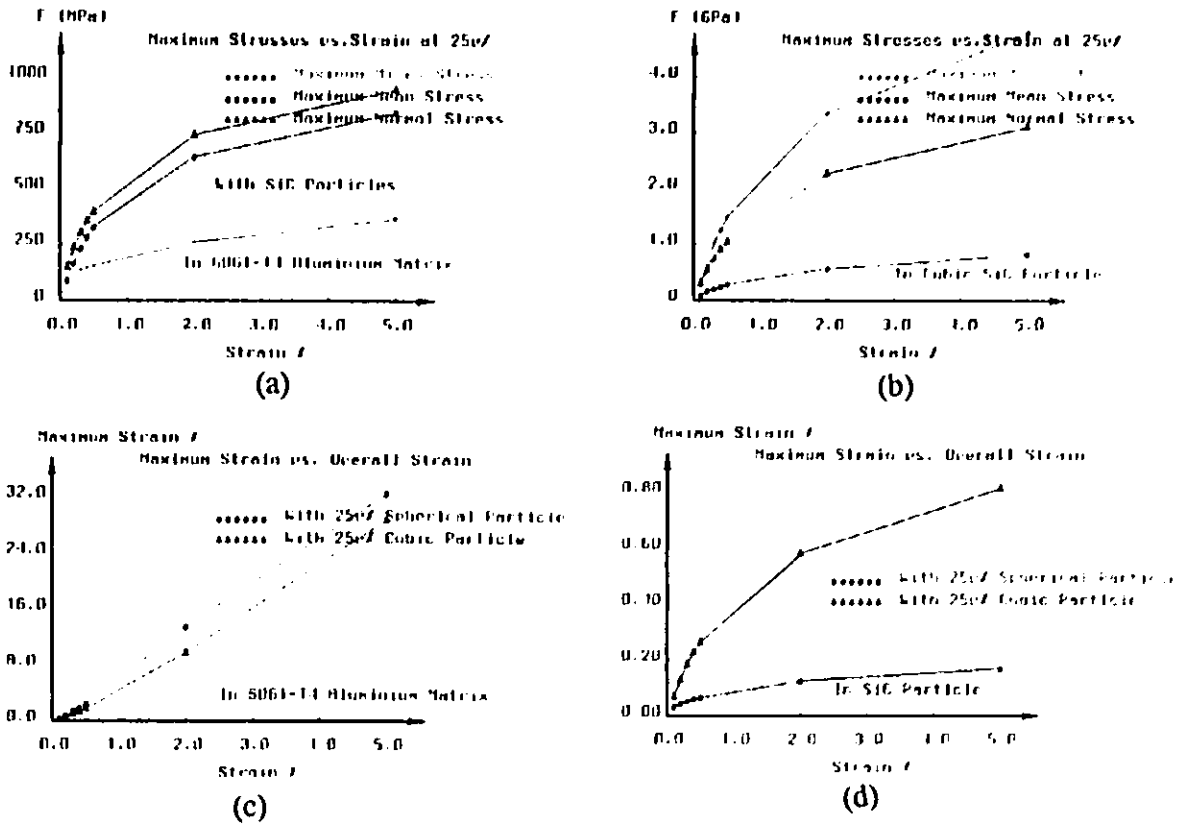

Figure 6.17 The relationship of the maximum local components to the overall strain: (a) stresses in the matrix with cubic particles; (b) stresses within cubic particles; (c) strain in the matrix with cubic or spherical particles; (d) strain within cubic particle and spherical particle.

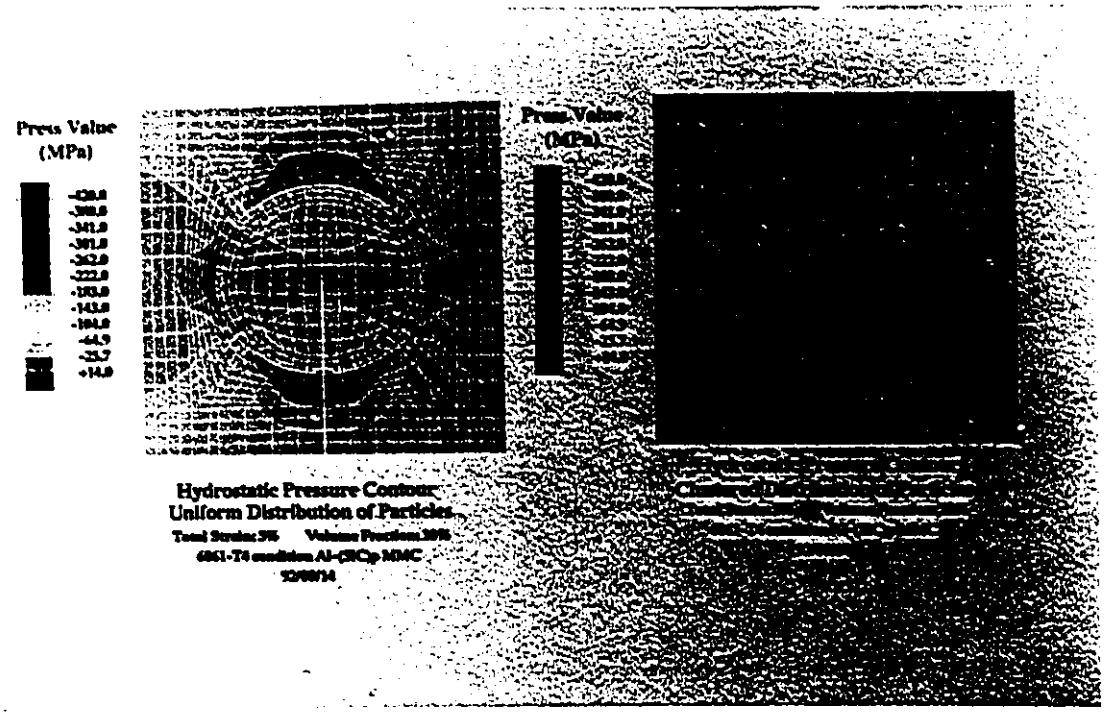

(a) The hydrostatic pressure contours.

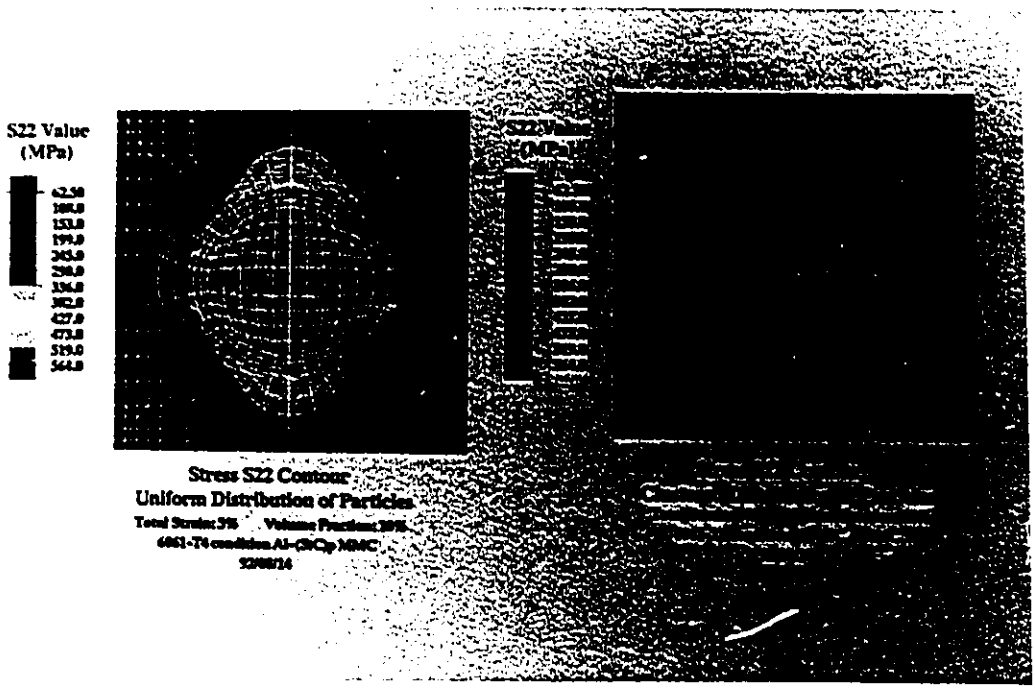

(b) The tensile stress contours.

Figure 6.18 Effect of tensile clustering on the component contours in 6061-T4 Al/$(SiC)_p$ MMCs with 10% volume fraction at 5.0% engineering strain.

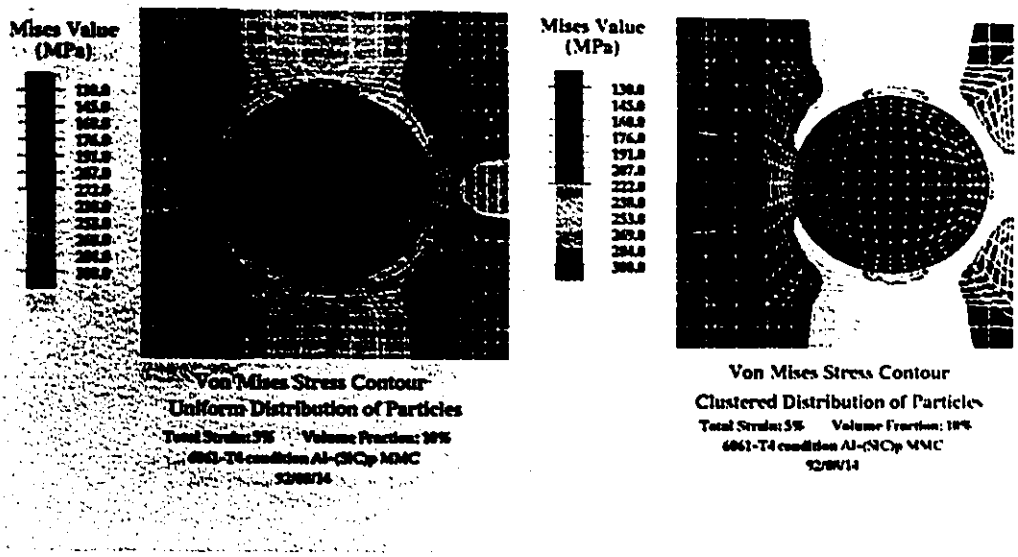

(a) The Von Mises stress contours.

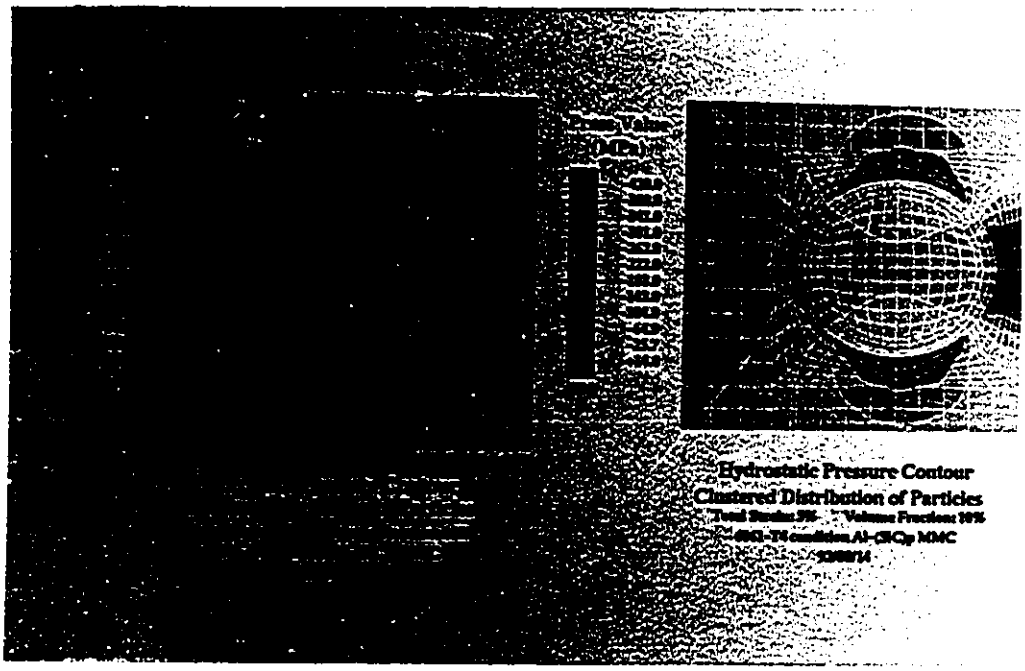

(b) The hydrostatic pressure contours.

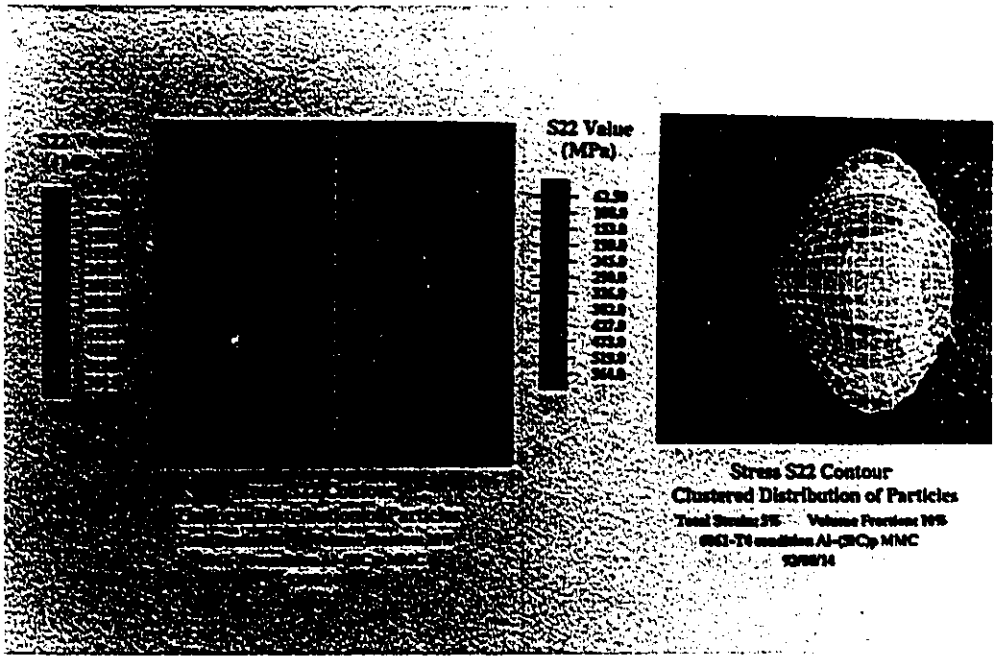

(c) The tensile stress contours.

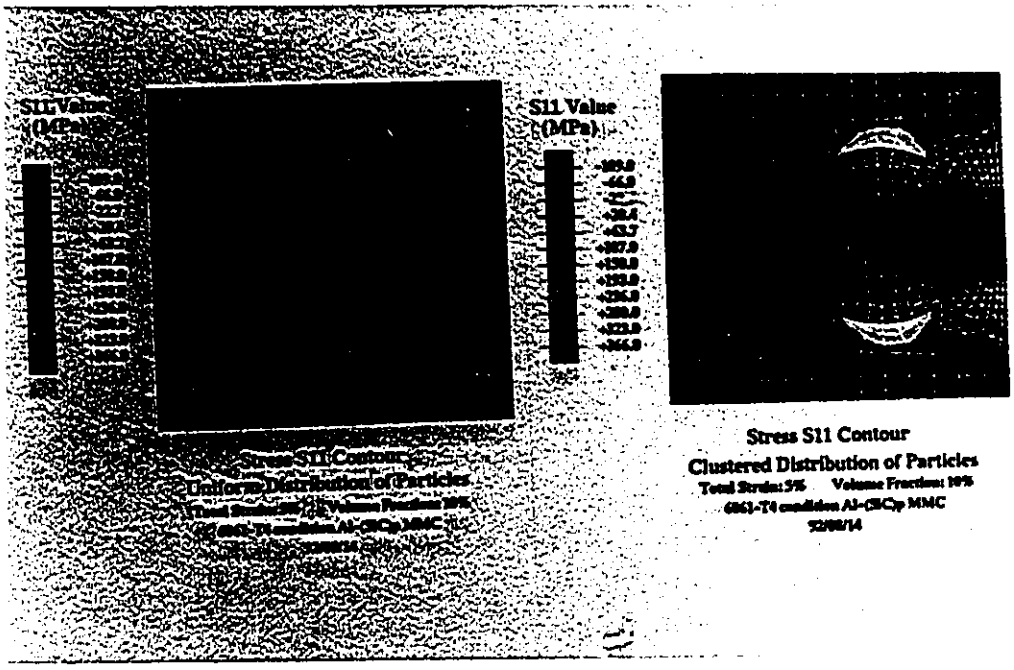

(d) The transverse stress contours.

Figure 6.19 Effect of side clustering on the component contours in 6061-T4 Al/$(SiC)_p$ MMCs with 10% volume fraction at 5.0% engineering strain.

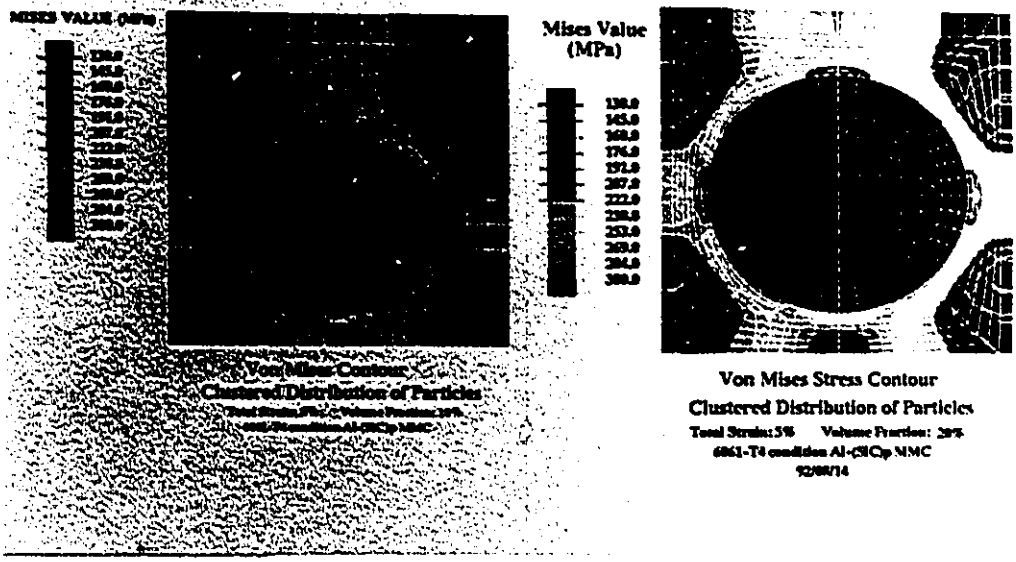

(a) The Von Mises stress contours.

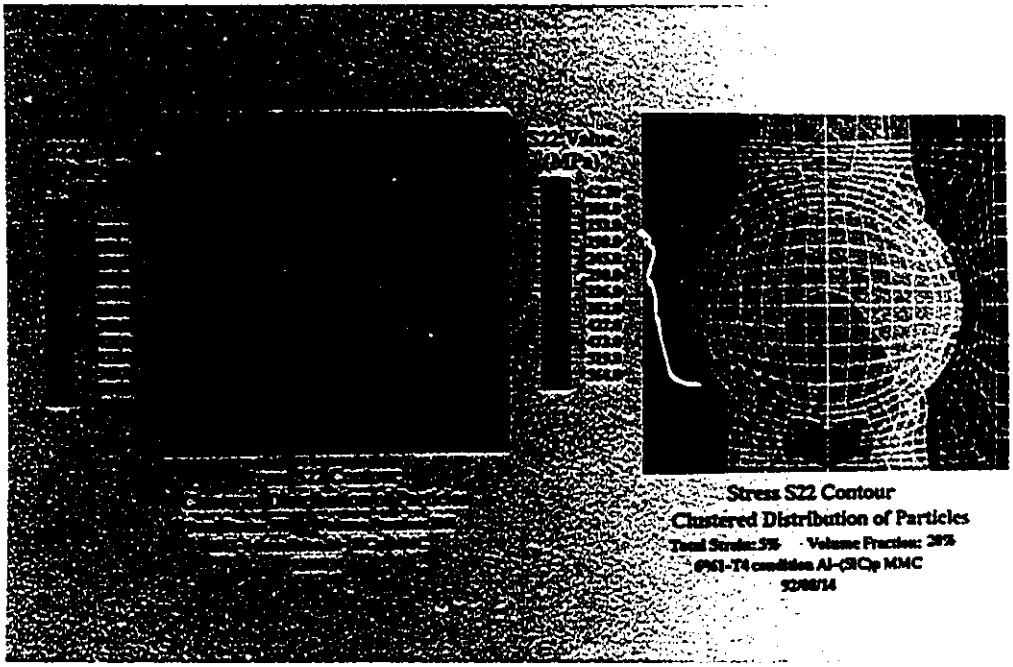

(b) The tensile stress contours.

Figure 6.20 A comparison of the effect of tensile clustering on the component contours in 6061-T4 Al/$(SiC)_p$ MMCs at 5.0% engineering strain with 10% and 20% volume fractions.

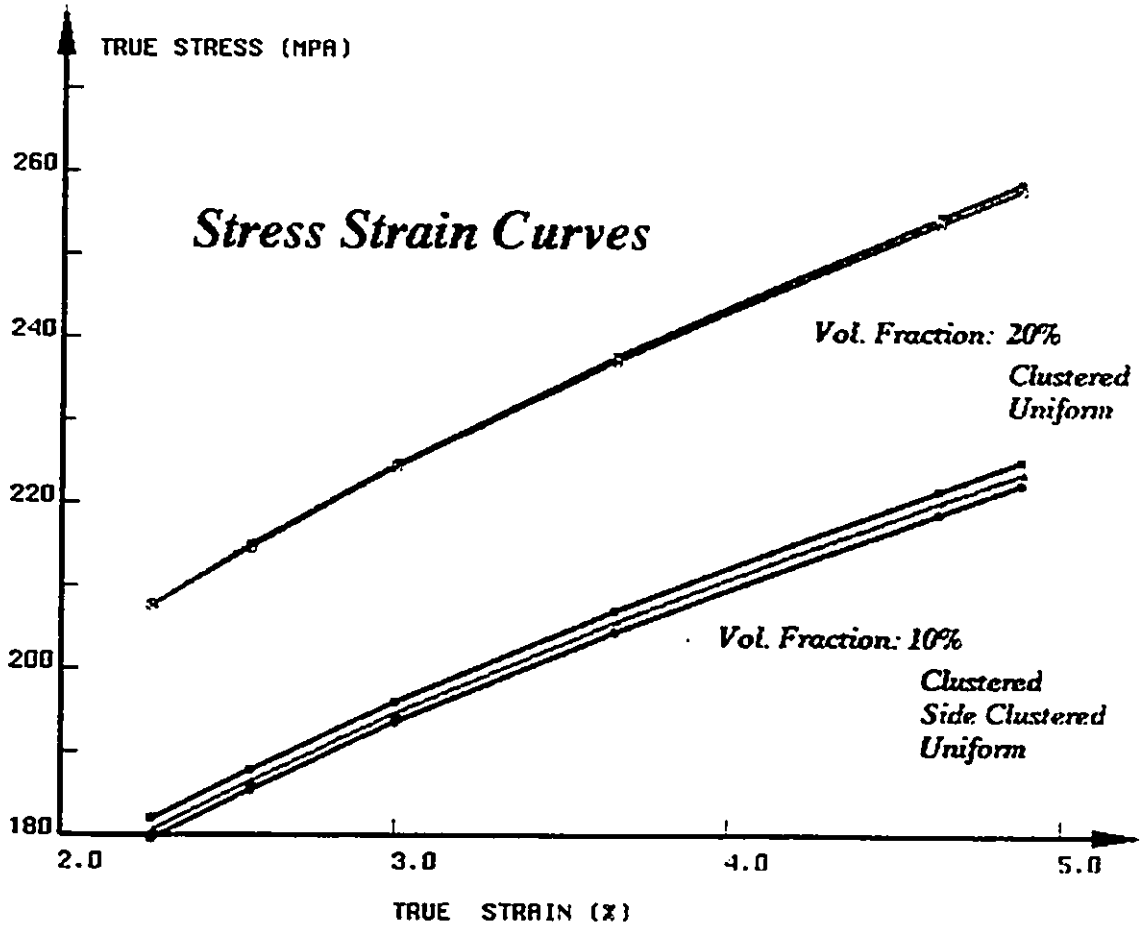

Figure 6.21 The overall stress strain curves with clustered and uniform particles

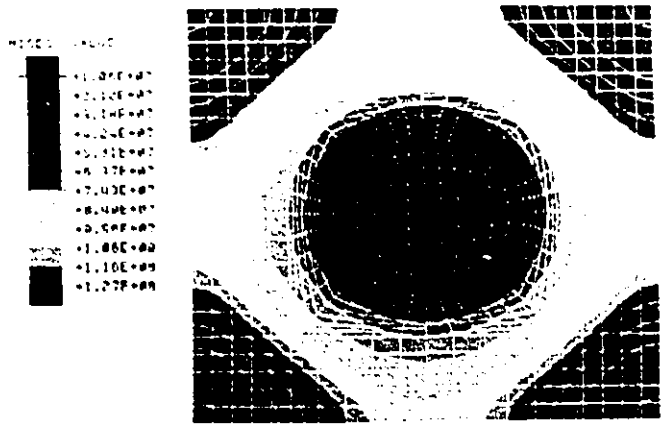

(a) The Von Mises stress contours.

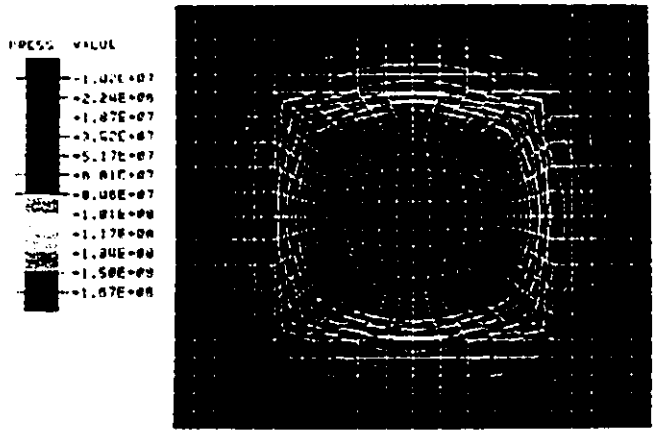

(b) The hydrostatic pressure contour.

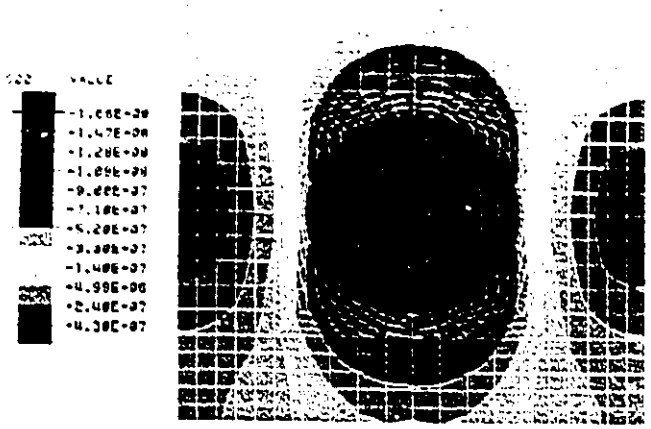

(c) The tensile stress contour.

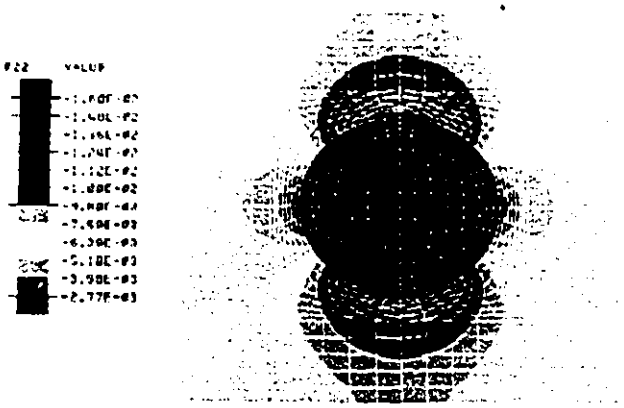

(d) The tensile strain contour.

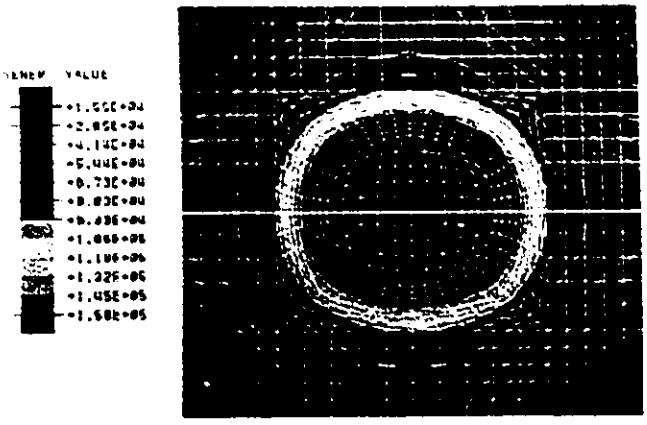

(e) The strain energy density contour.

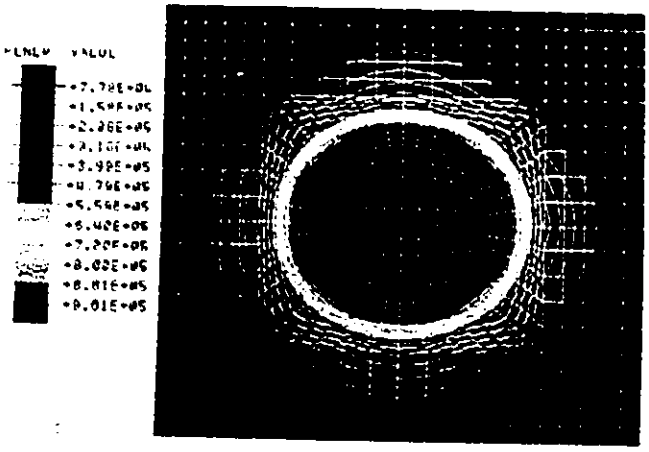

(f) The plastic energy density contour.

Figure 7.1 Effect of the thermal contraction on component contours in 6061-T4 Al/$(SiC)_p$ with 5% volume fraction.

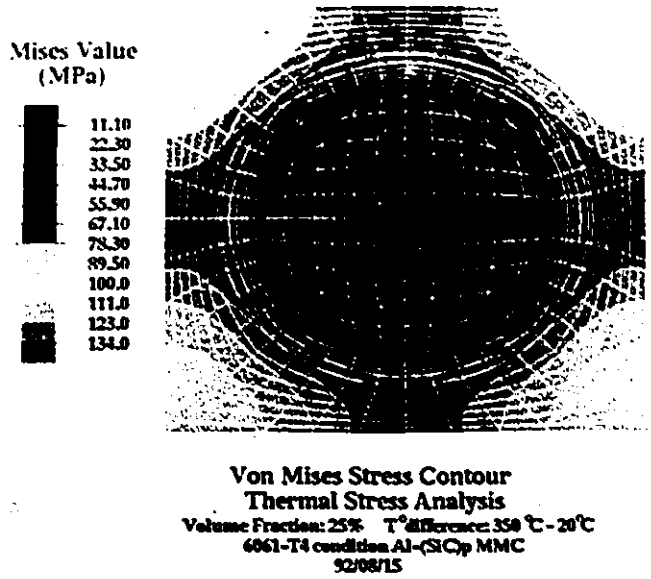

(a) The Von Mises stress contour.

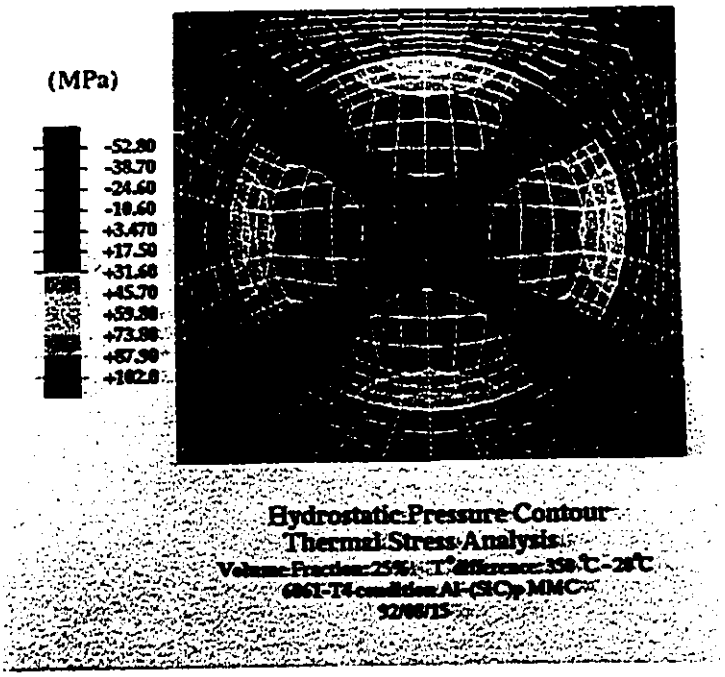

(b) The hydrostatic pressure contour.

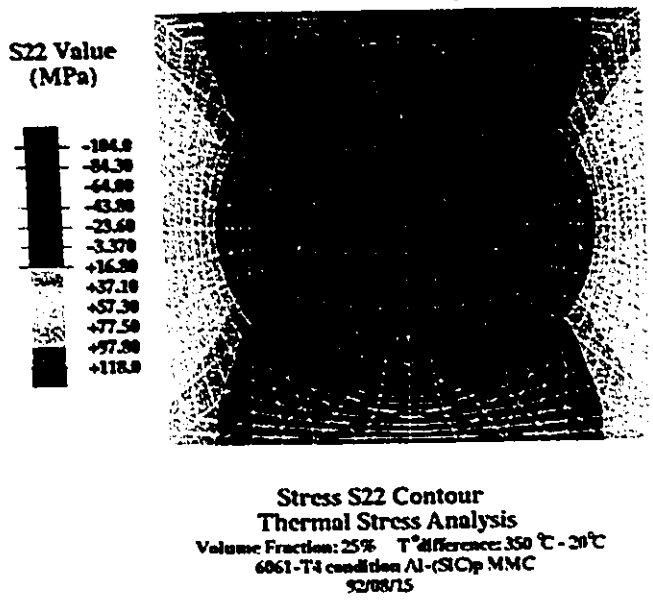

(c) The tensile stress contour.

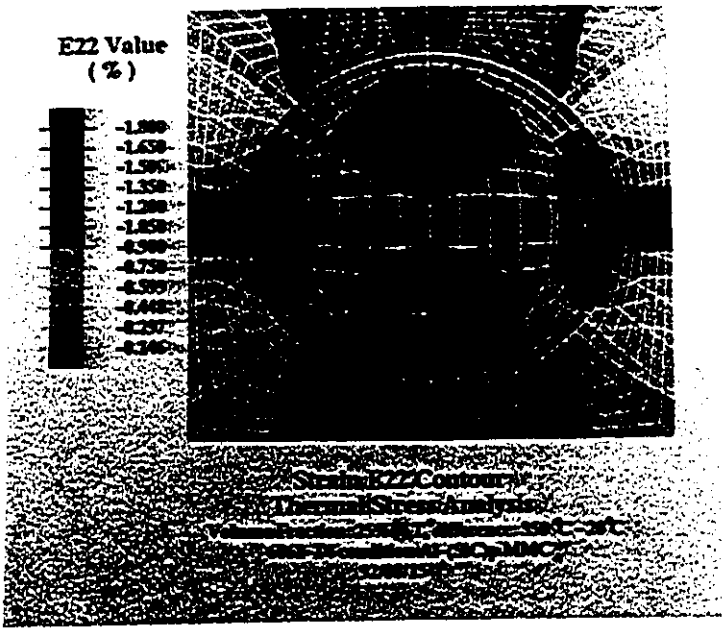

(d) The tensile strain contour.

Figure 7.2 Effect of the thermal contraction on component contours in 6061-T4 Al/$(SiC)_p$ with 25% volume fraction.

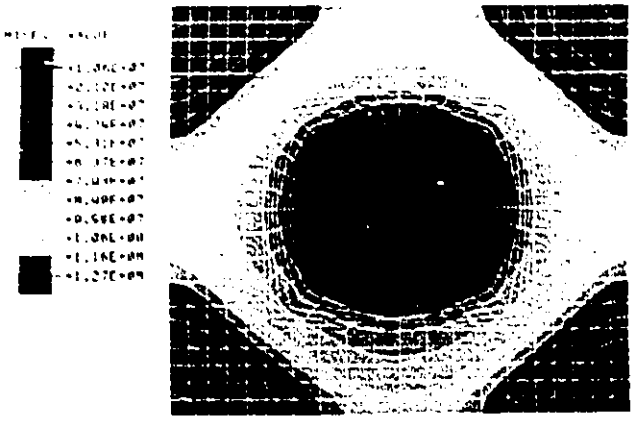

(a) at 0.0% engineering strain.

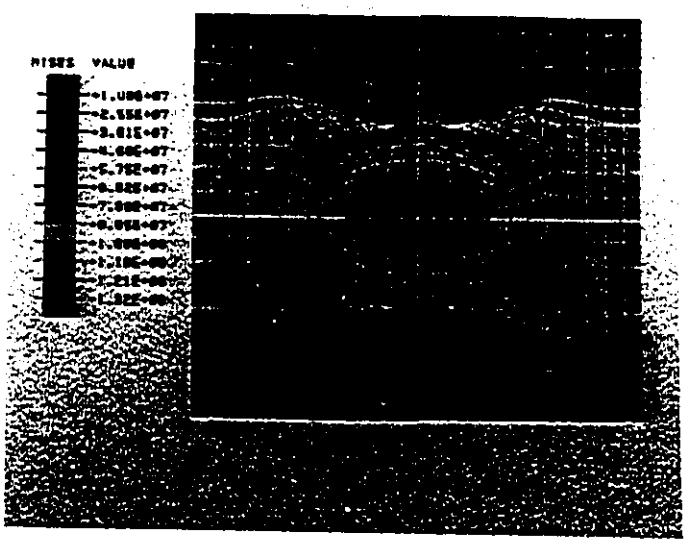

(b) at 0.1% engineering strain.

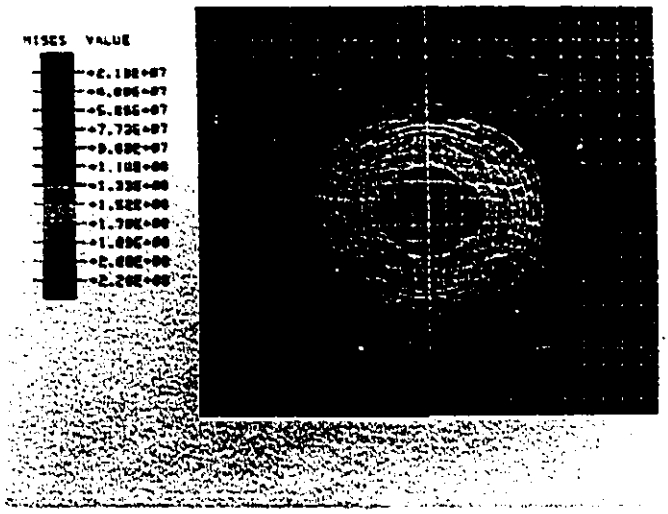

(c) at 0.2% engineering strain.

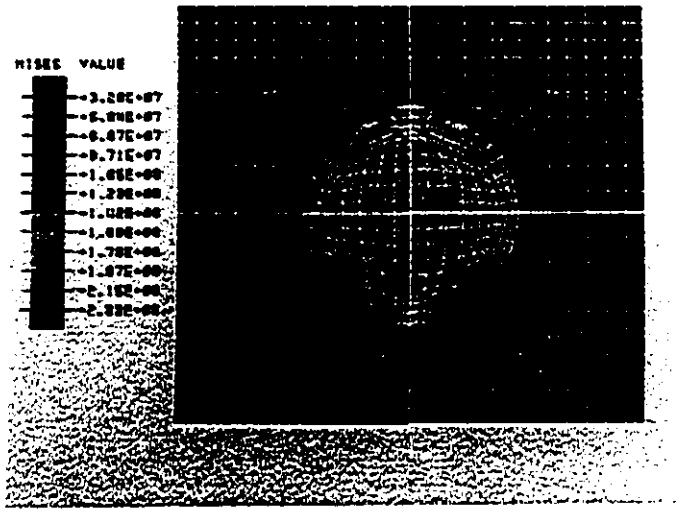

(d) at 0.3% engineering strain.

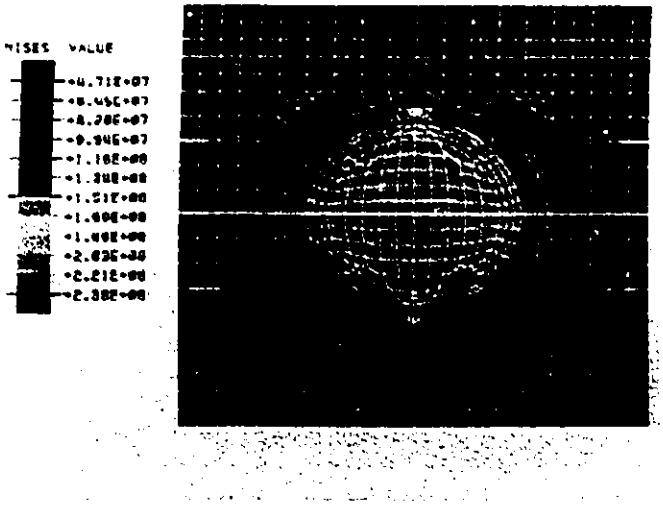

(e) at 0.4% engineering strain.

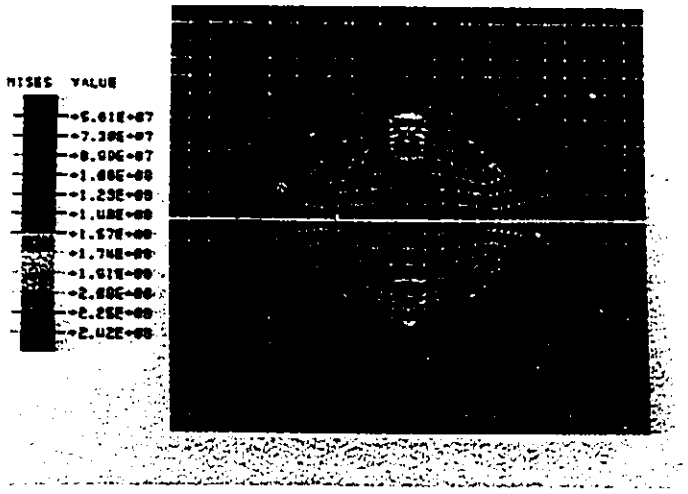

(f) at 0.5% engineering strain.

Figure 7.3 The Von Mises stress redistribution with increase of the tensile loading in 6061-T4 Al/$(SiC)_p$ with 5% volume fraction.

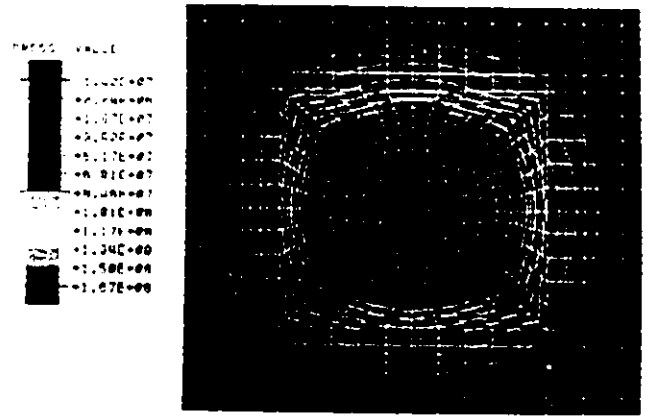

(a) at 0.0% engineering strain.

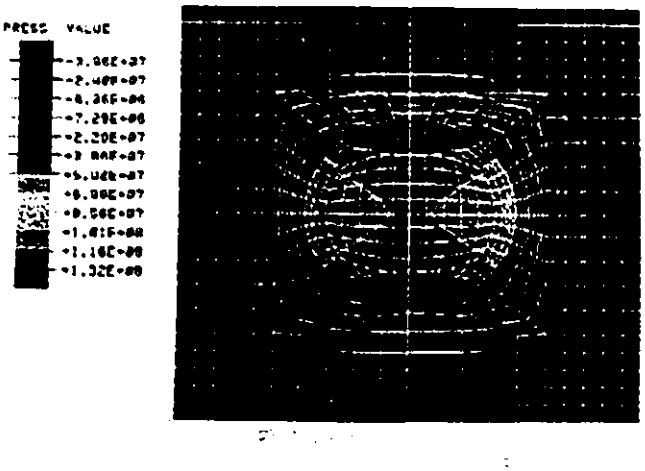

(b) at 0.1% engineering strain.

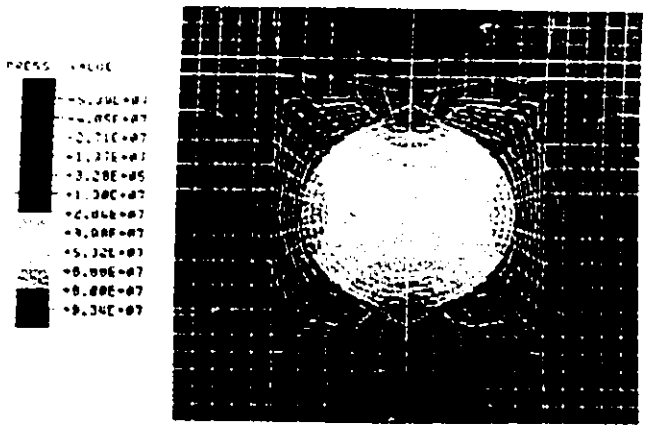

(c) at 0.2% engineering strain.

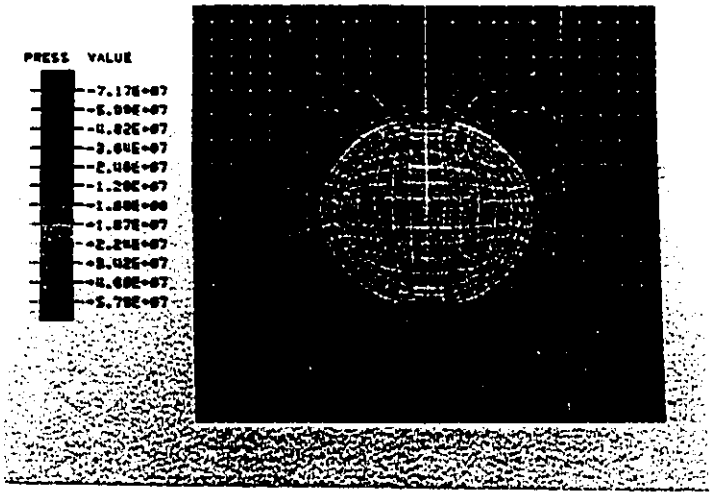

(d) at 0.3% engineering strain.

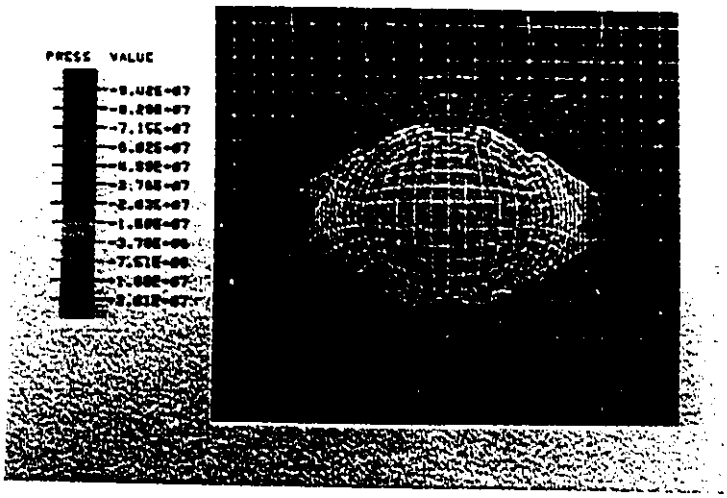

(e) at 0.4% engineering strain.

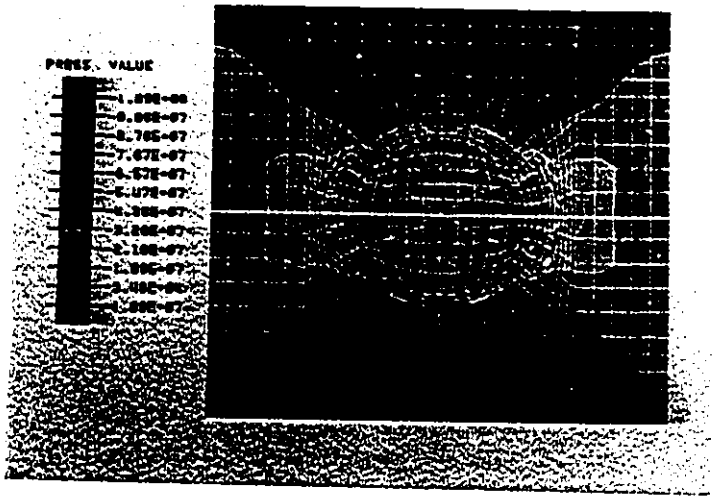

(f) at 0.5% engineering strain.

Figure 7.4 The hydrostatic pressure redistribution with increase of the tensile loading in 6061-T4 Al/$(SiC)_p$ with 5% volume fraction.

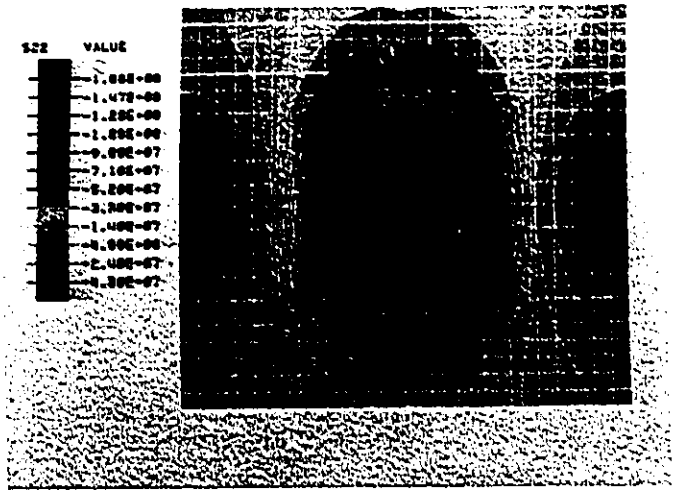

(a) at 0.0% engineering strain.

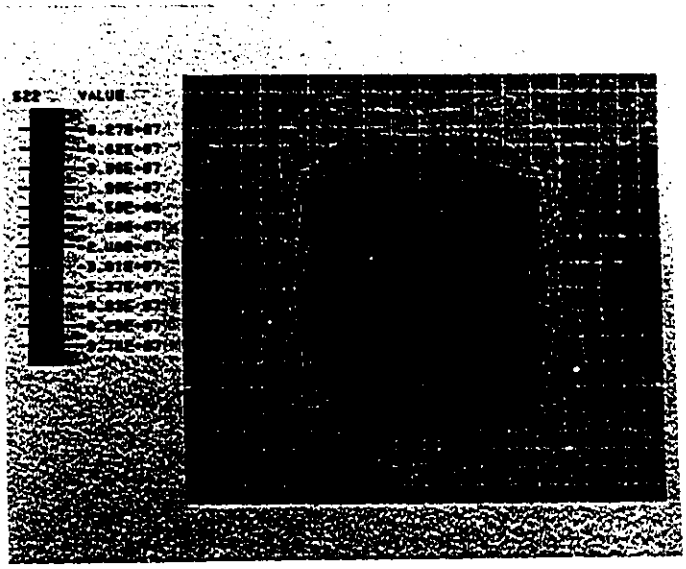

(b) at 0.1% engineering strain.

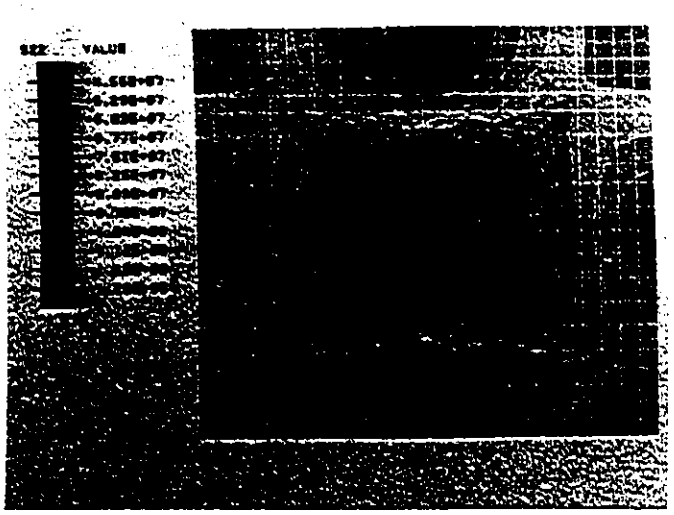

(c) at 0.2% engineering strain.

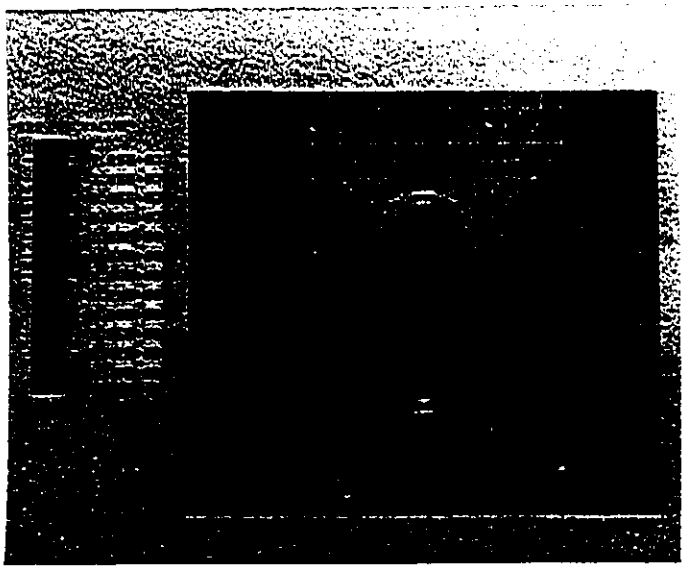

(d) at 0.3% engineering strain.

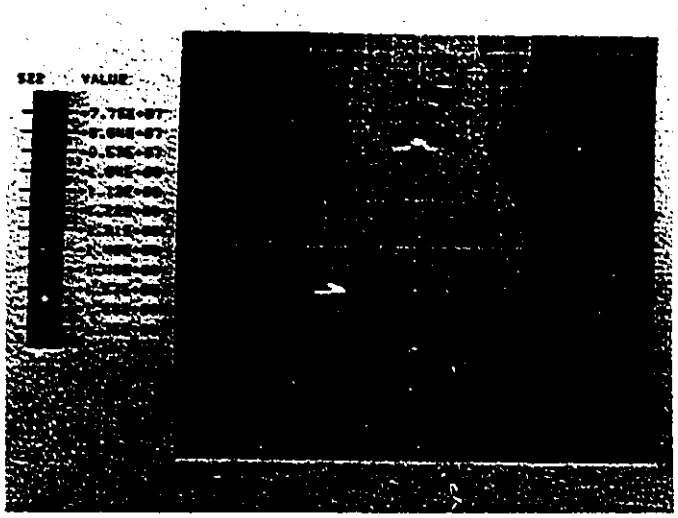

(e) at 0.4% engineering strain.

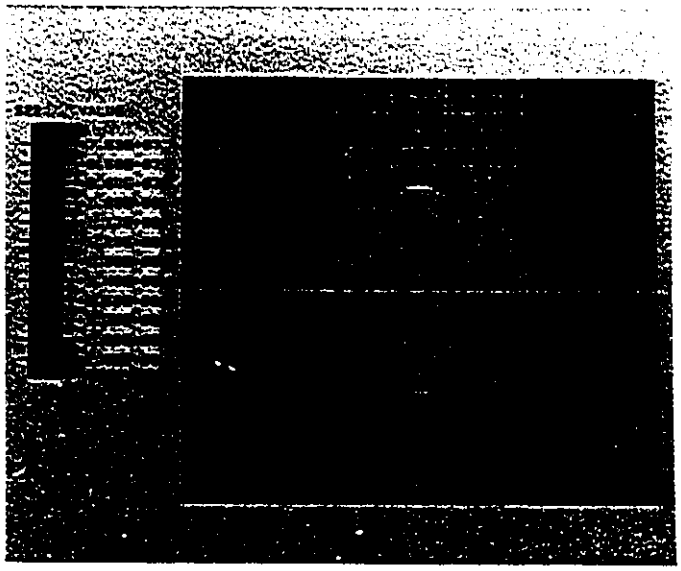

(f) at 0.5% engineering strain.

Figure 7.5 The tensile stress redistribution with increase of the tensile loading in 6061-T4 Al/$(SiC)_p$ with 5% volume fraction.

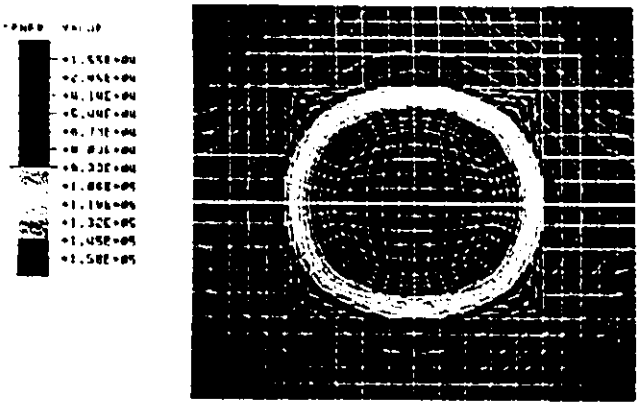

(a) at 0.0% engineering strain.

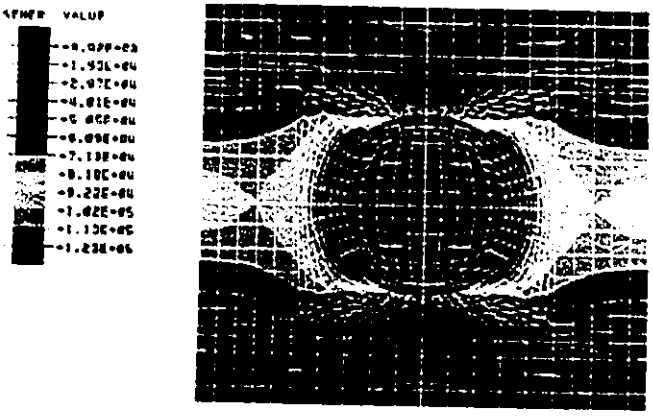

(b) at 0.1% engineering strain.

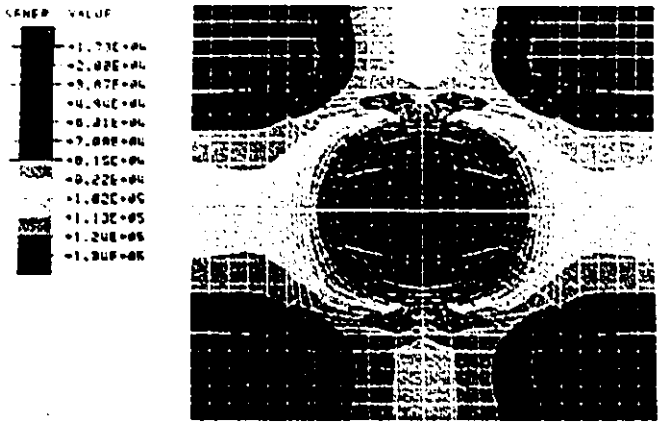

(c) at 0.2% engineering strain.

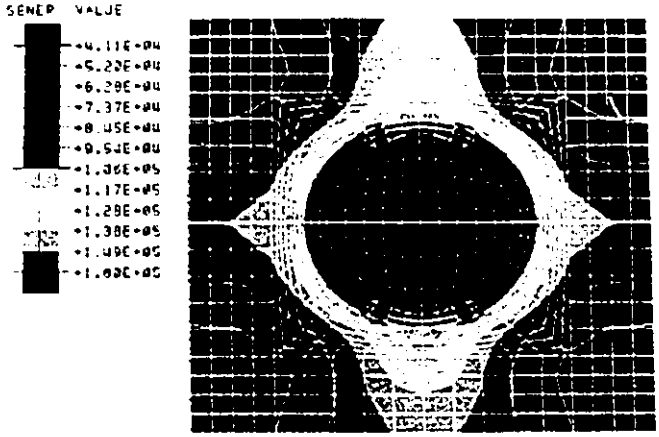

(d) at 0.3% engineering strain.

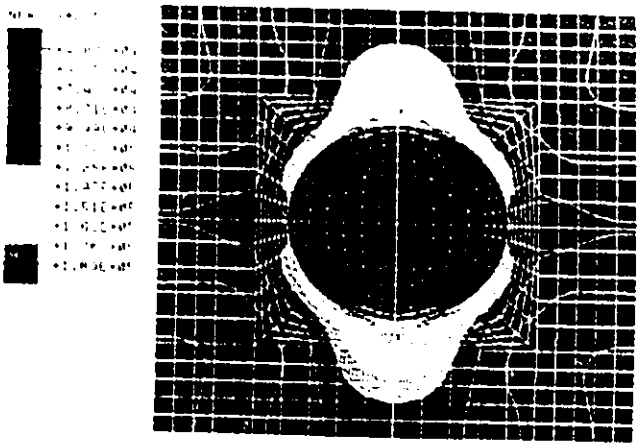

(e) at 0.4% engineering strain.

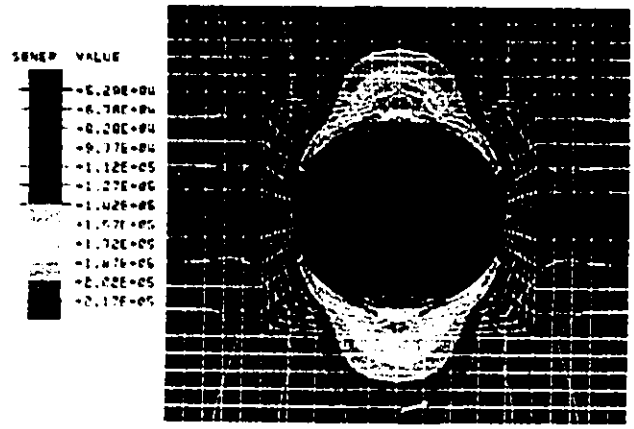

(f) at 0.5% engineering strain.

Figure 7.6 The strain energy density redistribution with increase of the tensile loading in 6061-T4 Al/(SiC)$_p$ with 5% volume fraction.

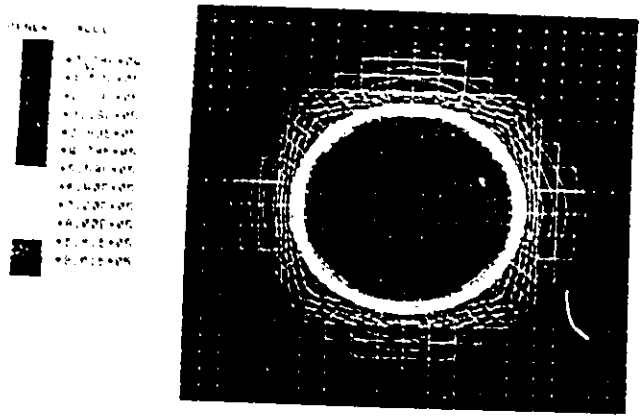

(a) at 0.0% engineering strain.

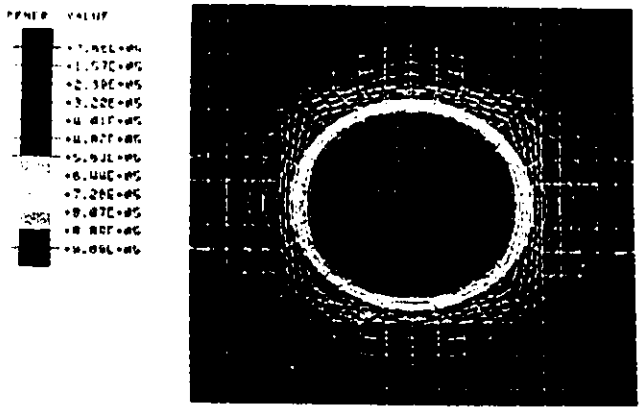

(b) at 0.1% engineering strain.

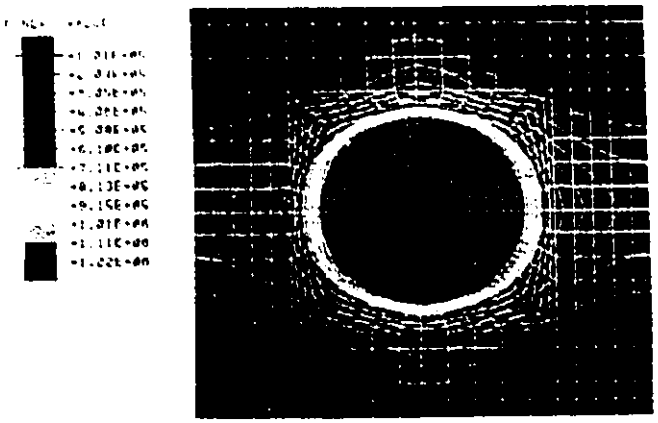

(c) at 0.2% engineering strain.

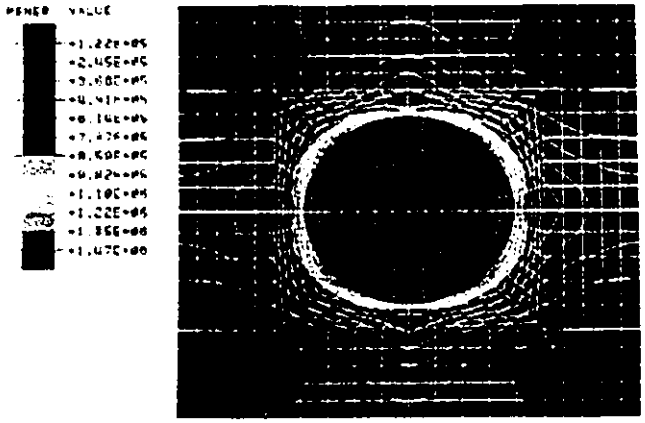

(d) at 0.3% engineering strain.

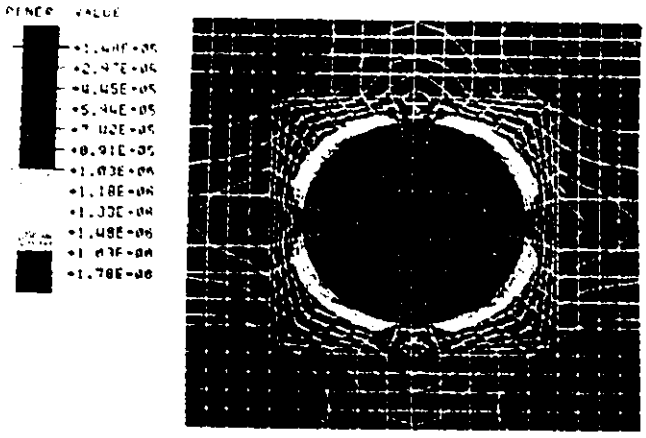

(e) at 0.4% engineering strain.

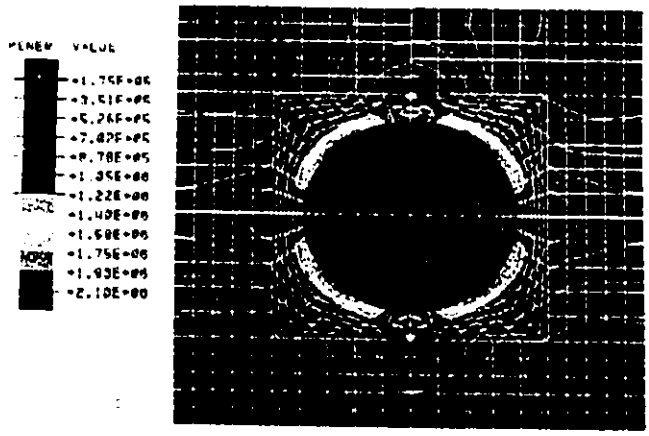

(f) at 0.5% engineering strain.

Figure 7.7 The plastic energy density redistribution with increase of the tensile loading in 6061-T4 Al/$(SiC)_p$ with 5% volume fraction.

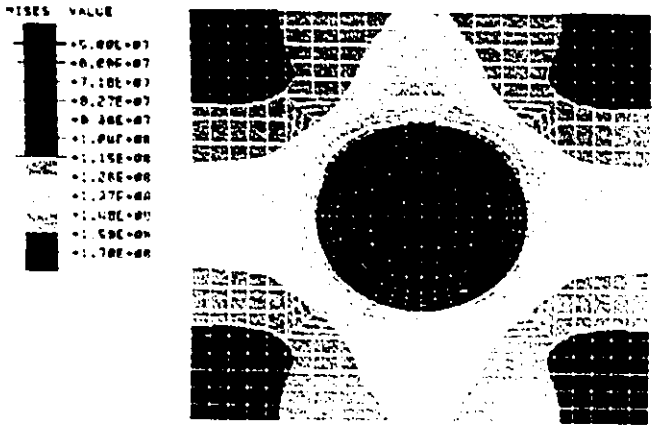

(a)

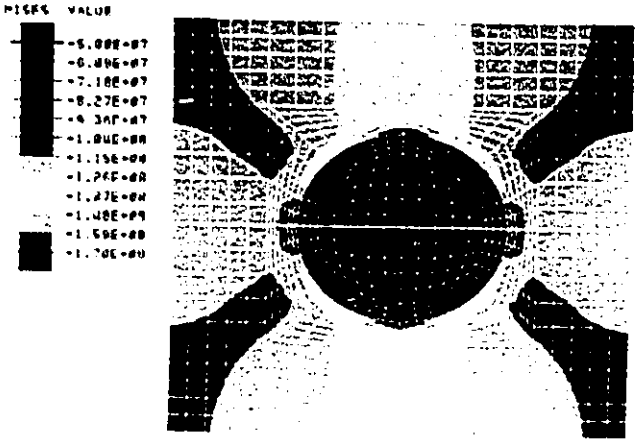

(b)

Figure 7.8 A comparison of the Von Mises stress contours in 6061-T4 Al/$(SiC)_p$ MMCs with 5% volume fraction at 0.5% overall strain: (a) with thermal stress; (b) without thermal stress.

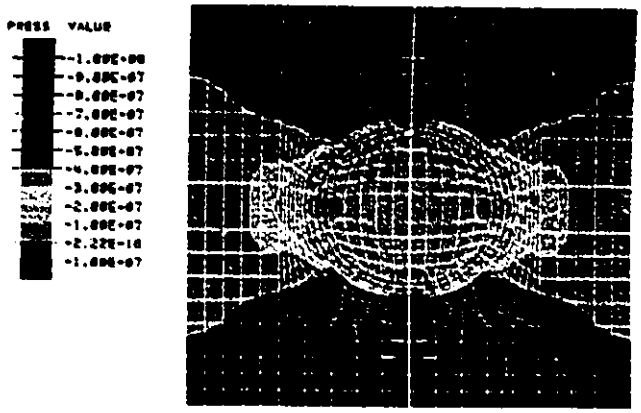

(a)

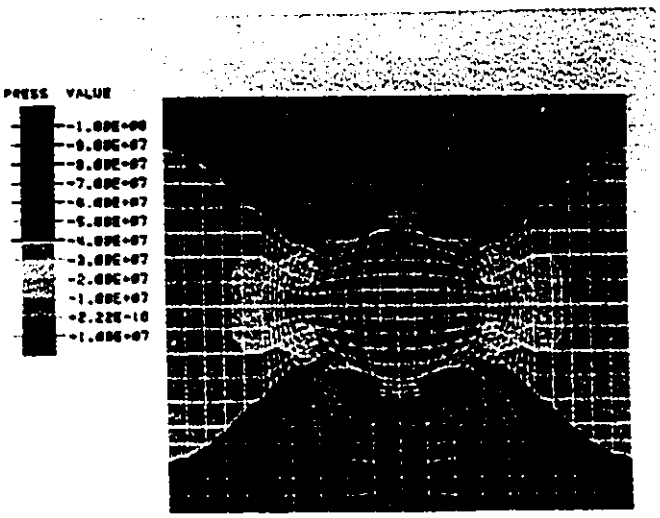

(b)

Figure 7.9 A comparison of the hydrostatic pressure contours at 0.5% overall strain: (a) with thermal stress; (b) without thermal stress.

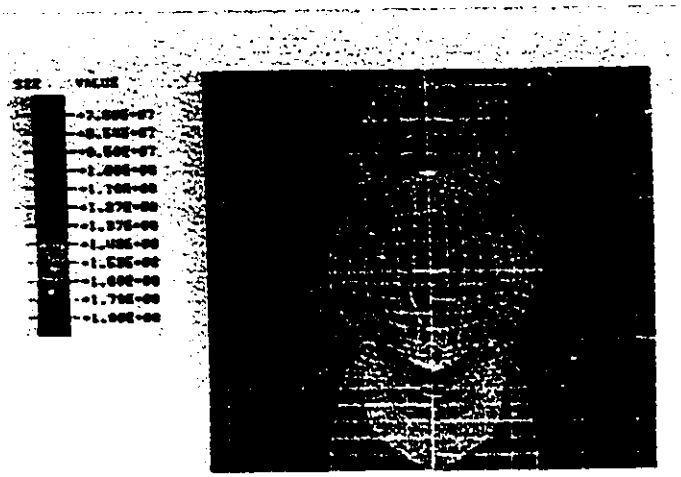

(a)

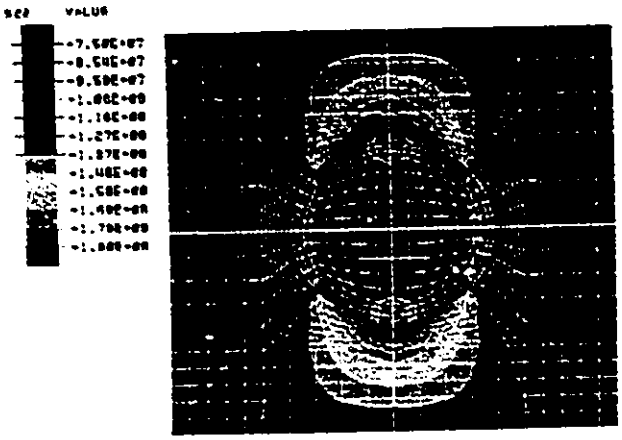

(b)

Figure 7.10 A comparison of the tensile stress contours at 0.5% overall strain: (a) with thermal stress; (b) without thermal stress.

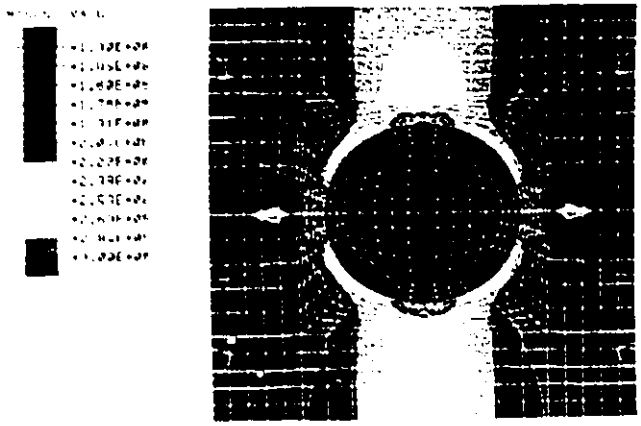

(a)

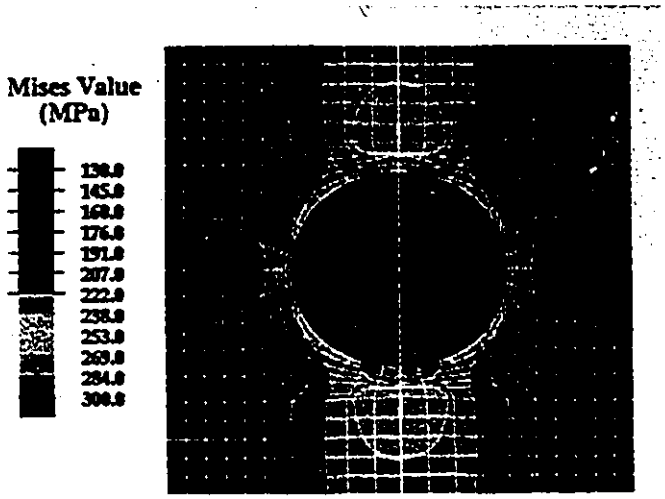

(b)

Figure 7.11 A comparison of the Von Mises stress contours in 6061-T4 Al/$(SiC)_p$ MMCs with 5% volume fraction at 5% overall strain: (a) with thermal stress; (b) without thermal stress.

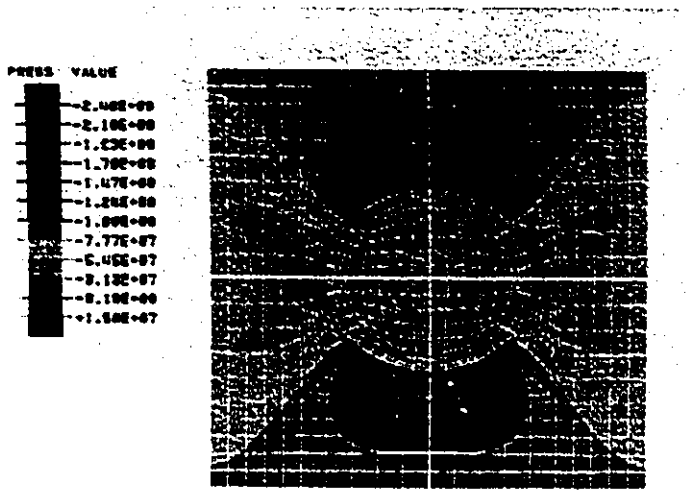

(a)

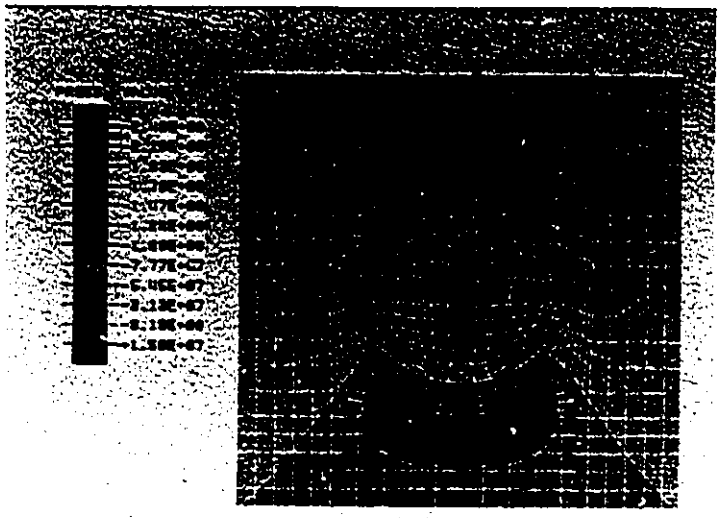

(b)

Figure 7.12 A comparison of the hydrostatic pressure contours at 5% overall strain: (a) with thermal stress; (b) without thermal stress.

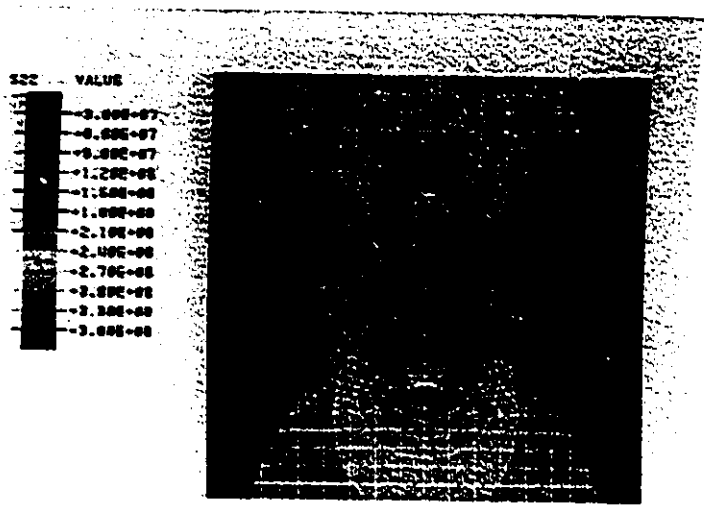

(a)

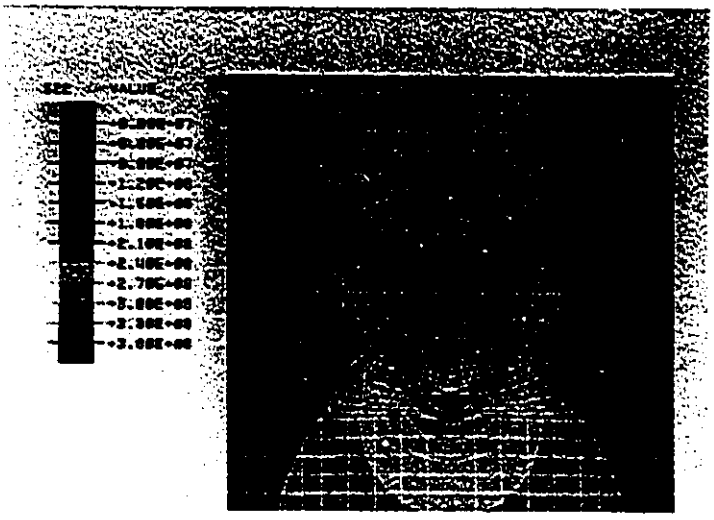

(b)

Figure 7.13 A comparison of the tensile stress contours at 5% overall strain: (a) with thermal stress; (b) without thermal stress.

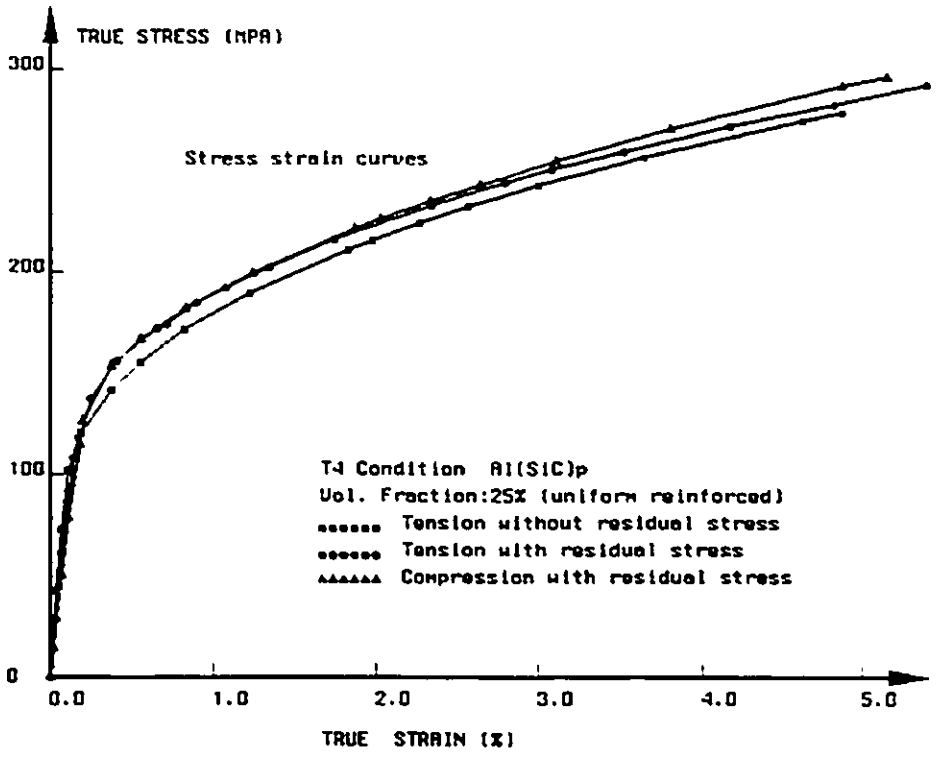
TRUE STRESS (MPA)
300
200
100
0
Stress strain curves
T4 Condition Al(SiC)p
Vol. Fraction:25% (uniform reinforced)
Tension without residual stress
Tension with residual stress
Compression with residual stress
0.0
1.0
2.0
3.0
4.0
5.0
TRUE STRAIN (%)

(a)

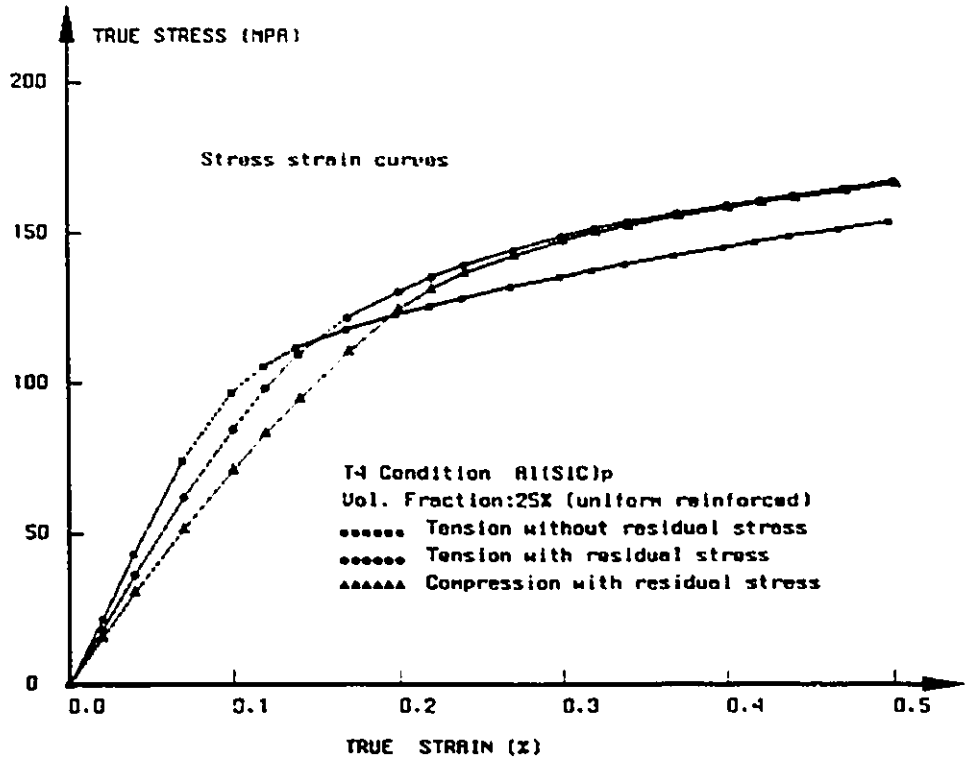

(b)

Figure 7.14 The stress strain curves predicted in 6061-T4 Al/(SiC)$_p$ MMCs under tensile loading and under compressive loading with 25% volume fraction with consideration of thermally induced stresses. (a) 0%-5% strain range. (b) 0.0%-0.5% strain range.

TABLES

Table 3.1 Material Properties

Materials	Young's M.	Poisson R.	Bulk M.	Shear M.
SiC	E^*=450 GPa	ν=0.17	k^*=227 GPa	μ^*=192 GPa
Aluminium	E=70 GPa	ν=0.33	k=68.6 GPa	μ=26 GPa

M. =Modulus R. =Ratio

Table 5.1 Mesh Arrangement at Different Volume Fractions

Volume Fraction	Node Number	Element Number
5.0%	2241	1750
10.0%	1910	1479
15.0%	1639	1262
20.0%	1253	966
25.0%	1126	875